Selenium modification of Rh(111) surfaces

Structure and electroactivity for oxygen reduction

Dissertation
zur
Erlangung des Doktorgrades (Dr. rer.nat)
der
Mathematisch-Naturwissenschaftlichen Fakultät
der
Rheinischen Friedrich-Wilhelms-Universität Bonn

vorgelegt von

Shahid Iqbal

aus

Islamabad, Pakistan

Bonn，2015

Angefertigt mit Genehmigung der Mathematisch-Naturwissenschaftlichen Fakultät
der
Rheinischen Friedrich-Wilhelms-Universität Bonn

Promotionskommission

Erster Gutachter: Prof. Dr. Helmut Baltruschat
Zweiter Gutachter: Prof. Dr. Thomas Bredow
Fachnaher Gutachter: Prof. Dr. Werner Mader
Fachfremder Gutachter: Prof. Dr. Karl Maier

Tag der mündlichen Prüfung: 16.07.2015

Erscheinungsjahr: 2015

Bonn, 16.07.2015

Shahid Iqbal

For my Motherland (Pakistan),

My Parents,

My beloved Wife

Contents

Chapter 1:	**Fundamentals**	**1**
1.1	Research overview	1
1.2	Introduction: oxygen reduction reaction (ORR)	1
1.3	Interfacial electrochemistry at model surface	3
1.3.1	The electrode/electrolyte interface	4
1.3.2	*fcc* (111) surfaces	5
1.4	Adsorption at single crystal surface	6
1.4.1	Physisorption	7
1.4.2	Chemisorption	7
1.4.3	Adsorbate superstructures	7
1.4.4	Adsorption sites	8
1.5	Electroctalysis	10
1.5.1	Surface modification and electrocatalysis	10
1.5.2	Fundamentals of film growth on substrate	11
1.5.3	Electronic effect	12
1.5.4	Atomic ensemble effect	13
1.6	Fuel cells	13
1.6.1	Operational characteristics of fuel cell	16
1.6.2	Catalysis and fuel cell	18
1.6.3	Electrochemistry of hydrogen and its catalysis	18
1.6.4	Electrochemistry of oxygen and its catalysis	19
1.7	Chapters overview	21
	References	23
Chapter 2:	**Methodology**	**25**
2.1	Cyclic voltammetry (CV)	25
2.1.1	Electron transfer and mass transport controlled processes	25
2.1.2	Hydrodynamic techniques	28
2.1.3	Dual thin layer flow through cell	28
2.2	Chemicals, solutions and electrode material	30
2.3	Laboratory glassware cleaning solution	31
2.3.1	Conventional electrochemical glass cell 'H-Cell'	31
2.3.2	Reference Electrode	32
2.3.3	Cleaning and preparation of single crystals	33
2.4	Deposition of Se sub-monolayer and more than monolayer at fcc(111)	35

	single crystals	
2.4.1	Spontaneous adsorption	36
2.4.2	Forced adsorption	36
2.5	Scanning Tunneling Microscope (STM)	36
2.5.1	EC-STM Operation	39
2.6	Atomic Force Microscope (AFM)	40
2.6.1	Contact Mode	43
2.6.2	Tapping or intermittent contact mode	44
2.6.3	Non-Contact Mode	45
2.6.4	Lateral Force Microscopy	46
2.6.5	Force Distance Curve	47
2.6.6	The Tomlinson model of friction	48
2.6.7	Forces in fluids	49
2.7	Cleaning of the STM/AFM cell	50
2.7.1	STM tips	50
2.7.2	Isolation of the tips	51
2.8	Scanning Probe Microscope (SPM)	52
2.8.1	AFM cantilever	52
2.8.2	STM/AFM Images analysis	53
2.8.3	Lateral force friction analysis	54
2.9	Differential Electrochemical Mass Spectrometry (DEMS)	54
2.10	Inductive heating method for single crystal electrode preparation	55
	References	56
Chapter 3:	**The Oxygen Reduction Reaction (ORR)**	**59**
3.1	Introduction	59
3.2	Experimental	62
3.3	Results and Discussion	63
3.3.1	Electrochemistry of selenium on Rh(111)	63
3.3.2	Scanning Tunnelling Microscope (STM) measurements on Se/Rh(111)	65
3.3.2.1	In situ STM of Se on Rh(111): Potential dependence modification	65
3.3.3	In situ AFM of Se on Rh(111): Potential dependence modification	73
3.4	Adlayer structure on Rh(111)	73
3.5	Conclusions	80
	References	81
Chapter 4:	**Quantitative determination of H_2Se at model metal fcc(111) selenide surface: DEMS and SPM studies**	**83**
4.1	Introduction	83
4.2	Experimental	86

4.2.1	Preparation and modification of massive single crystal electrodes with Se	86
4.2.2	DEMS calibration	87
4.3	Results and Discussion	88
4.3.1	Selenide determination on selenium modified fcc(111) surfaces	88
4.4	Surface morphology of the selenium modified fcc(111) surfaces using SPM	94
4.4.1	Reductive stripping of Se and its morphology by AFM	94
4.4.2	Oxidative stripping of Se and its morphology by STM	98
4.5	Discussion	99
4.6	Conclusions	101
	References	102

Chapter 5: ORR on Rh(111) and Se modified Rh(111) surface 104

5.1	Introduction	104
5.2	Experimental	106
5.2.1	Preparation and electrochemistry of massive Rh single crystal electrodes	106
5.2.2	CO charge transients	107
5.3	Results and discussion	107
5.3.1	Determination of the PTZC for Rh(111) by CO displacement	107
5.3.2	ORR on Rh(111)	110
5.3.3	ORR on Se modified Rh(111)	113
5.3.3.1	Surface modification of Rh(111) ($4x10^{-5}$ M H_2SeO_3)	113
5.3.3.2	Surface modification of Rh(111) with diffusion controlled concentrated solution of Se (10^{-6} M H_2SeO_3) and its ORR activity	114
5.3.3.3	Surface modification of Rh(111) with Se ($4x10^{-5}$ M H_2SeO_3)	116
5.4	Conclusions	120
	Reference	121

Chapter 6: Oxygen reduction at inductively heated modified chalcogenide Surfaces and its morphology 123

6.1	Introduction	123
6.2	Experimental	124
6.2.2	Heat treatment of Se modified Rh(111) electrode	125
6.2.3	CO stripping	125
6.3	Results and discussion	126
6.3.1	CO characterization of Se modified Rh(111) and its NSAs	126
6.3.2	ORR activity of heat treated Se/Rh(111)	130
6.3.3	Surface morphology of heat treated Se/Rh(111)	134
6.3.4	Potential dependent stability	135
6.3.4	Stability in air	137

6.3.5	Effect of temperature on surface morphology	137
6.4	Conclusions	140
	References	141
Chapter 7:	**Friction studies**	**142**
7.1	Importance of friction on Selenium modified fcc(111) surfaces	142
7.1.1	Introduction	142
7.1.2	Experimental	143
7.1.3	Results and discussion	144
7.1.3.1	Friction on a pure Rh(111)	144
7.1.3.2	Friction on selenium modified Rh(111) surface	147
7.1.3.3	Atomic stick slip on Se modified Rh(111)	151
7.1.3.4	Friction on selenium modified Au(111) and Pt(111) surfaces	152
7.2	Friction at organic adsorbates	156
7.2.1	Friction on pyridine	156
7.2.2	Preparation and modification of massive single crystal electrodes	156
7.2.3	Results and Discussion	157
7.3	Surface morphological studies of Nafion®/Pt(100) interface	163
7.3.1	Introduction	163
7.3.2	Experimental	165
7.3.3	Results and Discussion	167
7.3.4	Conclusions	173
	References	174
	Summary	**176**
	Appendix A	**179**
	Appendix B	**188**
	Appendix C	**199**

Notations

A	Current efficiency	N	Step density
A_{Geom}	Geometric surface area	n	Terrace width
A_{real}	Real surface area	Q_F	Faradaic charge
C	Concentration	Q_H	Charge of H_{ad} at Pt surface
C_0	Initial concentration	Q_i	Ionic charge
C_{eq}	Concentration at equilibrium state	r	Atomic radius
E	Potential	t	Time
e	Elemental charge, 1602 x 10^{-19} C	u	Electrolyte flow rate
E_0	Initial potential	z	The number of electrons transferred
E_{ads}	Adsorption potential	α	Angle between terrace plane and surface plane
E_u	Final potential	Γ_{CO}	CO concentration at Pt surface
F	Faraday constant, 96485 C·mol^{-1}	Γ_H	Number of surface active sites
I_F	Faradaic current	Δd	Inter-planer spacing
I_i	Ionic current	θ_{step}	Coverage at step
j	Current density	ϑ_{CO}	Relative coverage of CO
K^*	Calibration const. of DEMS	ν	Potential scan rate
D	Diffusion coefficient	τ	Time constant
η	Overpotential	Φ	Work function
		Ψ	Binding energy

Abbreviations

AES	Auger electron spectroscopy	MCFC	Molten carbonate fuel cell
AFC	Alkaline fuel cell	MSCV	Mass spectrometric cyclic voltammetry
AFM	Atomic force microscopy	ML	Monolayer
bcc	Body catered cubic	PAFC	Phosphoric acid fuel cell
CE	Counter electrode	PEMFC	Polymer electrolyte membrane fuel cell, Proton exchange membrane fuel cell
CN	Coordination number	PTFE	Poly tetrafluoroethylene
CO_{ad}	CO adsorbed layer	PZC	Potential of zero charge
CV	Cyclic voltammetry	OHP	Outer Helmholtz plane
DAFC	Direct alcohol fuel cell	ORR	Oxygen reduction reaction
DTLFC	Dual thin layer flow through cell	Ph	Potential hold
DEMS	Differential electrochemical mass spectrometry	Ps	Potential step
DFT	Density functional theory	Pt(pc)	Polycrystalline platinum
DMFC	Direct methanol fuel cell	rds	Rate determining step
EC-NMR	Electrochemical nuclear magnetic resonance	RE	Reference electrode
EIS	Electrochemical impedance spectroscopy	RHE	Reversible hydrogen electrode
EMS	In-situ electrochemical mass spectrometry	RRDE	Rotating ring disk electrode
EQCM	Electrochemical quartz microbalance	SCE	Saturated calomel electrode
fcc	Face centered cubic	SEIRAS	Surface enhanced IR absorption spectroscopy
FCs	Fuel cells	SERS	Surface enhanced raman spectroscopy
FM	Frank-van der Merwe growth mode	XPS	X-ray photoelectron spectroscopy
FTIR	Fourier transform infrared spectroscopy	SK	Stranski-Krasanov growth mode
GDL	Gas diffusion layer	SOFC	Solid oxide fuel cell
hcp	Hexagonal close packed	SPM	Scanning probe microscopy
IHP	Inner Helmholtz Plane	STM	Scanning tunnelling microscope
LDOS	Local density of state	SXS	Surface X-ray scattering
LEED	Low energy electron diffraction	TDS	Thermal deposition spectroscopy
LFM	Lateral force microscopy	UHV	Ultrahigh vacuum
LH	Langmuir-Hinshelwood		

Chapter 1: Fundamentals

1.1 Research overview

Hydrogen-oxygen fuel cells hydrogen gas is oxidized at the anode in aqueous solution. The protons on the other hand, are carried through the membrane to the cathode, where oxygen is reduced to achieve the general fuel cell reaction. This stage is called the oxygen reduction reaction (ORR), and is known to be very slow in comparison to the fuel oxidation stage. To stimulate kinetics at the cathode and to produce a tolerance with respect to small organic molecule (especially in direct methanol/ethanol fuel cells), an optimized ORR catalyst is required. The available platinum based material is quite effective in speeding up the oxidation but it is often poisoned by the process in the presence of small organics. Also, platinum is not cost effective for commercial use. Over the years, researchers have focussed on developing alternative catalysts to overcome the cost and tolerance issues. Other than precious metals, metal chalcogenides are considered promising because they selectively promote ORR and tolerate organics. Available research in this field primarily focuses on nanoparticles and hence provides little knowledge about the role of the chalcogenides adlayers for the promotion of selective ORR catalysis. Theoretical studies on model metal chalcogenide surfaces provide basic understanding of the mechanism of ORR. However, most studies while considering theoretical assumptions overlooked experimental issues. In addition, research has not yet resolved the stability issues of the adsorbed chalcogenide layer. Investigation of such processes on cathode surfaces in low temperature fuel cells has the advantage of improving efficiency for energy conversion and furnishing environmental benefits. Therefore, this thesis focuses on model electrodes such as rhodium and selenium modified rhodium to probe the adlayers structure and to understand the ORR mechanism.

1.2 Introduction: oxygen reduction reaction (ORR)

The oxygen reduction reaction (ORR) is an important reaction in the area of electrocatalysis and fuel cell technology. The oxygen electrochemistry is complex and proceeds via a multi-electron charge-transfer mechanism. It is relevant not only to fundamental electrochemistry but also to materials science. The aim of such investigation is to improve the efficiency of such a process at the cathode surface in low

temperature fuel cells. The kinetics of oxygen reduction and its improvement is one of the key issues in the electrochemical energy storage and energy supply. In low temperature polymer electrolyte membrane fuel cells (PEMFC), the largest part of the energy loss is due to the huge overvoltage of oxygen reduction of more than 400 mV resulting in a loss of one third of the thermodynamically achievable voltage [1].

The oxygen cathode is used in some other applications such as metal air batteries. Its use in Zn-O_2 rechargeable batteries is also being tested, and even for Li ion batteries. The Li ion batteries are especially important because of the great weight advantages [2, 3]. Further, in chlor-alkali electrolysis cells, utilization of oxygen consuming cathodes results in drastic reduction of energy consumption compared to conventional cathodes [4].

Of all the available cathode materials, platinum (Pt) is still the best known catalyst. However, for ORR on Pt electrodes, the theoretical reversible oxygen potential of 1.23 V was never achieved. It is worth mentioning that in the case of hydrogen oxygen fuel cells, both anodic and cathodic reactions should occur at potentials as close as possible to thermodynamic electrode potential. This depends on the nature of electrode material, catalysts and electrolyte.
(M. R. Tarasevich, A. Sadkowski, E. Yeager. In Comprehensive Treatise in Electrochemistry, J. O'M. Bockris, B. E. Conway, E. Yeager, S. U. M. Khan, R. E. White (Eds.), Chap. 6, Plenum, New York (1983).)

The ORR on a platinum electrode is one of the most widely studied electrochemical reactions. However, as the ORR proceeds via a multi-electron mechanism with various elementary steps involving different intermediates, it is still not completely understood. Especially, the irreversible nature of the cathodic oxygen reduction reaction in aqueous solutions even at elevated temperatures is least understood. Usual electrochemical kinetic measurements provide information only about the rate controlling step and the number of e^- preceding it and do not throw light on the entire multi-electron mechanism. In addition, redox processes in the hydrogen oxygen fuel cell occur at different potentials and could result in alteration in surface properties of the electrode surface. The situation becomes complicated with the involvement of a large number of possible pathways for the ORR.

Extensive efforts have been put forward in realizing the factors which affect the catalysis of the ORR. In general, not enough fundamental knowledge is available to implement a rational approach for designing better electrocatalysts. Damjanovic tried to address this situation in his famous review cited after Nanotechnology in Electrocatalysis for Energy [5], as under

(1) Few materials (only noble metals and alloys) can withstand the highly positive potential associated with the oxygen reduction (or evolution) without undergoing dissolution themselves and hence contributing to the overall current.
(2) The mechanistic analysis of oxygen–reduction reactions is relatively complex owing to the numerous reaction steps and reaction intermediates with the energy of adsorption varying with the electrode potential and coverage. Furthermore, the reduction of O_2 may proceed either by a two-electron process to hydrogen peroxide or by a four-electron process leading to water. Hydrogen peroxide may, at least partially, reduce to water, or it may catalytically decompose.
(3) In the potential range in which oxygen dissolution occurs, the electrode surface may be covered with oxide or relatively bare, so meaningful conclusions on the catalysis may not be drawn.
(4) Due to the low-exchange current densities, the electrode reactions may become potential controlling, particularly at low current densities. So even traces of impurities can profoundly affect the overall kinetic.

1.3 Interfacial electrochemistry at model electrode surfaces

The study of the metal surfaces and their interfaces from an electrochemical point of view is relevant in many advanced technological processes which involve energy conversion reactions, for example, fuel cells and batteries [6]. Historically, simple electrochemical techniques were employed for measurement of current and charge using controlled potential to characterize the electrode-electrolyte interface [6]. The potentiodynamic techniques could be employed on a variety of well defined surfaces in a given electrolyte to generate responses which could be considered characteristics of these surfaces in the given electrolytes.

1.3.1 The electrode/electrolyte interface

Presently surface sensitive techniques, which are sensitive enough to characterize interfacial composition, are helpful in getting a detailed picture of the structural dynamics and mechanistic aspects of the interfacial reactions. This information facilitates the determination of the strength of the adsorbents [7]. Moreover, the development of theoretical methods offers a detailed picture of the structure and reactivity relation at the electrode-electrolyte interface of model surfaces. (A detailed description of the characterization techniques and theoretical modelling of surface and structure relation of electrode-electrolyte interface on model surfaces is presented in *G. A. Somoraji, Y. Li 'Introduction to Surface Chemistry and catalysis, Wiley 2010 and W. Schmickler, E. Santos, Interfacial Electrochemistry, Oxford University Press, 2010*)

It is generally believed that all electrochemical phenomena happen at the electrochemical interface. Conventionally, it is referred to as the spatial region which consists of the portion of the electrode surface in contact with the electrolyte and depicted as in fig. 1.1.

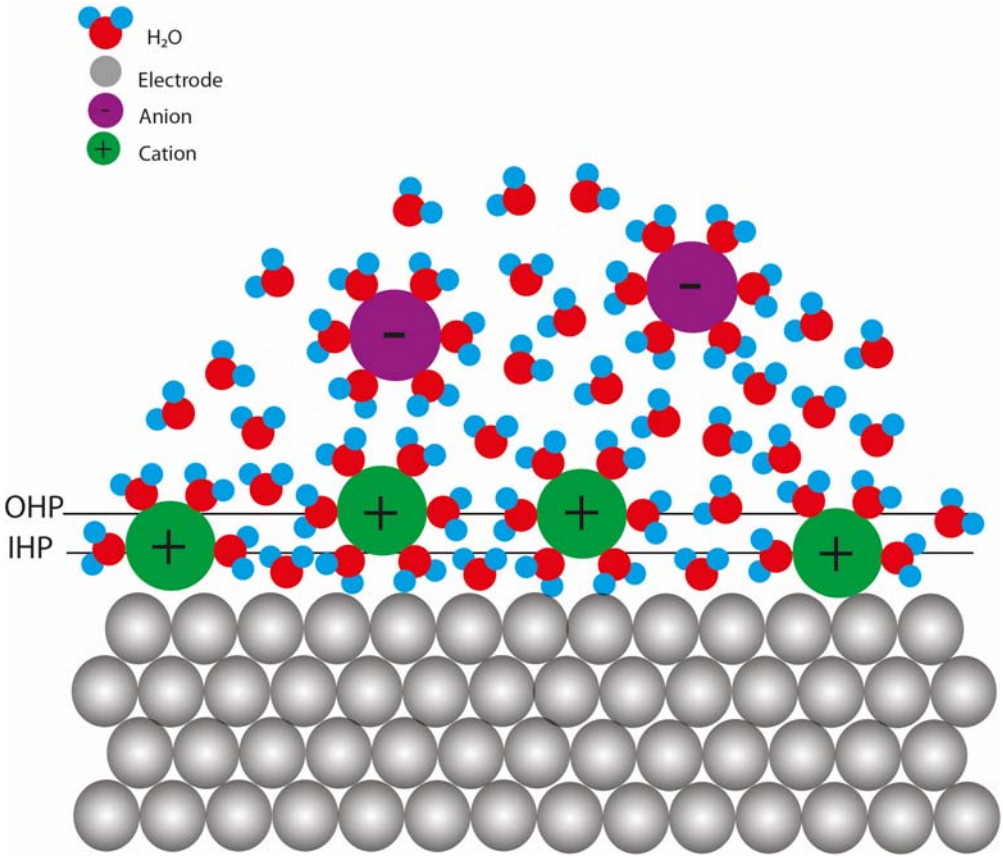

Figure 1.1: Pictorial representation of a negatively charged electrochemical interface.

The specifically adsorbed anions that are covalently bonded to electrode surface constitute the inner Helmholtz plane (IHP). Whereas solvated anions develop electrostatic interaction with the electrode surface which constitutes the outer Helmholtz plane (OHP). Consequently, an intense electric field of strength about 10^9 V/m is easily generated [8]. The transfer of the charge at the interface is responsible for the electrochemical reaction.

At the atomic level, every metal is relatively heterogeneous and polycrystalline. These surfaces are often atomically rough and posses defects, such as steps, kinks and vacancies. These surfaces contain atoms of the same element which are arranged in various combinations. Each of these combinations possesses different local electronic structure which results in various physical and chemical properties. This is the case for the polycrystalline surface and explains the reason for not using them for the atomic scale experimental and theoretical studies. A well defined ordered structure is required for a better understanding of the processes that occurs at the atomic level. Most of the transition metals crystallize either in cubic or hexagonal configuration. The cubic system can be divided further into body centred or face centred (*bcc* or *fcc*). A large number of metals suited for electrocatalysis studies usually adopt the *fcc* structure e.g., Pt, Pd, Rh and Ir. A single crystal surface is prepared by precise cutting of a defined surface along a given crystallographic plane [9]. The characterization of this surface is based on Miller indices (*hkl*), which also provide information related to the orientation of atoms in a space lattice. The three basic low Miller index planes provide the origin of a building block of a surface. These are extensively examined based on their low surface energies, relatively high stability, and higher symmetries. Moreover, as mentioned earlier, the electrochemical behavior of either can generally be explained as a sum of the individual properties of these low index surfaces.

1.3.2 *fcc* (111) surfaces

The focus of the current investigation is to study the electrocatalytic reaction on electrochemically modified Rh(111). The main objective is exploration of (111) plane of *fcc* system, which is generated by cutting an *fcc* surface composed from equidistance vectors from origin along x, y and z-axis. This results in an atomically smooth surface with hexagonal symmetry as depicted in fig. 1.2.

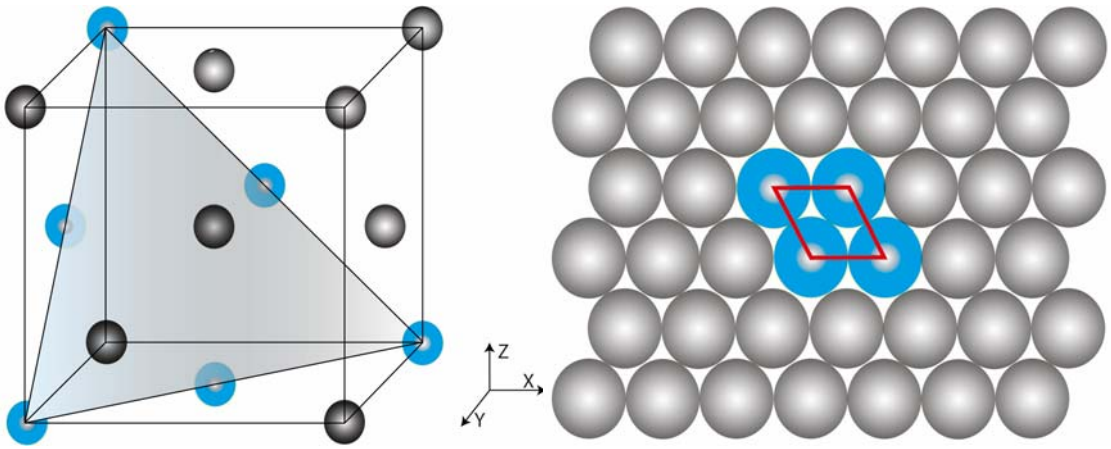

Figure 1.2: Unit cell of a face centred cubic structure (left) and atomic structure of the corresponding (111) surface with position of (111) plane (right).

1.4 Adsorption at single crystal surface

The process of adhering of the atom, ions or molecules to a surface is known as adsorption. These binding forces are normally weak and the process is reversible. Hence the adsorption/desorption phenomenon is considered crucial for various reactions occurring at the electrode-electrolyte interfaces.

The specific adsorption is preceded by chemical bond formation and normally happens at specific sites. In most practical applications, adsorptions involving interaction with moderate strengths are considered advantageous. If the adsorbate binds strongly to the surface, it causes reduction in catalytic activity of the surface. This binding strength of the adsorbates with a particular metal laid the foundation of the Sabatier principle [10]. The Sabatier principle serves as the basis for the development of the famous volcano plot for most electroactive metals. The most common example is the adsorption of the CO on Pt, which results in poisoning of the surface and hence decrease in the electrocatytic activity [11-14].

This is one of the major factors in the overall efficiency loss in methanol fuel cell.
Adsorption based on the amount of their enthalpies is broadly classified into physiosorption and chemisorption.

1.4.1 Physiosorption

In physiosorption, adsorbates are bonded to adsorbents through relatively weak attractive forces, which are normally long range Van der Waals type interactions. These kinds of interactions experienced by all atoms and molecules are mainly electrostatic in nature. The energy associated with physiosorption is small enough and is comparable to that of enthalpies for liquefaction or vaporization in the range of 2-30 kJ/mol.

1.4.2 Chemisorption

In chemisorption, adsorbates are bonded chemically to adsorbents through relatively strong attractive forces, which are either covalent or ionic in nature. The energies associated are much larger than that from physiosorption and range from 40 to 250 kJ mol^{-1}. The strong interactions may change the chemical state of adsorbate. It may dissociate and can form new adsorbates. Similarly, substrate structure may also change, either with the relaxation of interlayer spacing in the top most layers or by overall reconstruction of top layer atomic structure.. In case of well defined surfaces, adsorbate-surface interaction often results in appearance of an ordered structure. This may be a two dimensional array formed essentially of adsorbate or a mixture of adsorbate-substrate atoms. The adsorbed adlayers can be classified as 'impurity-induced reconstruction' 'ordered adsorbate layer' or 'ordered surface phase'.

1.4.3 Adsorbate superstructures

Most atoms and molecules form adlayers on single crystalline surfaces. The determination of the atomic structure of these adlayers involves several analytical techniques. Scanning tunneling microscope (STM) and low energy electron diffraction (LEED) are considered the most appropriate. In addition, X-rays photon electron spectroscopy (XPS) provides a quantitative estimate of adsorbate surface coverage. A real space image of adsorbate with atomic resolution is obtained with STM. These techniques help in determining the two dimensional lattice of the superstructure in relation to associated underlying substrate. This facilitates the establishing of the tentative structural model.

The surface concentration of adsorbate on a substrate is known as coverage of

adsorbate, θ, and it is mathematically represented as

$$\theta = \frac{\text{Number of adsorption sites occupied by adsorbate}}{\text{Total number of adsorption sites on the surface of the substrate}} = \frac{\Gamma}{\Gamma_{max}} \qquad 1.1$$

When θ = 1, the adsorbate species form a monolayer or either given as ratio of adsorbate species to the number of surface atoms of the substrate

$$\vartheta = \frac{\Gamma}{N_{surf.\ atoms}} \qquad 1.2$$

When ϑ = 1

This corresponds to one adsorbate atom or molecule per one substrate atom

.

1.4.4 Adsorption sites

The atoms arranged in a closed packed manner possess six fold symmetry, and the obtained planes are known as closed packed planes. Stacking up these planes on each other results in either hexagonal closed packed (*hcp*) or face centered closed packed (*fcc*) structure, which gives an ABA configuration for hcp and ABC configuration for fcc. Positioning two closely packed planes on each other results in creation of interstitial sites, which are of two types. These interstitial sites are arranged in an alternate way. In case of octahedral, the interstitial site touches 6 atoms and in tetrahedral the interstitial site touches four atoms as shown in fig. 1.3

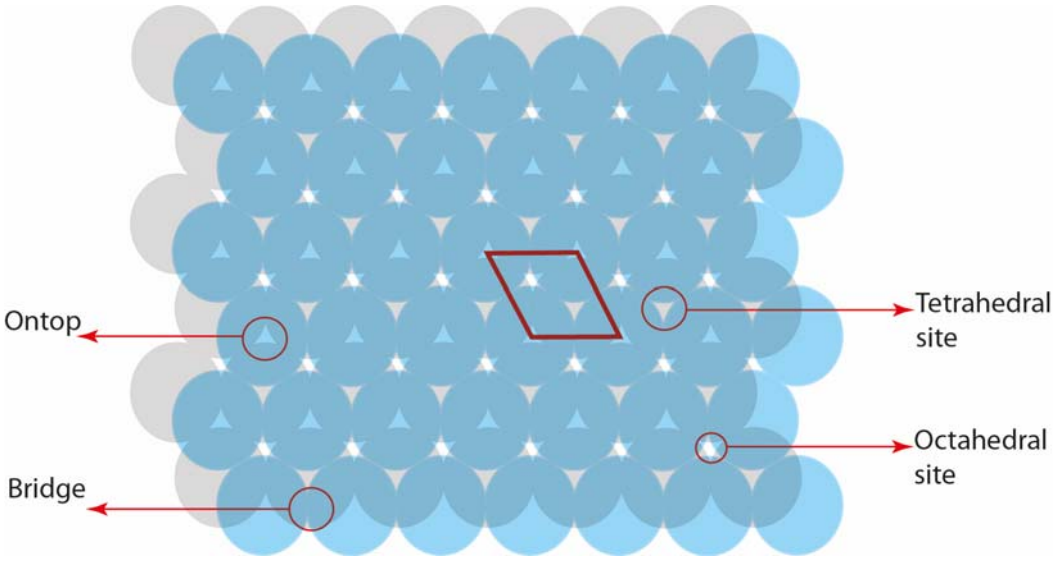

Figure 1.3: Ball models of the different adsorption sites on a *fcc*-(111) surface

In case of face centered cubic (*fcc*) system closely packed planes are arranged in a repetition pattern of ABC in such a way that atoms of second layer (B) resides on

interstitial sites generated due to layer (A) with 50 % occupancy. Similarly, closely packed plane (C) resides on those interstitial site of layer (B) which match with that of unoccupied interstitial sites in layer (A), and continue as presented in fig. 1.3.

The adsorbing species on *fcc*-(111) surfaces may attach at different positions: e.g., on-top if the adsorbent is attached to a single atom of the surface. It is called bridge when it adsorbed between two neighboring metal atoms or three-fold hollow if it occupies three contiguous surface sites. At this point, these three-fold hollow interstitial site can be of two types in case of *fcc*-(111) surface as mentioned above, *fcc*-hollow (octahedral), if the threefold-hollow site coincides with a hole in the layer underneath, or *hcp*-hollow (tetrahedral), if the three-fold hollow site coincides with an atom in the layer underneath (see fig. 1.3).

Anion adsorption on the metal surfaces is of fundamental concern in electrochemical reactions. The electrode-electrolyte interface is regarded as an electric double layer developed by a charged metal surface with oppositely charged ions in solution in its close proximity. The interactions of ionic species with the electrode surface occur either purely by electrostatic forces or by chemical bond formation depending upon their chemical nature. Strongly solvated ions (such as ClO_4^-, F^-) prefer electrostatic interaction, whereas weakly solvated ions (such as, SO_4^{2-}, halides) favour chemical type interaction. These are often termed as nonspecific and specific adsorption respectively. It is generally believed that these specifically adsorbed species on electrode surfaces can significantly alter their electrocatalytic activity [15, 16]. The less specifically adsorbed sulfate/bisulfate species were most widely studied as adsorbed anion on well-defined surfaces, since sulfuric acid is utilized as a supporting electrolyte for electrochemical characterization of Au and Pt single crystal electrodes [15, 17-20].

The phenomenon of adsorption is explained assuming that the adsorbing species comes to rest after adsorption at the reaction site, where reactions take place in a dynamic fashion. Hence, for a reaction to proceed, a molecule has to interact with a number of atoms from the beginning to the final product involving intermediates. The surface modification of electrodes is very helpful in investigating the mechanisms of certain electrochemical reactions such as in the case of ORR [21-23]. In our current work, the main intention is to investigate the role of the geometry of atomic ensembles in

electrocatalysis, and also on the development of adlayer structures, namely selenide-modified Rh(111), which will be discussed in detail in the chapter 3. In order to get a brief idea about the adlayer structure on a metal surface, it is explained in (*G. A. Somorjai, Y. Li, Introduction to Surface Chemistry and Catalysis, 2nd Edition, John Willey & Sons Inc., New Jersey, 2010*).

1.5 Electrocatalysis

The similarities between the heterogeneous catalysts and electro-catalyst are that both involve the adsorption of the reactant on their surface, the generation of adsorbed reaction intermediates, and bond breaking and bond forming to yield products. However, the key difference between them is that in the case of electro-catalysts a potential is imposed in a controlled manner during the course of the reaction at the electrode-electrolyte interface. N. Kobosev and W. Monblanowa introduced the term electrocatalysis in 1934 *(N. Kobosev and W. Monblanowa, Acta Physicochim. URSS, 1 (1934) 611)*, which was later practically demonstrated for the hydrogen evolution reaction (HER) kinetics on various metals and determined metal-hydrogen bond energy and enthalpy of metal sublimation [24].

The activity of an electrocatalyst is strongly influenced by its chemical composition and structure. Therefore, the rate of an electrocatalytic reaction on the electrocatalyst surface depends mainly on its atomic structure. In addition to this the presence of active sites for adsorption of reactants to form bonds ultimately facilitates the formation of reaction intermediates and final products. In most of the practical applications of electrocatalysis, the relation of substrate structure-reactivity to selectivity is not completely understood. An understanding of this relationship is necessary for the development of efficient catalysts.

The well-defined single-crystal surfaces as model electrocatalysts have been extensively explored to investigate the influence of surface crystallography on reaction kinetics and also to evaluate the adlayer structure at the atomic and molecular scale. This process helps us understand the structure-reactivity relationships [25].

1.5.1 Surface modification and electrocatalysis

The electrocatalytic properties of an electrocatalyst can be modified by decorating its

surface with another metal using chemical or electrochemical means [26]. This modification could lead to either geometric or ensemble effects (purely due to the alteration of the present adsorption and reaction sites), electronic or ligand effects (mainly results in due to modification of electronic properties of substrate surface atoms) and bifunctional mechanism.

1.5.2 Fundamentals of film growth on substrate

The growth of the thin film was explained first theoretically on the basis of thermodynamcis of growing layer by Bauer, which was confirmed later on experimentally for growth of metal on metal [27]. Three important modes of nucleation and film growth were named after their inventors. These are Volmer-Weber, Frank-Van der Merwe, Stranski-Krastanov.

a) Volmer and Weber (VW) growth is characterized by three-dimensional island formation. This results from to the stronger interactions between the adatoms and weaker interaction between the adatoms and substrate. The formed islands are independent of crystallographic misfit [27] and a rough multilayer film results.
b) Frank and Van der Merwe (FM) growth mode proceeds by deposition of metal in a layer-by-layer manner. In this mode the interactions are stronger between the adatom and substrate than those between adatoms, which causes growth of the second layer only once the first layer is complete [28, 29].
c) Stranski and Krastanov (SK) growth is an intermediate mode between layer by layer and island mode. This mode proceeds in two steps; first a layer grows up to one, or a few monolayers followed by island formation above the first (or most recently) completed layer [30].

Each of these growth mechanisms is depicted schematically in fig. 1.4.

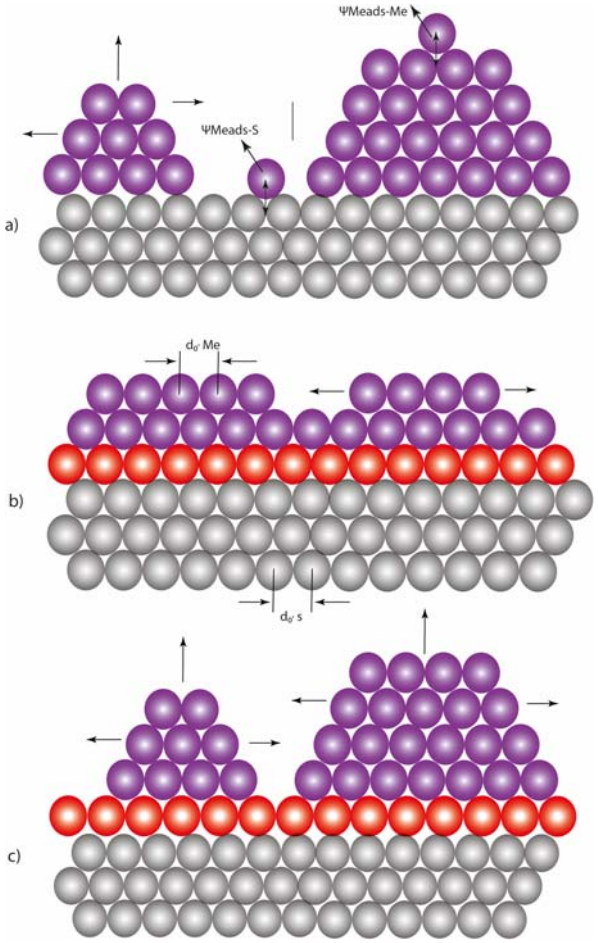

Figure 1.4: schematic representation of different growth modes in metal deposition on the foreign substrate. Cross-section views of (a) Volmer-Weber (VW: island formation), (b) Frank-van der Merwe (FM: layer by layer), and (c) Stranski-Krastanov (SK: layer plusisland) model for the film growth. Graphics reproduced based on ref. [30].

1.5.3 Electronic effect.

The physical and chemical properties of an electrode surface depend on its electronic structure, and also determine its role in electrocatalysis. Therefore, a detailed understanding of the electronic properties of an electrode surface, especially the potential of zero charge (PZC) and local density of state (LDOS) is essential to get an insight into electrocatalytic reactions at an atomic level [31]. Generally, the catalytic properties of a metal surface are modified by deposition of a foreign metal in submonolayer regime (partial coverage). Due to this modification, foreign metal adatoms may also undergo strain effects [32], which causes either the adatoms or the substrate metal atoms to occupy positions different from the equilibrium position in the bulk. The resulted surface modification leads to alteration in the electronic structure of the host metal, known as the electronic effect. This change of the electronic structure causes variation in the binding energy of adsorbed reactants and intermediates. Hence,

the modified surface reveals either increase or decrease in catalytic activity to bare metal surface.

1.5.4 Atomic ensemble effect

A group of minimum number of surface atoms with specific geometric arrangement will act as active sites for chemisorptions of reactants and intermediates. This is known as ensemble effect. The study of this effect is essential not only for understanding the electrocatalytic reaction mechanism, but also it is helpful in rational design of efficient electrocatalysts. These effects are useful in identifying the number of surface atoms required for binding and adsorption (molecule or intermediate). The effect also explains how a competing reaction can be selectively blocked, as a different atomic ensemble would be required. This can be beneficial in the case of a catalyst poison, when the adsorbent reactants or intermediates require more than one free neighbouring site (ensemble). Consequently, the poison can be inhibited by blocking that particular site without lowering the activity of the surface for the catalyzed reaction.

Detailed studies of the mechanism of these effects are helpful in designing new and improved catalysts required for fuel cell technologies. The mechanism of these effects is elaborated by *Balturschat et al. in Catalysis in Electrochemistry: From Fundamentals to Strategies for Fuel Cell Development, Chapter 9 A John Wiley & Sones, Inc, 2011, p 297* and *Feliu et al. in Fuel Cell Catalysis Chapter 7: Clues for the Molecular-Level Understanding of Electrocatalysis on Single-Crystal Platinum Surfaces Modified by p-Block Adatoms, 2009 John wiley & Sons Inc.*

1.6 Fuel Cells

The electrochemical devices which are capable of converting chemical energy (free energy of reactants) into electrical energy (e.g., for the reaction of molecular hydrogen and oxygen to water) in a spontaneous fashion occur in fuel cell and batteries.

The principle of the first practical fuel cell was demonstrated by Sir William Grove in 1839 [33]. This invention was well advanced in its time. It took just about a century for scientists to employ fuel cells practically and to utilize them as a source for on board

electrical power in space vehicles launched by NASA in early 1960. Presently, it is considered as one of the pillars for decentralized energy supply networks.

Several kinds of fuel cells exist (as summarized in fig. 1.5), of these the polymer electrolyte fuel cell (PEFC) is very important. PEFC is considered as one of the 21st century energy conversion devices and emerged as the most promising power source for a wide range of applications. However before PEFC really can contribute, their efficiency has to be considerably increased. It is thermodynamically established that the energy stored in hydrogen and several alcohols and aldehydes is much higher than for battery materials. At present, these substances are the most promising candidates for use as fuels in fuel cells. This provides the main motivation to develop the fuel cell technology and the so-called 'Hydrogen Vision'.

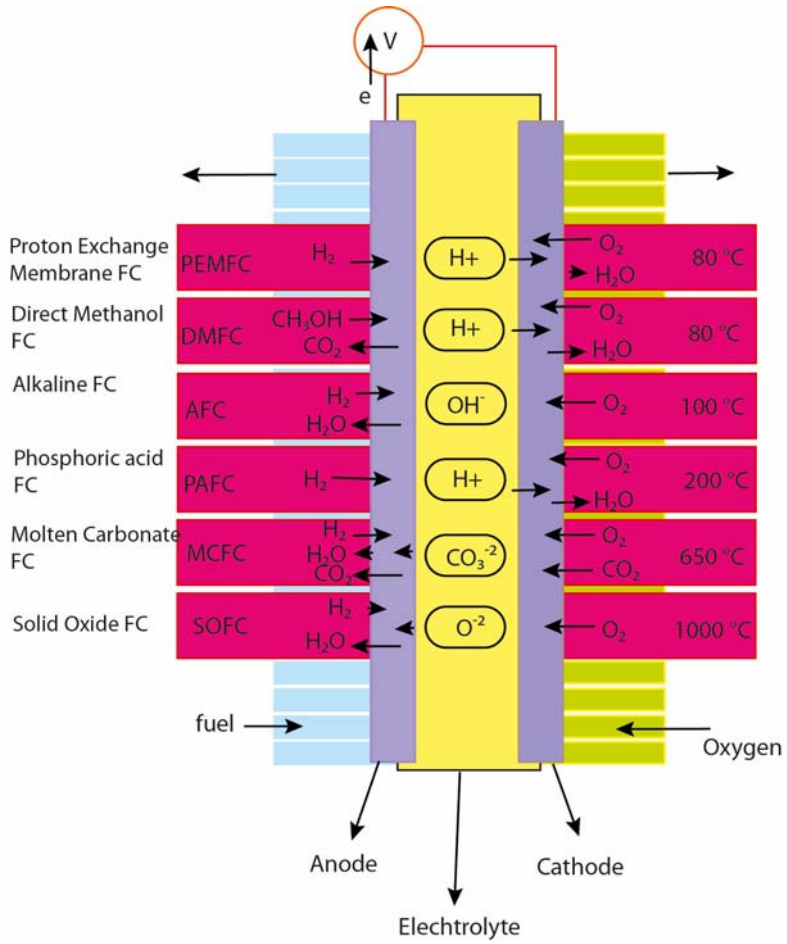

Figure 1.5: Various types of fuel cells

In the course of past years, among all available kinds of fuel cells technology some cells

improved significantly, for example alkaline fuel cells (AFC). However, large scale commercial uptake depends on improvement in the amount of catalyst loading and reduction in the cost of expensive materials. The improved alkaline fuel cells continued to find application in space missions, because cryogenic storage of gaseous fuels reduces their overall volume. Additionally alkaline fuel cells are used in the industrial energy sector. A detailed description on various kinds of fuel cells, associated advantages and shortcomings can be found in [34, 35].

As mentioned above the most likely technology for developing into highly efficient fuel cells is that of PEMFC as their performance is much better than other low temperature fuel cells. Like other cells, they are mainly composed of two electrodes separated by an ionomeric membrane. A schematic of which is shown in fig. 1.6.

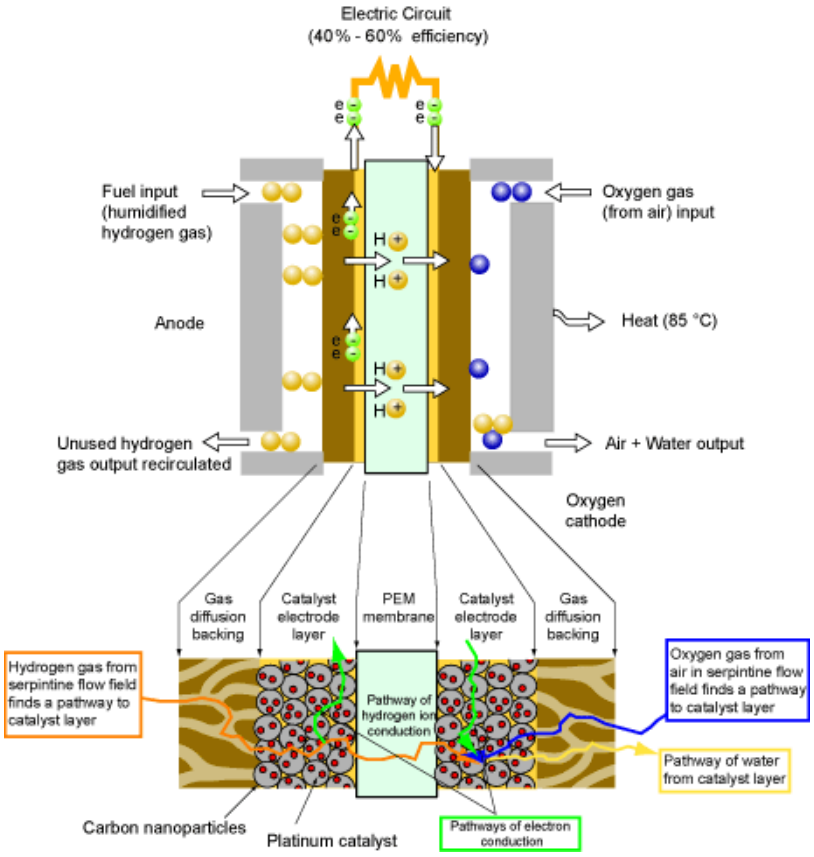

Figure 1.6: The Schematic of PEMFC and its architecture.
(http://physics.nist.gov/MajResFac/NIF/pemFuelCells.html)

The hydrogen fuel enters from anodic part and oxygen from the cathodic part of the cell. The overall cell reaction with their standard potential can be summarized as below

$$H_2 + 1/2\, O_2 \Leftrightarrow H_2O, \qquad E^{\circ}_{cell} = 1.23\ V \qquad 1.3$$

This overall reaction can be split in to anodic and cathodic half cell reactions as below

$$H_2 \Leftrightarrow 2H^+ + 2e^-, \qquad E^\circ_{anode} = 0\ V \qquad 1.4$$

$$O_2 + 4H^+ + 4e^- \Leftrightarrow 2H_2O, \qquad E^\circ_{cathode} = 1.23\ V \qquad 1.5$$

The electrochemical oxidation of hydrogen generates protons at the anode. These are transported to the cathode via an ionically conducting polymer membrane which separates the electrodes within the cell. The generated electrons can reach the cathode through the external circuit and complete the reduction of oxygen to produce water. Under ideal conditions at reversible cell potential the associated Gibbs free energy is -235.76 KJ/mol and standard enthalpy is -285.15 KJ/mol.

The PEMFC are mainly operated using gaseous fuel in the presence of solid electrolyte. It is used in common applications which need low temperature operation. However, its disadvantage is it will only operate with hydrogen which is free from carbon monoxide. This is a technically expensive solution. Nafion is the most commonly employed polymer electrolyte. It contains persulfonic acid ionomers similar in structure to that of polytetrafluoroethylene (PTFE) with additional sulfonic acid groups present at ending side chains. These sulfonic acid groups enhance the cell's overall ionic conductivity and its micellar-like architecture are suitable for water uptake.

The electrodes in the PEMFC are made of nanoparticles of Pt or Pt alloys adhered to a porous carbon (Vulcan XC-75 R). These are separated by the Nafion as described above. The porous carbon backing supports Pt nanoparticles, which allow the humidified gaseous fuel to reach the electrode surface. This is known as the gas diffusion layer (GDL),

1.6.1 Operational characteristics of PEMFC

The thermodynamic reversible cell voltage in the case of PEMFC is around 1.23 V. The operational losses in an actual cell at a given current density to that of the thermodynamically reversible potential for water formation are generally known as overvoltage (or overpotential). These losses are further divided into activation, ohmic and concentration overpotentials respectively, which are illustrated using a polarization curve as shown in fig. 1.7.

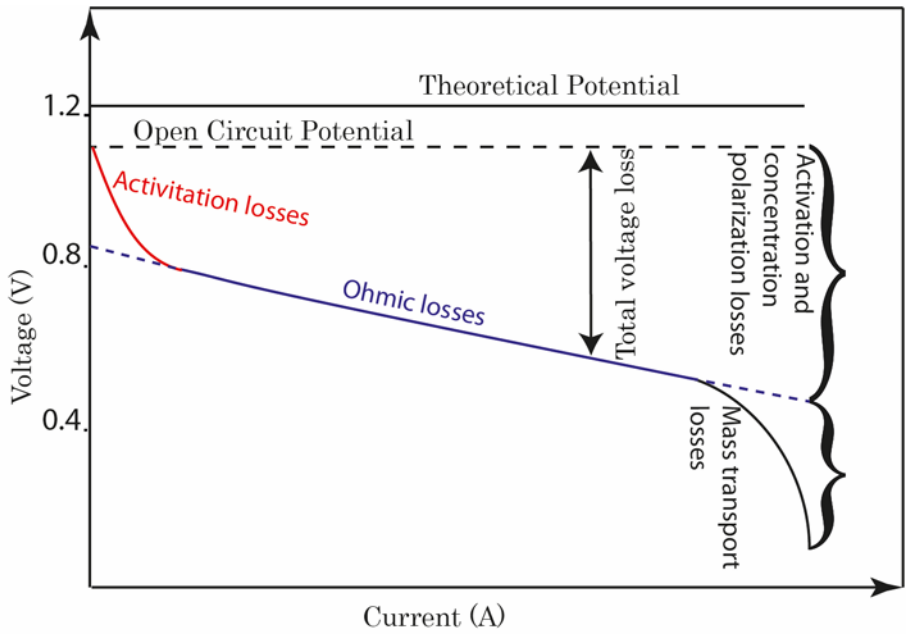

Figure 1.7: A typical polarization curve which represents polarization losses for a membrane fuel cell electrode

Activation losses are essentially a result of electrode kinetics and are more prominent in the low current densities. The kinetics of oxygen reduction is very sluggish especially in the hydrogen oxygen fuel cell, and hence are the main cause of activation losses. However, when the fuel is methanol, then the activation loss is due to both methanol oxidation and oxygen reduction.

Ohmic losses are the result of internal resistance of flow of electrons. In actual fuel cell setup, overpotential (caused by limited conductivity of protons through the electrolyte (Nafion membrane), decreases the cell's performance at intermediate current densities.

Mass transport overpotential is most prominent when a fuel cell is operating at high current densities. At high current densities, consumption of reactants is very fast, which results in depletion of the reactants in the close proximity of the electrodes. Here the supply of the reactants is somewhat mass transport limited causing the reaction to proceed at a slow rate. Moreover, accumulation of water across the GDL also limits the transport of the reactant.

Similarly, the overvoltages generated due to unavoidable side reactions are normally termed as mix potentials. These are normally caused by cross-over of the fuel via the electrolyte from the anodic to the cathodic compartment or vice versa. Especially in the

methanol fuel cell at open circuit potential, this is the main reason of this kind of overvoltage. Occasionally, it gets worse due to the incomplete oxidation of methanol (CO, H_2CO, HCO, etc.).

All these overvoltage losses lower the overall cell voltage output in the overall cell potential window. Since the power output of fuel cell is obtained by simple multiplication of voltage with current density, research is focused on minimizing these overpotential losses in order to maximize cell power output.

1.6.2 Catalysis and Fuel Cells

The electrochemical reaction takes place at the interfaces of the fuel cell electrodes by accepting or donating electrons. Normally, during this chemical reaction, electrode materials are not involved. For this reason, any electrode material on which an appreciable amount of reaction takes place is known as a catalyst electrode. However, in reality, this term is restricted to those materials which enable a reaction at a technically accepted level. The overall catalytic activity of an electrode material mainly depends on: the chemisorptions of the reactants at its surface, ease of interfacial reaction by breakdown of adsorbed molecules into atoms, and the degree by which the activation barrier for charge transfer is reduced.

1.6.3 Electrochemistry of hydrogen and its catalysis

In most fuel cells, Pt based electrocatalysts are being utilized as anode and cathode. The oxidation of hydrogen in aqueous solutions proceeds via a Tafel-Volmer or Heyrovsky-Volmer mechanism.

$$H_{ad} + H_2O \rightarrow H_3O^+ + e^-, \ \text{(in acidic solution)} \qquad 1.6$$

$$H_{ad} + OH^- \rightarrow H_2O + e^-, \ \text{(in alkaline solution)} \qquad 1.7$$

In the case of the Tafel-Volmer mechanism, the overall oxidation process is considered to proceed in partial reaction steps: adsorption of hydrogen molecule on the electrode surface (reaction 1.8), dissociation of molecular hydrogen (reaction 1.9, Tafel reaction), and then hydration and ionization of adsorbed hydrogen (reaction 1.10, Volmer reaction).

$$H_2 \text{ or } H_2 \text{ (dissolved)} \rightarrow H_{2,ad} \qquad 1.7$$

$$H_{2,ad} + 2Pt \rightarrow Pt - H_{ad} + Pt - H_{ad} \quad \text{(Tafel reaction)} \quad 1.8$$

$$Pt - H_{ad} + H_2O \rightarrow Pt + H_3O^+ + e^- \quad \text{(Volmer reaction)} \quad 1.9$$

Whereas, in the case of the Heyrovsky-Volmer mechanism, hydration and partial ionization occur in a quasi-single step as under

$$H_{2,ad} + H_2O + Pt \rightarrow (Pt\text{–}H_{ad} \cdot H_3O^+) + e^- \rightarrow H_{ad} + H_3O^+ + e^- \quad \text{(Heyrovski reaction)} \quad 1.20$$

$$Pt - H_{ad} + H_2O \rightarrow H_3O^+ + e^- + Pt \quad \text{(Volmer reaction)} \quad 1.21$$

It is generally believed that the hydrogen adsorption on the electrode surface is the rate determining step in both mechanisms. However, recent studies showed that the Tafel-Volmer mechanism dominated at lower potential, whereas the Heyrovsky-Volmer mechanism prevailed at higher potentials [36-39].

Hydrogen is used as a fuel in low temperature fuel cells. The wide spread utilization of hydrogen as a fuel is somewhat limited due to various issues associated its clean production, storage, and transportation [40, 41]. Thus small organic molecules such as methanol, ethanol and methanoic acid are considered as alternative fuels. However, the poor kinetics of electrochemical oxidation of these fuels when compared with hydrogen, and catalytic poisoning issues by CO adsorption due to electrooxidation, hinder the wide spread use of these fuel cells [42]. The complete oxidation of these organic molecules to CO_2 is extremely difficult. Even in ethanol the C-C bond splitting is a very slow process. The oxidation of these fuels is not the concern of this thesis and detailed explanation of their mechanism is already given in various publications of our group [43-46].

1.6.4 Electrochemistry of oxygen and its catalysis

The electrochemistry of oxygen on metal electrodes such as Pt, Ag and Au etc. in aqueous electrolytes is much more complex. Over the entire pH range, the equilibrium rest potential of the oxygen reduction reaction on the Pt electrode is much lower than the thermodynamic reversible potential. In general, the rest potential of the oxygen electrode is established slowly, is less reproducible and is considered to be a mixed potential of oxygen reduction and oxidation of the Pt surface [47, 48].

This might cause difficulty in breaking the oxygen-oxygen bond during ORR and

proceeding indirectly via H_2O_2 formation. The overall reversible reduction of oxygen in aqueous (both in acidic as per eq. 1.22 and alkaline, eq. 1.23) electrolytes is represented by following equations

$$O_2 + 4H^+ + 4e^- \Leftrightarrow H_2O\ , \quad E^\circ_{NHE} = +1.23\ V \qquad 1.22$$

$$O_2 + 2H_2O + 4e^- \Leftrightarrow 4OH^-, \quad E^\circ_{NHE} = +0.401\ V \qquad 1.23$$

The thermodynamic electrode potentials were calculated based on standard conditions of temperature, pressure and standard free energy of formation of water and OH^- ions. It is required to observe ORR at a potential close to the thermodynamic electrode potential at a satisfactory reaction rate. In aqueous electrolytes, the lower value of the experimentally observed oxygen reduction potential than the theoretical one, is generally believed to be caused by hydrogen peroxide (H_2O_2) formation.

The unstable nature of hydrogen peroxide in aqueous solutions leads to its decomposition even at room temperature. This decomposition is strongly accelerated by metal surfaces (catalysts) such as Pt. This leads to the establishment of mixed O_2^- H_2O_2 potential in the close vicinity of metal surface.

These electrochemical reduction reactions are irreversible due to the mixed potential at electrode surface. This process caused deviation of the experimental potential from theoretical one. Even with most active Pt electrode at standard conditions, rest potentials for reduction of oxygen were observed to vary from 1~1.1 V vs. NHE. A detailed discussion about ORR theory and mechanism is presented in *chapter 6 of Comprehensive Treatise of Electrochemistry Vol- 7 (B. E. Conway et. al Eds.) from M.R. Tarasevich, A. Sadkovwski and E. Yeager.*

High efficiency of the fuel cells is always desired. This can only be achieved by fabricating new catalysts with better kinetics or by improving the kinetics of existing catalysts, and it is fairly challenging. One way of finding an optimal composition of a catalyst (besides of course "trial and error") is by high throughput screening or by a combinational approach. The combined approach offers fast and cost effective solutions to problems involving large numbers of potential candidate compounds [49, 50].

Several Pt binary, ternary and quaternary alloy compositions were identified as candidates for both the oxygen reduction reaction and for methanol tolerance especially

for low temperature fuel cell applications. Alloys of Pt and ruthenium (Ru) electrodes have been known for a long time to exceed the electrocatalytic activity of pure platinum electrodes toward the electrooxidation of methanol in acid electrolytes [51]. Our main focus is to address sluggish kinetics of the oxygen reduction reaction and to develop better cathode materials, as well as small organic molecule tolerance.

So besides the cost issues, major challenges in making fuel cells commercially viable are the lessening of the cathodic overpotential and the need to augment tolerance/selectivity in the presence of small organic molecules.

1.7 Chapters overview:

This research is concerned with the study of cathode catalyst for ORR using selenium modified Rh(111) as a model system to understand the role of selenium adlayers (electronic or ensemble effect) in electrocatalysis. Aim of the current research is to get a fundamental understanding the role of chalcogenides (especially selenide) in cathodic electrocatalysis in general and also address the stability of selenium adlayers on Rh(111) during the potential region of ORR and some suggestion for a further work. The overview of the research is briefly outlined below.

One of the goals of the research is to use a combination of electrochemical, non electrochemical in situ methods (such as electrochemical scanning probe microscopy (EC-SPM)), differential electrochemical mass spectrometery (DEMS) and induction heating to gain understanding of the fundamental properties of selenium modified Rh(111) surfaces. The experimental techniques adopted for this research and their principles are discussed in detail in the chapter 2.

Chapter 3 (which is the first real experimental section) explores the effects of adsorbent adlyers, the effect of potential controlled roughening, and adlayer structure of Se on Rh(111). In the chapter 4, the main focus is on the stability issues of selenium adlayers. DEMS was employed for quantitative estimation of reductive stripping of selenium adlayers. In addition surface morphology of modified surface during reductive and oxidative stripping was monitored using electrochemical SPM techniques.

Chapter 5, deals with the determination of pztc on Rh(111) and detailed investigation

for the ORR activity of Rh(111) and selenium modified Rh(111) surfaces by using a DTLFC as an alternative to rotating ring disc electrode. The utilization of thermal treatment of adsorbed adlayers to get smooth and stable adlayers probably based on place exchange mechanism is discussed in detail in the Chapter 6. Thermally treated adlayers were also characterized for ORR activity and their surface morphology was examined using scanning tunnelling microscope. Moreover, the number of free Rh sites was checked by CO adsorption and stripping, possibly inhibition of CO adsorption of these surfaces was due to atomic ensemble or electronic effect.

Chapter 7 deals with the friction studies on selenium modified fcc(111) surface (namely Rh, Pt and Au) for various coverages. Atomic resolution is obtained for submonolayer deposits and calculates friction coefficient of these modified surfaces. In addition, molecular adsorption on model surfaces is explored. Atomically smooth deposits of Nafion on Pt(100) is also observed. Moreover, thickness of Nafion adlayer on Pt(100) is determined by scratching and tip penetration method. The influence of friction using pyridine on Au (111) is also studied.

A detailed procedure for calculating the calibration matrix for the scanner and adlayer matrices for SO_2^- and Se adlayers on Rh(111) concerning to chapter 3 are presented as Appendix A. A general overview of the electrochemical modification of fcc(111) surface and fcc(100) surface concerning to Chapter 4 are presented in Appendix B.
A detailed characterization of dual thin layer flow through cell (DTLFC) as a hydrodynamic technique concerning to chapter 5 and 6 is discussed in Appendix C

References

[1] L. Carrette, K. A. Friedrich, and U. Stimming, Fuel Cells 1:5 (2001).
[2] S. M. K. W. Otto Haas, Vol. 68, 1996, p. 524.
[3] J. F. Drillet, F. Holzer, T. Kallis, S. Muller, and V. M. Schmidt, Physical Chemistry Chemical Physics 3:368 (2001).
[4] J. M. Ziegelbauer, A. F. Gulla, C. O'Laoire, C. Urgeghe, R. J. Allen, and S. Mukerjee, Electrochimica Acta 52:6282 (2007).
[5] A. Lavacchi, H. Miller, and F. Vizza, in Nanotechnology in Electrocatalysis for Energy, Vol. 170, Springer New York, 2013, p. 63.
[6] S. Gilman, Journal of Physical Chemistry 67:78 (1963).
[7] D. Kolb, 11:125 (1978).
[8] W. Schmickler and E. Santos, in Interfacial Electrochemistry, Springer Berlin Heidelberg, 2010, p. 163.
[9] L. A. Kibler, Preparation and Characterization of Noble Metals Single Crystal Electrodes, University of Ulm, 2003.
[10] A. B. Laursen, A. S. Varela, F. Dionigi, H. Fanchiu, C. Miller, O. L. Trinhammer, J. Rossmeisl, and S. r. Dahl, Journal of Chemical Education 89:1595 (2012).
[11] C. A. Lucas, N. M. Markovic, B. N. Grgur, and P. N. Ross, Surface Science 448:65 (2000).
[12] C. A. Lucas, N. M. Markovic, and P. N. Ross, Surface Science 448:77 (2000).
[13] C. A. Lucas, N. M. Markovic, and P. N. Ross, Surface Science 425:L381 (1999).
[14] M. Hachkar, T. Napporn, J. M. Leger, B. Beden, and C. Lamy, Electrochimica Acta 41:2721 (1996).
[15] J. A. Rodriguez, S. Chaturvedi, and M. Kuhn, Journal of Chemical Physics 108:3064 (1998).
[16] O. M. Magnussen, Chemical Reviews 102:679 (2002).
[17] D. A. Scherson and D. M. Kolb, Journal of Electroanalytical Chemistry and Interfacial Electrochemistry 176:353 (1984).
[18] H. Angerstein-Kozlowska, B. E. Conway, A. Hamelin, and L. Stoicoviciu, Journal of Electroanalytical Chemistry 228:429 (1987).
[19] J. Clavilier, R. Faure, G. Guinet, and R. Durand, Journal of Electroanalytical Chemistry 107:205 (1980).
[20] J. Clavilier, Journal of Electroanalytical Chemistry 107:211 (1980).
[21] N. Alonso-Vante, H. Tributsch, and O. Solorza-Feria, Electrochimica Acta 40:567 (1995).
[22] O. Solorza-Feria, K. Ellmer, M. Giersig, and N. Alonso-Vante, Elrotrochimica Acta, Vol. 39 39:1647 (1994).
[23] J. Ma, A. Habrioux, C. Morais, and N. Alonso-Vante, Physical Chemistry Chemical Physics 16:13820 (2014).
[24] W. T. Grubb, Nature 198:883 (1963).
[25] G. Somorjai, Chemistry in Two Dimensions: Surfaces, Cornell University Press, Ltd., London, Ithaca and London, 1981.
[26] J. O. M. Bockris and H. Wroblowa, Journal of Electroanalytical Chemistry 7:428 (1964).
[27] E. Bauer and H. Poppa, Thin Solid Films 12:167 (1972).
[28] F. C. Frank and J. H. van der Merwe, Proceedings of the Royal Society of London A: Mathematical, Physical and Engineering Sciences 198:205 (1949).
[29] F. C. Frank and J. H. van der Merwe, Proceedings of the Royal Society of London A: Mathematical, Physical and Engineering Sciences 200:125 (1949).
[30] E. Budevski, G. Staikov, and W. J. Lorenz, Electrochemical Phase Formation and

Growth, VCH, Weinheim, 1996.
[31] T. Bligaard and J. K. Norskov, Electrochimica Acta 52:5512 (2007).
[32] L. A. Kibler, A. M. El-Aziz, R. Hoyer, and D. M. Kolb, Angewandte Chemie-International Edition 44:2080 (2005).
[33] W. R. Grove, Philosophical Magazine Series 3 14:127 (1839).
[34] M. Winter and R. J. Brodd, Chemical Reviews 104:4245 (2004).
[35] B. C. H. Steele and A. Heinzel, Nature 414:345 (2001).
[36] J. X. Wang, T. E. Springer, and R. R. Adzic, Journal of The Electrochemical Society 153:A1732 (2006).
[37] P. M. Quaino, J. L. Fernandez, M. R. Gennero de Chialvo, and A. C. Chialvo, Journal of Molecular Catalysis A: Chemical 252:156 (2006).
[38] B. Babic, J. Gulicovski, L. Gajic-Krstajic, N. Elezovic, V. R. Radmilovic, N. V. Krstajic, and L. M. Vracar, Journal of Power Sources 193:99 (2009).
[39] S. A. Vilekar, I. Fishtik, and R. Datta, Journal of The Electrochemical Society 157:B1040 (2010).
[40] R. Ströbel, M. Oszcipok, M. Fasil, B. Rohland, L. Jörissen, and J. Garche, Journal of Power Sources 105:208 (2002).
[41] J. W. Gosselink, International Journal of Hydrogen Energy 27:1125 (2002).
[42] F. Vigier, C. Coutanceau, F. Hahn, E. M. Belgsir, and C. Lamy, Journal of Electroanalytical Chemistry 563:81 (2004).
[43] A. A. Abd-El-Latif, E. Mostafa, S. Huxter, G. Attard, and H. Baltruschat, Electrochimica Acta 55:7951 (2010).
[44] E. Mostafa, A. A. Abd-El-Latif, and H. Baltruschat, ChemPhysChem 15:2029 (2014).
[45] E. Mostafa, A. A. Abd-El-Latif, R. Ilsley, G. Attard, and H. Baltruschat, Physical Chemistry Chemical Physics 14:16115 (2012).
[46] B. Lanova, H. Wang, and H. Baltruschat, Fuel Cells 6:214 (2006).
[47] D. A. J. Rand and R. Woods, Journal of Electroanalytical Chemistry and Interfacial Electrochemistry 47:353 (1973).
[48] A. J. Appleby, Journal of Electroanalytical Chemistry and Interfacial Electrochemistry 35:193 (1972).
[49] E. Reddington, A. Sapienza, B. Gurau, R. Viswanathan, S. Sarangapani, E. S. Smotkin, and T. E. Mallouk, Science 280:1735 (1998).
[50] M. K. Jeon, J. H. Liu, K. R. Lee, J. W. Lee, P. J. McGinn, and S. I. Woo, Fuel Cells 10:93 (2009).
[51] H. A. Gasteiger, N. A. Markovic, J. Philip. N. Ross, and E. J. Cairns, Electrochimica Acta 39:1825 (1994).

Chapter 2: Methodology

In this chapter, various experimental methods being employed in the present work are explained in detail. These methods are: Voltammetric techniques, Scanning Probe Microscopy namely Scanning Tunneling Microscopy (STM) and Atomic Force Microscopy (AFM), in particular contact mode, Lateral Force Microscopy (LFM) and Differential Electrochemical Mass Spectrometry (DEMS).

2.1 Cyclic voltammetry (CV)

Cyclic voltammetry is an ideal technique for fast characterization of the electrode/electrolyte interface. The technique requires scanning the electrode potential over a certain range linearly with time, at the same time detecting the current value. A triangular potential sweep is applied to the working electrode (fig. 2.1). The potential is increased from the initial value E_0 to a final value E_u then returned back to the initial value to complete a cycle at a constant rate. The sweep rate varies from a few microvolts to a hundredth of volts per second.

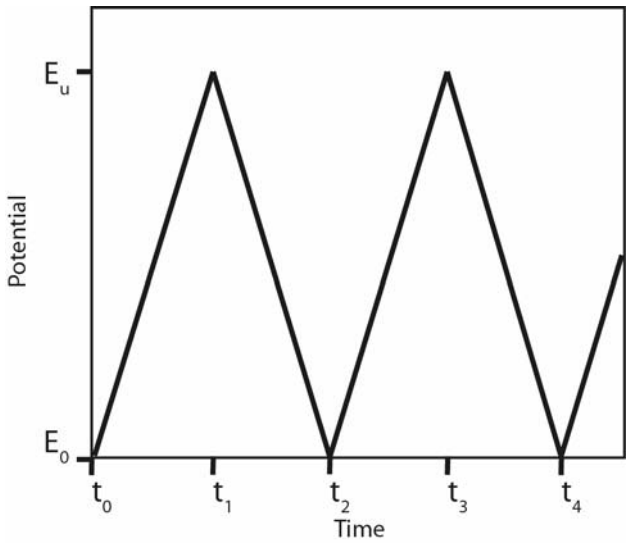

Figure 2.1: The triangular potential waveform

2.1.1 Electron transfer and mass transport controlled processes

The rate of an electrochemical reaction is dependent on both electrode potential, which can be manipulated, and mass transfer. A simple model in fig. 2.2 is used to elaborate the charge and mass transfer processes during an electrochemical reaction.

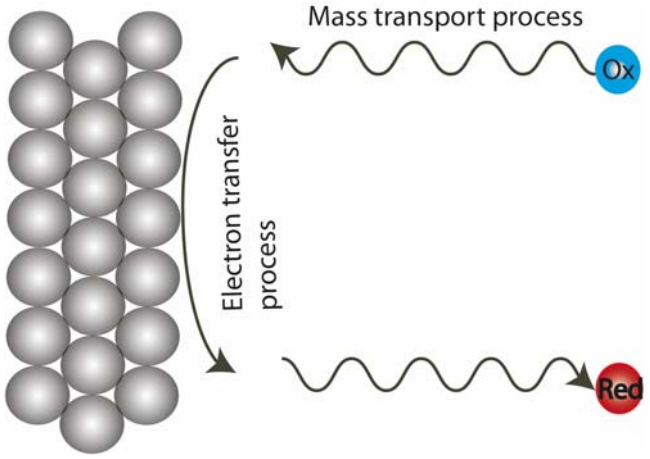

Figure 2.2: Electrochemical model describing electron and mass transport process

The factors affecting the voltammetric profile are illustrated in fig. 2.3. By varying the electrode potential in the negative direction (reduction) or in the positive direction (oxidation), the electron transfer rates are suddenly increased and cross through a region where the current is limited by both electrons and mass transport processes.

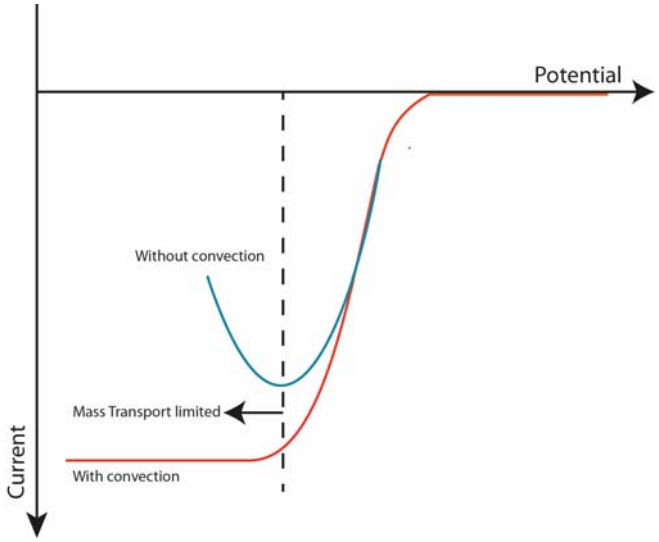

Figure 2.3: Voltammetric profile under convection (red solid curve) and convection free solution

At maximum reaction the currents are entirely mass transport-limited. The voltammetric peak current corresponds to a solution without convection, the plateau current corresponds to a solution with convection.

The rate of an electrochemical reaction is controlled by the electron transfer (non-

diffusion) limited current and evaluated using the Butler-Volmer equation.

$$j = j_a - j_c = j_0(e^{\alpha_a nF\eta/RT} - e^{-(1-\alpha_c)nF\eta/RT}) \quad 2.1$$

Where j_0 is the exchange current density, α is the transfer coefficient, n is the number of electrons exchanged, F is the Faraday constant, R is the real gas constant and T is temperature, η is the overpotential ($E-E_{eq}$).

Similarly, if the electrochemical reaction is controlled by a mass transport (diffusion) limited current, then the process is explained on the basis of Fick's first law of diffusion, which describes a one dimensional diffusion through a planar surface as

$$J = -D\,(dc/dx) \quad 2.2$$

Where J is the flux, dc/dx represents the concentration gradient and D is the diffusion coefficient (the rate constant for the movement of the substance).

Hence, the above expression for diffusion limited processes can be written for current density

$$j = zFD(\partial c/\partial x)_{x=0} = zFD\frac{C_{x=\infty} - C_{x=0}}{\delta_N} \quad 2.3$$

As the reaction proceeds, the surface concentration approaches zero, $C_{x=0} \sim 0$, the limiting current is obtained by

$$j_{lim} = zFD\frac{C_{x=\infty}}{\delta_N} \quad 2.4$$

During a mass transport (diffusion controlled) process, if convective transport is absent, then the diffusion gradient changes and the limiting current will decay as a function of time and can be expressed according to the Cottrell's equation,

$$j_{lim} = zFD^{\frac{1}{2}}C_{x=\infty}\frac{1}{\sqrt{\Pi t}} \quad 2.5$$

However, in the case of continuous convection, for example under stirring or flow conditions, the variation of the diffusion gradient at the electrode surface is inhibited and the decay of the limiting current is no longer a function of time, but depends mainly on the rate of convection and diffusion layer. When the convection is maintained by rotation such as in a rotating disc system, the eq. 2.4 takes the form

$$j_{lim} = -0.62zFAD^{\frac{2}{3}}\nu^{\frac{1}{6}}\omega^{\frac{1}{2}}C_{x=\infty} \quad 2.6$$

Where δN is the Nernst diffusion layer thickness and its value is $\delta_N = 1.6D^{\frac{1}{3}}\nu^{\frac{1}{6}}\omega^{\frac{-1}{2}}$

For channel electrodes, Yamada and Matsuda developed and tested experimentally a relationship between mass transport limited current and the flow rate based on the fundamental considerations of the Levich [1].

$$j_{lim} = 1.467 \cdot n \cdot F \cdot c\,(D \cdot A/b)^{2/3} \cdot u^{1/3} \qquad 2.7$$

2.1.2 Hydrodynamic techniques

A controlled mass transport condition must be maintained for the investigation of the mechanism of an electrochemical reaction. Especially in the electrocatalytic reaction of oxygen reduction, which is the most significant and important reaction in low temperature fuel cell applications. The most frequently employed technique to study the kinetic and mechanism of oxygen reduction reaction is the rotating ring disc electrode. Rotation of the disc causes a forced convective mass flow of electrolyte to the electrode.

Due to electrochemical reaction, products formed at the rotating disc electrode are forced radially away to be detected on the surrounding ring [2]. The most suited and well established method to study the kinetics and mechanism of multi-electron reaction is the RRDE set up. Other hydrodynamic techniques are also being explored for multi electron reaction. These includes the wall jet disc electrode (WJDE) setup [1], [3], channel flow cell [4] and dual thin layer flow through cell [5] are being explored for multi-electron reactions as well. In our current studies we utilized slightly modified dual thin layer flow cell which was actually developed in our group for DEMS [6]. A detailed description for characterization of this modified cell is presented in the chapter 5.

2.1.3 Dual thin layer flow through cell

To ascertain defined convection during oxygen reduction reaction (ORR) and to detect formed H_2O_2, we used the modified dual thin layer flow through cell (DTLFC), identical to that used in differential electrochemical mass spectrometers (DEMS) experiments [6]. A constant flow of electrolyte is achieved in these cells using syringe/peristaltic pumps.

The DTLFC is manufactured from Kel-F, which consists of two separate compartments. In the upper compartment the electrochemical process takes place at the disk electrode

surface (e.g., Pt or Se modified Rh(111)); reaction products and intermediates are transported with the electrolyte through six capillaries to the lower compartment. There, the second Pt disc electrode was used to detect products before the electrolyte leaves the cell via a capillary at the centre. A peristaltic/syringe pump at the outlet of the cell controlled the flow rate of the electrolyte. To assure a continuous operation of a flow through reactor, a supporting electrolyte served as a medium for both reactants and products. A reversible hydrogen electrode (RHE) was used as the reference electrode. Two Pt wires were used as counter electrodes in the inlet and outlet and connected to the potentiostat via two different resistances (100 kΩ and 1100 Ω respectively) to optimize the current distribution and decrease the (ohmic losses) IR drop resistance. The experiments were carried out at room temperature. A schematic view and actual setup is shown in fig. 2.4.

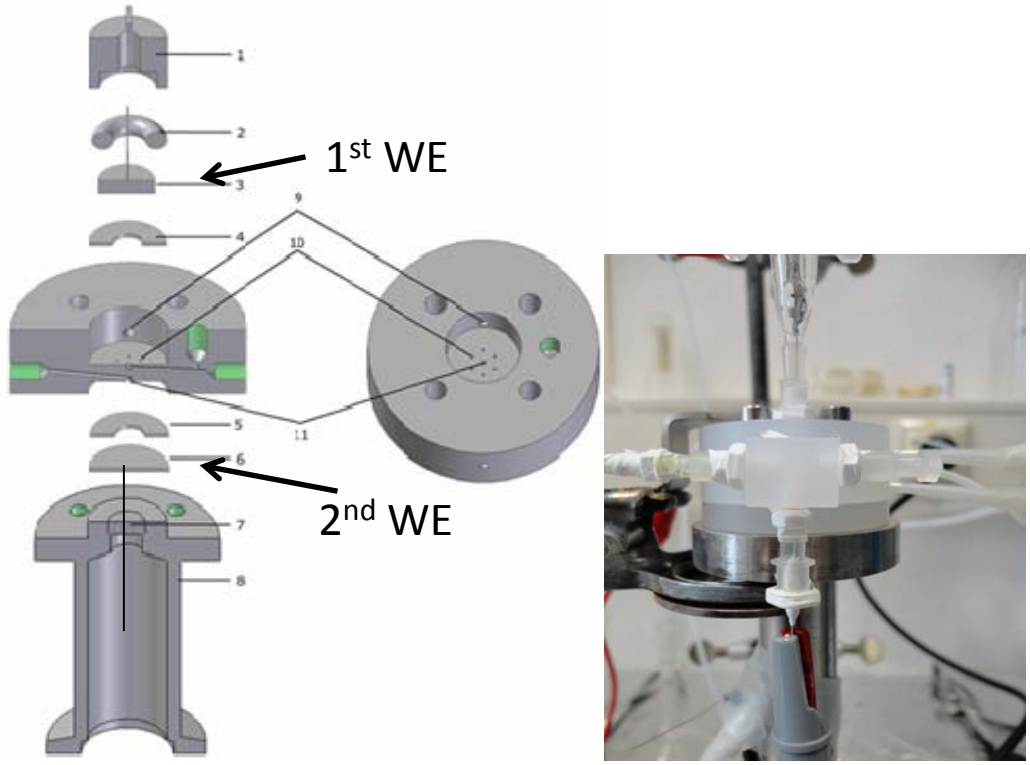

Figure 2.4: Schematic drawing of the dual thin layer flow through cell carton, disk electrodes (3&6), Gortex Teflon spacers (4&5), six capillaries links upper and lower compartment for electrolyte movement (10), holes for argon purging (9), holes for incoming and outgoing of electrolyte (11) actual photo of setup.

2.2 Chemicals, solutions and electrode material

Chemicals

All chemicals used for the preparation of solutions (electrolytes), cleaning solutions for glass apparatus and electrode materials in this work are summarized in tables 1.1-1.3. All the solutions were prepared using ultra-pure water (18.2 MΩ, <4 ppb TOC) from a Milli-Q water purification system and then de-aerated with analytical grade argon (Ar) and argon:hydrogen gas mixture.

Table 1.1: List of used chemicals and gases

Name	Formula	Company	Purity (%)
Ammonium Hydroxide	NH_4OH	Chem Solute	25
Copper(II) Sulfate	$CuSO_4.5H_2O$	KMF Laborchemie	99
Hydrogen Peroxide	H_2O_2	Merck	30
Perchloric Acid	$HClO_4$	Sigma-Aldrich	70
Ruthenium (III) nitrosylnitrate	$Ru(NO)(NO_3)_3$	Alfa Aesar	31.3
Sulfuric Acid	H_2SO_4	Merck	Suprapure, 95-97
Nafion® perfluorinated resin solution		Sigma Aldrich	5 wt. % in lower aliphatic alcohols and water, contains 15-20% water
Pyridine	C_5H_5N	Sigma Aldrich	
Potassium Bromide	KBr	Alpha Aesar	99.5 %
Sodium Sulfide hydrate	$Na_2S.xH_2O$	Acros Organics	60-63%
Selenious Acid	H_2SeO_3	Aldrich	98 %
Iron(III) sulfate hydrate	$Fe_2(SO_4)_3 \cdot xH_2O$	KMF laborchemie handels-Gmbh	99%
Argon	Ar	Praxair	5.0
Carbon Monoxide	CO	Praxair	4.7
Hydrogen	H_2	Air Liquids	5.0
Argon-Hydrogen	Ar:H_2 (95:5)	Air Liquids	5.0
Oxygen	O_2	Air Liquids	5.0
Polymer emulsion		Glasophor GY850030, BASF	

Table 1.2: List of used disc electrodes

Crystal Type	Manufacturer	Diameter (cm)
Pt(Pc)	Metal Crystals	1
Rh(Pc)	MaTeck	1
Ru(Pc)	Goodfellow	1
Pt(111)	Goodfellow	0.9
Pt(100)	Kristallhandel Kelpin	0.9
Rh(111)	Kristallhandel Kelpin	1
Rh(100)	MaTeck	1
Ru(0001)	Goodfellow	1
Au(111)	MaTeck	1
Pt/Ir wire (80:20)	MaTeck	0.25 mm

Table 1.3: List of used bead crystals.

Pt(Pc)	Home made	~2.4 mm
Au(Pc)	Home made	~2.5 mm
Rh(Pc)	Home made	~1.5 mm
Pt(111)	icryst	2.58 mm
Pt(100)	icryst	2.02 mm

2.3 Laboratory glassware cleaning solution

A chromic acid bath was prepared by dissolving 21.4 g of chromium (VI) oxide (CrO_3) in 1 litre of sulfuric acid solution (640 ml of concentrated H_2SO_4 + 340 ml of H_2O). This solution was used to oxidize organics and metal contaminants from the lab glassware by immersion overnight. Similarly, for removal of sulfate ions from already cleaned glassware using a chromic acid bath, a concentrated potassium hydroxide bath (5 M KOH) was used. Instead of using a chromic acid bath, due to the toxic properties of hexavalent chromium compound, an alternative chemical free cleaning method such as steam distillation was also used.

2.3.1 Conventional electrochemical glass cell 'H-cell'

For single crystalline electrode preparation and its electrochemical modification under controlled environment, a conventional electrochemical glass cell (which is known as an 'H-cell') was used. A typical glass H-cell is composed of three compartments as shown in fig. 2.5. The central compartments contained the working electrode in hanging meniscus configuration. This part also contained ports for gas purging (de-aerating / cooling) and for insertion of the electrolyte. The compartment, which is separated from

the main compartment by a frit, contains the counter electrode either in the form of metal sheet or wire (Pt or Au). The reference electrode was immersed in the compartment with the Luggin capillary, which served to minimize ohmic losses. Additionally, stopcocks restricted the diffusion of metal ions from central compartment to the reference compartment.

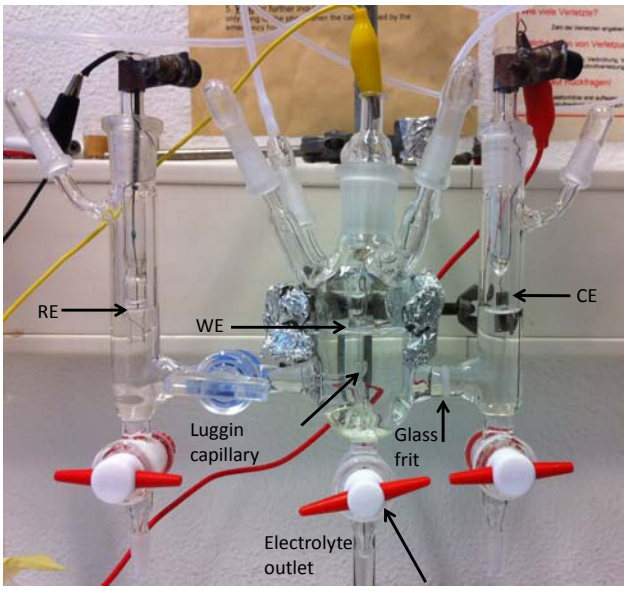

Figure 2.5: Actual photo of an H-cell for the electrochemical experiments.

2.3.2 Reference Electrodes

Reversible Hydrogen Electrode (RHE)

A home built RHE electrode based on Will's design [7] was used in this research work. A pictorial representation used to explain the process for the preparation of a RHE is shown in fig. 2.6. Initially, the glass bulb containing the Pt wire was filled with supporting electrolyte (0.1 M $HClO_4$) using a vacuum suction system. A potential difference of 1.5 V was applied using a power supply between a Pt wire (Anode) immersed in the electrolyte and the Pt wire of the RHE electrode (cathode) to produce hydrogen and oxygen in a way much similar to performed by Sir William Grove [8].

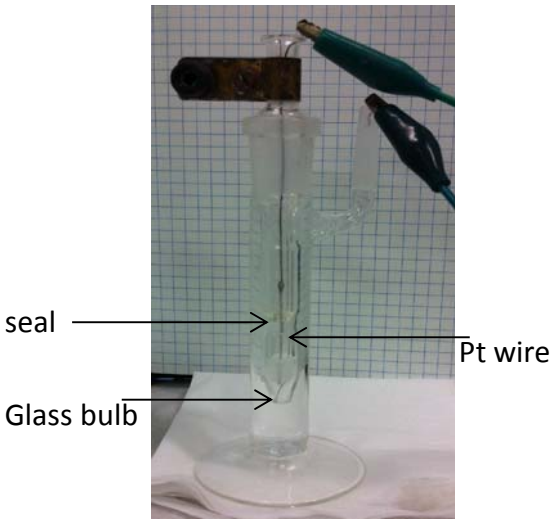

Figure 2.6 Actual photo of reversible hydrogen electrode.

Pt/PtO quasi reversible electrode

The Pt wire was cleaned thoroughly in concentrated H_2SO_4 solution and then rinsed with Milli-Q water. This cleaned Pt wire was used as a quasi-reference electrode in electrochemical scanning probe (EC-STM/AFM) measurement

2.3.3 Cleaning and preparation of single crystals

Metal electrode surfaces are very active and prone to be contaminated by adsorbent. Also, freshly polished single crystal surfaces supplied by manufacturers contain silica impurities and needed thorough cleaning. Chemical treatments used are as follows:

Chemical treatment

Hydrofluoric (HF) acid has the capacity to dissolve (react) with most of the oxide and silicates present in a metal electrode. Normally, this treatment is used for newly fabricated single crystal electrodes. Special care has to be taken while dealing with HF. The usual metal contaminants such as copper deposits (due to spot welding of the contact wire with the metal surface) or other deposited metals, are removed by immersing the electrode first in concentrated nitric acid (HNO_3) solution followed by immersion in ammonia/hydrogen peroxide (NH_3/H_2O_2 1:1) mixture to remove traces of silver diffused into the electrode surface. The chemically treated electrode is then electrochemically cleaned by potential cycling to get a pure metal surface. Sometimes this process is repeated several times to get a contamination free metal surface. A simple example of electrochemical cleaning of Rh(111) electrode is presented in fig. 2.7

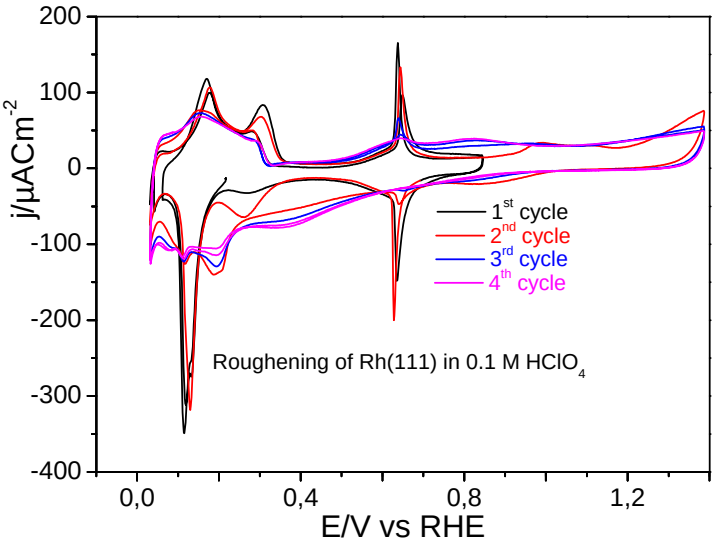

Figure 2.7: Cyclic voltammogram for Rh(111) roughening in 0.1 M $HClO_4$ @ 50 mV/s

Preparation of single crystalline surfaces

The single crystal electrode surfaces were prepared by the flame annealing method developed by Clavilier [9]. Flame annealing of the crystal was carried out using a butane flame. The metal was heated in a flame until it was cherry red, and then held at that temperature for thirty seconds to a minute before being transferred to a/the glass cell under a controlled environment of Ar or Ar/H_2 mixture for cooling [10].

Special care has to be taken in case of Au electrodes due to its lower melting point. Intermittent heating of the electrode surface for a slightly longer period of time (~4 minutes) at much lower temperatures, (so that the surface becomes light pink and not cherry red leads to better preparation).

The flame annealed electrode with a drop of Ar/H_2 saturated water (to avoid oxidation of the surface) was transferred to a home built H-cell containing Ar saturated electrolyte. Afterwards the hanging meniscus contact was established. The quality of the surface preparation was checked by performing potential scanning from 0.03 to 0.85 V. The sharpness of the characteristic features for hydrogen adsorption/desorption and hydroxide or sulfate adsorption/desorption provide information about the surface cleanliness and preparation. Higher potentials are avoided to prevent the surface from being oxidized and roughened. The electrode was then (or after selenium modifications) transferred either to DTLFC or STM/AFM cell for further characterization.

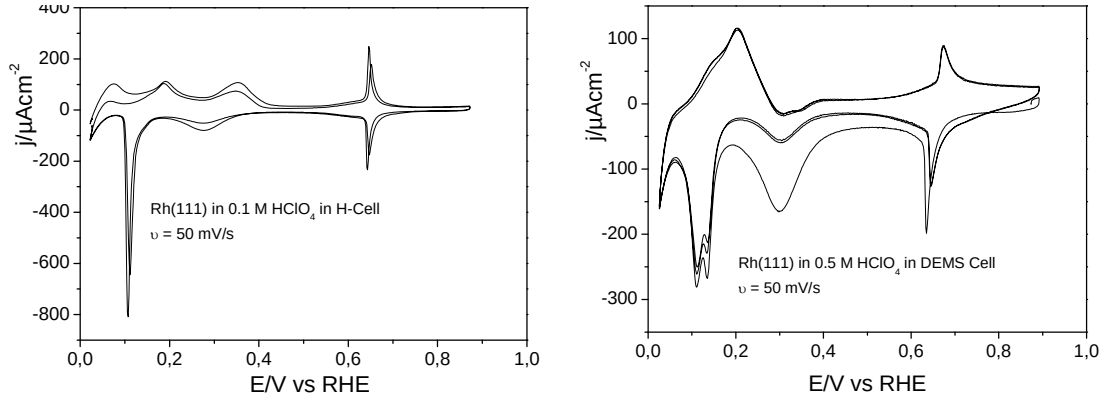

Figure 2.8: Typical characteristic CV for Rh(111) in 0.1 M $HClO_4$ at 50 mV/s a) in H-cell and b) in DTLC cell in 0.5 M $HClO_4$ at flow rate of 2.5 μL/s.

The differences in the CV of the Rh(111) in the H-cell to in the DEMS cells is mainly due to reduction of ClO_4^- to Cl^- occurring in the latter due to the higher concentration of $HClO_4$ due to the continuous flow of electrolyte (fresh electrolyte causes more ClO_4^- reduction) are shown in fig. 2.8. In addition contamination due to the materials used in DEMS cell was unavoidable.

2.4 Deposition of Se submonolayer and multilayer at fcc(111) single crystals

The sub-monolayer and multilayer deposits of selenium on Rh(111), Pt(111) and Au(111) surfaces were performed from 1 mM H_2SeO_3 in 0.1 M $HClO_4$ solution using both electro-deposition and spontaneous adsorption methods.

The whole process begins with the preparation of single crystalline surfaces described elsewhere [9-12]. It was then transferred to an H-cell containing the selenium containing electrolyte. Hanging meniscus contact was established at open circuit potential. Sub-monolayer deposits of selenium were obtained by potential cycling from rest to around +0.65 V in the cathodic direction. Multilayered deposits were achieved by further scanning the potential in the cathodic direction from rest potential to around till +0.15 V. In the former case a coverage of around ϑ = 0.2~0.3 and in the latter case a ϑ =1.5~1.6 monolayer was achieved based on deposited charge calculations after background correction. In both cases complete suppression of both hydrogen under potential deposition (UPD) peaks and hydroxide butterfly peaks was observed in a CV recorded afterwards in supporting electrolyte (0.1 M $HClO_4$).

2.4.1 Spontaneous adsorption

Adsorption of selenium on fcc(111) single crystal surfaces was achieved simply by immersing them into 1 mM H_2SeO_3 at open circuit potential for three minutes. Spontaneous adsorption of selenium on Au(111) and Pt(111) was readily achieved, and completely suppress the hydrogen region with a surface coverage of $\vartheta = 0.3$ on Pt(111) [13] and Au(111), however, in the case of Rh(111) this process was too slow.

2.4.2 Forced adsorption

A slight modification of spontaneous adsorption was followed by partial reduction of adsorbent using hydrogen gas. This method was successfully developed by Clavilier et al. [14] for palladium deposition on a Pt(111) surface. Later on our group, in collaboration with the Attard group, used this method for the preparation of ruthenium (Ru) quasi single crystalline surfaces on Pt single crystal electrode substrate surfaces [15], [16]. Multi-layered deposits of Ru were achieved on Pt single crystalline substrate by repeated forced deposition. The deposited metal was annealed using resistive heating, which utilizes a low voltage high current power source to heat the modified electrode under controlled environment. This procedure resulted in epitaxial growth and the deposited metal followed the pattern of underlying substrate. Initially this process was used for Ru quasi single crystal on platinum bead crystals. This was later extended to large disc crystals especially for Pt(111) and Pt(100) surfaces.

2.5 Scanning Tunneling Microscope (STM)

The basic idea behind the development of Scanning Tunneling Microscopy (STM) has been known for about a century. The quantum tunneling was first explained by J. R. Oppenheimer and later on elucidated by Fowler and Nordheim [17, 18].

Binnig et al. practically demonstrated for the first time that the tunnel current varies exponentially with distance of the tip in a controlled manner on an Si(111) surface [19]. Their concept of using tunnel current to monitor height resulted in the development of the first scanning tunneling microscope; they were able to image the real structure of the 7x7 reconstruction of Si(111) in 1983 [20].

The STM yields information about the surface structures on an atomic scale. The principal idea for such an approach was quite simple and based on tunneling of

electrons from one metal surface to the other. This mechanism is illustrated schematically in fig. 2.9, and its detailed explanation is based on quantum mechanical principles.

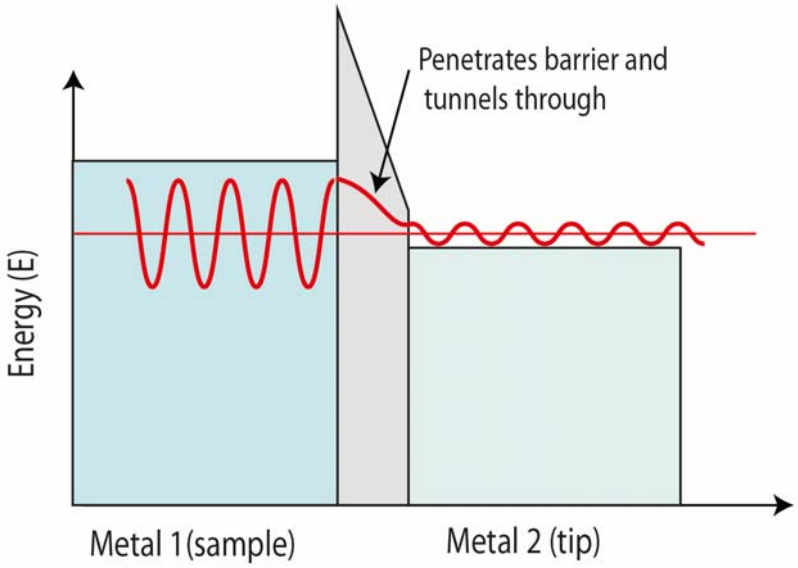

Figure 2.9 Energy diagram of the tip and the substrate with a potential barrier.

In a real setup, a small metal probe (usually an atomically sharp tip) is brought very close to the surface (< 1 nm). This results in a flow of a small, locally confined current between them on application of a bias voltage; thus atomic resolution is achieved as shown in fig. 2.10. The extremely high precision capability of the STM in obtaining resolution to atomic level is based on the physical properties of the tunneling current. It exhibits an exponential relation with a barrier gap and is represented as follows:

$$I_t = V_b \cdot e^{(-k_2 d)} \qquad 2.8$$

Where k_2 is the barrier height and V_b is the potential difference (bias voltage) and equal to $V_{substrate}$-V_{tip}. Under electrochemical conditions, the bias voltage is given by E_{tip}-$E_{substrate}$ [21].

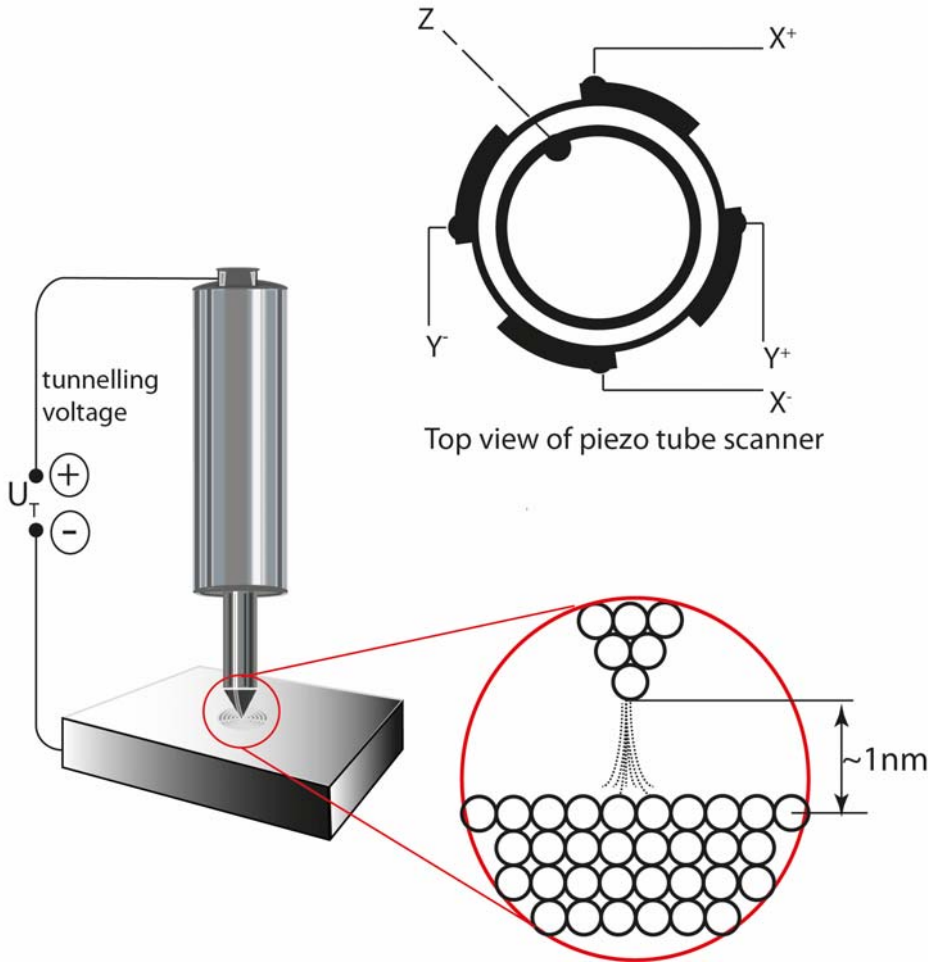

Figure 2.10: Graphical representation of working principle of STM, atomic scale view of tip-sample is presented in a circle. Schematic of the piezo tube scanner with respective X, Y and Z electrode also presented.

The STM can image a surface by scanning the tip over it (by lateral control voltages ± U_x, ± U_y). A feedback controller receives the tunneling current and maintains the tip height d either by constant current or constant height mode as shown in fig. 2.10

1) In constant current mode (the tunneling current is monitored constantly as the tip is scanned across the surface). This mode is used to obtain surface morphology in general and particularly the structure of the single crystal surfaces. The occurrence of defects such as steps, kinks, facets and adsorbates can also be traced. A relatively fast feedback is required for keeping the tunneling current constant.

2) The constant height mode (in which the tunneling current varies due to changing tip/substrate distance as the tip is scanned parallel to the surface), is used to examine practically flat and rather smooth surfaces. On rough surfaces, the tip may run into a

protrusion. The scanning rate of the tip may be increased because no essential feedback control is needed for the tip height adjustment, thus the thermal drift problems are less severe. This mode is usually used for obtaining atomically resolved adlayer structures.

2.5.1 EC-STM operation

One of the major advantages of the STM compared to other surface analysis techniques is that it permits in situ imaging of a substrate with atomic level resolution in real space such as in air or solution [22].

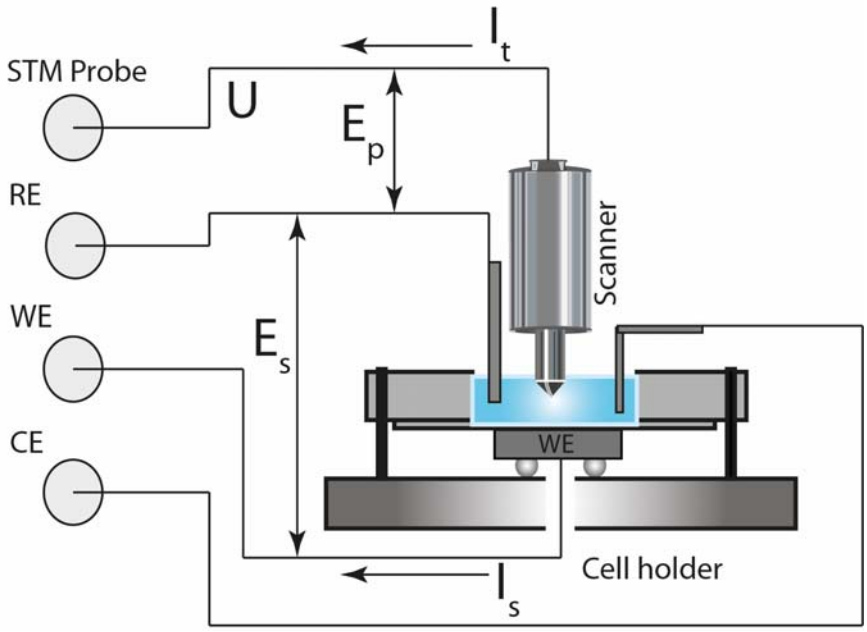

Figure 2.11: Schematic drawing of EC STM setup.

In case of an electrochemical STM; a bipotentiostat is used to control the electrode potential of the STM tip and that of the substrate separately. Hence it is useful for probing the electrode/electrolyte interface.

A schematic of EC-STM with the two working electrode (tip and substrate) configuration is shown in fig. 2.11. The electrochemical current flowing through the substrate and the counter electrode can be monitored from the output of a current follower, similarly the tunneling current can be measured by another current follower.

In a standard EC STM configuration, the tip current consists of tunnelling current and faradaic current due to the reactions at the tip ($I_{tip} = I_{tunneling} + I_{faradiac}$). It is generally accepted that the currents (faradaic) which are generated during an electrochemical

reaction are large enough to bury the underlying tunnelling current, which are normally of the order of nA or even pA in case of STM.

2.6 Atomic Force Microscope (AFM)

Soon after the invention of STM, researchers started thinking about visualization of non-conducting samples especially in biological samples. Binnig et al. had the idea of extending STM for non-conducting substrate by controlled monitoring of the tip-sample interactions. They called this an atomic force microscope (AFM) [23]. The main interactive forces involved between the tip and the sample are the Van der Waals forces, which may be either the short range repulsive force (in contact mode) or the long range attractive force (in non-contact-mode) as explained in fig. 2.12.

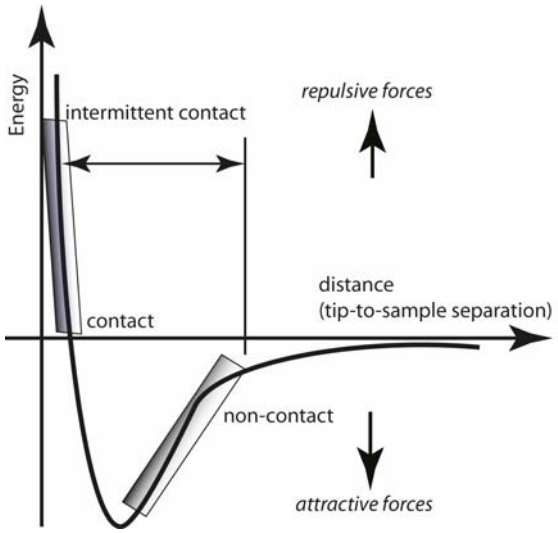

Figure 2.12: Lennard - Jones potential with scheme of the areas in which the respective mode of the AFM is used.

The basic operation of the atomic force microscope is mainly dependent on a lever arm, the so-called Cantilever (fig. 2.13) with an integrated sharp tip made of silicon or silicon nitride.

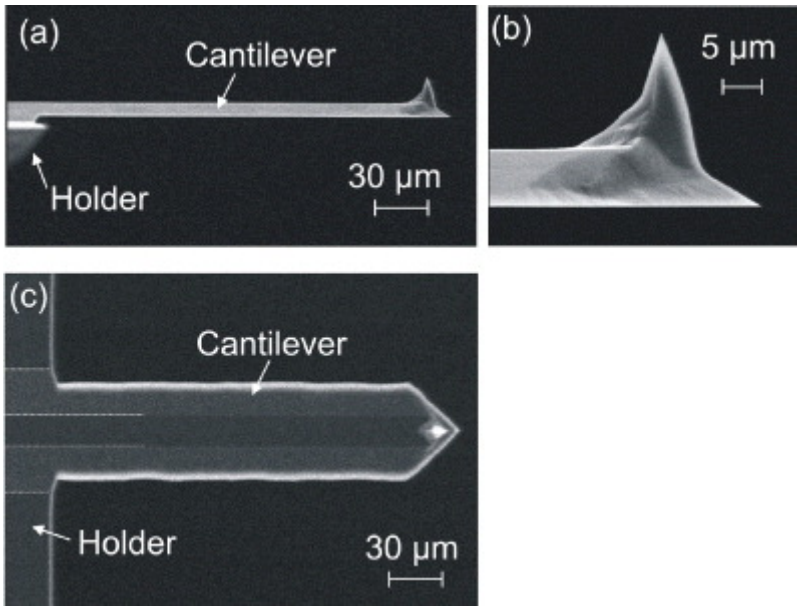

Figure 2.13: SEM micrographs showing (a) a side view of a cantilever, (b) an enlarged side view of the end of the cantilever carrying the sensor tip and (c) a view from the bottom side where the tip is mounted [24].

The chemical etching followed by lithography of silicon was used to fabricate cantilevers. A detailed description for the preparation can be found in references [25, 26]. Commercial AFM cantilevers have dimensions 50 to 500 microns in length, with thickness of 0.5 to 7.5 microns and have breadth of about 20 to 80 microns. Based on the above mentioned dimensions the spring constant varies from of 0.01 to 100 Nm^{-1}.

In order to detect atomic scale forces with the tip-sample interactions, the cantilever must fulfill various requirements. Among them, the spring constant of the cantilever is very important and this spring constant k of the cantilever should be smaller than the spring constant between two atoms in a substrate. Thus, considering the vibration frequency ω of atoms in a crystalline solid, typically 10^{13} Hz or higher with an average atomic mass of ~10^{-25} kg, the force constant has a value of ~ 10 Nm^{-1} [27] according to eq. 2.9

$$k = \omega^2 m \qquad 2.9$$

Therefore, the spring constant of the cantilever should be in the range of ~1 Nm^{-1}. Also, the cantilever should possess a large resonance frequency ω_0. This will enhance the sensitivity and also reduce mechanical vibrations. For larger resonance frequencies, the net mass of the cantilever m_c must be smaller as per eq. below

$$\omega_o = \sqrt{(k/m_c)} \qquad 2.10$$

The heart of the AFM unit is its precise deflection control unit. The initial design utilized an STM tip to monitor and detect the cantilever deflection [19].This detection system was replaced by an optical fiber detector [28], position sensitive detectors [29], and others [30, 31]. Among them, the position sensitive detector is the most sensitive and is used in the leading commercially available AFM units. A schematic view of this deflection principle is shown in fig. 2.14.

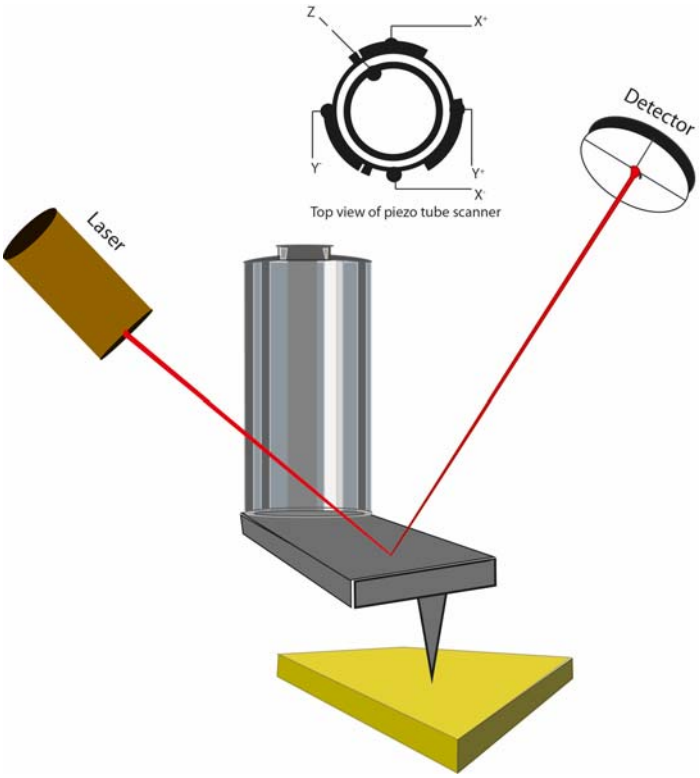

Figure 2.14: Schematic setup of an AFM.

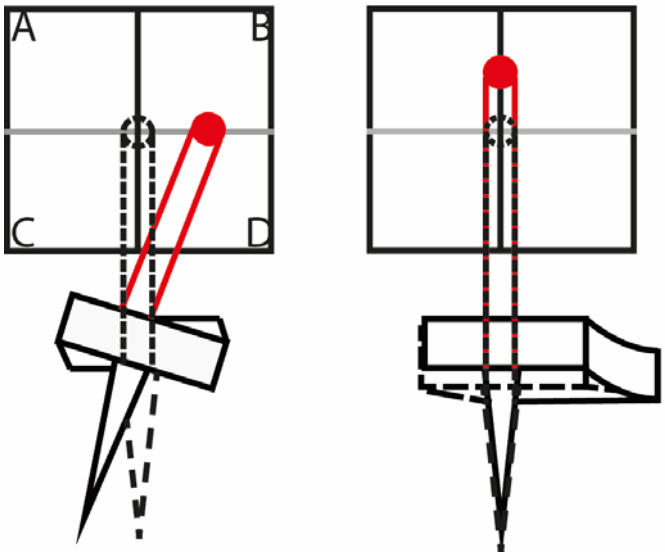

Figure 2.15: Schematic drawing explains the effect of cantilever movement. Twisting of the cantilever (left) indicates change in lateral deflection and (right) vertical movement of the cantilever results in vertical deflection. These changes are elaborated respectively on a photodetector represented by the square with quadrants labeled A, B, C and D.

In an actual setup, the cantilever tip is made to approach the sample surface by applying certain set point (constant normal force). A laser beam is focused on the back side of the cantilever tip. This beam is adjusted to obtain a net zero signal on the photodetector. A photodetector is an optical detection system used to monitor movement (deflection/torsion) of the cantilever tip. The photodetector consists of four quadrant photodiodes. Once the cantilever is near to the surface of the sample it interacts with the sample and is deflected from its rest position. The deflection can be perpendicular to the cantilever plane (z-direction) or it can be twisted along the horizontal axis as shown in figure 2.15. The signal generated, activates the feedback circuit to maintain a certain fixed tip-sample distance while scanning. This detection system is very sensitive and capable of determining the bending of the cantilever in the sub-angstrom range.

In general, the tip-sample interactions yield imaging either by a static method or a dynamic method. These can be accomplished by fixing the cantilever to a cantilever retainer which is either not connected to an actuator (static mode) or connected to an actuator (dynamic mode) [32]. The actuator contains a small piezo motor which is used to oscillate/vibrate the cantilever above the substrate surface with certain fixed frequency. The most common example of the static mode is the contact mode, in which the cantilever tip makes direct contact with the sample surface. Whereas the dynamic mode the cantilever is made to oscillate above the sample surface without being in contact (or contact for a short time) while maintaining a fixed distance between the cantilever tip and sample.
A brief description of both methods is given below:

2.6.1 Contact Mode

In this mode, the tip sample interaction is managed by exerting a constant force to achieve a mechanical contact with the sample. Due to this contact, the tip of the cantilever bends from its rest position. Here, the attractive forces are dominant and cause bending of the cantilever towards the sample surface. This deflection at a given setpoint during the interaction is monitored by the photodiode, which generates a control signal for the z-deflection of the z-piezo. This control signal activates the feedback loop, which ensures a constant force between tip and substrate surface. Consequently, at a fixed force, an image can be obtained by raster scanning the tip and

sample relative to each other. This mode facilitates imaging of the surfaces at higher scan speed, and is also capable of obtaining atomically resolved structures [33].

In addition, rough surfaces with extreme vertical topography differences (ditches, steep slopes, etc.) are often best imaged in the contact mode. Moreover, as a result of the tip movement over the surface, the tip twists in the lateral direction. This twisting of the cantilever tip is measured via the torsion of the cantilever, which provides information related to the local friction between the tip and the sample. (this is explained briefly in lateral force microscopy (LFM)).

The main disadvantage of contact mode is the mechanical contact with the tip which could not only damage the surface can also affect the cantilever tip. This can be avoided by using dynamic AFM mode (tapping and non-contact). These are briefly described below.

2.6.2 Tapping or intermittent contact mode

The most common dynamic AFM mode is the tapping mode. In this measurement method, the cantilever is vibrated by a small piezo motor to oscillate the cantilever near to its resonant frequency. The free amplitude of oscillation is far beyond the tip sample interaction, which is about 20-100 nm. During the grid-like scanning, the cantilever tip lightly touches the sample surface at each oscillation in its lower turning point. An attractive or repulsive interaction between the tip and the sample results in reduction in amplitude of free oscillation. The reduction in amplitude of this oscillation to a specified target value (e.g., 90% of the free amplitude) is used as a control signal in tapping mode for the Z-deflection of the piezo-scanner to maintain a constant force between tip and surface. Therefore, similar to contact mode, the z-piezo voltage signal is used to reconstruct the topography of the sample surface. The tapping mode is mainly used when the interaction of the tip with the sample surface is kept as low as possible. In other words only a pointwise scanning of the surface is performed, which resulted in particular no shear forces through the lateral scan movement.

A schematic of a cantilever during intermittent contact mode along is shown in fig. 2.16. Typical tapping or intermittent contact mode of operation is carried out using amplitude modulation detection with a lock-in amplifier. Direct force is not measured in this mode.

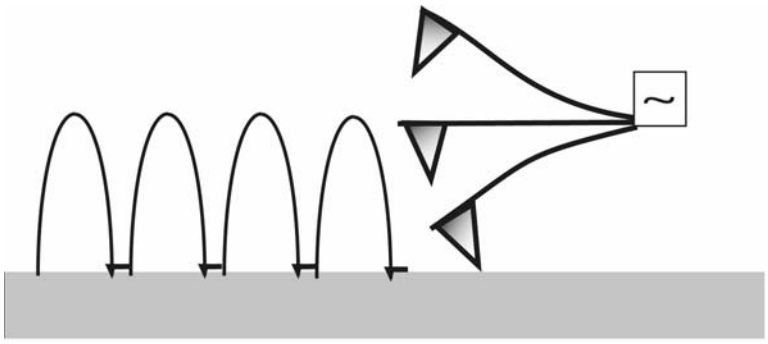

Figure 2.16: Schematic view of intermittent or tapping mode.

2.6.3 Non-contact mode

The non-contact mode is analogous to the tapping mode, however, the oscillating cantilever has a free amplitude of about <10 nm. The imaging principle is based on the reduction of resonance frequency mainly by attractive Van-der-Waals or other interactions with greater range. Therefore, the AFM tip in the lower turning point of its oscillation experiences only repulsive forces, i.e., it never makes mechanical contact with the substrate surface ('non-contact'). The advantage of the non-contact mode is that the surface cannot experience modification or destruction during the scan. The main drawback of this mode is that it produces poorly resolved images with lower lateral resolution due to a relatively large distance between the tip and sample surface. A typical response signal of a cantilever during non contact mode along with schematic description of this process is shown in fig. 2.17.

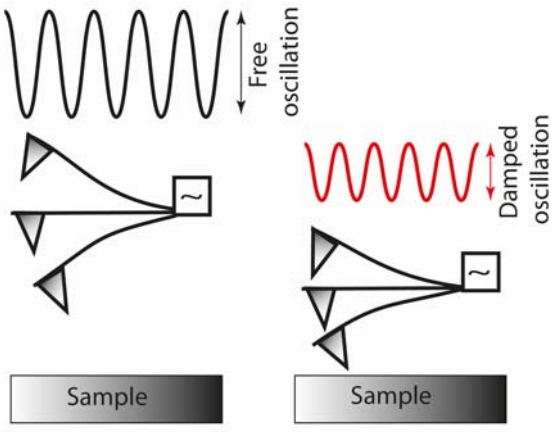

Figure 2.17: Resonance signal of non contact mode cantilever above and close to the surface.

2.6.4 Lateral force microscopy

As already mentioned in contact mode, the signals for vertical and lateral twisting of the cantilever are recorded simultaneously. The lateral twisting of the cantilever is observed when a constant force is applied between tip and sample while they are moving against each other. This leads to a frictional force, and the measure of this force microscopically is called lateral force microscopy (LFM). The tilt signal is recorded, which indicates dependence on the friction between the cantilever tip and the substrate surface. The cantilever twists differently on different sample surfaces and therefore can be used to monitor the material composition of the sample surface as shown in fig. 2.18. It also leads to an energy loss and causes wear and tear of both interacting surfaces. Since the contact established between surfaces at a region of micro-roughness is confined to a small part of the surface, thus increasing the force, it resulted in decreases of friction. The relationship between the effective normal force F_N and the frictional force F_{Lat} is given by eq. 2.11:

$$F_{Lat} = \mu \cdot F_N \qquad 2.11$$

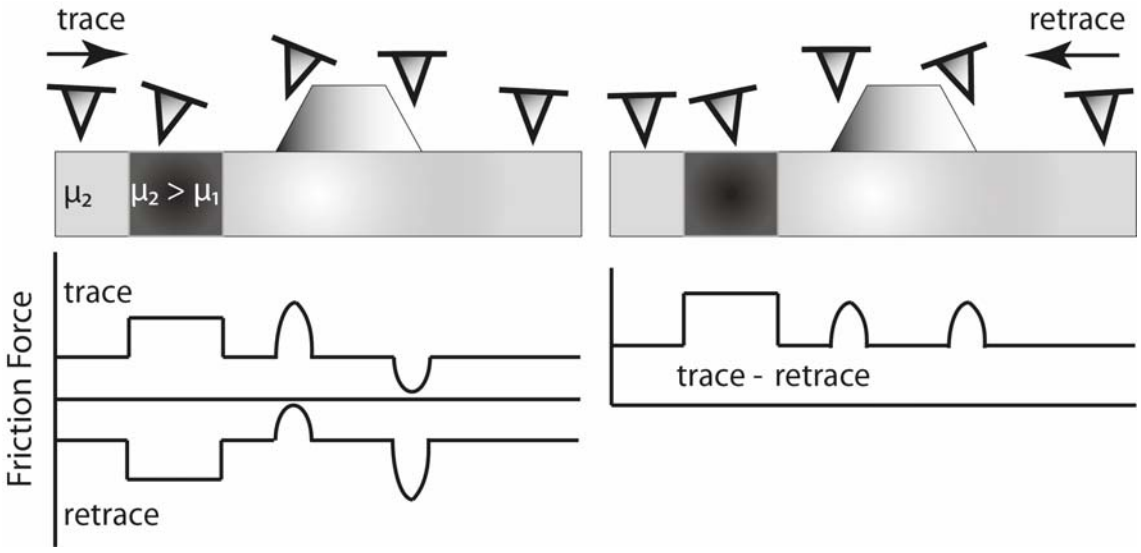

Figure 2.18: Schematic drawing of a surface with a centrally located step with low, smooth areas on either side. The flat part on the left contains a domain with a relatively high frictional coefficient. Profile of the cantilever's deflection as it encounters topographic features as well as different frictional coefficients as it scans from left to right and right to left are plotted as LFM signal which indicates the horizontal deflection of the cantilever. Resulting friction signal is obtained by subtraction of both friction signals is also shown.

The friction coefficient μ is material specific and has values that typically lie between 0.01 and 1. The microscopic surface structure and the chemical composition of the surface play a major role in frictional microscopy. Material differences due to adsorbed films, impurities, oxide layers or structural defects often change the friction coefficient significantly.

2.6.5 Force distance curve

The force in atomic force microscopy is monitored by plotting a force distance curve. In order to determine force as a function of distance F(D), the tip should make mechanical contact with the sample surface. The cantilever tip approaches the surface and then it is reversed to its starting point. During the course of approach and retraction the tip experiences variation in interaction forces with the contacting surface. These forces caused the tip to move towards or away from the surface while approaching and retracting respectively. In actual practice two factors, namely long-range forces and sample elasticity, interfere with finding the point of contact. The deflection of the cantilever is plotted against the distance from the sample position along the z-axis. This follows a simple relationship (i.e. Hook's Law) between the applied force, F, and the deflection of cantilever, d_c:

$$F = -k \cdot d_c \qquad 2.12$$

Where k is the spring constant of the cantilever.

A sketch of the force distance curve along with tip sample interaction during approach and retract is presented in fig. 2.19. The force distance curves can be explained on the basis of established force laws, particularly those determined using the surface force apparatus (SFA) [34]. This describes force as a function of the tip-sample separation distance (D) rather than as a function of the z-piezo position. Therefore, the force-distance curves should be altered to express force as a function of distance, F(D), which can be accomplished by subtracting the deflection of cantilever from the z-piezo movement.

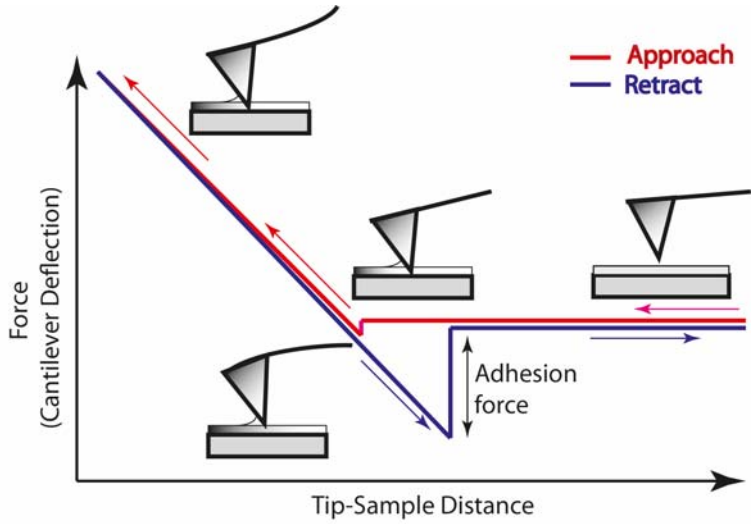

Figure 2.19: Schematic view of force distance curve.

2.6.6 The Tomlinson model of friction

The AFM can be used to obtain friction images with atomic resolution. Tomlinson devised a simple model to explain friction at nano-scale, which was further elaborated by Prandtl [35]. This model is used currently for nano-tribology applications and generally known as Prandtl Tomlinson (or simply Tomlinson model).

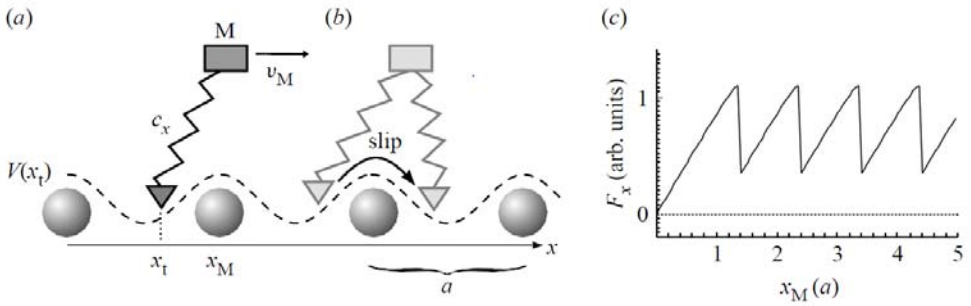

Figure 2.20: (a) peak position in the potential minimum friction force increases with lateral movement (stick); (b) Peak jumps to the next potential minimum (Slip); (c) the frictional force sawtooth signal at atomic stick-slip [36].

A schematic description of this model is elaborated in fig. 2.20. An elastic object (a cone with mass M) was considered as a cantilever model, which was connected to a mobile support having spring constant of k. It was dragged horizontally with a constant velocity on a surface defined by the atomic lattice that possessed spatial and energetic corrugation to demonstrate friction at atomic scale [36].

The displacement of the cantilever at an atomic scale (which is in this model) corresponds to lattice spacing 'a' with potential minima. During the continuous movement of the cantilever over the surface both the cantilever and surface atoms, occupied a common potential minimum. This resulted in the transition of cantilever from one potential minimum to the next potential minimum. This transition was somewhat resilient and accompanied by 'stick', while the torsion of the cantilever increased. However, the transition of the cantilever tip to the new minimum was somehow more abrupt. The sudden relaxation was termed as 'slip' accompanied by cantilever relaxation with decrease in torsion. The process, thus, is named 'stick-slip'. The frictional signal, which was observed during the movement of the cantilever, is presented in the form of a sawtooth curve in fig. 2.20c. Mate et al. were the first to obtain atomically resolved stick slip frictional pattern on highly oriented pyrolytic graphite (HOPG) [37]. At present, this effect is well known and further explanation can be found in following publications, [34, 38-41].

2.6.7 Forces in fluids

The frictional forces involve fluids between the interacting bodies. Even in case of dry friction under ambient conditions, there is always present a thin layer of adsorbed water between the grinding surfaces. Hence, the study of friction in the presence of lubricants or electrolytic solutions is of particular interest from both an applied and a fundamental point of view.

The Atomic force microscopic measurements performed in liquids are different from those performed in vacuum. The tip-sample interactions properties are influenced by the solid-liquid interface. For example, Van der Waals forces behave more complicatedly in liquids, and show strong dependence on the dielectric properties of the liquids. All liquids with considerable dielectric moments considerably decrease the Van der Waals force in relation to vacuum. Since capillary forces are not operative in electrolytes hence, interactions with large range forces are reduced significantly [42].

Furthermore, the effect of applied potentials on friction studies of adsorbed species and the formation of electrical double layers on single crystal surfaces under controlled environment are currently hot topics,

In our group, my predecessors (Podgyanyy, Nielinger and Hausen) conducted a series of nano tribology studies on single crystal electrodes under an electrochemical environment [43-46]. These studies were related to a change in coefficient of friction in the system of copper monolayer on gold (111) and the increase of the friction force in the formation of the adsorbed layer. However, structural aspects (sulfate on gold (111)) were not clearly understood. This research investigated frictional forces on single crystal surfaces with adsorbed layers. The degree of interaction of the cantilever with the surface and the reasons for the change of the friction coefficients are examined. Similarly, the effects of some adsorbates on the friction and adhesion forces are also determined.

2.7 Cleaning of the STM/AFM cell

All ancillaries (STM/AFM electrochemical cell, cantilever holder, reference and counter electrode wires) which are used while performing EC-STM/AFM required thorough cleaning. For this purpose these ancillaries were boiled in dilute sulfuric acid followed by boiling in Milli-Q water before use. The AFM cantilever holder (quartz glass and the gold plated cantilever holder were flushed with ethanol and then thoroughly rinsed with Milli-Q water.

2.7.1 STM tips

An ideal STM tip should be atomically sharp, have good electrical conductivity, be mechanically stable and allow the entire tunnel current to flow through the tip atoms. For applications in the electrolyte, the tip should be electrochemically inert. In addition, the tip must be insulated except for a small area at the top end. For the measurements in this work insulated platinum/iridium (90:10) tips were used. These were made from a wire having a diameter of 0.25 mm using procedure of local etching [47-49]. A less toxic etching solution was used instead of existing sodium cyanide (NaCN), which is a combination of 2 M KOH and 4 M KSCN. Moreover, in the presence of thiocyanate the etching process time is decreased and also results in atomically sharp and regular tips. The etching process was performed in a small beaker with an annular anode made of Pt wire completely submerged in the etching solution. A d.c. signal of 1.6V with a superimposed a.c. square wave signal of 6.5V at 1kHz was applied while performing etching of the wire. The lower part of the wire was covered with a Teflon tube, which

was then inserted in the etching solution. Once the exposed part of the wire comes in contact with the etching solution, etching of the tip starts immediately. The wire was then withdrawn a little to develop a hanging meniscus configuration as shown in fig. 2.21. The etching of the tip continued around the meniscus and yielded an atomically sharp tip. The lower half of the wire fell, together with Teflon tubing, into the beaker and was discarded. The upper tip was thoroughly rinsed with Milli-Q water and then applied an electrophoretic paint for isolation

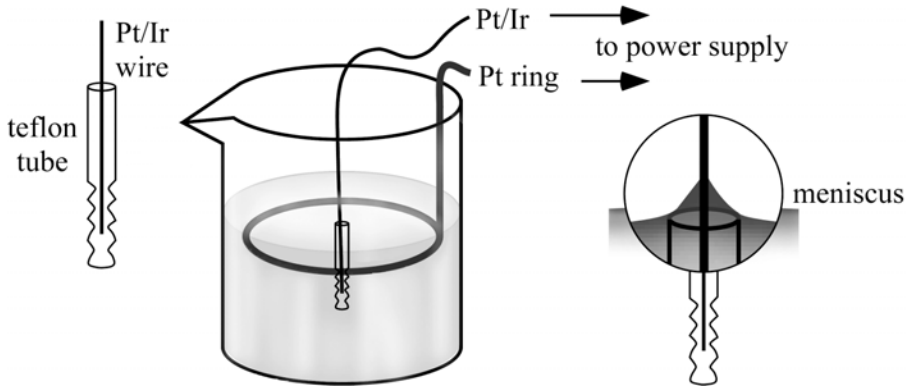

Figure 2.21: Schematic representation of the construction as for the production of STM tips is used. Picture from [50].

2.7.2 Isolation of the tips

For the electrochemical STM measurement the faradaic currents at the tip should be at minimum. Therefore, it is necessary to avoid electrochemical currents at the tip by applying special coatings in such a way that only the foremost part of the tip is exposed to the electrolyte. This was achieved by insulating the tips with an electrophoretic paint (emulsion polymer GLASSOPHOR GY850030, BASF). For this purpose, the half of the STM tip was immersed in the electrodeposition paint. A voltage between the STM tip (positive pole) and a Pt wire immersed in the electrophoretic paint (negative pole) was applied. The coating was performed by applying 12 V for about 40 seconds. The coated tips were heat cured by placing in an oven at 200°C for 10 minutes. By this curing, paint adhered firmly to the tip and only cracked at the outermost part of the tip. Finally, the finished tips were examined under an optical microscope for cracks in the paint and defects in the tip itself. In an alternative method the etched tips were isolated using a molten polymer glue followed by curing using a simple hair dryer.

2.8 Scanning probe microscope (SPM)

The Molecular Imaging model Pico-SPM scanning probe STM and AFM were used for current experimental work. This SPM was coupled to a bipotentoistat model PicoStat for electrochemical control. The system was controlled by a digital controller III-E type from Digital Instrument (DI) with NanoScope software for data evaluation purpose. Two scanner modules with 1 x 1 micron for STM and one 6 x 6 microns for AFM were used. For performing electrochemistry in STM/AFM cell, a home built external function generator (developed by the electronics workshop of the University of Bonn) was connected to the Picostat. The home built STM or AFM measurement cell is made of Kel-F with a large cell volume and an additional small electrolyte chamber for the reference electrode connected via a small hole to the main chamber. This made it possible to avoid metal ion diffusion to the reference chamber during metal deposition in the main chamber as shown in fig. 2.22.

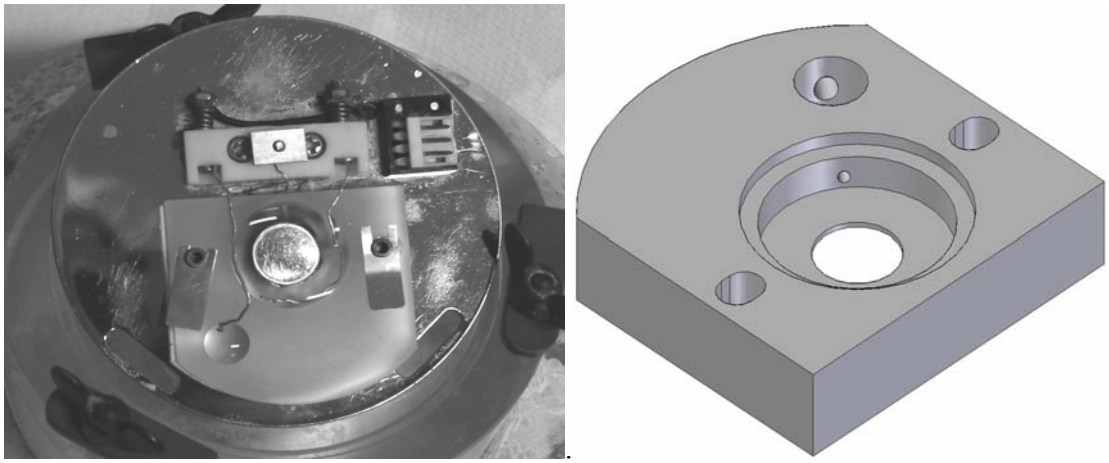

Figure 2.22: Actual photo STM/AFM electrohemical cell (left) schematic view of electrochemical STM/AFM cell (right).

2.8.1 AFM cantilever

For all measurements commercially available cantilevers were used. These cantilevers were made from silicon and obtained from Nanosensors (Switzerland) and Veeco Probes (USA).

Other specifications are summarized in Table 2.1.

Table 2.1: Cantilever specifications PPP-CONTSC-20 & MPP-31100

Type	Material	Coating	Spring constant (N/m)	Length (μm)	Width (μm)	Thickness (μm)	Frequency (kHz)	Lateral force constant (N/m)
PPP-CONTSC	Silicon	Non-coated	0.2~0.3	225	44	1.2~1.5	31~37	50
MPP-311000	Silicon	Non-coated	0.9	440	30	4	300	190

The simpler rectangular design with single arm cantilever allowed easy adjustment of the laser. In addition; reflectivity of the laser from the back side of the cantilever is large enough to generate a stable signal at the photodetector despite the non-existence of a coating. The main drawback of these kinds of cantilever is that the topographic image resolution is relatively poor.

2.8.2 STM/AFM images analysis

All the STM/AFM images are shown in the shades of brown. The corresponding z value (height scale), is the area shown in reddish brown (lower value) to rosy brown (higher value). Scaling in the x and y directions always correspond to each other. Height values are comparative to each other in the AFM/STM topographic images. The lighter the shade (shown as rosy brown), the higher the height of the structure. Conversely, the darker the shade (shown as reddish brown), the lower the height of the structure. When required within the image (STM/AFM), the variation in height profile was shown through section analysis.

For the AFM, friction difference images were obtained by subtracting the friction trace image from the friction retrace image, explained in detail in the next section.
In these images, bright shades corresponded to areas of high friction and vice versa. The frictional forces were represented as a voltage signal, which is proportional to the bending of the cantilever. Conversion of voltage signal to force signal is a somewhat complicated procedure. For normal forces, the conversion constant is deduced from force distance curve at various loads. However, in the case of lateral forces, lateral force constant of each cantilever has to be determined. This depends on the geometry of the cantilever and varies from cantilever to cantilever. The detailed experimental procedure for the determination of spring constants can be found in references [51, 52].

For the purpose of evaluation, in addition to each individual frictional force a line scan (Section Analysis) of the friction image was presented side by side. The higher the volt signals in the section analysis at different parts of the image, the greater the friction on those areas. An atomically resolved STM images for adlayers were shown with, and without filtering.

2.8.3 Lateral force friction analysis

The lateral force friction signal was the result of the twisting force (torsion) on the cantilever in a lateral direction. This twisting of the cantilever is material specific and hence is affected differently for different coefficients of friction. In addition, topographic effects such as step edges also influence general lateral twisting. All this information can be obtained from a single difference friction image. For this purpose, LFM scans in both directions were simultaneously recorded along with the topographic image. Friction on material specific area and at different geometric sites appeared differently in one scan direction than that in the opposite scan and therefore would be distinguished as represented in fig. 2.19.

As mentioned earlier, material specific contribution resulted due to the twisting of the cantilever and their values are direction specific. However, the topographic effects are not directional specific and can easily be distinguished from material induced effects.

2.9 Differential Electrochemical Mass Spectrometry (DEMS)

DEMS is an experimental technique, which allows simultaneous detection of volatile products and intermediates generated during an electrochemical reaction via a coupled online mass spectrometer. The concept of this method was initially realized by Bruckenstein and Gadde and given the name Electrochemical Mass Spectroscopy (EMS) [53]. Later, Wolter and Heitbaum reduced the delay in the detection response time [54]. The electrochemical device (potentiostat) and mass spectrometer are the basic components of the DEMS. For a detailed description of this technique see [6].

The primary objective of this technique was the quantitative determination of intermediates and final products during electrochemical oxidation or reduction of fuels in general. However, in current work, this technique is utilized for the quantitative determination of reduced selenide deposited on the single crystalline substrates.

2.10 Inductive heating method for single crystal electrode preparation

Clavilier et al. in 1980 developed a cost effective and convenient method for single crystal electrode preparation using flame annealing and quenching especially for Pt single crystal surfaces [9]. Before this method single crystal surfaces were prepared under ultra-high vacuum (UHV) and were very complicated and time consuming to prepare. Later this method was extended to the preparation of other single crystal metal surfaces such as Au[11], Ag[55], Ir[56], Rh and Pd [57]. The quenching process has now been replaced by slow cooling down in a clean gas atmosphere and the surface protected with a droplet of oxygen free Milli-Q water.

Active noble metal surfaces which are sensitive to oxygen and readliy develop oxide layer such as palladium (Pd), Pt, Rh, Iridium (Ir) and Ru are annealed in an inert environment using resistive heating [58]. However, this method requires large currents for annealing and is problematic for electrode surfaces with large diameter.

Induction heating is another method used for the preparation of single crystal surfaces and was successfully utilized by Kibler et al. [59]. Induction heating is considered to be the idea lmethod for preparing single crystal surfaces which are difficult to prepare by flame annealing such as Ru(0001) [60] also when formation of an alloy is desired [61], [62] and for place exchange of adlayer atoms with substrate atoms [63].

The basic principle of induction heating involves heating a conductive metal by radio frequency electromagnetic radiation. This induces eddy currents within the metal and resistance causes joule heating. The main advantage of induction heating is that it is a non-contact mode of heating in a controlled environment, and so reduces the chances of contamination in comparison to the other heating methods of flame and resistive heating. This technique is used to obtain stable adlayers of Se on Rh(111) surface. The electrochemically modified Se/Rh(111) surface was inductively heated at various temperatures under controlled environment to generate Se/Rh(111) surfaces having different morphologies.

References

[1] J. Yamada and H. Matsuda, Journal of Electroanalytical Chemistry 44:189 (1973).

[2] W. J. Albery and M. L. Hitchman, Ring-disc electrodes [by] W. J. Albery and M. L. Hitchman, Clarendon Press, Oxford, 1971.

[3] A. C. Fisher, R. G. Compton, C. M. A. Brett, and A. M. C. F. O. Brett, Journal of Electroanalytical Chemistry and Interfacial Electrochemistry 318:53 (1991).

[4] W. J. Albery, C. C. Jones, A. R. Mount, and R. G. Compton, in Comprehensive Chemical Kinetics, Vol. Volume 29, Elsevier, 1989, p. 129.

[5] Z. Jusys, J. Kaiser, and R. J. Behm, Electrochimica Acta 49:1297 (2004).

[6] H. Baltruschat, Journal of the American Society for Mass Spectrometry 15:1693 (2004).

[7] F. G. Will, Journal of The Electrochemical Society 133:454 (1986).

[8] W. R. Grove, Philosophical Magazine Series 3 14:127 (1839).

[9] J. Clavilier, R. Faure, G. Guinet, and R. Durand, Journal of Electroanalytical Chemistry 107:205 (1980).

[10] J. Clavilier, M. Wasberg, M. Petit, and L. H. Klein, Journal of Electroanalytical Chemistry 374:123 (1994).

[11] A. Hamelin, XXX Structure of metals, Plenum Press, 1985.

[12] M. Hourani and A. Wieckowski, Journal of Electroanalytical Chemistry and Interfacial Electrochemistry 227:259 (1987).

[13] J. M. Feliu, R. Gomez, M. J. Llorca, and A. Aldaz, Surface Science 289:152 (1993).

[14] J. Clavilier, M. J. Llorca, J. M. Feliu, and A. Aldaz, Journal of Electroanalytical Chemistry and Interfacial Electrochemistry 310:429 (1991).

[15] S. E. Huxter and G. A. Attard, Electrochemistry Communications 8:1806 (2006).

[16] N. Bogolowski, S. Huxter, A.-E.-A. A. Abd-El-Latif, G. A. Attard, and H. Baltruschat, Journal of Electroanalytical Chemistry 646:68 (2010).

[17] J. R. Oppenheimer, Proceedings of the National Academy of Sciences 14:363 (1928).

[18] R. H. Fowler and L. Nordheim, Proceedings of the Royal Society of London A: Mathematical, Physical and Engineering Sciences 119:173 (1928).

[19] G. Binnig, Helvetica Physica Acta 55:726 (1982).

[20] G. Binnig, H. Rohrer, C. Gerber, and E. Weibel, Physical Review Letters 50:120 (1983).

[21] M. Wilms, M. Schmidt, G. Bermes, and K. Wandelt, Review of Scientific Instruments 69:2696 (1998).

[22] D. M. Kolb, Electrochimica Acta 45:2387 (2000).

[23] G. Binnig, C. F. Quate, and C. Gerber, Physical Review Letters 56:930 (1986).

[24] F. J. Espinoza-Beltran, K. Geng, J. M. Saldana, U. Rabe, S. Hirsekorn, and W. Arnold, New Journal of Physics 11 (2009).

[25] T. R. Albrecht, S. Akamine, T. E. Carver, and C. F. Quate, Journal of Vacuum Science & Technology a-Vacuum Surfaces and Films 8:3386 (1990).

[26] O. Wolter, T. Bayer, and J. Greschner, Journal of Vacuum Science & Technology B 9:1353 (1991).

[27] D. Ruger, Physics Today 43:23 (1990).

[28] Y. Martin, C. C. Williams, and H. K. Wickramasinghe, Journal of Applied Physics 61:4723 (1987).

[29] G. Meyer and N. M. Amer, Applied Physics Letters 53:1045 (1988).

[30] T. Göddenhenrich, H. Lemke, U. Hartmann, and C. Heiden, Journal of Vacuum

Science & Technology A 8:383 (1990).
[31] R. Linnemann, T. Gotszalk, L. Hadjiiski, and I. W. Rangelow, Thin Solid Films 264:159 (1995).
[32] F. J. Giessibl, Reviews of Modern Physics 75:949 (2003).
[33] T. Schimmel, T. Koch, J. Küppers, and M. Lux-Steiner, Applied Physics A 68:399 (1999).
[34] B. Bhushan, J. N. Israelachvili, and U. Landman, Nature 374:607 (1995).
[35] L. Prandtl, ZAMM - Journal of Applied Mathematics and Mechanics / Zeitschrift für Angewandte Mathematik und Mechanik 8:85 (1928).
[36] L. Jansen, H. Hölscher, H. Fuchs, and A. Schirmeisen, Physical Review Letters 104:256101 (2010).
[37] C. M. Mate, G. M. McClelland, R. Erlandsson, and S. Chiang, Physical Review Letters 59:1942 (1987).
[38] E. Gnecco, R. Bennewitz, T. Gyalog, and E. Meyer, Journal of Physics-Condensed Matter 13:R619 (2001).
[39] P. A. Thompson and M. O. Robbins, Science 250:792 (1990).
[40] N. S. Tambe and B. Bhushan, Nanotechnology 16:2309 (2005).
[41] R. M. Overney, E. Meyer, J. Frommer, D. Brodbeck, R. Luthi, L. Howald, H. J. Guntherodt, M. Fujihira, H. Takano, and Y. Gotoh, Nature 359:133 (1992).
[42] U. Hartmann, Advanced Materials 2:594 (1990).
[43] N. Podgaynyy, S. Iqbal, and H. Baltruschat, Surface Science 631:67 (2015).
[44] M. Nielinger, F. Hausen, N. Podghainiy, and H. Baltruschat, in Friction, Wear and Wear Protection (A. Fischer and K. Bobzin, eds.), Wiley-VCH, Weinheim, 2009, p. 178.
[45] F. Hausen, M. Nielinger, S. Ernst, and H. Baltruschat, Electrochimica Acta 53:6058 (2008).
[46] M. Nielinger and H. Baltruschat, Physical Chemistry Chemical Physics 9:3965 (2007).
[47] L. Libioulle, Y. Houbion, and J. â. M. Gilles, Review of Scientific Instruments 66:97 (1995).
[48] A. D. Muller, F. Muller, M. Hietschold, F. Demming, J. Jersch, and K. Dickmann, Review of Scientific Instruments 70:3970 (1999).
[49] J. Lindahl, T. Takanen, and L. Montelius, Journal of Vacuum Science & Technology B 16:3077 (1998).
[50] F. Hernandez, in Mathematisch-Naturwissenschaftliche Fakultät, Rheinische-Friedrich-Wilhelms-Universität Bonn, Bonn, 2006.
[51] J. Ralston, I. Larson, M. W. Rutland, A. A. Feiler, and M. Kleijn, Pure and Applied Chemistry 77:2149 (2005).
[52] H. J. Butt, B. Cappella, and M. Kappl, Surface Science Reports 59:1 (2005).
[53] R. R. Bruckenstein and J. Gadde, Journal of the American Chemical Society 93:793 (1971).
[54] O. Wolter and J. Heitbaum, Ber. Bunsenges. Phys. Chem. 88:2 (1984).
[55] A. Hamelin, L. Doubova, D. Wagner, and H. Schirmer, Journal of Electroanalytical Chemistry and Interfacial Electrochemistry 220:155 (1987).
[56] S. Motoo and N. Furuya, Journal of Electroanalytical Chemistry 167:309 (1984).
[57] K. Sashikata, N. Furuya, and K. Itaya, J. Vac. Sci. Technol. B B 9:457 (1991).
[58] A. Cuesta, L. A. Kibler, and D. M. Kolb, Journal of Electroanalytical Chemistry 466:165 (1999).
[59] L. A. Kibler, A. Cuesta, M. Kleinert, and D. M. Kolb, Journal of Electroanalytical Chemistry 484:73 (2000).
[60] A. M. El-Aziz and L. A. Kibler, Electrochemistry Communications 4:866

(2002).
[61] A. M. El-Aziz, R. Hoyer, and L. A. Kibler, ChemPhysChem 11:2906 (2010).
[62] V. Stamenkovic, B. S. Mun, K. J. J. Mayrhofer, P. N. Ross, N. M. Markovic, J. Rossmeisl, J. Greeley, and J. K. Norskov, Angewandte Chemie-International Edition 45:2897 (2006).
[63] A. S. Bandarenka, A. S. Varela, M. Karamad, F. Calle-Vallejo, L. Bech, F. J. Perez-Alonso, J. Rossmeisl, I. E. L. Stephens, and I. Chorkendorff, Angewandte Chemie International Edition 51:11845 (2012).

Chapter 3: Surface morphology and adlayer structure of Se on Rh(111)

This chapter illustrates the use of scanning probe techniques for visualizing the adlattices of atoms, ions or molecules at an atomic level. The adlayer structure of SO_4^{2-} was observed on Rh(111). Based on these images the orientation of the Rh(111) substrate was determined and a mathematical procedure was developed to determine the drift, correct for it and calibrate the STM scanner used (appendix A). Thus, the adlayer lattice for selenium on Rh(111) was identified. Furthermore, changes in the surface morphologies of these surfaces under potential control were observed. This information will help us in understanding the fundamental aspects of these selenium modified model catalysts.

3.1 Introduction:

The traditional electrochemical techniques have long been utilized to study the function of specifically adsorbed anions in order to elucidate electrode-electrolyte interactions. The result obtained for these interactions only provides macroscopic level information about the interface concerned. Access to microscopic (atomic) level information of these electrochemical interfaces is made possible by using structure and coverage sensitive techniques such as ultrahigh vacuum (UHV), low energy electron diffraction (LEED) and x-ray photoelectron spectroscopy (XPS). In addition utilization of in situ scanning probe microscopy (SPM) and in situ infra-red spectroscopy (IR) enables us to visualize the real adlattice of adsorbed species on a substrate surface [1, 2].

Magnussen et al, using in situ STM, reported an ordered structure of sulfate/bisulfate with (√3X√7) symmetry for Au(111) in sulfuric acid [3]. In addition, similar commensurate adlayer structures were observed for other fcc(111) surfaces namely Rh(111) [1, 4], Ir(111) [5] Pd(111) [6] by Wan et al. and by Funtikov et al. and Braunschweieg et al. on Pt(111) [7-9].

The aqueous solutions of chalcogenides (S, Se, Te) are also considered as significant types of adsorbates. The surface chemistry of metal chalcogenides was explored extensively. Among precious metal catalysts, Rhodium and Ruthenium modified with chalcogenides were investigated as possible alternatives to Pt for selective oxygen reduction reaction catalysis [10].

In UHV, adsorption of H_2S or S^{2-} at room temperature and heating the sample lead to ordered structures on different metal surfaces. For the basal planes Re(0001), Rh(111) and Ru(0001), a variety of simple and more complex adsorbate structures were observed with the help of low-energy electron diffraction (LEED) and scanning tunnelling microscopy (STM), depending on dosage of the adsorbate (H_2S or S_2). For Re(0001), in order of increasing coverage, a c(√3x5)rect. (θ = 0.2 ML), a p(2x2) (1/4 ML), a (3√3x3√3)R30° (0.35 ML), a $\begin{pmatrix} 3 & 1 \\ 1 & 3 \end{pmatrix}$ (0.4 ML), and a (2√3x2(3)R30°) (0.5 ML) structure were observed.[11-13] In all cases sulfur is adsorbed on the threefold hollow site and the sulfur adatoms form three-, four- and six-adatom clusters. For Rh(111) an ordered c(4x2) structure at low S coverage, a ((3x(3)R30° at 0.33 ML, a (4x4) at 0.5 ML and a (7x7) structure at 0.75 ML were found, with sulfur adsorbed either on fcc hollow sites only or on fcc and hcp hollow sites [14-17] . At very high sulfur dosages, even the formation of an amorphous film of RhS_x was observed with synchrotron-based high-resolution photoemission spectroscopy (HRXPS) [1].

For Ru(0001) at room temperature in the range of 0 to 0.25 ML a p(2x2) overlayer structure (island formation) was found, at around 0.33 ML a ((3x(3)R30 (with disordered domain walls), at around 0.5 ML a c(2x4) and a structure, and in the range of 0.55-0.6 ML a ((7x√7)R19.1° commensurable structure were found[18-21], with sulfur exclusively adsorbed on the hcp threefold sites up to a coverage of 0.33 ML. Above 0.61 ML the formation of a second sulfur layer starts. In thin films of molecular sulfur on Ru(0001) even cyclooctasulfur S_8 was found and characterized by XPS and UPS [22].

For the ordered structures of sulfur on Pt(111) for a p(2x2) structure at 0.25 ML, a ((3x(3)R30° at 0.33 ML and a c(7x√3) rect structure at 0.43 ML were identified as function of coverage.[23-25] Similarly, for Pt(111) modified with selenium, Kiskinova et al. found a p(2x2) and (3x√3))R^o overlayer at low selenium coverages between 0.1 and 0.4 ML at 20K after adsorption of selenium at 80K. For selenium coverages around 0.5 ML the authors found a (4x4) structure.[26] On the stepped Pt(S)-[9(111)x(100)] single crystal Gdowski et al. found a p(2x2) and (√3x√3)R30-S overlayer structure from adsorbed H_2S. Also the adsorption of sulfur was studied on t single crystalline and polycrystalline electrodes [27-31].

Surprisingly, we did not find any literature on the adsorbate structures of selenium on Rh(111) or Ru(0001), neither in UHV nor using STM. Even less is known about the structures of the chalcogenides on Ru and Rh single crystals in an electrochemical environment. Itaya et al. found a (2x√3) rect adlayer for adsorbed sulfur on Ru(0001), which changed to a (√7x√7)R19.1° and then to a disordered structure as the potential was scanned from 0.3 to 0.6 V vs. RHE [23].

The selenium electrochemistry plays a vital role in the generation of compound semiconductors, which are important for optoelectronic application. In this connection detailed electrochemical and scanning probe microscopic studies were performed to characterize Se adlayers on Au(111) surface [24, 25]. The detailed electrochemical behaviour of the Se on Au(111) was found to be complex and its atomic layer deposits are characterized by three surface limited reduction peaks. These reduction peaks occur at potentials negative to the Se(IV)/Se(0) redox couple and therefore, strictly speaking, even the first (most positive) reduction peak is not an underpotential deposition. In a recent publication, the authors claimed that the first reduction peak corresponds to the conversion of adsorbed selenate (Se(VI)) (formed before at more positive potentials) to selenite (Se(IV)), whereas the formation of the atomic Se(0) occurs at the third reduction peak by four electron reduction of the adsorbed Se(IV) [24]. The STM studies of Se adlayers on Au(111) revealed that the most dominant Se adlayer structure was (√3x√3)R30°. However, at high Se coverages the (√3x√3)R30° commensurate structure changed to a heterogeneous structure composed of clusters, chains and pits due to the slow Se deposition kinetics [25].

In our current work, we tried to systematically investigate the atomic scale adlayer structure of sulfate (SO_4^{2-}) to check the system suitability. We then observed the adlayer structure of submonolayer of selenium on Rh(111) using in situ scanning probe microscopic (STM and AFM) techniques. This study aims at providing an improved understanding of the metal chalcogenide (especially Rhodium Selenide) structures and compositions at atomic level. This information would help the development of cathode material better suited for fuel cell applications.

3.2 Experimental:

Preparation and electrochemistry of massive Rh single crystal electrodes

The Rh(111) was prepared by annealing followed by cooling down in a mixture of Ar:H_2 (2:1) [26]. Rh(111) single crystals with a diameter of 10 mm were used (Kristallhandel Kelpin, Germany). All solutions were prepared from 18.2 MΩ Milli-Q water and de-aerated with high purity argon gas (99.999%). Electrochemical experiments in 0.1 M $HClO_4$ and 0.1 M H_2SO_4 (spectro pure grade) were carried out in a conventional three electrode H-cell in a hanging-meniscus configuration with a large Pt sheet as the counter electrode. A reversible hydrogen electrode was employed as a reference electrode. Selenium submonolayer and multilayer deposits were produced in a similar H-cell containing 1 mM H_2SeO_3 (Analytical grade). A bi-potentiostat from Pine Instruments Inc. model AFBPC1 in combination with a user interface developed in Labview software was used for recording cyclic voltammograms (CV). Relative coverages are given as a ratio of adsorbate species (the absolute coverage Γ), to the number of surface Rh-atoms (N_{Surf}), designated as $\vartheta = \Gamma / N_{Surf}$ and are calculated from the deposition charge according to

$$\vartheta_{Se} = Q_{Se}^{tot} / (z \cdot Q_{Rh(111)}) \qquad 3.1$$

Where, z = total number of electrons required for the reduction of selenite to selenium and $Q_{Rh(111)}$ is the charge density of a monolayer for the adsorbed hydrogen on Rh(111). All STM and AFM measurements were performed with a Nanoscope III E controller (Digital Instruments, Santa Barbara, CA) and a commercially available STM and AFM scanner (Molecular Imaging) fitted with an electrochemical cell. All STM measurements were done at room temperature using Pt/Ir (90:10) tips having diameter of 0.25 cm, which were etched in a KSCN + KOH bath and coated with melted polymer glue to reduce the area in contact with the electrolyte. A Pt wire was used as the counter electrode, another Pt electrode was used as quasi reference electrode (potentials are converted to the RHE scale using $E_{Pt/PtO}$ = 0.9 V vs RHE). It was immersed in the same solution separated from the STM cell by a capillary. All AFM experiments were performed with soft cantilevers: n^+-doped Si cantilever by Nanosensors (PPP-CONT-10), k_n = 0.09 N/m. The torsional force constant was determined via Sader's method [27] and found to be 50 Nm^{-1}. This method is based on the measurement of the resonant frequency and quality factor of the cantilever.

3.3 Results and Discussion:

3.3.1 Electrochemistry of selenium on Rh(111)

A typical cyclic voltammogram (CV) of Rh(111) in 0.1 M $HClO_4$ is shown in fig. 3.1. The detailed explanation about the voltammetric feature of Rh(111) is available elsewhere [1, 26, 28].

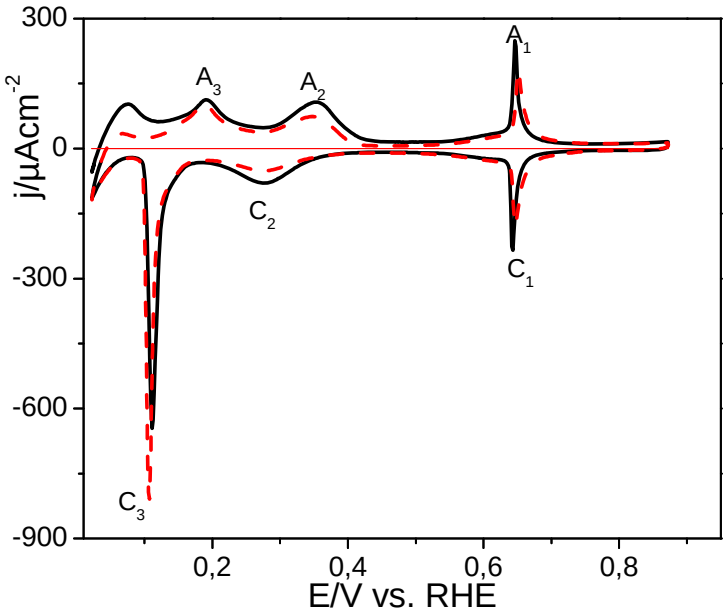

Figure 3.1: Cyclic voltammogram of Rh(111) in 0.1 M $HClO_4$, first seep (——), second sweep (-------), sweep rate 50 mV/s.

The voltammetric profiles for submonolayer and multilayer deposits of selenium on Rh(111) are shown in fig. 3.2. For Se submonolayer deposits the potential was scanned from 1.0 V vs RHE which is close to the rest potential. The Se submonolayer on Rh(111) manifests itself in fig. 3.2a by three peaks C_1, C_2 & C_3 in a surface limited process before the multilayer deposition start as per following reaction.(assuming Se deposition proceed similar to Au(111)) [24].

$$H_2SeO_{3\ ads} + 4H^+ + 4e^- \rightarrow Se + 3H_2O \qquad 3.2$$

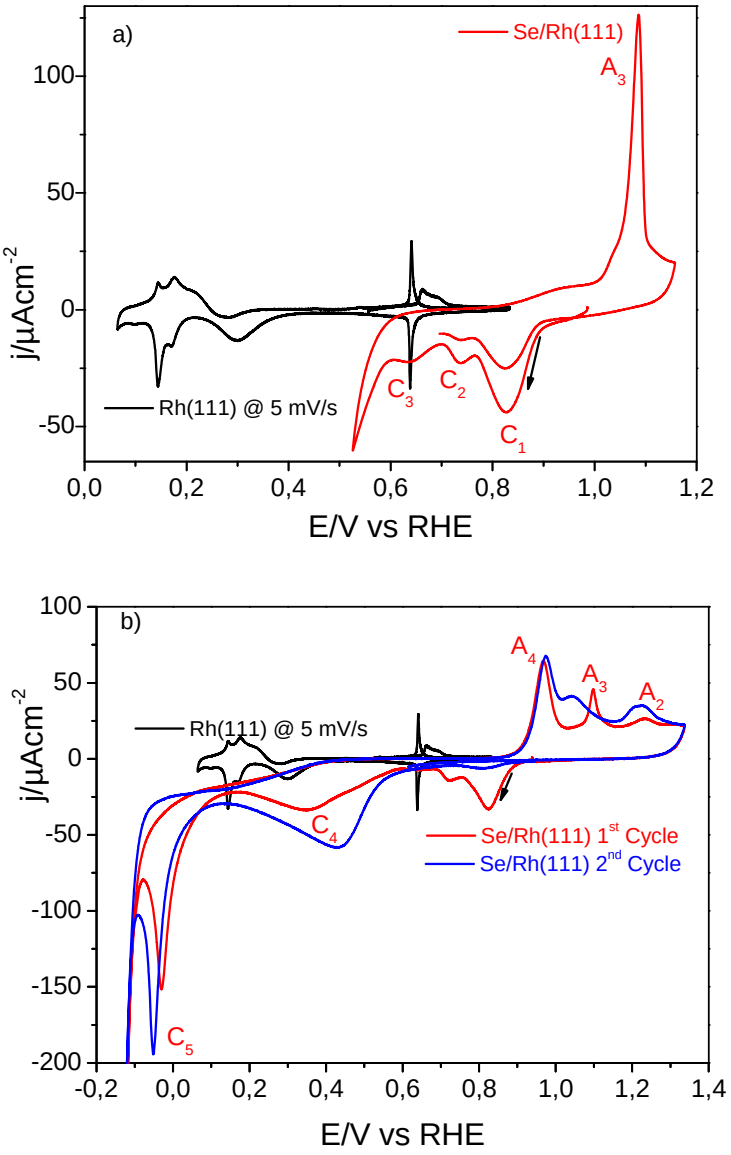

Figure 3.2: The cyclic voltammograms of Rh(111), sweep rate 5 mV/s together with a) monolayer and b) multilayer of Se deposition/dissolution on Rh(111) from 1mM H_2SeO_3 + 0.1 M $HClO_4$, sweep rate 10 mV/s.

The total selenium deposition charge density calculated after background correction (double layer correction) was found to be 411 µC cm^{-2} with a separate charge density of each peak is 300, 57 and 52 µC cm^{-2} respectively. The irreversible nature of the Se adlayer is evident from the oxidative stripping of the adsorbed selenium around 1.1 V (Peak A_4) with a calculated charge density of around 400 µC cm^{-2} after background correction (double layer correction). On scanning the potential to a more negative potential of around 0.35 V as shown in fig. 3.2b, another deposition (peak C_4) appears. This peak C_4 represents Se deposits of up to two monolayers and not the bulk deposition, this might be due to high resistivity of Se (10^{10} Ωcm) also observed by Stickney and co-workers on Au single crystalline surfaces [25, 29].

Peak C_5 is caused by generation of Se^{2-} from multilayer adsorbed Se (Peak C_4) and can react chemically with H_2SeO_3 present in the solution and hence form metallic Se:

$$Se + 2H^+ + 2e^- \rightarrow H_2Se \qquad 3.3$$

$$2H_2Se + H_2SeO_3 \rightarrow 3Se + 3H_2O \qquad 3.4$$

During oxidative stripping of Se, bulk Se stripped off around 1.0 V (Peak A_4) followed by stripping of the monolayer (peak A_3). Peak A_2 is probably due to stripping of a intermetallic compound similar to the one observed in case of Se on Au(111) [24].

3.3.2 Scanning Tunneling Microscope (STM) measurements on Se/Rh(111)

In situ STM measurement provides insight into the surface structure of the metal substrate as well the adlayers, which is crucial for understanding the electrochemical behaviour of modified surfaces. STM images were obtained for selenium modified Rh(111) under electrochemical conditions.

3.3.2.1 In situ STM of Se on Rh(111): Potential dependence modification

In the following series of STM images, selenium was deposited in situ electrochemically using 1 mM H_2SeO_3 in an STM cell as shown in the corresponding CV, where the potential was scanned from 0.9 V to +0.68 V and then held at a potential at +0.74 V vs RHE. In all STM experiments, the first image was taken at rest potential which is typically around 0.8 V vs RHE.

The modified surface was then visualized using STM and we found that under the submonolayer regime the surface was initially only modified at steps edges and remained more or less smooth on the terraces at the atomic scale. On scanning the potential from 0.74 V to 0.54 V vs RHE in a cathodic direction, the surface changed from steps to terraces quickly, and within a short time the whole surface became modified as evident from the consecutive STM images shown in fig. 3.3.

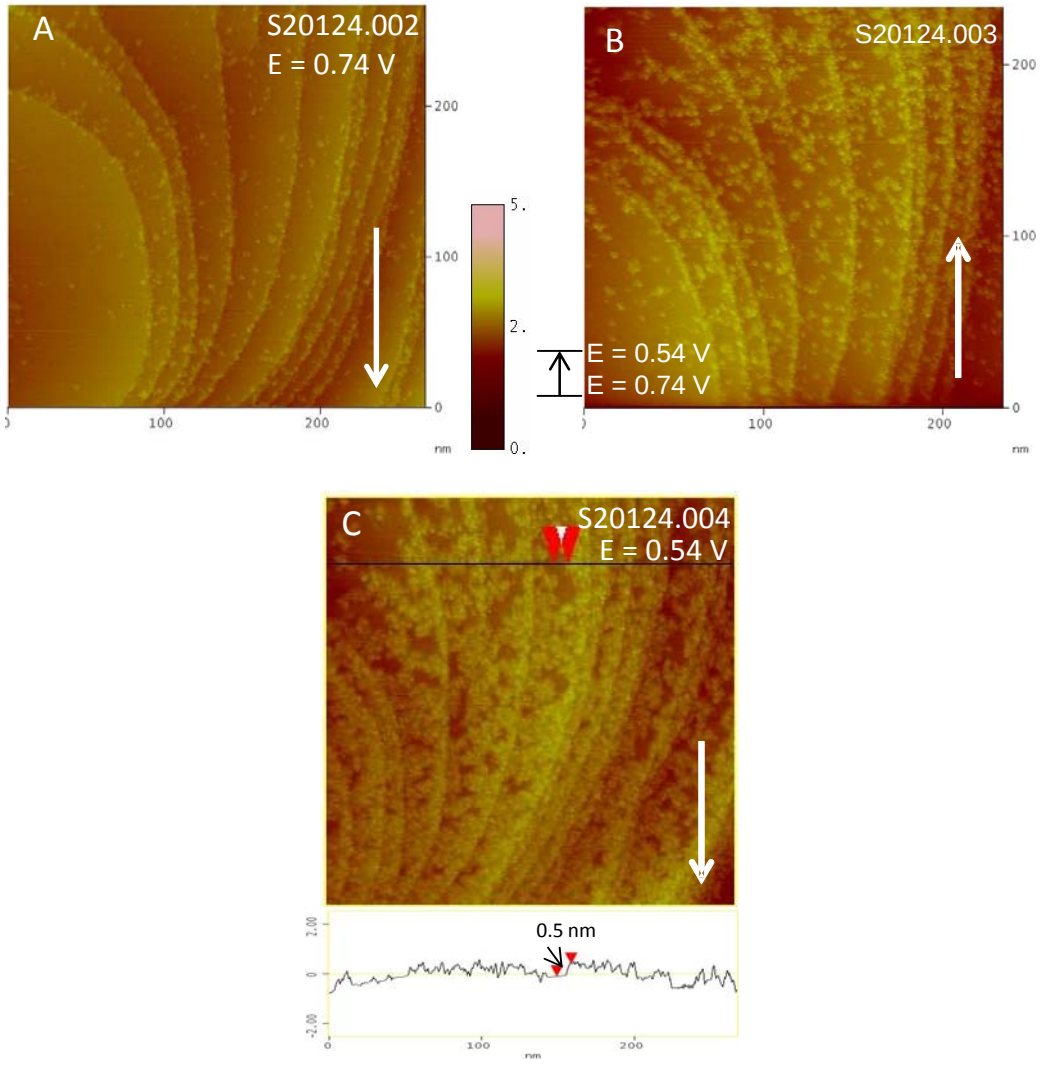

Figure 3.3: STM images for gradual Se deposition on Rh(111) in 1 mM H_2SeO_3
(A) Initial Rh(111) modification with Se at step edges at 0.74 V (B-C) the electrode potential is switched from 0.74 to 0.54 V and then stopped at 0.54 V as indicated on the side of the image with cross section of the image C, leading to gradual modification of the whole surface, sample bias of 50 mV, set point = 1 nA & scan rate of 5 Hz. Arrows indicate scan direction

In another set of experiment, Se modification of the Rh(111) surface was performed in situ by sweeping the potential from 0.9 V to 0.7 V vs RHE in 1 mM H_2SeO_3 (fig. 3.4) and then holding the potential at a more positive potential. In order to avoid further surface modification when sweeping the potential to more negative values a thorough rinsing with 0.1 M $HClO_4$ was performed. A decrease of the potential from 0.74 V to 0.54 V vs RHE leads to no noticeable decoration/modification of the Rh(111) surface (fig. 3.5, first STM image A at 0.54).

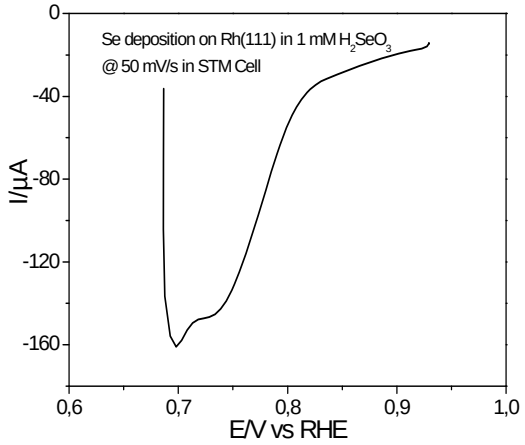

Figure 3.4: In situ CV for Se modification of Rh(111) in 1 mM H_2SeO_3 having $\vartheta_{Se} = 0.18$ sweep rate 50 mV/s.

A gradual decrease in potential to 0.41V results in surface modification such as the one observed in the presence of selenious acid (fig. 3.3) first at the steps edges. Though this modification is slow and proceeds at much lower potential than in the presence of selenious acid, (this might be due to the presence of some minor amount of selenious acid solution remaining in the STM cell while exchanging the Se containing electrolyte with 0.1 M $HClO_4$ or due to an adsorbed adlayer of selenite during selenium deposition) further extending the potentials to more negative values around 0.3 V resulted in modification at the steps extending to the terrace until finally the whole surface was modified/decorated.

We then tried to elucidate whether these structural changes are due to the further increasing Se coverage when decreasing the potential or to a potential induced structural transformation without further deposition of Se. The submonolayer deposits of Se on Rh(111) were obtained in the H-cell from 10^{-4} M H_2SeO_3 and then the Se modified surface was transferred to the STM cell containing 0.1 M $HClO_4$. The CVs for the preparation together with the modification of the Rh(111) is shown in fig. 3.6 a) along with the STM images. The charge corresponding to Se deposition is calculated for the overall Rh(111) surface. This leads to a surface coverage value of $\vartheta = 0.1$.

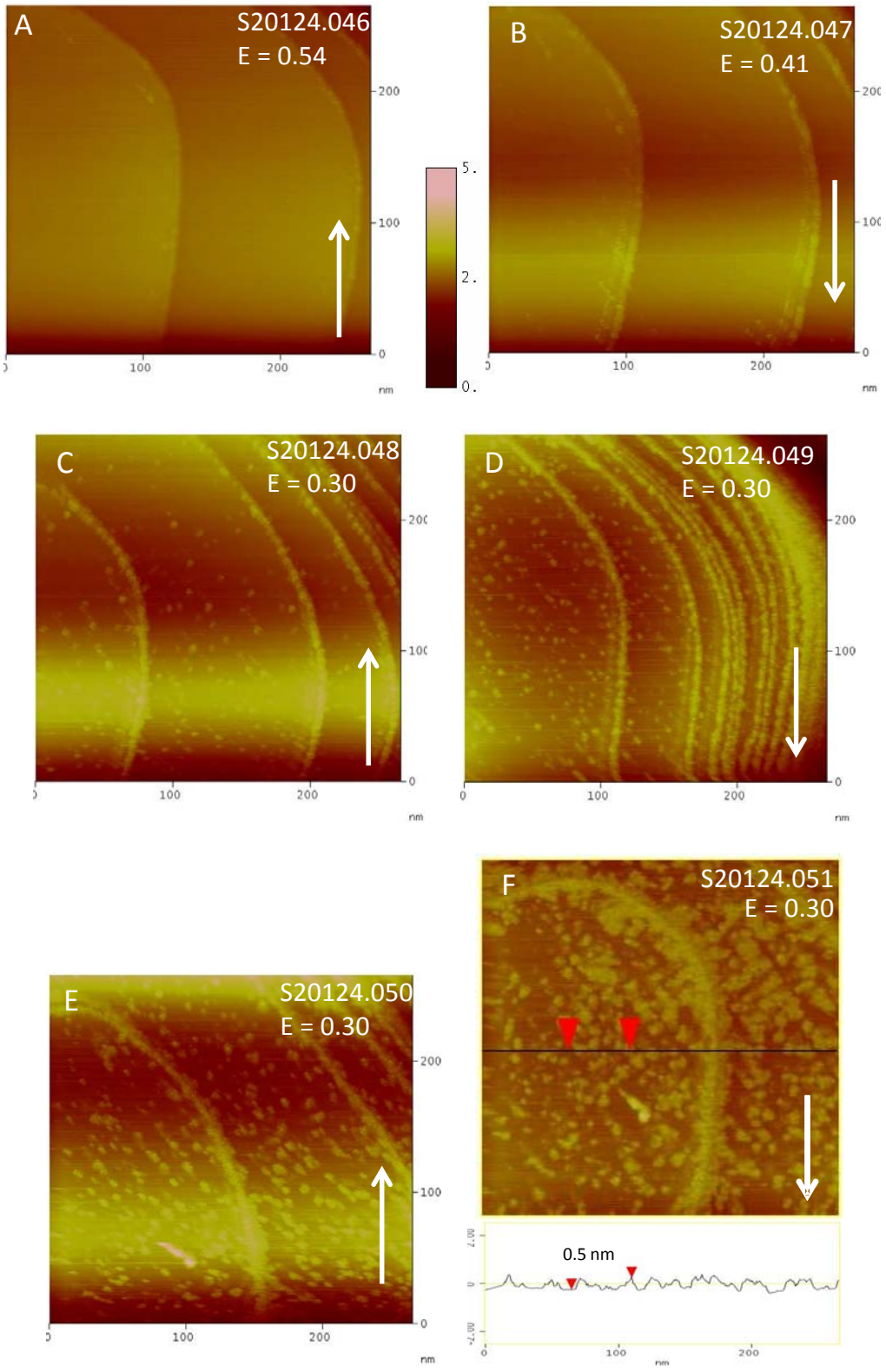

Figure 3.5: STM images for gradual Se deposition on Rh(111) in 0.1 M $HClO_4$
(A) Se modified Rh(111) smooth surface (B) the electrode potential is switched from 0.54 to 0. 41 V leading to modification initially only at step edges (C-F) on extending the potential to 0.3 V the gradual modifications of the surface proceed at lower rate and at lower potential than observed in Se containing solution. The height of the modified surface is indicated by the cross section on image F. Sample bias of 50 mV, set point = 1 nA & scan rate of 5 Hz. Arrows indicate scan direction.

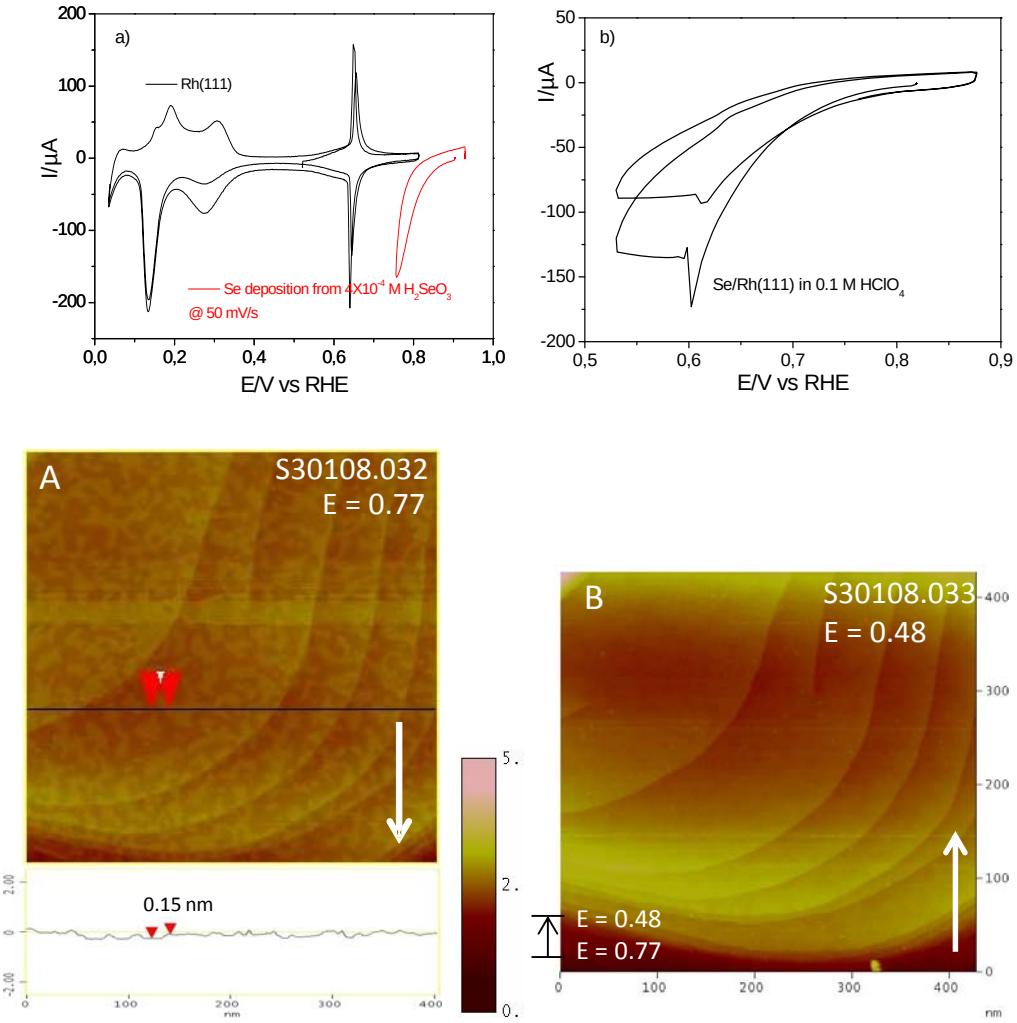

Figure 3.6: STM images for Se modified Rh(111) in 0.1 M $HClO_4$ (ϑ = 0.10). (A): Deposited Se appeared as islands with a height of 0.15 nm as indicated by cross section and it covered ~ 50 %.of the Rh(111) surface (B) The electrode potential switched from 0.77 to 0. 48 V caused coalesce of isolated Se islands. Sample bias of 50 mV, set point = 0.8 nA & scan rate of 4 Hz. Arrows indicate scan direction. a) CVs for pure Rh(111) together with Se modification (——) in H-cell and b)Se modified Rh(111) (——) in the STM cell, sweep rate 50 mV/s.

The STM image shows a partial coverage of Rh(111) with Se appearing in the form of patches of atomically smooth islands, which have a height 0.15 nm. These patches of islands start to merge at a negative potential ~ 0.5 V and given rise to a smooth surface. During this potential sweep the spike caused by reduction of the OH_{ads} on the clean Rh(111) surface is still visible. (Possibly due to Selenate /Selenite conversion) Although the surface appears atomically smooth, it was not possible to obtain the atomic resolution of these adlayers. Merged islands reappeared at positive potentials (0.65 V) while scanning anodically (around OH_{ads}) and merged again once the potential (0.6 V)

was scanned in cathodic direction (around OH_{des}) as shown in CV in the STM (fig. 3.6b and fig. 3.7a). Possibly Se atoms are mobile at potentials negative of the spike at 0.6 V, whereas at more positive potentials the Se atoms are forced into rich domains by the coadsorbing OH species.

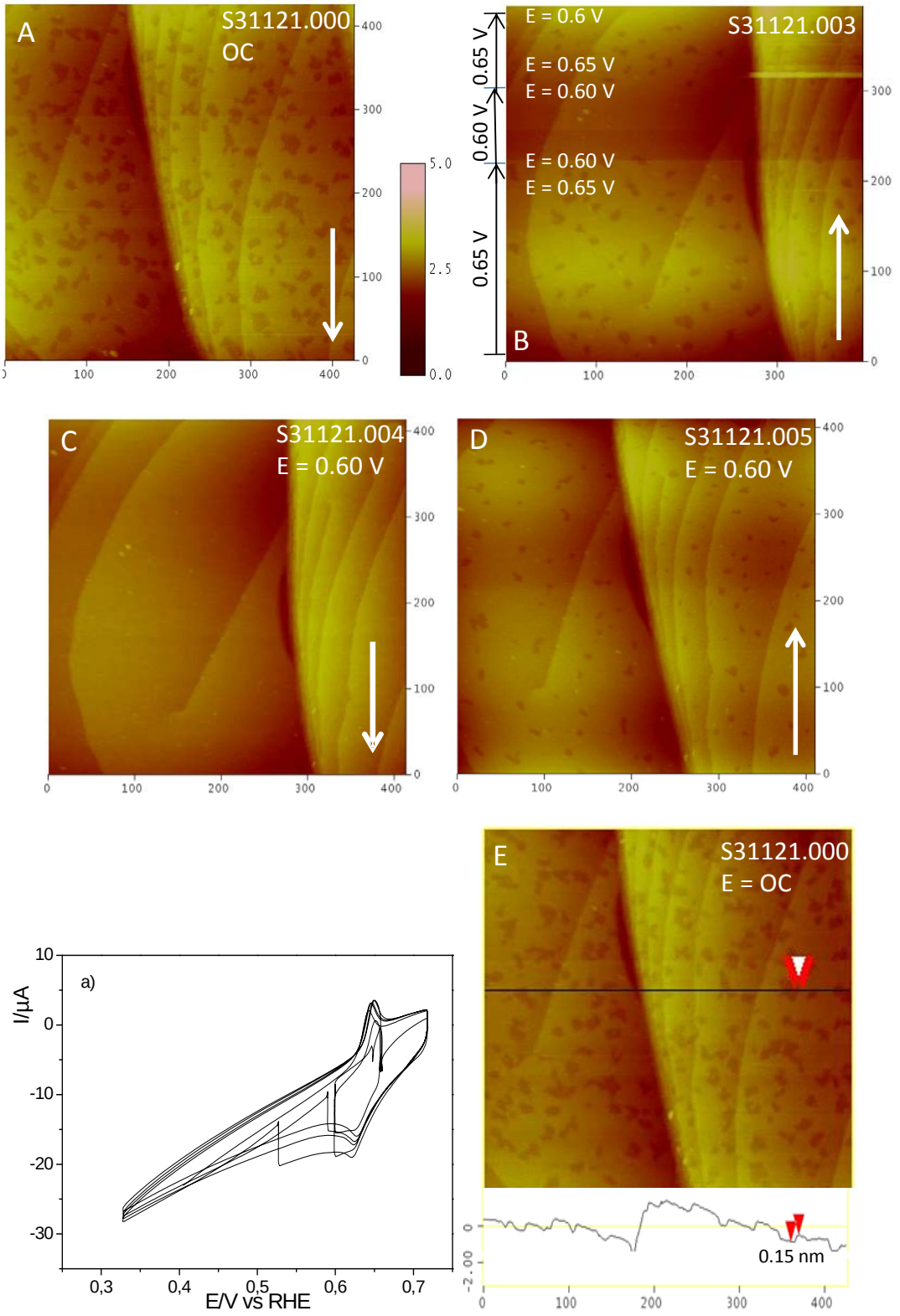

Figure 3.7: STM images for Se modified Rh(111) in 0.1 M $HClO_4$ (ϑ =0.16). (A) Deposited Se covered most of the Rh(111) surface with a height of 0.15 nm (B-D) the

electrode potential switched from 0.65V to 0.60 V caused Se dispersion on whole surface and Rh(111) patches appeared again at 0.65 V. (E) Se modified Rh(111) STM image at open circuit with cross section showing the height of Se deposits. Sample bias of 40 mV, set point = 0.7 nA & scan rate of 4 Hz. Arrows indicate scan direction. a) CV for Se modified Rh(111) (——) in the STM cell, sweep rate 50 mV/s is also shown.

A similar effect had been observed for the coadsorption of Sn and Cu and Sn and CO on Pt(111) electrode [30]. However, the Se adlayer protects the surface not only from contamination but also prevents surface oxidation. The surface morphologies of selenium modified surfaces and their corresponding CV in the H-cell and STM cell are shown in fig. 3.8a.

A tentative interpretation of the disappearance of the islands (fig. 3.6 and 3.7) upon sweeping the potential in negative direction is as follow:
At potentials positive of the spike 0.65 V vs. RHE in the supporting electrolyte - the sharpness of the spike indicates a phase transformation - Se and OH are co-adsorbed, the height difference of only 0.15 nm is due to the different apparent heights of the adsorbates. At potentials before the spike, OH is desorbed (or rather less strongly bound), and the Se adsorbate atoms are free to move, diffuse and spread over the whole surface.

In another experiment a selenium coverage of, $\vartheta \approx 0.2$ of (as calculated from the deposition charge by integrating the charge between potentials (0.9 to 0.68 V)) was deposited in the H-cell and STM images were again taken in Se free solution (0.1 M $HClO_4$). The STM images revealed that with this Se coverage a major part of the surface is completely covered with only a minor percentage of holes which disappear on scanning the potential in cathodic direction. However, at more negative potentials of ~0.4 V vs RHE the appearance of the surface modifications starts at the steps and continue to spreading across the whole surface. This is in agreement with the previous results performed in selenium containing solution. This roughening of the surface on Rh(111) was observed only at this coverage of Se, which in our case was around ϑ = 0.2 of the whole surface. This transition seemed to be irreversible and was of atomic level, resulted in roughening of the surface as shown by series of STM topographic images with variation in potential in fig. 3.8.

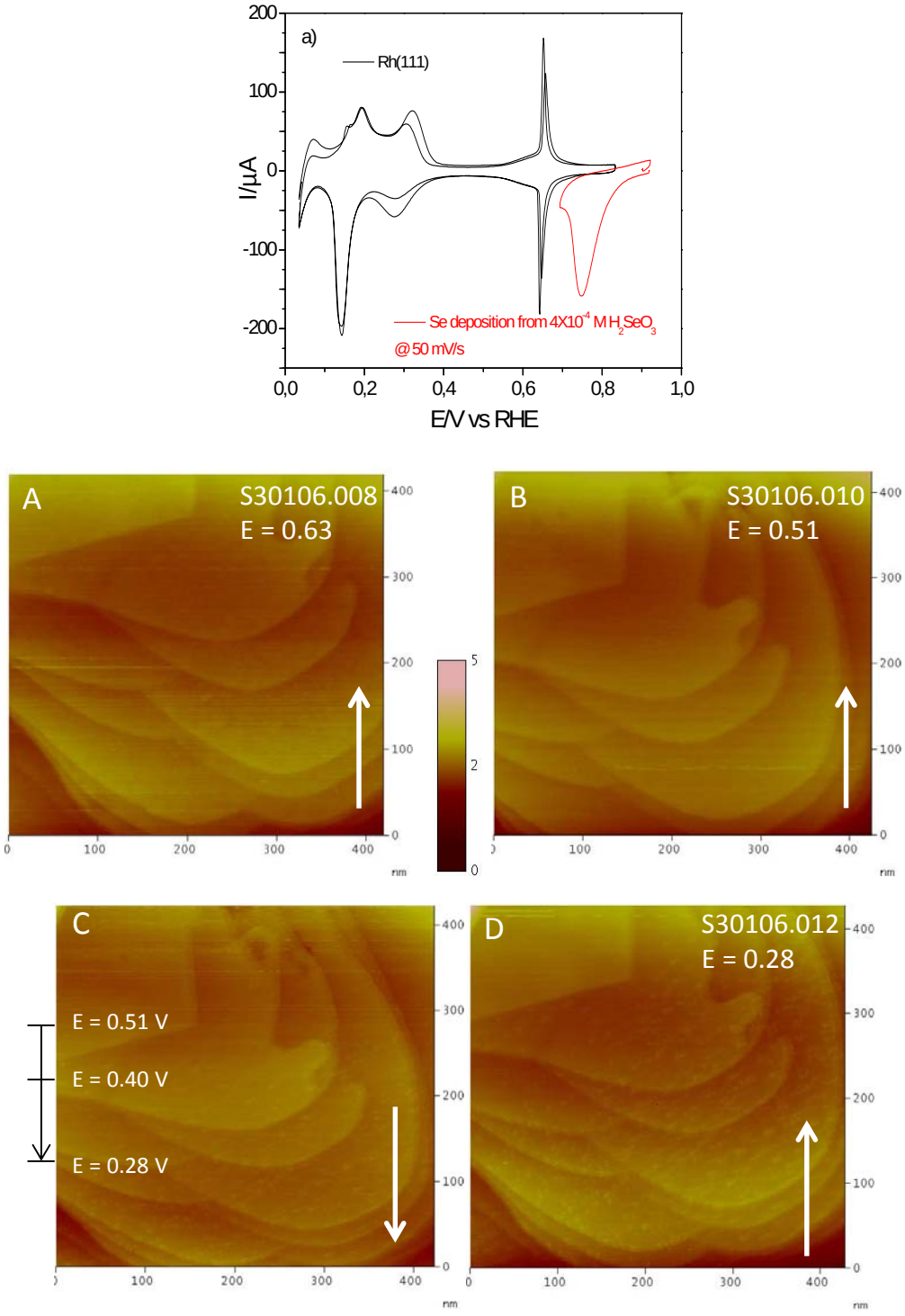

Figure 3.8: STM images for Se modified Rh(111) in 0.1 M $HClO_4$ (ϑ =0.2). (A) Deposited Se completely covered the Rh(111) surface (B) on switching to potential from 0.63 V to 0.51 V resulted in atomically smooth surface (C-D) once potential switched from 0.51 to 0.28 then stopped as indicated on the side of image leads to gradual modification start around 0.4 V and continue at lower potentials. Sample bias of 50 mV, set point = 0.8 nA & scan rate of 5 Hz. Arrows indicate scan direction. a) CVs for pure Rh(111) together with Se modification (——) in H-cell and Se modified Rh(111) (——) in the STM cell, sweep rate 50 mV/s.

3.3.3 In situ AFM of Se on Rh(111): Potential dependence modification

The AFM morphological studies were performed on Se modified Rh(111) with a similar surface coverage of ϑ =0.2 like that in case of STM. The AFM images confirmed the previously obtained STM images of similar coverage of Se modified Rh(111) surface. Step wise modification and roughening transition are shown in fig. 3.9.

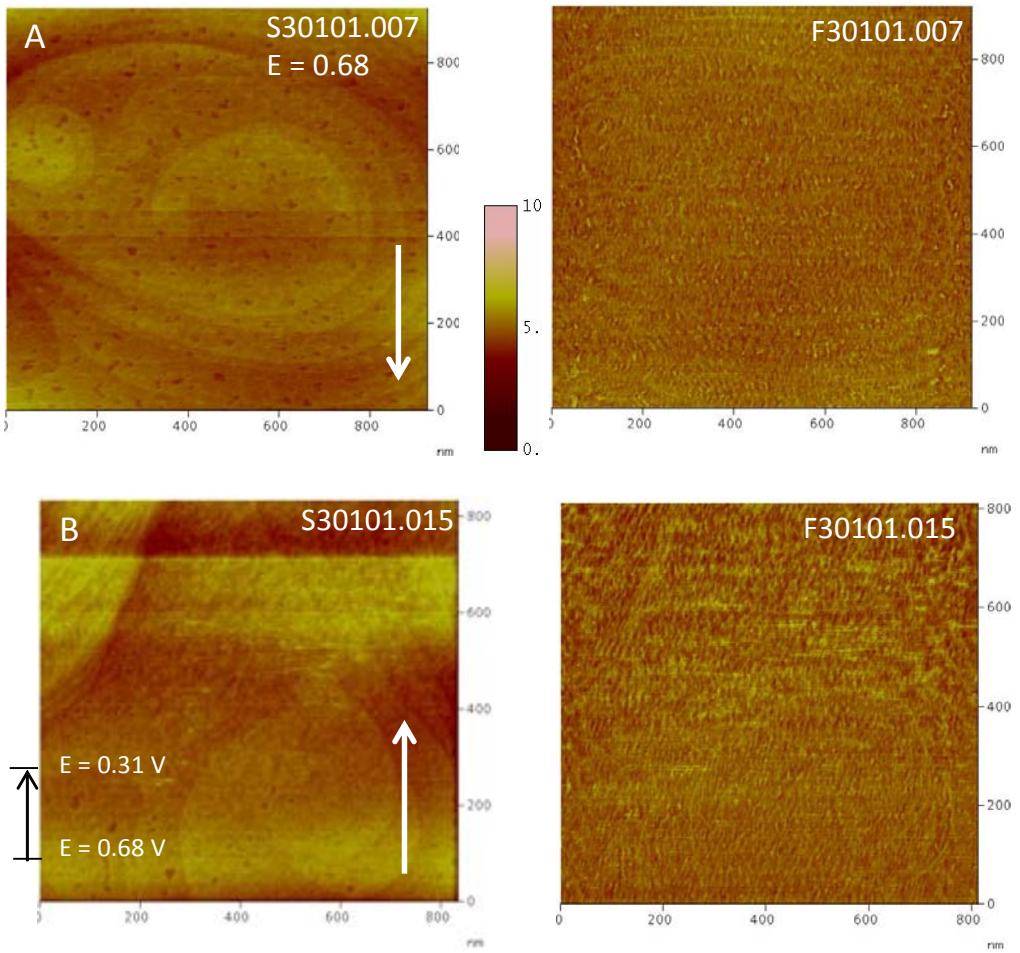

Figure 3.9: AFM topographic and friction images for Se modified Rh(111) in 0.1 M $HClO_4$ (ϑ = 0.20). A) Deposited Se completely covered the Rh(111) surface, holes indicate Se free surface (B) sweeping the potential from 0.68 V to 0.31 V leads to gradual modification starting around 0.4 V which continues at lower potentials. Set point = 0.4 V and scan rate of 3 Hz. Arrows indicates scan direction.

3.4 Adlayer structure on Rh(111)

As explained earlier, less specifically adsorbed anions, namely sulfate/bisulfate, formed an ordered adlayer (√3X√7) structure on fcc(111) surfaces. Wan et al. were the first to observe the sulfate/bisulfate commensurate superstructure of the (√3X√7) lattice on Rh(111) [4].

For this reason, the system performance of the STM unit was checked by obtaining the

sulfate/bisulfate commensurate adlayer (√3X√7) lattice structure on Rh(111). This also serves for calibrating the STM scanner Fig. 3.11 shows atomically resolved consecutive STM images of sulfate/bisulfate adlayers on Rh(111) along with the corresponding CV of Rh(111) in 0.1 M H_2SO_4 in the STM cell under potential control condition as shown in fig. 3.10. Surprisingly, we observed the sulfate/bisulfate superstructure with coadsorbed hydronium ions at much lower tunnelling currents and at a lower scan speed than Wan et al. for a similar system as shown in fig. 3.11. (they obtained similar results at tunnelling current of 20 nA and at 80 Hz scan rate, whereas we observed at 1 nA and at 15 Hz) [4] For the purpose of calibration, the experimentally obtained vectors for the sulfate/bisulfate adlayers were related to the theoretical ones using a calibration matrix (M) as per below equation. (further details are explained in Appendix A).

$\vec{A} = M \cdot \vec{a}$, where $\vec{A}$ is the theoretically determined matrix vector and $\vec{a}$ is the experimentally determined matrix vector for the sulfate adlayer respectively.

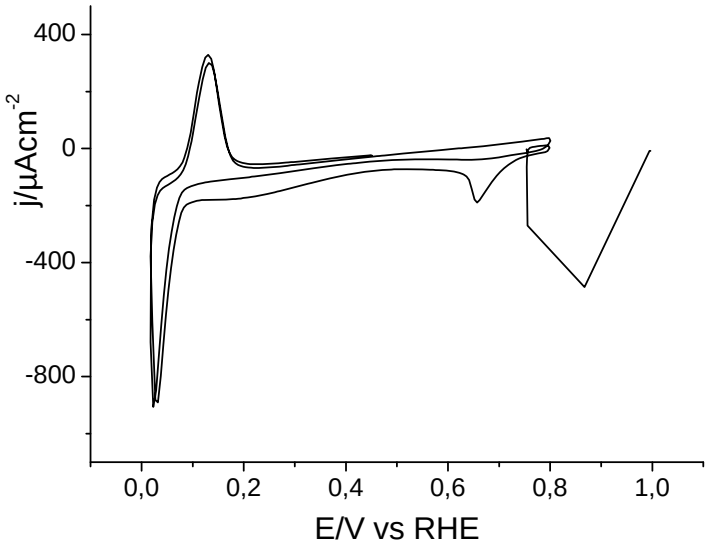

Figure 3.10: In situ CVs of Rh(111) of Rh(111) in 0.1 M H_2SO_4 sweep rate of 50 mV/s.
.

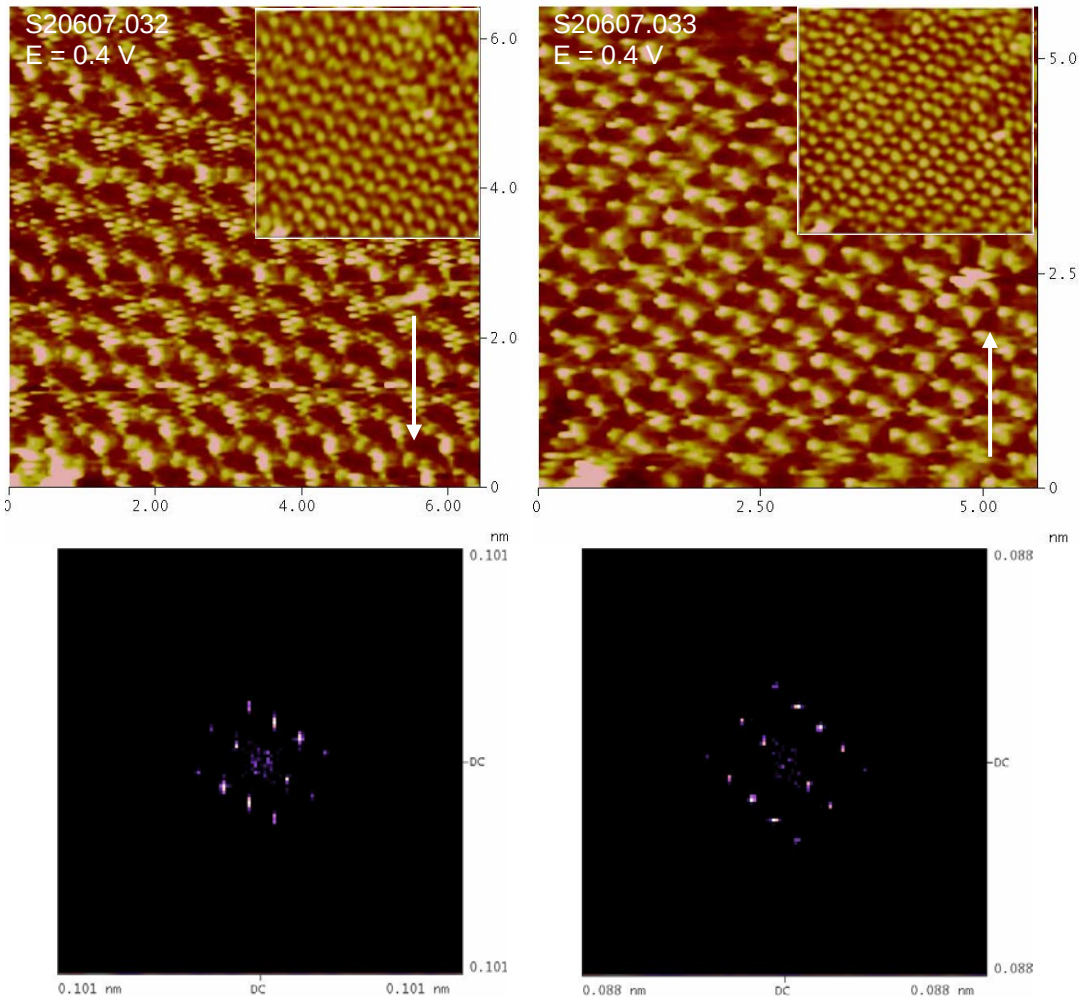

Figure 3.11: STM consecutive images of the ordered sulfate adlayer on Rh(111) in 0.1 M H_2SO_4 at 0.4 V vs RHE. Sample bias of 50 mV, set point = 1.1 nA & scan rate of 15 Hz. The insets show the filtered STM images also the Fourier transform are given.

After obtaining the SO_4^{2-} adlayer structure, the solution in the STM cell was replaced with 1 mM H_2SeO_3 +0.1 M $HClO_4$ solution. The selenite ions exchange with adsorbed sulfate at rest potential (no atomic structure, only smooth surface). The atomically resolved images for the Se adlayer structure on Rh(111) were obtained at a potential of 0.6 V vs RHE. At this potential, an approximate value for ϑ = 0.23~0.25 (based on previous experiments). The original images along with filtered images with their Fourier transforms are presented in fig. 3.12. Both the sulfate adlayers and Se adlayers were obtained during the same set of experiments to ensure the same lateral orientation of the substrate.

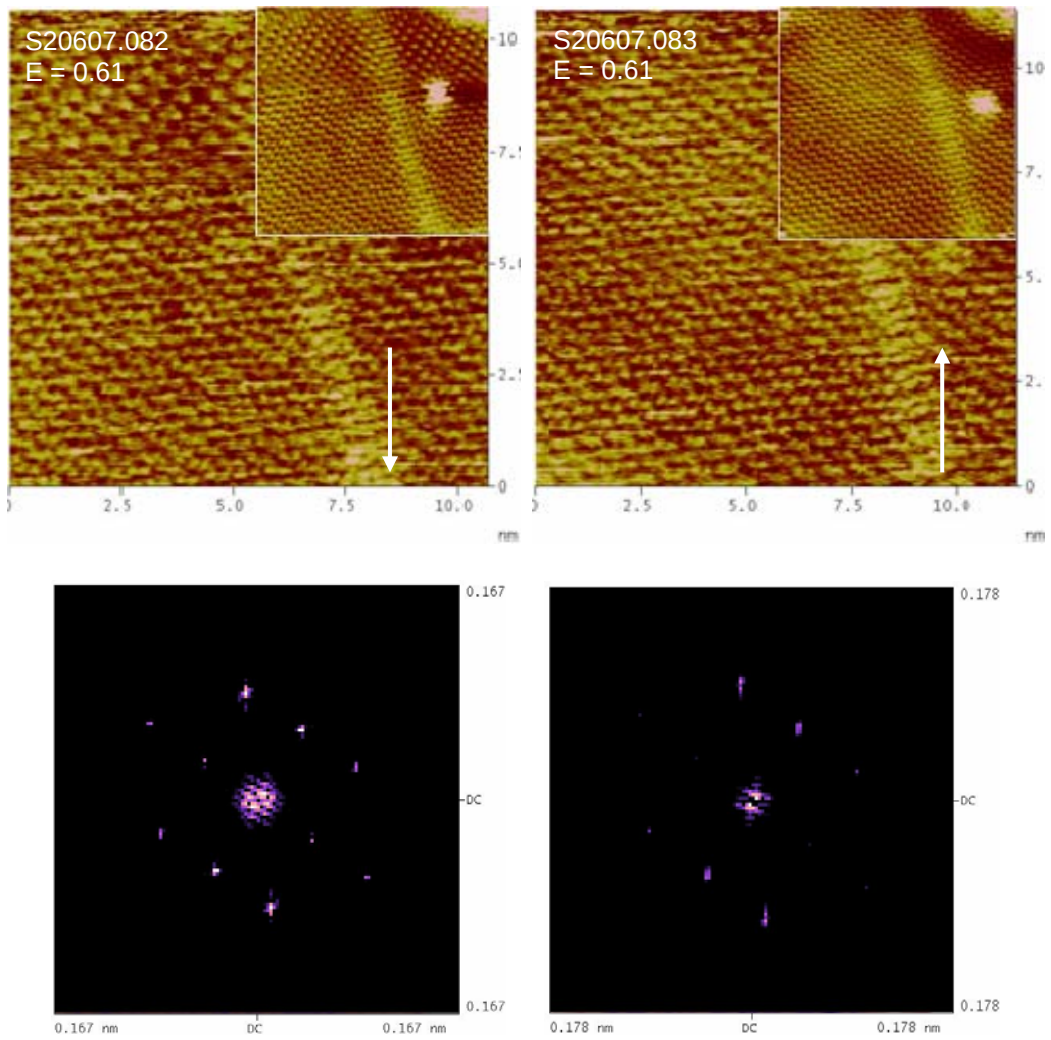

Figure 3.12: STM consecutive images of the ordered Se adlayer on Rh(111) in 1 mM H_2SeO_3 + 0.1 M $HClO_4$ at 0.61 V vs RHE. Sample bias of 50 mV, set point = 1.4 nA & scan rate of 15 Hz. The insets show the filtered STM images also the Fourier transform are given.

In another set of experiment, Se was electrochemically deposited in situ up to a coverage of about $\vartheta = 0.2$ (The potential was then held at a slightly more positive value in order to avoid surface roughening as shown in fig. 3.13.) The Se adatoms not only prevent contamination of the surface but also inhibit oxidation of the surface. The atomically resolved STM images of the Se adlayer structure are shown in fig. 3.14.

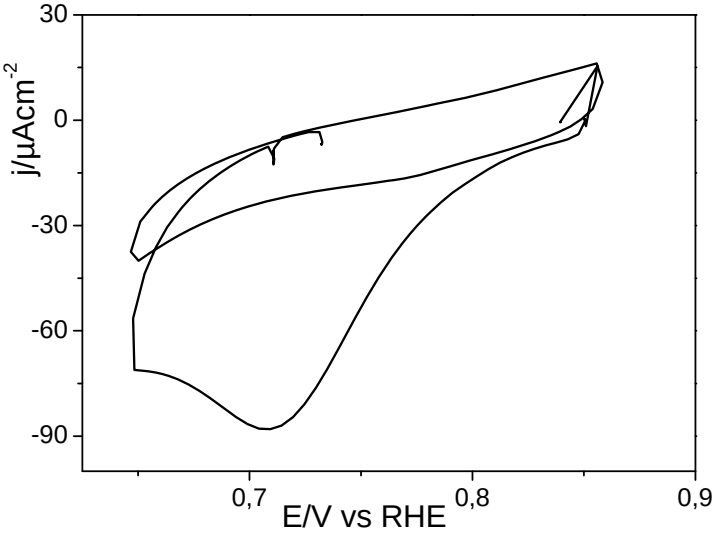

Figure 3.13: In situ CV of Rh(111) in 10^{-4} M H_2SeO_3 solution in STM cell at sweep rate of 50 mV/s.

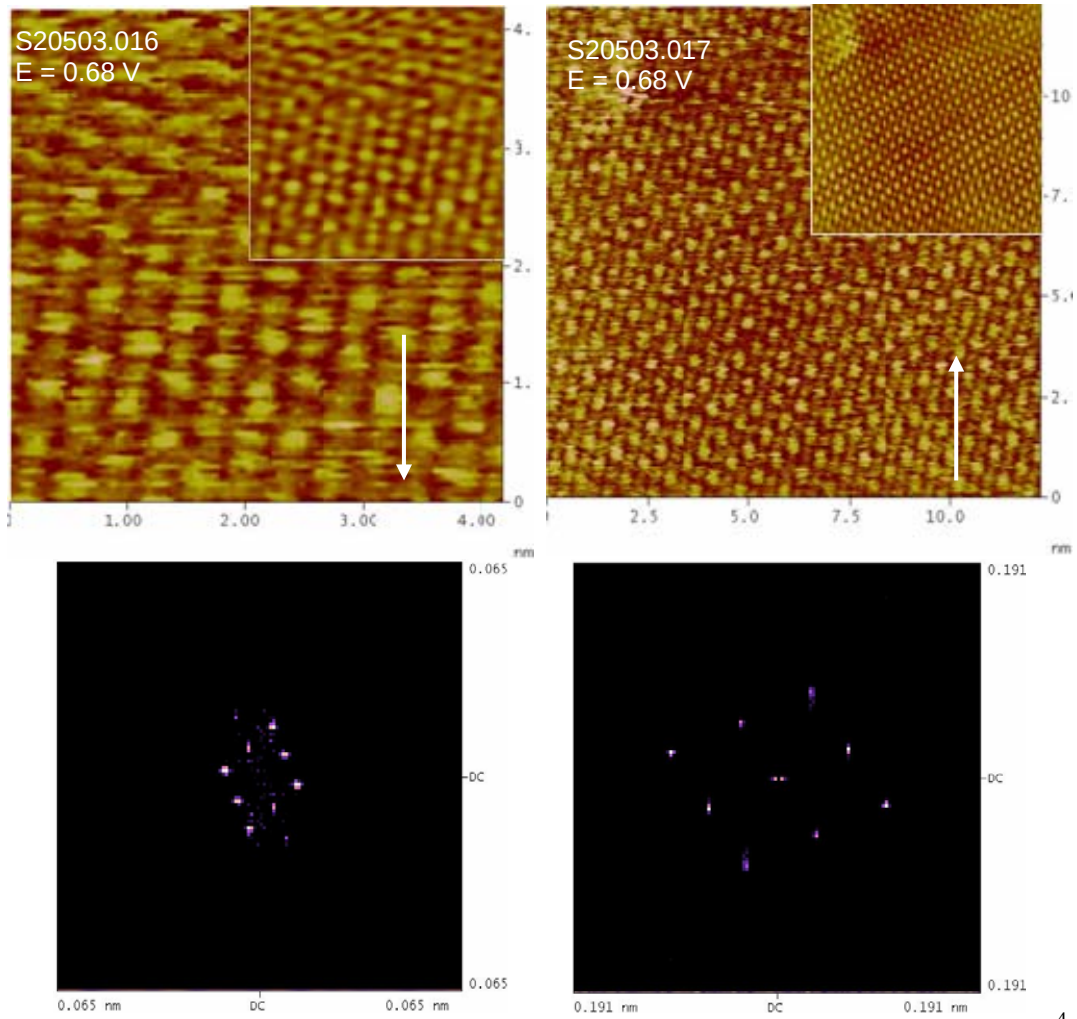

Figure 3.14: STM consecutive images of the ordered Se adlayer on Rh(111) in 10^{-4} M H_2SeO_3 + 0.1 M $HClO_4$ at 0.68 V vs RHE. Sample bias of 50 mV, set point = 0.45 nA & scan rate of 15 Hz. The insets show the filtered STM images also the Fourier transform are given.

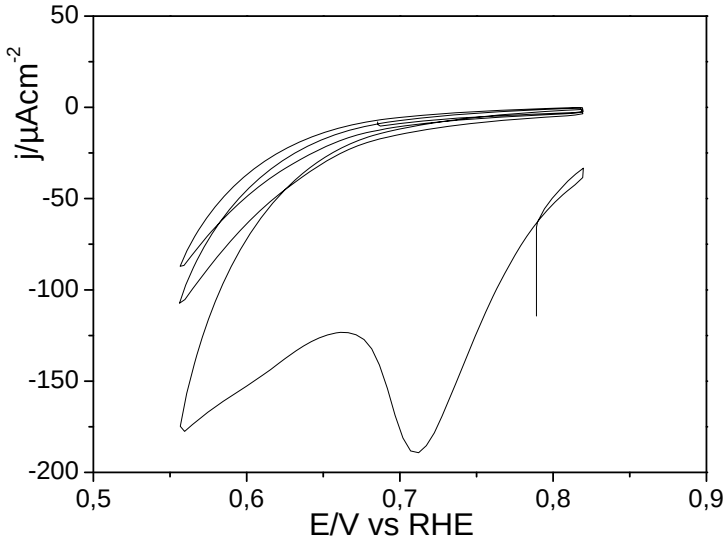

Figure 3.15: In situ CV of Rh(111) in 10^{-4} M H_2SeO_3 solution in the AFM cell at sweep rate of 50 mV/s.

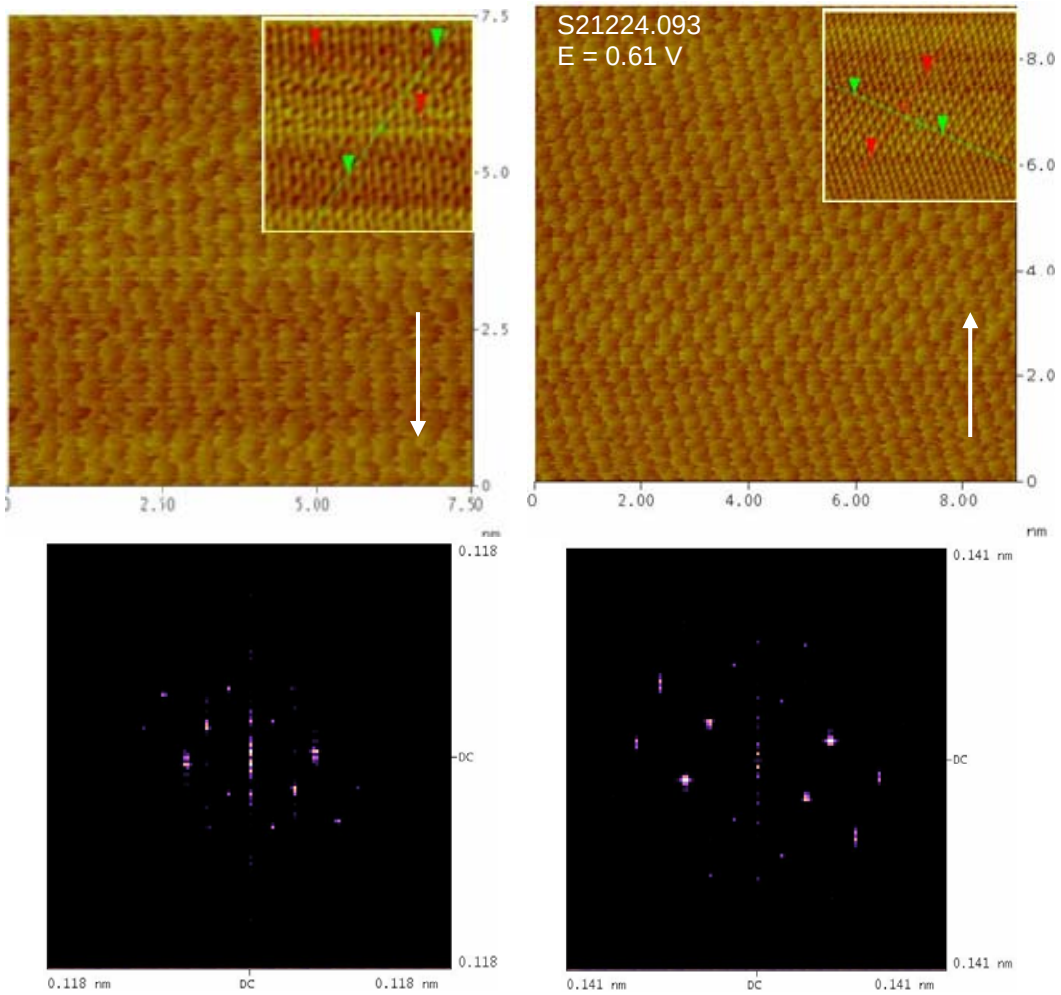

Figure 3.16: AFM consecutive images of the ordered Se adlayer on Rh(111) in 10^{-4} M H_2SeO_3 + 0.1 M $HClO_4$ at 0.61 V vs RHE. Set point = 0.4 V & scan rate of 5 Hz. The insets show the filtered AFM images also the Fourier transform are given.

The AFM measurements were also performed on selenium modified Rh(111) in a AFM cell using 10^{-4} M H_2SeO_3. In order to avoid modification of steps and terraces, the electrolyte was replaced with 0.1 M $HClO_4$ and the potential was held at 0.61 V vs RHE. (The obtained series of AFM images will be presented in chapter 7, here I will only discuss atomically resolved images for the selenium adlayer.) Figure 3.15 shows the *in situ* CV of Se deposition on Rh(111). The atomically stick slip resolved AFM images for Se adlayer on Rh(111) are shown in the fig. 3.16. The distance between the two adjacent atoms was found to be ~ 0.48 nm. A model with Se adlayer structure on Rh(111) is proposed is shown in fig. 3.17b.

Both the sulfate and the Se adlayer lattice vectors were corrected for the thermal drift comparing images of both scan directions (see appendix A). The Se adlayer lattice vectors were then corrected using the calibration matrix obtained from the sulfate adlayer lattices. Additionally, the matrix notation for the adlayer structures for both sulfate and Se on Rh(111) were obtained. The component vectors for the substrate and the sulfate adlayer are related to the adlayer matrix according to

$\vec{A} = S \cdot \vec{Z}$, where $\vec{A}$ is theoretical matrix vector for sulfate adlayer and $\vec{Z}$ is the theoretically determined matrix vector for Rh(111) substrate. A 2x√3 structure was obtained by STM with a surface coverage of ϑ = 0.25. Thus, as described in the appendix A, the matrix for the Se adlayer according to

$\vec{L} = S \cdot \vec{Z}$ is $\begin{pmatrix} 2 & 1 \\ 0 & 1 \end{pmatrix}$.

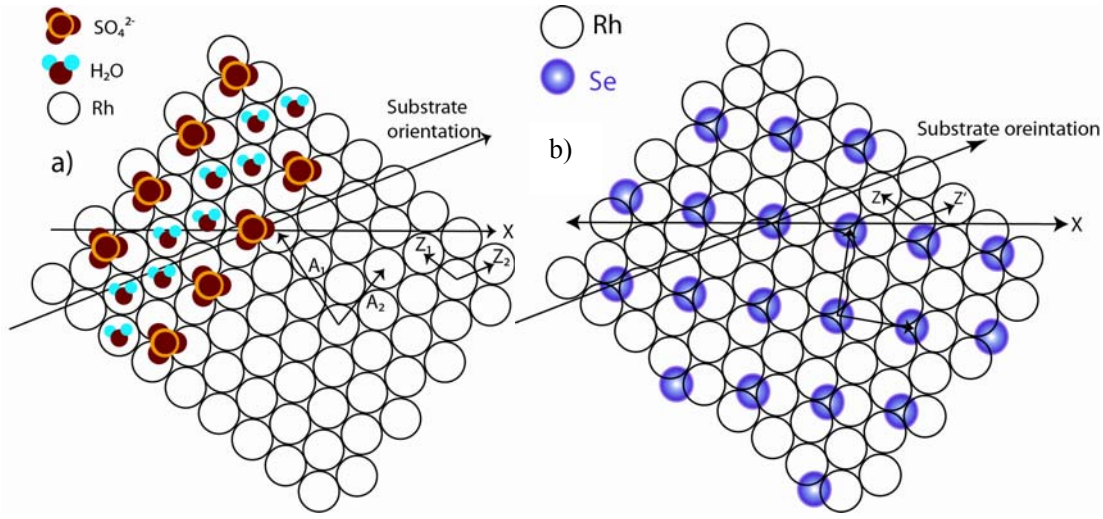

Figure 3.17: Sulfate a) and Se b) adlayer models

3.5 Conclusions:

The chapter focused on atomically smooth deposits of Se on Rh(111) to determine the Se adlayer structure. The Se/Rh(111) system is complex and in situ STM studies showed that with Se surface coverage of around $\vartheta = 0.3$, a roughening starts at the steps. This then extended to terraces; within a short time the whole surface is modified. It was observed that the surface roughening occurs around 0.55 V in SeO_3^{2-} containing solution. Moreover, around $\vartheta = 0.1$ atomically smooth isolated domains of Se are observed which merge together at more negative potentials in Se free solution. A minimum surface coverage of $\vartheta = 0.2$ is required to observe this roughening in SeO_3^{2-} free solution, which, however occurs at more negative potentials than observed in SeO_3^{2-} containing solution.

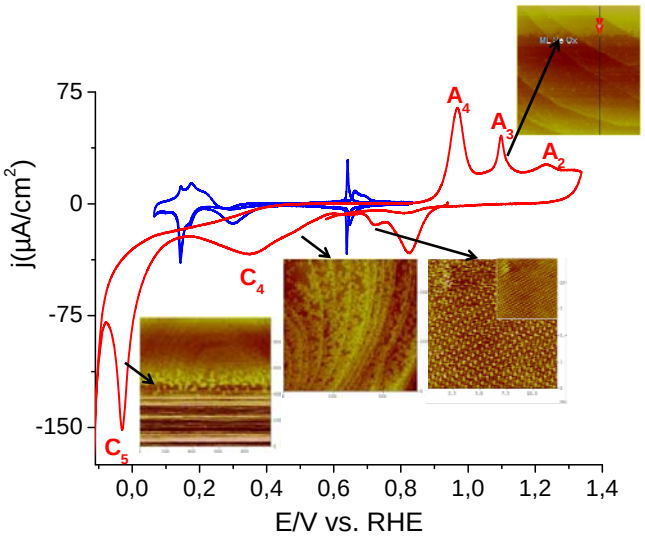

Figure 3.18: Potential dependant Se adsorption desorption and surface morphologies.

The sulfate adalyer structures were imaged to get information about the substrate orientation and it was also used for system calibration. The Se adlayer structure was atomically resolved by both STM and AFM. A $2x\sqrt{3}$ structure was obtained by STM with a surface coverage of $\vartheta = 0.25$, coinciding well with the deposited charge. A similar structure was also observed in friction images (atomic stick slip). These images could only be obtained at coverages close to but just below those at which the roughening of the surface starts. Figure 3.18 shows an overview of the structural changes observed as a function of potential. This roughening is most probably due to the place exchange between Rh and Se atoms similar to well known roughening of Pt surfaces in the oxygen adsorption region. Stickney et al also observed similar roughening transition on Se modified Au(111) [25] and Baltruschat et al observed it on Pt(111) with As [31].

References

[1] J. A. Rodriguez, S. Chaturvedi, and M. Kuhn, Journal of Chemical Physics 108:3064 (1998).
[2] O. M. Magnussen, Chemical Reviews 102:679 (2002).
[3] O. M. Magnussen, J. Hageböck, J. Hotlos, and R. J. Behm, Faraday Discussions 94:329 (1992).
[4] L. J. Wan, S. L. Yau, and K. Itaya, Journal of Physical Chemistry 99:9507 (1995).
[5] L. J. Wan, M. Hara, J. Inukai, and K. Itaya, Journal of Physical Chemistry B 103:6978 (1999).
[6] L.-J. Wan, T. Suzuki, K. Sashikata, J. Okada, J. Inukai, and K. Itaya, Journal of Electroanalytical Chemistry 484:189 (2000).
[7] A. M. Funtikov, U. Linke, U. Stimming, and R. Vogel, Surface Science 324:L343 (1995).
[8] A. M. Funtikov, U. Stimming, and R. Vogel, Journal Of Electroanalytical Chemistry 428:147 (1997).
[9] B. Braunschweig and W. Daum, Langmuir 25:11112 (2009).
[10] F. Dassenoy, W. Vogel, and N. s. Alonso-Vante, The Journal of Physical Chemistry B 106:12152 (2002).
[11] A. Barbieri, D. Jentz, N. Materer, G. Held, J. Dunphy, D. F. Ogletree, P. Sautet, M. Salmeron, M. A. Vanhove, and G. A. Somorjai, Surface Science 312:10 (1994).
[12] D. F. Ogletree, R. Q. Hwang, D. M. Zeglinski, A. L. Vazquezdeparga, G. A. Somorjai, and M. Salmeron, Journal of Vacuum Science & Technology B 9:886 (1991).
[13] D. G. Kelly, A. J. Gellman, M. Salmeron, G. A. Somorjai, V. Maurice, M. Huber, and J. Oudar, Surface Science 204:1 (1988).
[14] J. S. Foord and A. E. Reynolds, Surface Science 164:640 (1985).
[15] K. C. Wong, W. Liu, and K. A. R. Mitchell, Surface Science 360:137 (1996).
[16] K. C. Wong, W. Liu, M. Saidy, and K. A. R. Mitchell, Surface Science 345:101 (1996).
[17] H. A. Yoon, M. Salmeron, and G. A. Gomorjai, Surface Science 395:268 (1998).
[18] S. R. Kelemen and T. E. Fischer, Surface Science 87:53 (1979).
[19] D. Jurgens, G. Held, and H. Pfnur, Surface Science 303:77 (1994).
[20] D. Heuer, T. Mueller, H. Pfnuer, and U. Koehler, Surface Science 297:L61 (1993).
[21] T. Mueller, D. Heuer, H. Pfnuer, and U. Koehler, Surface Science 347:80 (1996).
[22] J. Hrbek, S. Y. Li, J. A. Rodriguez, D. G. vanCampen, H. H. Huang, and G. Q. Xu, Chemical Physics Letters 267:65 (1997).
[23] L. Y. O. Yang, S. L. Yau, and K. Itaya, Langmuir 20:4596 (2004).
[24] M. Alanyalioglu, U. Demir, and C. Shannon, Journal of Electroanalytical Chemistry 561:21 (2004).
[25] T. E. Lister and J. L. Stickney, Journal of Physical Chemistry 100:19568 (1996).
[26] J. Clavilier, M. Wasberg, M. Petit, and L. H. Klein, Journal of Electroanalytical Chemistry 374:123 (1994).
[27] J. E. Sader, J. W. M. Chon, and P. Mulvaney, Review of Scientific Instruments 70:3967 (1999).
[28] C. K. Rhee, M. Wasberg, P. Zelenay, and A. Wieckowski, Catalysis Letters 10:149 (1991).
[29] T. E. Lister, B. M. Huang, R. D. Herrick, and J. L. Stickney, Journal of Vacuum Science & Technology B 13:1268 (1995).

[30] X. Xiao, S. Tillmann, and H. Baltruschat, Physical Chemistry Chemical Physics 4:4044 (2002).
[31] X. Y. Xiao and H. Baltruschat, Langmuir 19:7436 (2003).

Chapter 4: Quantitative determination of H_2Se at model metal *fcc*(111) selenide surface

This chapter explores the stability of the adsorbed selenium on model metal *fcc* surfaces such as Rh(111), Pt(111) and Au(111). It focuses on the electrochemical dissolution of the selenide from selenium modified model surfaces through differential electrochemical mass spectrometry under controlled flow through conditions.

4.1 Introduction:

Chalcogenide modified noble transition metal surfaces are potential candidates for cathode materials in fuel cell applications [1]. It is observed that these metal chalcogenides such as the selenides of ruthenium and rhodium possess high methanol tolerance, making them better suited for cathode material in DMFCs and mixed reactant fuel cell applications [2]. Alonso-Vante et al. are the pioneers in reporting the electrocatalytic activity of metal chalcogenides for oxygen reduction reactions [3]. However, the much lower ORR activity as compared to Pt and the stability issues of metal chalcogenides under fuel cell operating conditions make a further optimization necessary [4].

Historically, metal selenides were studied because of their application in optoelectronic devices. Alonso-Vante and co-workers [3] synthesized a series of non chevrel phase compounds of the type Mo-Ru-Se and demonstrated that these compounds showed better ORR activity than those of non-noble metal electrodes. This opened the door for researchers to investigate a new class of alternate materials for ORR [5]. However, difficulties associated with their synthesis such as harsh condition (high temperature, pressure etc.,) resulted in relatively high cost of manufacturing close to that of noble metals. Consequently, it hindered their wide spread utilization.

Later on, Alonso-Vante and co-workers synthesized a variety of binary systems of ruthenium chalcogenides, Ru_xX_y (X = S, Se, and Te) simply by reacting metal carbonyls with elemental chalcogens in xylene solvent [6]. These materials were found to be fairly active for oxygen reduction reaction and even selective in presence of high concentration of small organic molecules.

The structural aspects of Ru_xSe_y clusters were revealed by using extended X-ray

absorption fine structure (EXFAS). Based on these calculations, it was anticipated that the Se atoms would be mostly coordinated to outer sites on the ruthenium cluster. An hcp cluster model for the $Ru_{99}Se_{54}$ particle was proposed by Alonso-Vante and co-workers [7] based on following consideration:

a) Se atoms were arranged in a random fashion on Ru particles.

b) Se atoms were arranged in a random fashion on Ru particle; both models were presented in fig. 4.1.

This proposed model clearly depicted the availability of enough free Ru sites for an efficient electrocatalysis.

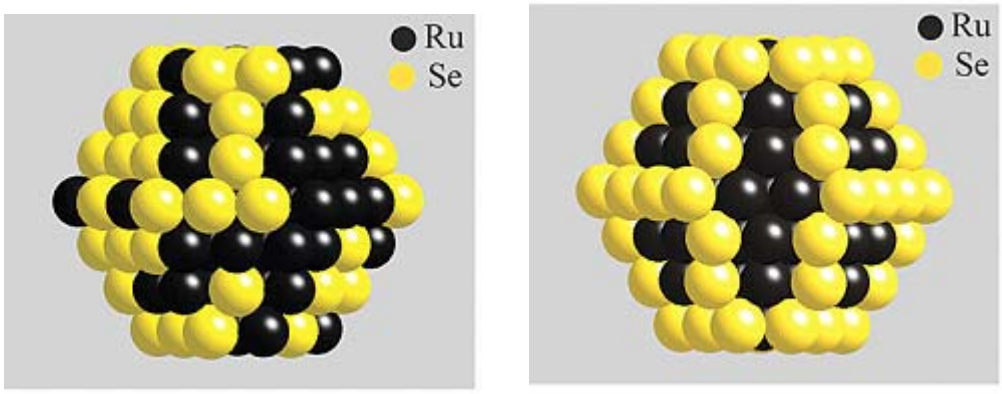

Figure 4.1: Cluster model structures for $Ru_{99}Se_{54}$ show the selenium bonding onto the ruthenium clusters a) With a statistical distribution; (b) with an ordered positioning [7].

The transition metal chalcogenides showed better catalytic activity for molecular oxygen reduction as compared to non transition metal chalcogenides. The reactive nature of the selenium, especially in metal chalcogenides was explained based on the assumption that the adsorbing selenium made a shell around the metal core (which is a source of electron reservoir) and protected its oxidation. Generally, all metals are prone to oxidation by air and form metal surface oxides. However, in this case the metal core remained intact and its electron reservoir acted as a source which promoted catalysis of the ORR [8]. This assumption was confirmed by the stability and structural studies of the reduced states of the Ru_x and Ru_xSe_y clusters. These studies showed that the Ru_x particles were prone to oxidation by air, whereas Ru_xSe_y particles were chemically stabilized against air oxidation. Moreover, high temperature studies (up to 300°C) showed that the selenium stabilized the Ru_x as the Ru_xSe_y nanostructures and hence facilitated the electrocatalysis by the electronic effect.

The stability issues of these metal chalcogenides posed concerns for the commercial viability of these materials as fuel cell cathodes. It was found that the oxidative dissolution of selenium occurs in parallel to a ORR at low over-potentials. Moreover, in case of Ru_xSe_y nanoparticles, formation of the RuO_2 around 0.9 V vs RHE in acidic solution also reduced the ORR activity [2, 9].

Though selenium protects the ruthenium surface from oxidation, for a better ORR activity a compromise between the inhibition of metal surface oxidation and its blocking must be ensured. The electrochemical nuclear magnetic resonance (EC-NMR) and XPS studies of Ru_xSe_y nanoparticles proved that the Se, which is a semi conducting material, attained metallic characteristics while interacting with the substrate Ru atoms. This change was expected due to the transfer of electron from Ru to the Se [10].

The electrochemistry of Se(IV) at solid electrodes is complex and was mainly studied using the EQCM in addition to CV. The electrochemical reduction of Se(IV) in aqueous solution proceed either by four electrons (eq. 4.1) or by six electron (eq. 4.2) process,[11]

$$H_2SeO_3 + 4H^+ + 4e^- \rightarrow Se(0) + 3H_2O \qquad 4.1$$

$$H_2SeO_3 + 6H^+ + 6e^- \rightarrow H_2Se + 3H_2O \qquad 4.2$$

On Au and Pt, electrochemical deposition of Se starts with the deposition of a submonolayer, followed by bulk deposition on the top of the adsorbed Se as per eq. 4.1.

$$Se(0) + 2H^+ + 2e^- \rightarrow H_2Se \qquad 4.3$$

It was also considered that at more negative potentials both the direct 6 electron reduction (eq. 4.2) and the indirect four electron reduction (eq. 4.1) for bulk Se deposits followed by reductive dissolution of adsorbed Se via two electrons(eq. 4.3) to generate H_2Se compete with each other [12]. In addition, metallic red Se(0) nanoparticles were also generated by a coupled chemical reaction of the electrochemically generated selenide with selenious acid within the solution (eq. 4.4) [13].

$$H_2SeO_3 + 2H_2Se \rightarrow 3Se + 3H_2O \qquad 4.4$$

Moreover, alloy formation of Se with Au was suggested [14]. Surface morphologies in selenious acid solution [15-17] were elucidated by AFM. Stickney and coworkers studied the atomic structure of the Se adlayers on all low index planes of Au by STM.

However, up till now, no detailed studies were performed to quantify the products of the reductive dissolution of selenium adsorbed on polycrystalline or single crystalline model electrode surfaces in a quantitative manner.

The current work deals with the detailed investigation of the processes which occur during Se deposition/dissolution. The main emphasis is on the formation and the quantitative detection of the selenide species and oxidative stripping of selenium from various fcc(111) surfaces with the aid of DEMS. The surface morphological features of these surfaces were evaluated using SPM as a function of potential. In addition, formation of metallic selenium by the coupled chemical reaction of generated H_2Se with selenious acid was also confirmed.

4.2 Experimental:

4.2.1 Preparation and modification of massive single crystal electrodes with Se

The usual annealing process followed by cooling down in argon atmosphere was successfully used for the preparation of Pt(111) and Au(111) and was also used for Rh(111) electrode using a mixture of Ar:H_2 (2:1) gas as described elsewhere [18-21]. Rh(111), Pt(111) and Au(111) single crystal electrodes with a diameter of 10 mm were used,(Kristallhandel Kelpin, Germany, Goodfellow UK and Mateck Germany respectively). All solutions were prepared from 18.2 MΩ Milli-Q water and de-aerated with high purity argon gas (99.999%).

Electrochemical experiments in 0.1 M $HClO_4$ and 0.1 M H_2SO_4 (spectro pure grade) were carried out in a conventional three electrode H-cell in a hanging-meniscus configuration with a large Pt sheet as counter electrode. A reversible hydrogen electrode was employed as a reference electrode. Selenium submonolayer and multilayer deposits were produced in a similar H-cell containing 1 mM H_2SeO_3 (Analytical grade). A bi-potentiostat from Pine Instruments Inc. model AFBPC1 in combination with a user interface developed in Labview software was used for recording cyclic voltammograms (CV).

All of the experiments for the quantitative determination of selenide were performed in the dual thin layer flow through cell (DTLFC). This DTLFC was connected to the

Balzers quadrupole mass spectrometer (QMG-422) for differential electrochemical mass spectrometry (DEMS). A controlled flow of the electrolyte is maintained using a peristaltic pump (Spetec Germany) Detailed information about this complete setup is discussed elsewhere [22].

All STM and AFM measurements were performed with a Nanoscope III E controller (Digital Instruments, Santa Barbara, CA) and a commercially available STM and AFM scanner (Molecular Imaging) fitted with an electrochemical cell. All STM measurements were done at room temperature using Pt/Ir (90:10) wire having diameter of 0.25 cm, which was etched in a KSCN + KOH bath and coated with molten polymer glue to reduce the area in contact with the electrolyte. A Pt wire was used as the counter electrode and another one as quasi-reversible reference electrode. All potentials were converted to the reversible hydrogen electrode (RHE) using E (Pt)= 0.9 V vs RHE. It was immersed in the same solution separated from the STM cell by a capillary. All AFM experiments were performed with soft cantilevers: n^+-doped Si cantilever by Nanosensors (PPP-CONT-10), k_n = 0.09 N/m. The torsional force constant was determined via Sader's method [23] and found to be 50 Nm^{-1}. This method is based on the measurement of the resonant frequency and quality factor of the cantilever.

Relative coverages are given as a ratio of adsorbate species (the absolute coverage Γ), to the number of surface atoms (N_{Surf}), designated as $\vartheta = \Gamma / N_{Surf}$. For Rh(111), Pt(111) and Au(111), where $N_{Surf} = 2.2\ \mathrm{nmolcm^{-2}}$.

4.2.2 DEMS calibration

The relation between the faradaic current I_F and the ion current I^i_{MS} of the fragment *i* in the mass spectrometer is given by

$$I^i_{MS} = K^{*i}_{MS} \cdot I_F / z \text{ or, } Q^i_{MS} = K^{*i}_{MS} \cdot Q_F / z \qquad 4.5$$

where z is the number of electrons involved.

Calibration of the DEMS setup for H_2Se is difficult. Therefore, for the determination of the calibration constant (K^*), oxygen was used assuming that its ionization probability is similar to that of Se. Then $K^{*tot}_{H_2Se} = K^{*tot}_{O_2}$, where K^{*tot} refers to the sum of the ion currents or charges of all fragments: $\sum I_{MS} = K^{*tot} \cdot I_F / z$ or $\sum Q_{MS} = K^{*tot} \cdot Q_F / z$. 4.6

For calibration, oxygen was evolved at a Pt electrode, and a value of $K^*_{O_2} = 4.4 \cdot 10^{-6}$ was obtained.

The relative intensity of atomic oxygen (m/z = 16) during O_2 ionization from NIST MS data is 20 % of that of m/z= 32. Therefore

$$K^{tot}_{O_2} = K^*_{O_2} \cdot 1.2 \text{ (based on oxygen evolution, Charge)} \qquad 4.7$$

For H_2Se, HSe is the most abundant fragment.

$$K^*_{HSe} = z\frac{Q_{MS_{HSe}}}{Q_{F_{HSe}}} \qquad 4.8$$

During selenide ionization HSe, H_2Se and Se are detected in the following relative intensities (100, 25 and 20% respectively),

Hence, $Q^{tot} = Q_{HSe} + Q_{H_2Se} + Q_{Se}$ which is $Q^{tot} = Q_{HSe} \cdot (1 + 0.25 + 0.2)$ 4.9

Therefore, $K^{tot}_{HSee} = K^*_{HSe} \cdot 1.45$ and then $K^*_{HSee} = K^*_{O_2} \cdot (1.2/1.45)$ 4.10

In order to calculate the number of moles of generated selenides from obtained charges the following formula was used (which is identical to the change of coverage)

$$\Delta\Gamma = n = \frac{Q_{MS_{HSe}}}{K^*_{O_2} \cdot (1.2/1.45) \cdot z \cdot F}, \text{ where F is the Faraday constant} \qquad 4.11$$

4.3 Results and Discussion:

4.3.1 Selenide determination on selenium modified fcc(111) surfaces

The electrochemical deposition of the Se on freshly prepared Rh(111) surface was performed in a conventional H-cell containing 1 mM H_2SeO_3 in a potential sweep from the rest potential (0.94 V) to 0.2 V. The corresponding deposition peaks are shown in fig. 4.2 together with the CV of Rh(111) in the supporting electrolyte. Up to 0.7 V a charge of 0.55 mC/cm² (after background subtraction of the double layer contribution) is deposited, corresponding to a coverage of $\vartheta = 0.55$ assuming a four-electron reduction (eq. 4.1). The deposition charge at 0.2 V amounts to 1.76 mC/cm², from which a coverage of $\vartheta = 1.76$ is calculated.

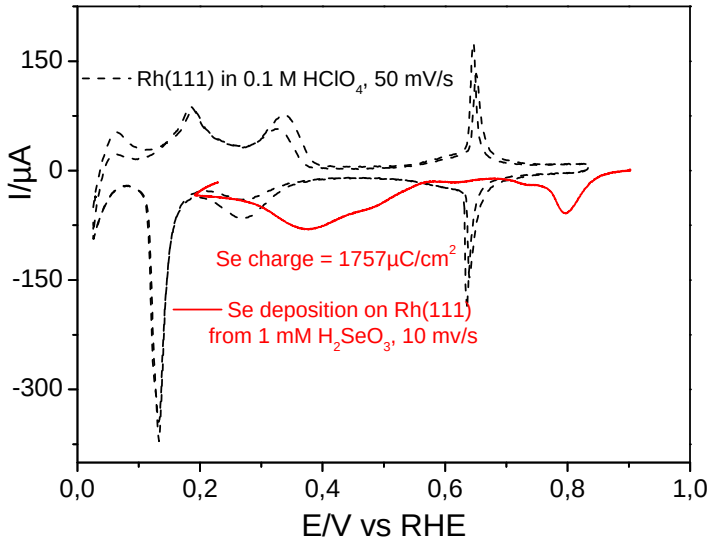

Figure 4.2. CVs of Rh(111) (-----)at a sweep rate of 50 mV/s together with multilayer Se deposit (——) from 1mM H_2SeO_3 sweep rate 10 mVs^{-1}.

After obtaining submonolayer and multilayer deposits of selenium, the modified electrode was transferred to the DEMS setup at open circuit potential. In DEMS the reductive and oxidative stripping of Se from Rh(111) surface was performed in selenium free electrolyte under controlled mass transfer condition. Figure 4.3 shows the cyclic voltammograms for the reductive and oxidative stripping of adsorbed already deposited selenium on Rh(111). and corresponding mass spectrometric cyclic voltammograms (MSCVs) for m/z = 80(HSe), m/z = 79(Se) and m/z = 2 (H_2) at a flow rate of 3.5 µL/s in argon saturated 0.5 M $HClO_4$. The reductive dissolution of adsorbed selenium as H_2Se around -0.1 V vs. RHE was observed during the first cathodic scan while insignificant traces were visible in the second scan. In the next scans no further reductive dissolution was observed. In our experiment, reductively dissolution was performed in Se(IV) ions free solution. Hence, the reductive dissolution of already adsorbed Se(0) caused the formation of H_2Se as per eq. 4.3.

The reductive desorption is paralleled by a desorption peak at -0.1 V in the cyclic voltammogram during the first sweep, close to the onset of hydrogen evolution (charge = 0.5 mC cm^{-2}) corresponding to $\vartheta = 1$. The calculated selenide amount determined using DEMS from Se/Rh(111) was found to be $n(H_2Se) = 2.02\ nmol/cm^2$ (cf. table 4.1) The decreased Se coverage in the subsequent sweeps leads to a shift of H_2 evolution to more positive potentials. The remaining adsorbed selenium was stripped anodically with a broad peak centred around 1.2 V and a charge corresponding to $\vartheta \approx 0.23$, again assuming a four electron oxidation. Of course, no mass signal of H_2Se was detected

during this oxidative stripping. Oxidative stripping resulted in a further positive shift (~0.04 V) of the subsequent hydrogen evolution as is also evident from the increased MS signal for hydrogen.

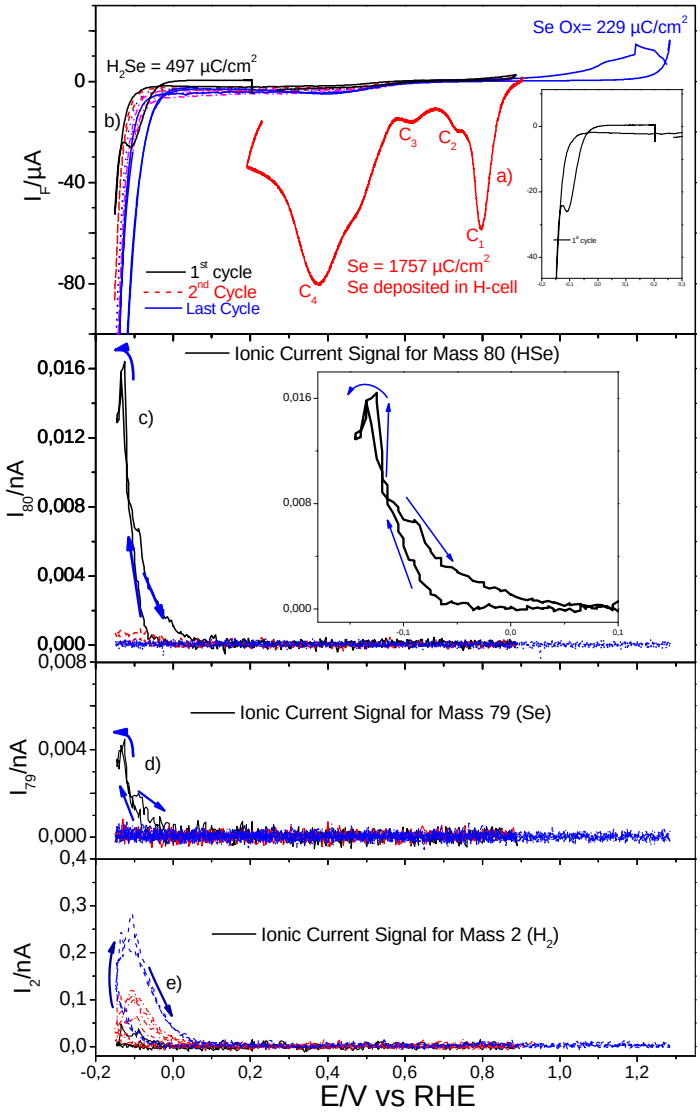

Figure 4.3: Simultaneously recorded CVs (a-b) for Se deposition on Rh(111) in H-cell (curve a) together with reductive and oxidative stripping of Se (curve b) and MSCVs in the DEMS cells for (c) HSe (m/z = 80), (d) Se (m/z=79) and e) H_2 (m/z=2) in 0.5 M $HClO_4$; scan rate 10 mV s^{-1}, flow rate 3.5 µl s^{-1}; inset shows the reductive dissolution of Se.

Figure 4.4 show the cyclic voltammograms for the reductive and oxidative stripping of adsorbed selenium (ϑ = 0.54 ML coverage deposited in the H-cell on pure Rh(111)) and corresponding mass spectrometric cyclic voltammograms (MSCVs) for m/z = 80(HSe) and m/z = 2(H_2) at a flow rate of 3.5 µl/s. The reductive dissolution of adsorbed selenium was not observed, as evident from the mass signal of m/z = 80. The corresponding mass signal for hydrogen evolution was also very small in the first few

scans. This indicated that very few rhodium sites were available for generation of hydrogen at more negative potentials. Note that the H_2 evolution rate remained lower than in the experiment of fig. 4.3. Once oxidative stripping of the selenium was performed, a large amount of hydrogen evolution was observed around 0.0 V with positive shift of potential (~0.15 V) than that of selenium covered surface. This behaviour was different as observed on surfaces with multilayer selenium coverage. The possible explanation would be the intermetallic compound formation in the latter case. Furthermore, for selenium coverages below monolayer, oxidative stripping did not lead to a complete loss of the single crystallinity of Rh(111) as evident form the reproduction of the characteristic hydroxide peak after selenium oxidation (from charge calculation around 50 % recovery of single crystallinity). Also, the oxidative stripping Se charge was calculated by subtracting the charge due to oxidation of the surface in the next scan after stripping of the Se. This feature was not observed on surfaces with multilayer selenium coverage after Se oxidation.

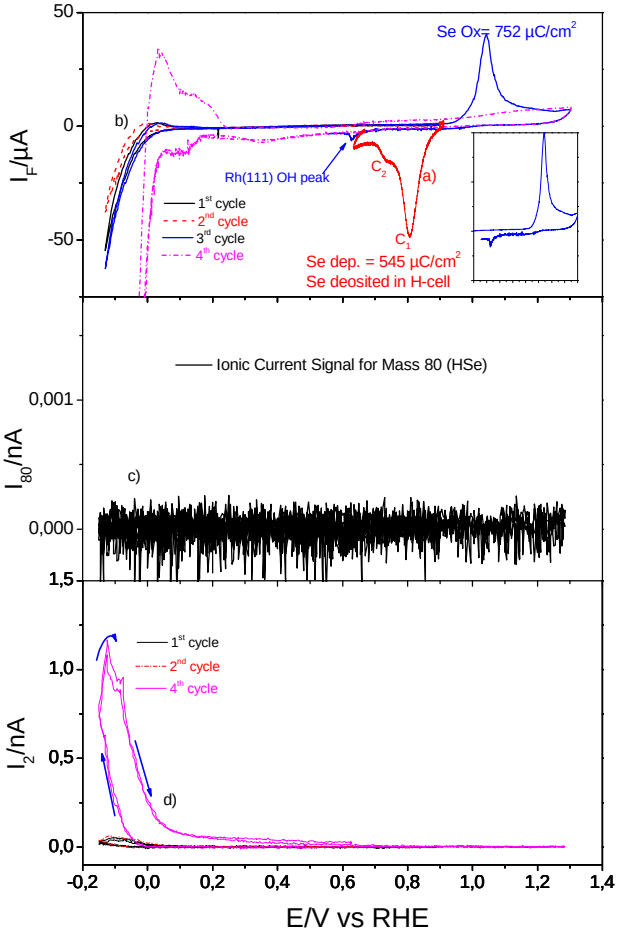

Figure 4.4: Simultaneously recorded CVs (a-b) for Se deposition on Rh(111) in H-cell (curve a) together with reductive and oxidative stripping of Se (curve b) and MSCVs in the DEMS cell for (c) HSe (m/z = 80), (d) H_2 (m/z=2) in 0.5 M $HClO_4$; scan rate 10 mV s^{-1}, flow rate 3.5 µl s^{-1}; inset shows the oxidative dissolution of Se and appearance of OH_{ads} peak.

The same experiments were performed on a selenium covered Pt(111) electrode. Figure 4.5 shows the cyclic voltammograms for the reductive and oxidative stripping of adsorbed selenium (ϑ = 1.54) and the corresponding mass spectrometric cyclic voltammograms (MSCVs) for m/z = 80(HSe) and m/z = 81(H_2Se). The reductive dissolution of adsorbed selenium (2.3 nmol cm^{-2}) around -0.15 V vs. RHE was only observed during the first cathodic scan.

All features are similar to the corresponding experiment on Rh(111). Coverage data obtained for the deposition charge, detected amount of H_2Se and the oxidation charge are summarized in the table 4.1.

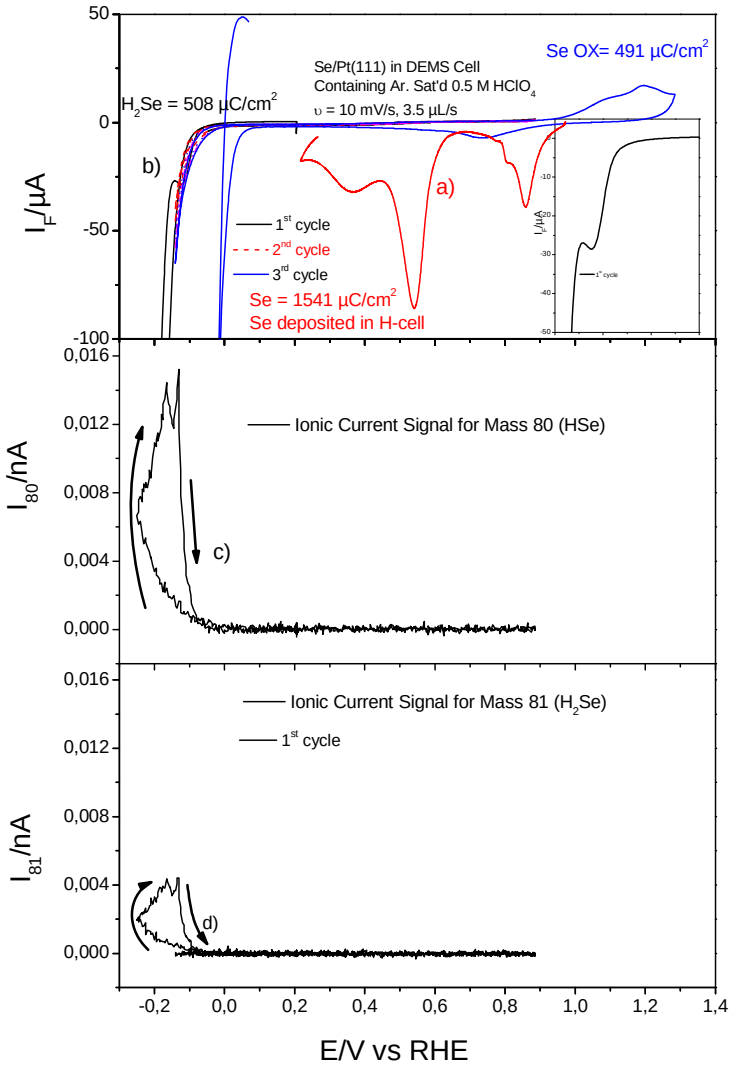

Figure 4.5: Simultaneously recorded CVs (a-b) for Se deposition on Pt(111) in H-cell (curve a) together with reductive and oxidative stripping of Se (curve b) and MSCVs in the DEMS cell for (c) HSe (m/z = 80), (d) H_2Se (m/z=81) in 0.5 M $HClO_4$; scan rate 10 mV s^{-1}, flow rate 3.5 µl s^{-1}; inset shows the reductive dissolution of Se.

Figure 4.6 shows the cyclic voltammograms for the reductive and oxidative stripping of selenium and the corresponding mass spectrometric cyclic voltammograms (MSCVs) for m/z = 80(HSe) and m/z = 2(H_2) for a slightly covered Pt(111) surface.

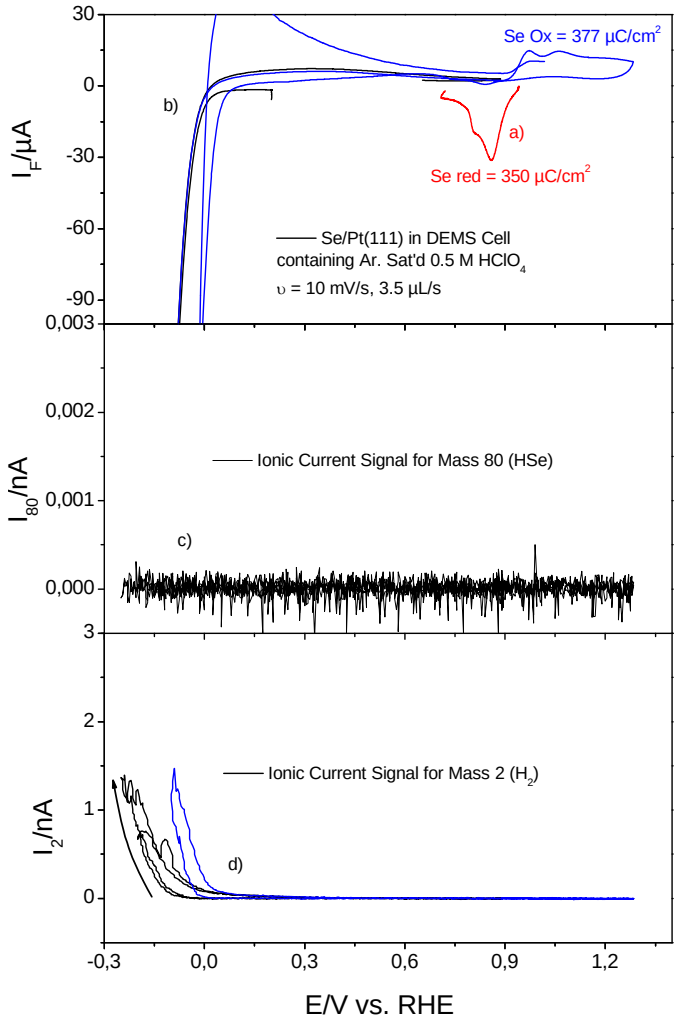

Figure 4.6: Simultaneously recorded CVs (a-b) for Se deposition on Pt(111) in H-cell (curve a) together with reductive and oxidative stripping of Se (curve b) and MSCVs in the DEMS cell for (c) HSe (m/z = 80), (d) H_2 (m/z=2) in 0.5 M $HClO_4$; scan rate 10 mV s^{-1}, flow rate 3.5 µl s^{-1};

Similar experiments were performed for large Se coverages ($\vartheta = 1.65$) on Au(111) (fig. 4.7). Again, the reductive dissolution of adsorbed selenium ($\Delta\vartheta = 1.58$) at around -0.2 V vs. RHE is only observed during the first cathodic scan.

From the DEMS measurement on Au(111) the Se coverage was found to be

$n(H_2Se) = 2.26\ \text{nmol/cm}^2$

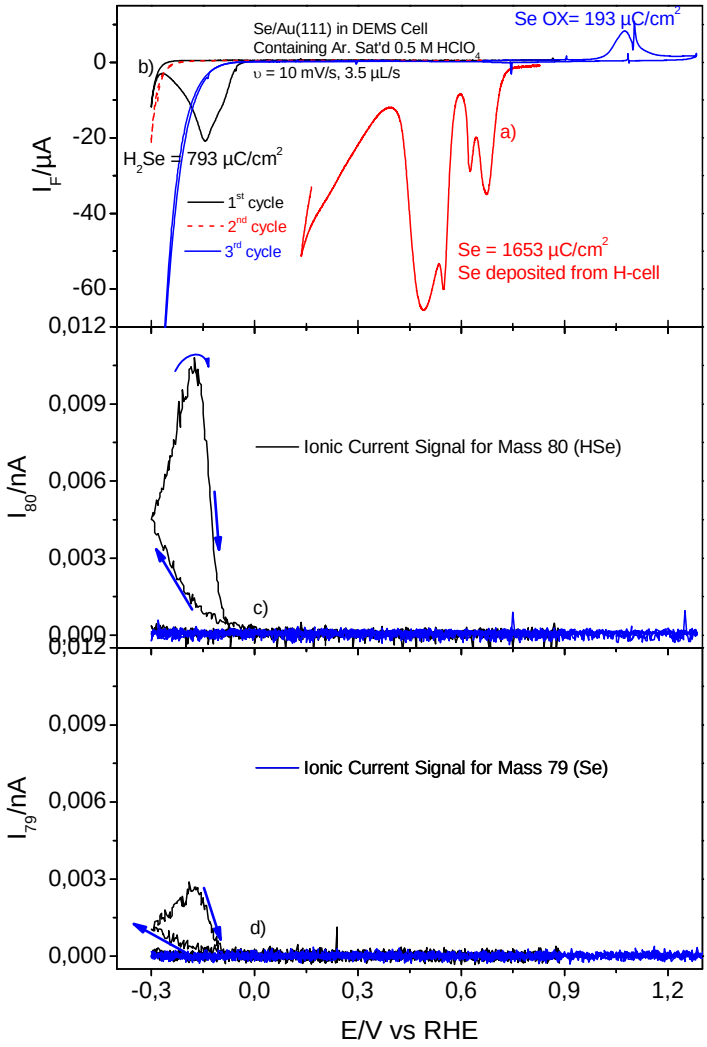

Figure 4.7: Simultaneously recorded CVs (a-b) for Se deposition on Au(111) in H-cell (curve a) together with reductive and oxidative stripping of Se (curve b) and MSCVs in the DEMS cell for (c) HSe (m/z = 80), (d) Se (m/z=81) in 0.5 M $HClO_4$; scan rate 10 mV s^{-1}, flow rate 3.5 µl s^{-1}.

4.4 Surface morphology of the selenium modified fcc(111) surfaces using SPM

The morphological feature of electrochemically modified noble metal surfaces with Se was investigated by using scanning probe microscopy. The main objective was to visualize the surface topography of the Se modified model electrode surface before and after reductive and oxidative dissolution of Se.

4.4.1 Reductive stripping of Se and its morphology by AFM

The pure Rh(111) was covered with around 0.2 ML of selenium in the H-cell to protect the surface from possible contamination. A typical CV for the preparation and its Se modification is shown in fig. 4.8. It was then transferred to the AFM cell containing 1

mM H_2SeO_3 electrolyte at open circuit potential. To avoid further Se deposition potential control was taken at a positive potential around 0.8 V vs. RHE (which is close to the open circuit potential).

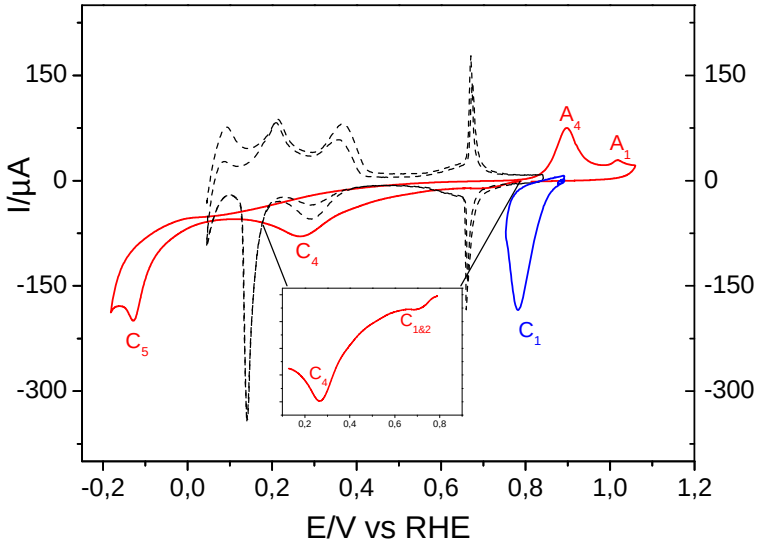

Figure 4.8: CVs of Rh(111) (-----)at a sweep rate of 50 mV/s together with Se deposition (——) in H-cell from 1mM H_2SeO_3 sweep rate 50 mVs^{-1} and in situ CV for Se deposition (——) in AFM cell from 0.1 mM H_2SeO_3 at sweep rate of 10 mV/s. A larger view as inset of in situ Se monolayer and bulk deposits.

Figure 4.9 shows a series of AFM images of Se modified Rh(111) surface in 1 mM H_2SeO_3 at various potentials. A corresponding CV for the Se electrochemistry on Rh(111) electrode in the AFM cell measured in a separate experiment is also presented in fig. 4.8. When the potential was held at +0.8 V vs. RHE, the steps and terraces of the Rh(111) surface remained smooth. Upon lowering the potential deposition in peak C_3 does not lead to a morphological change. However, the electrode surface starts to change at 0.55 V, i.e. the onset of peak C_4. The preceding experiments by DEMS showed that at this potential, multilayer deposition of Se is occurring. Deposition starts at the step edges. However, unlike typical metal deposition, the deposit does not start at the step and then smoothly to the terraces. Instead, as also revealed by the cross section, the structure is higher than a monolayer (0.47 nm instead of 0.2 nm). Then, also deposits on the terraces are formed. (This will be demonstrated in a subsequent paper in more detail using STM.) The resulting surface remains rough.

Further lowering the potential to around 0.0 V (peak C_5), where reductive dissolution of the deposited Se as H_2Se was demonstrated by DEMS, grains appear in the image

(height 2nm, diameter = 20 nm). The stripes in the lower part of this image suggest that these do not adhere well to the surface, but are mobile. The generated H_2Se reacts chemically with selenious acid as was already observed on the polycrystalline and Au(111) surface [12, 24] according to eq. 4.4. Nanoparticles of metallic Se(0) generated on the electrode surface caused the cantilever probe to slip on these particles.

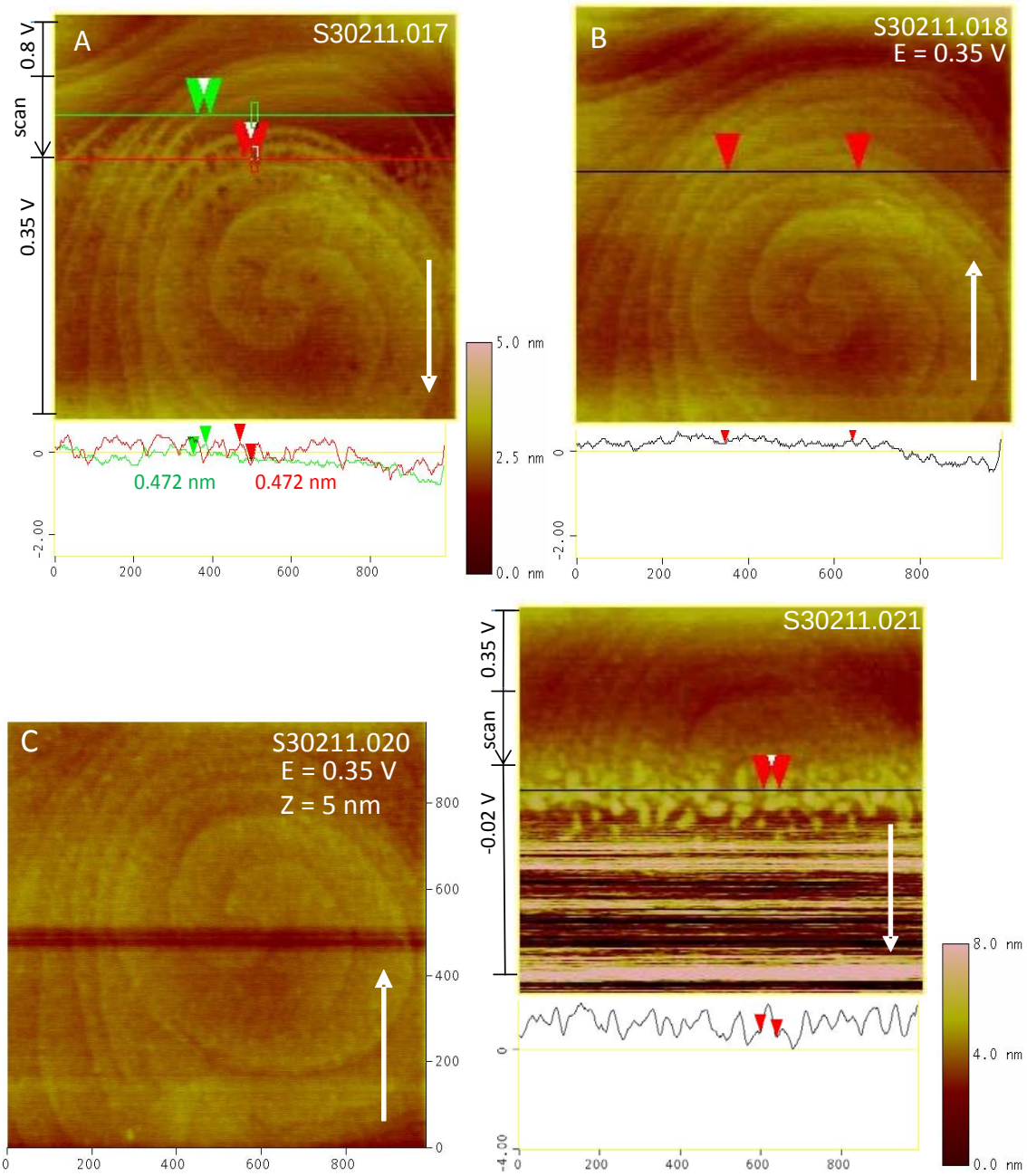

Figure 4.9: AFM topographic images for Se modified Rh(111) in 1 mM H_2SeO_3 with corresponding cross sections. (A-C) Deposited Se completely covered the Rh(111) surface on switching to potential from 0.8 V to 0.35 V and then stop potential leads to sudden multilayer deposition (D) on extending the potential from 0.35 V to -0.02 V resulted selenide formation. Set point = 0.4 V and scan rate of 3 Hz, cantilever: PPP CONTSC-20, k = 0.09 Nm^{-1}. Arrows indicates scan direction.

Actual snapshots of the generated metallic Se taken after the AFM measurements are shown in fig. 4.10. These Se nanoparticles weakly adhere to the surface and can easily be removed by thorough rinsing of the electrode surface with Milli-Q water.

Figure 4.10: An actual photo of the Se nanoparticles on Rh(111) electrode surface.

The surface modification of the Pt(111) and Au(111) surface with Se behaves differently from that on Rh(111) except for selenide formation at more negative potentials. The Se multilayer deposits appear rather smooth at a potential of 0.35 V from on Pt(111) as shown in fig. 4.11A. However, H_2Se formation on both Se modified Pt(111) and Au(111) leads to Se deposits similar to that observed on Rh(111).

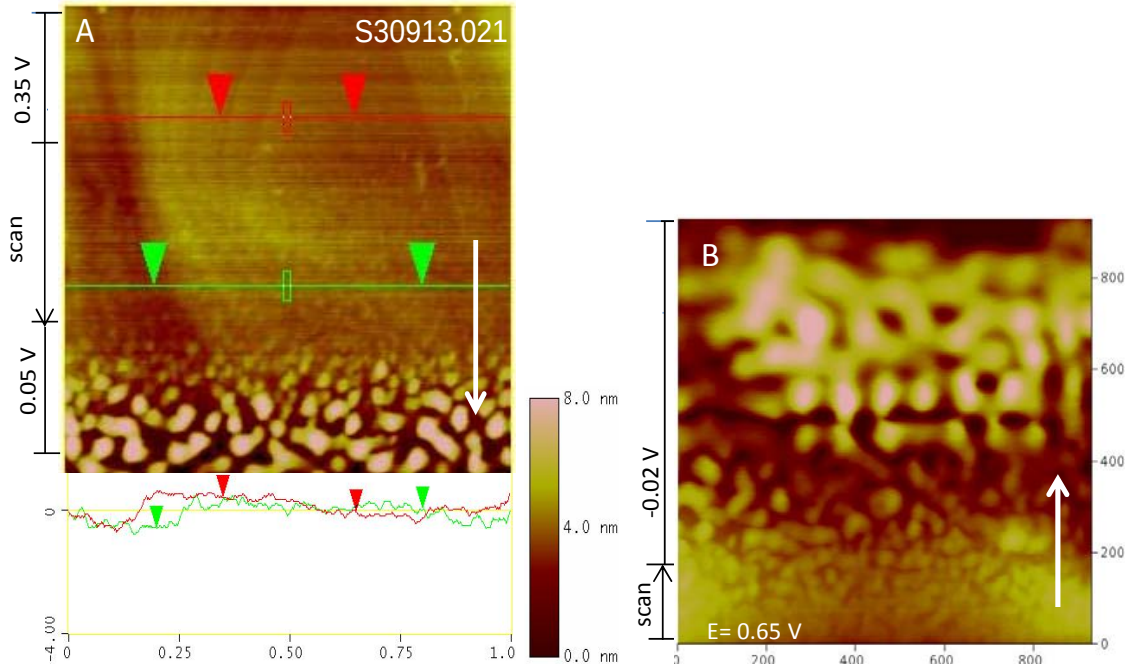

Figure 4.11: AFM topographic images for Se modified Pt(111) and Au(111) in 1 mM H_2SeO_3 with corresponding cross sections.
A) reductive dissolution of Se on Pt(111) and B) on Au(111) observed around 0.0 V vs. RHE resulted as indicated by potential along AFM images. Set point = 0.4 V and scan rate of 3 Hz, cantilever: PPP CONTSC-20, k = 0.09 Nm^{-1}. Arrows indicates scan direction.

4.4.2 Oxidative stripping of Se and its morphology by STM

The morphological change during stripping of a Se (sub-) monolayer from Rh(111) in 0.1 M $HClO_4$ is shown in the STM image fig. 4.13. Se was again adsorbed from 1 mM H_2SeO_3 in the conventional H-cell (fig. 4.12).

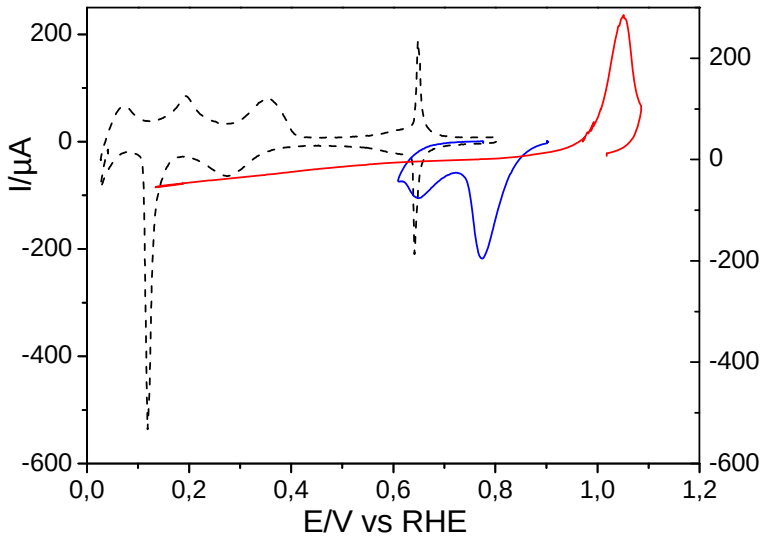

Figure 4.12: CVs of Rh(111) (-----) at a sweep rate of 50 mV/s together with Se deposition (——) in H-cell from 1mM H_2SeO_3 and oxidative stripping of adsorbed Se (——) in STM cell containing 0.1 M $HClO_4$ sweep rate 50 mVs^{-1}.

After a potential scan down to 0.1V with 50 mV/s (without any visible morphological change because no H_2SeO_3 is present), the adsorbed selenium is stripped off at +1.04 V vs. RHE in the subsequent anodic cycle (fig. 4.12). The cross-section of the STM image reveals that the height decreases during dissolution by 0.2 nm and therefore the removed Se adlayer had a thickness of 0.2 nm, corresponding to a monolayer.

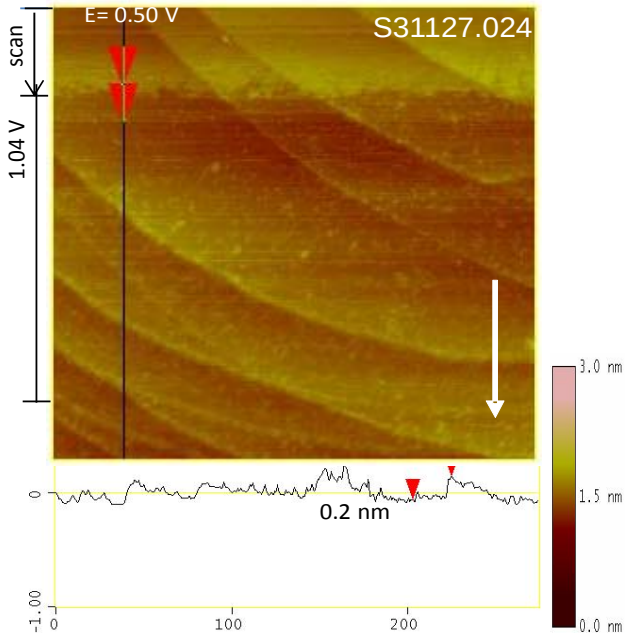

Figure 4.13: The STM images of Se/Rh(111) with cross section showing oxidative stripping of Se at 1.1 V vs. RHE. Sample bias of 50 mV, set point = 0.86 nA & scan rate of 5 Hz.

4.5 Discussion

The nature of bonding for the Se adatoms with Rh(111) should be entirely different from the Se-Se bond. This is already explored for Se interactions with Ru in ECNMR studies, which confirmed metallic bond formation between the two [10]. This might be the reason that no reductive dissolution of Se is visible at monolayer coverages. For reductive dissolution of up to $\vartheta \approx 0.4$ ML of Se on Au(111), our results using DEMS were in good agreement with the work done by Alanyalioglu et al. [24] using simple voltammetry.

From the AFM images it is clear that, on Rh(111), deposition of Se in peaks C_1 to C_3 leads to an atomically smooth Se layer. From the corresponding stripping experiment, it is evident that this layer has a thickness of 0.2 nm. Further deposition till pack C_4 leads to a rough surface, with height differences within a terrace of 0.5 nm. As shown in chapter 3, such a roughening also occurs when during the potential sweep in cathodic direction the potential is held at 0.7 V for some time. This roughening therefore is a slow process and probably due to a place exchange between Rh and Se, similar to the well known roughening of Pt and other noble metals upon oxygen adsorption at positive potentials [25-27]. Other examples of such roughening processes are Te on Au(111) [28]

and As on Pt [29].

A comparison of deposition charges and reductive and oxidative selenium stripping charges on various fcc(111) surface are summarized in table 4.1. The reductive dissolution was observed only for multilayered Se deposits formed below 0.6 V.

Table 4.1: Se deposition and stripping charges on fcc(111) surface

(Se deposition till 0.1 V) multilayer	Rh(111)	Pt(111)	Au(111)
Se dep	4.6 n mol/ cm^2	4.0 n mol/ cm^2	4.3 n mol/ cm^2
Se Ox	0.6 n mol/ cm^2	1.3 n mol/ cm^2	0.50 n mol/ cm^2
H_2Se, from CV	2.6 n mol/ cm^2	2.63 n mol/ cm^2	4.11 n mol/ cm^2
H_2Se from DEMS	2.02 n mol/ cm^2	2.30 n mol/ cm^2	2.26 n mol/ cm^2
(Se deposition till 0.65 V) monolayer	Rh(111)	Pt(111)	
Se dep	1.4 n mol/ cm^2	0.91 n mol/ cm^2	
Se Ox	1.95 n mol/ cm^2	1.0 n mol/ cm^2	
H_2Se	0	0	
DEMS	0	0	

From this table, it is evident that the amount of reductively stripped Se is similar on all three surfaces for the Se multilayer. This may of course be due to the similar amount of deposited Se. This Se deposition charge is in good agreement with previously studied Se on Au(111) surface [30].

The amount of reductively stripped Se as determined from the reduction charge is close to these values, except for Au(111) where the reduction charge is much larger for unknown reasons. On Pt(111), the amount of reductively desorbed Se plus that oxidatively desorbed corresponds well to the amount deposited. On Rh(111) (and also Au(111)) the amount of oxidatively desorbed Se seems to be too small. Interestingly, this is different after deposition of only a sub monolayer, where no cathodic stripping is observed: Not only on Pt(111), but also on Rh(111), both the deposition charge and the oxidative stripping charge (and the corresponding amount of Se) coincide. (The somewhat larger oxidation charge on Rh(111) may be due to simultaneous oxidation of the Rh surface.) As shown in the AFM images, under conditions of multilayer deposition, a surface roughening occurs, which is probably due to a place exchange

between Rh and Se. The subsurface Se thus formed cannot be (or not completely) oxidised during the anodic potential scan.

This also explains the longer H_2 evolution rate after multilayer deposition: The submonolayer deposit renders the surface inactive for H_2 evolution, nearly all Rh sites are blocked by Se. At the roughened surface, a mixed Rh-Se layer is covered by a monolayer of Se; the latter is reductively desorbed and Rh-atoms are exposed to the solution again.

It is astonishing that, in the potential region of peak C_4, deposition is limited to about $\vartheta = 0.2$. Lister et al. explained this by the high resistivity of Se (10^{10} Ω-cm) although the Se layer is only 0.5 nm thick [31].

4.6 Conclusions

In this chapter, the electrochemical modification of the fcc(111) electrodes such as Rh(111), Pt(111) and Au(111) with Se in the $HClO_4$ solution was studied using DEMS and SPM techniques. Through the experiments with the DEMS, not only was qualitative data obtained but also quantitative amounts of the reductively dissolved selenium as selenide at much lower potentials were studied. At this potential, and in the absence of selenium containing solution, the formation of the H_2Se species involved the transfer of two electrons only. However, in the presence of selenious acid H_2Se species could also proceed via six electrons. It was also observed that H_2Se species were generated only from surfaces covered with multilayer selenium deposits. No H_2Se could be generated when the Se surface coverage had ϑ values of $\vartheta \leq 0.5$. The SPM technique, especially AFM, also confirmed the formation of Se particles at a lower potential of around 0 V vs. RHE. STM was also employed to observe the oxidative dissolution of deposited Se. On Rh(111), the deposition of more than half a monolayer leads to a surface roughening caused by a place exchange of Rh and Se atoms.

References

[1] M. Shao, Electrocatalysis in Fuel Cells: A Non- and Low- Platinum Approach, Springer, 2013.

[2] D. C. Papageorgopoulos, F. Liu, and O. Conrad, Electrochimica Acta 53:1037 (2007).

[3] O. Solorza-Feria, K. Ellmer, M. Giersig, and N. Alonso-Vante, Elrotrochimica Acta, Vol. 39 39:1647 (1994).

[4] M. Neergat, V. G. and, and R. K. Singh, Journal of Electrochemical Society 158:7 (2011).

[5] R. W. Reeve, P. A. Christensen, A. J. Dickinson, A. Hamnett, and K. Scott, Electrochimica Acta 45:4237 (2000).

[6] N. Alonso-Vante, I. V. Malakhov, S. G. Nikitenko, E. R. Savinova, and D. I. Kochubey, Electrochimica Acta 47:3807 (2002).

[7] F. Dassenoy, W. Vogel, and N. Alonso-Vante, Journal of Physical Chemistry B 106:12152 (2002).

[8] M. Bron, P. Bogdanoff, S. Fiechter, I. Dorbandt, M. Hilgendorff, H. Schulenburg, and H. Tributsch, Journal of Electroanalytical Chemistry 500:510 (2001).

[9] D. Cao, A. Wieckowski, J. Inukai, and N. Alonso-Vante, Journal of The Electrochemical Society 153:A869 (2006).

[10] P. K. Babu, A. Lewera, J. H. Chung, R. Hunger, W. Jaegermann, N. Alonso-Vante, A. Wieckowski, and E. Oldfield, Journal of the American Chemical Society 129:15140 (2007).

[11] M. S. Kazacos and B. Miller, Journal of The Electrochemical Society 127:869 (1980).

[12] C. Wei, N. Myung, and K. Rajeshwar, Journal of Electroanalytical Chemistry 375:109 (1994).

[13] J. J. Lingane and L. W. Niedrach, Journal of the American Chemical Society 71:196 (1949).

[14] R. W. Andrews and D. C. Johnson, Analytical Chemistry 47:294 (1975).

[15] M. F. Cabral, V. A. Pedrosa, and S. A. S. Machado, Electrochimica Acta 55:1184 (2010).

[16] M. O. Solaliendres, A. Manzoli, G. R. Salazar-Banda, K. I. B. Eguiluz, S. T. Tanimoto, and S. A. S. Machado, Journal of Solid State Electrochemistry 12:679 (2008).

[17] M. C. Santos and S. A. S. Machado, Journal of Electroanalytical Chemistry 567:203 (2004).

[18] J. Clavilier, R. Faure, G. Guinet, and R. Durand, Journal of Electroanalytical Chemistry 107:205 (1980).

[19] A. Hamelin, in Modern Aspects of Electrochemistry, Vol. 16 (B. E. Conway, R. E. White, and J. O. M. Bockris, eds.), Plenum Press, 1985, p. 4.

[20] J. A. Rodriguez, S. Chaturvedi, and M. Kuhn, Journal of Chemical Physics 108:3064 (1998).

[21] J. Clavilier, M. Wasberg, M. Petit, and L. H. Klein, Journal of Electroanalytical Chemistry 374:123 (1994).

[22] H. Baltruschat, Journal of the American Society for Mass Spectrometry 15:1693 (2004).

[23] J. E. Sader, J. W. M. Chon, and P. Mulvaney, Review of Scientific Instruments 70:3967 (1999).

[24] M. Alanyalioglu, U. Demir, and C. Shannon, Journal of Electroanalytical Chemistry 561:21 (2004).

[25] F. T. Wagner and P. N. Ross, Journal of Electroanalytical Chemistry 150:141 (1983).
[26] K. Sashikata, N. Furuya, and K. Itaya, J. Vac. Sci. Technol. B B 9:457 (1991).
[27] T. Löffler, R. Bussar, X. Xiao, S. Ernst, and H. Baltruschat, Journal of Electroanalytical Chemistry 629:1 (2009).
[28] J. L. Stickney, T. E. Lister, B. M. Huang, and L. B. Goetting, Electrochimica Acta 40:143 (1995).
[29] X. Y. Xiao and H. Baltruschat, Langmuir 19:7436 (2003).
[30] T. E. Lister and J. L. Stickney, Journal of Physical Chemistry 100:19568 (1996).
[31] T. E. Lister, B. M. Huang, R. D. Herrick, and J. L. Stickney, Journal of Vacuum Science & Technology B 13:1268 (1995).

Chapter 5: ORR on Rh(111) and Se modified Rh(111) surface

The chapter focuses on the investigation of the ORR on Rh(111) and Se modified Rh(111) single crystalline surfaces. A dual thin layer flow through cell (DTLFC) was used for this purpose and detailed characterization of this setup is explained in Appendix C.

5.1 Introduction:

The use of a Pt catalyst in the Oxygen Reduction Reaction (ORR) has been widely studied given the significance of the reaction in electrocatalysis, fuel cells and sensor technology [1-3]. However, Pt catalysts do not work well in case of direct methanol fuel cells, since the Pt is easily poisoned by adsorption of the crossover methanol from the anode to the cathode compartment.

Among available alternative catalysts, metal chalcogenides are considered as potential catalysts due to their promising ORR activity and methanol tolerance. However, the oxygen reduction kinetics of these compounds is slower than that of Pt [4]. Historically, metal chalcogenides (Ru-chalcogenides) were studied because their electrochemical properties, semi-conducting properties and activity towards oxygen evolution make them suitable for photoelectrochemical devices [5]. Subsequently, it was discovered that these compounds were also appropriate for ORR catalysis.(Alonso Vante REF) Currently, these (namely Ru and Rh sulfides) are also used as oxygen depolarizing cathode (ODC) catalysts for the electrochemical synthesis of HCl. The Rh_xS_y nanoparticles synthesized using sulfur ion-free synthesis method possessing a balanced Rh–S phases mixture were found appropriate for oxygen depolarizer cathodes. This Rh-S phase mixture consists of three main phase [6]. So far the research on the electro-catalytic activity of metal chalcogenides has focused exclusively on nanoparticle catalysts [7-9].

In addition, it was found that the ORR is enhanced by the simple Se adsorption on massive Ru electrode. Multilayers of Ru were electrochemically deposited on Au substrate followed by its modification with Se, which were then used for ORR studies. Active surface area of these modified surfaces was also determined by Cu UPD method-[10]. Despite of their methanol tolerance, further investigations are required to improve their electro-catalytic activity. For the search for a better electrocatalysts, a systematic

examination of the catalysts surface interacting with the adsorbed intermediates is required.

In general, single crystalline surfaces were effectively explored as models for actual electrocatalysts. Pt and its well defined alloys as single crystals were utilized for understanding ORR process [11]. Till now, no ORR studies performed on Rh(111). The only available ORR studies on transition metal single crystalline surfaces are on Ru(0001). The ORR kinetics is affected by the oxidation state of the Ru and proceeds mainly via approximately four electrons, whereas, the first electron being the rate determining step [12].

In many cases, sub monolayer modification of the metal surfaces with foreign adatoms results in enhanced activity from the electrocatalytic point of view. Feliu et al studied the spontaneous irreversible adsorption of Se adatoms on Pt(hkl) electrode surfaces and observed stable binary surfaces on Pt(hkl) electrodes [13]. Similarly, Sung and co-workers studied the monolayer and sub monolayer adsorption of S on Pt(111). They discussed the influences of S adatoms on the thermodynamics of Pt(111) and observed weaker hydrogen UPD in the presence of S than in the absence [14].

The Selenium electrochemistry also plays a vital role in generation of compound semiconductors, which are important for optoelectronic application. In this connection detailed electrochemical and scanning probe microscopic studies were performed to characterize Se adlayers on Au(111) surface [15, 16].

Contrary to RuSe, less is known about the electrocatalytic activity of Rhodium selenide for ORR and their methanol tolerance ability [17, 18]. As mentioned earlier, till now, model surfaces of metal chalcogenides were not explored to enhance understanding of the electrocatalytic activity of these surface. Quite recently Tritsaris et al provided atomistic insights of well-defined noble metal chalcogenides for ORR and methanol tolerance based on density functional theory, especially selenides and sulfides of transition metal chalcogenides. They observed that all transition metal (Ru, Rh, Pd, Ir, Co, and W) with chalcogens (ϑ = 0.5) showed better ORR activity except Pd. Particularly, the selenide of Rh were found both ORR active and methanol tolerance [19].

Therefore, in our current work, we systematically investigated the ORR activity of Rhodium single crystalline surface Rh(111) and its electrochemical modification with Selenium (Se) submonolayer loadings in acidic media. ORR activity of these model Se/Rh(111) surfaces was carried out in the modified dual thin layer flow through cell (DTLFC) developed in our group for differential electrochemical mass spectrometric (DEMS) studies [20]. DTLFC setup was optimized and a similar setup previously explored for ORR activities [21, 22].

5.2 Experimental:

5.2.1 Preparation and electrochemistry of massive Rh single crystal electrodes

The traditional annealing and cooling down in Ar atmosphere was also successfully used for preparation of Rh(111) with slight modification .[23]. A mixture of Ar:H_2 (2:1) was used for cooling down after the annealing process. All solutions were prepared from 18.2 MΩ Milli-Q water and de-aerated with high purity Ar gas (99.999%). Electrochemical experiments were carried out in a conventional H-cell in a hanging-meniscus configuration containing 0.1 M $HClO_4$ (spectro pure grade). A large Pt counter electrode and reversible hydrogen was used as a reference electrode. Selenium submonolayer and monolayer deposits were performed in another H-cell from 1 mM H_2SeO_3 (Analytical grade). A Bi-potentiostat from Pine Instruments Inc. model AFBPC1 in combination with a user interface developed in Labview software was used for data acquisition and recording cyclic voltammograms. A Rh(111) single crystal, with a diameter of 10 mm, was obtained from Kristallhandel Kelpin, Germany. The ORR was performed using DLTFC, in which the Rh(111) disc electrode was fixed in the upper compartment and a Pt polycrystalline disc electrode was placed in the lower compartment. A continuous supply of oxygen saturated 0.5 M $HClO_4$ was maintained using the hydrostatic pressure of the electrolyte present in a glass supply bottle, which was connected to the inlet of the DTLFC. Different flow rates (2.5, 5 and 10 μL/s) were adjusted using a syringe pump or a peristaltic pump the peristaltic pump at the outlet. The cleanliness of the setup and retention of single crystallinity of Rh(111) during transfer and assembling of the DTLFC was verified by recording voltammograms of Rh(111) in Ar and in O_2 saturated 0.5 M $HClO_4$ electrolyte. The appearance of characteristic reversible features of hydroxide ions on Rh(111) at around 0.63 V indicated the cleanliness of the setup used.

5.2.2 CO charge transients

The ptzc on Rh(111) was determined by adsorbing CO at various fixed potentials (90, 200 & 290 mV vs. RHE) and recording the current time transients following the procedure of Clavilier et al. [24]. In these experiments the hanging meniscus arrangement was used, and CO was introduced to the gas phase above the electrolyte.

The surface area of the Rh(111) and Se modified Rh(111) surfaces was determined from the CO stripping charge. Here, the CO was adsorbed at a potential of 0.1 V vs RHE by injecting 3 ml of CO saturated solution into the Ar saturated 0.1 M $HClO_4$. The CO was allowed to adsorb on these surfaces while closing off the Ar gas supply. While maintaining a hanging meniscus contact the Ar was purged gently through the solution to remove excess CO from the bulk. Finally, the oxidative stripping of the CO was performed by cycling the potential between 0.1 to 0.9 V vs RHE.

5.3 Results and discussion

5.3.1 Determination of the PTZC for Rh(111) by CO displacement

A cyclic voltammogram of Rh(111) recorded at 10 mV/s is shown in fig. 5.1. It is identical to those published elsewhere [23, 25]. The reduction of perchlorate around 260 mV leads to diminution of or even disappearance of the second peak A_2 in the second sweep, and splitting of the main hydrogen peak C_3 is proposed due to the desorption of chloride from the surface (cf. eq. # 1) as represented in fig. 5.1. Detailed voltammetric studies of Rh(111) are already described elsewhere.

$$(ClO_4^-)_{aq} \Leftrightarrow (ClO_4^-)_{ads}$$

$$(ClO_4^-)_{ads} + 8H_3O^+ + 8e^- \rightarrow \ (Cl^-)_{aq\ or\ ads} + 12H_2O \text{ [26]} \qquad 5.1$$

In order to get more insight, and to unequivocally determine which of the peaks corresponds to hydrogen adsorption, the CO charge displacement experiments were conducted [24]. The charge-time transients were monitored at various fixed potentials below that for CO oxidation and are shown as insets in fig. 5.1. The CO adsorption causes displacement of other adsorbed atoms, ions or molecules from the electrode surface, which resulted in a current transient. Integration of the transients gives the displacement charges: therefore plotted in fig. 5.2 together with the charge curve obtained by integrating the current of the cyclic voltammogram. (The latter was shifted

in the y direction to achieve maximum coincidence with the charge values given by the transients) The potential at which the charge is zero is the point of zero charge. It was found to be 200 mV, confirming that peak C_3 is due to hydrogen adsorption only and does not contain any contribution from anion desorption. Previous determinations of the pztc were only performed in 0.1 M H_2SO_4 in which cyclic voltammetry is considerably different because of the strong adsorption of sulfate on Rh(111) electrode: Qinqin Xu et al. determined the ptzc on low index Rh(hkl) surfaces in 0.1 M H_2SO_4 using charge displacement and voltammetric techniques. They found pztc on Rh(111) between 0.105 to 0.12 V [27].

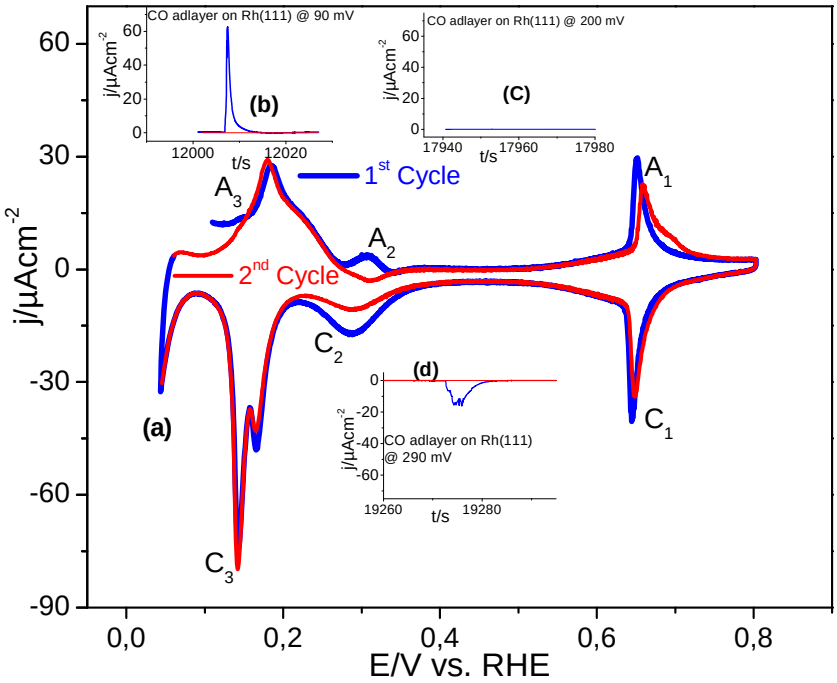

Figure 5.1: Cyclic voltamogram (a) of Rh(111) in Ar sat'd 0.1 M $HClO_4$, sweep rate 10 mV/s. Current-time transient for E_{abs} = 0.09, 0.2 and 0.29 V are represented by (b), (c) and (d) respectively. Transient charges are 71, -0.2 and -64 µC cm^{-2} respectively. CO charge transients at various potentials are shown as inset

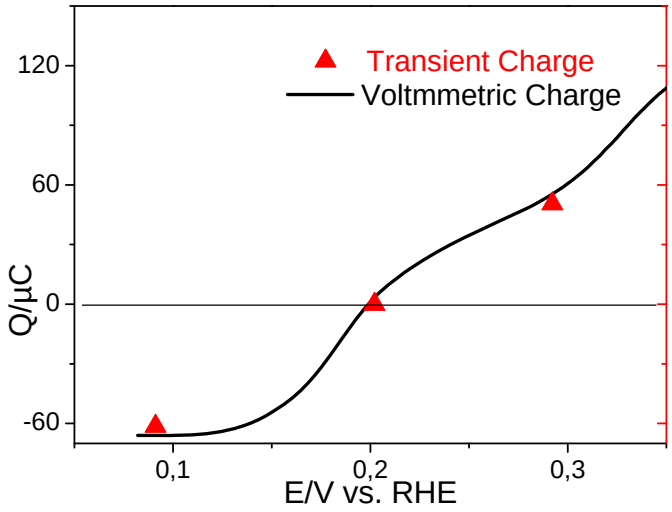

Figure 5.2: The current-time transient for adlayer CO (▲) and voltmmetric charges of Rh(111) (——) in 0.1 M $HClO_4$, sweep rate 10 mV/s, voltammetric charge is adjusted to most negative value.

The electro-oxidative stripping of adsorbed CO on Rh(111) has been studied in 0.1 M $HClO_4$. An adlayer of CO was adsorbed on Rh(111) around 0.1 V vs RHE by injecting CO saturated solution, the CO from the bulk solution was removed by gentle Ar purging. CO electro-oxidation was performed at a sweep rate of 5 mVs^{-1}. The CVs for Rh(111) with that of oxidative stripping of CO is shown in fig. 5.3. The complete suppression of the hydrogen adsorption/desorption region indicated that all the rhodium surface atom sites were blocked by CO. This resulted in a current close to zero until the onset of CO oxidation around E = 0.59 V. During the electro-oxidation of CO, a shoulder peak around E = 0.62 V with a maximum at E = 0.665 V followed by another shoulder around E = 0.73 V was observed. It is well known that the CO electro-oxidation on Rh(hkl) surfaces is complex and does not result in complete oxidation in the first cycle [28, 29] even at low sweep rate. The second and subsequent cycles resulted in the oxidation of remaining CO. However, the typical CV of Rh(111) was not achieved even after many cycles. Integration of the CO oxidation charge in the potential range from 0.4 V in anodic till 0.4 V in cathodic direction to avoid any contributions from adsorbed OH after CO oxidative stripping. Calculated charges for the CO electro-oxidation for the first and second scan were 321 and 2 µC cm^{-2} respectively. The CO surface coverage ϑ_{CO} is obtained using relation

$$\vartheta_{CO} = Q_{CO}^{tot} / (z \cdot Q_{Rh(111)}) \qquad 5.2$$

Where z is the number of electrons required for the electrochemical oxidation of

adsorbed CO, which is 2 electrons and $Q_{Rh(111)}$ was found to be 256 μCcm^{-2} by Clavilier et al. for complete monolayer on hydrogen on Rh(111) [23]. Hence, the CO surface coverage corresponds to approximately 63 % coverage of Rh(111), which is in good agreement to the value determined by Q. Xu et al. in 0.1 M H_2SO_4 [27]. For comparison, the maximum possible CO coverage reported for Pt(111) is 0.7 .[30]. Experimental values are typically lower. Therefore, one can assume that not more than 10% CO (if any) are left on the surface after the third cycle. It is therefore astonishing that only 27 % of the hydrogen adsorption charge are regained. In literature, the sweeps subsequent to the oxidation sweeps are not shown and it was only mentioned that they are different from that on clean Rh(111).

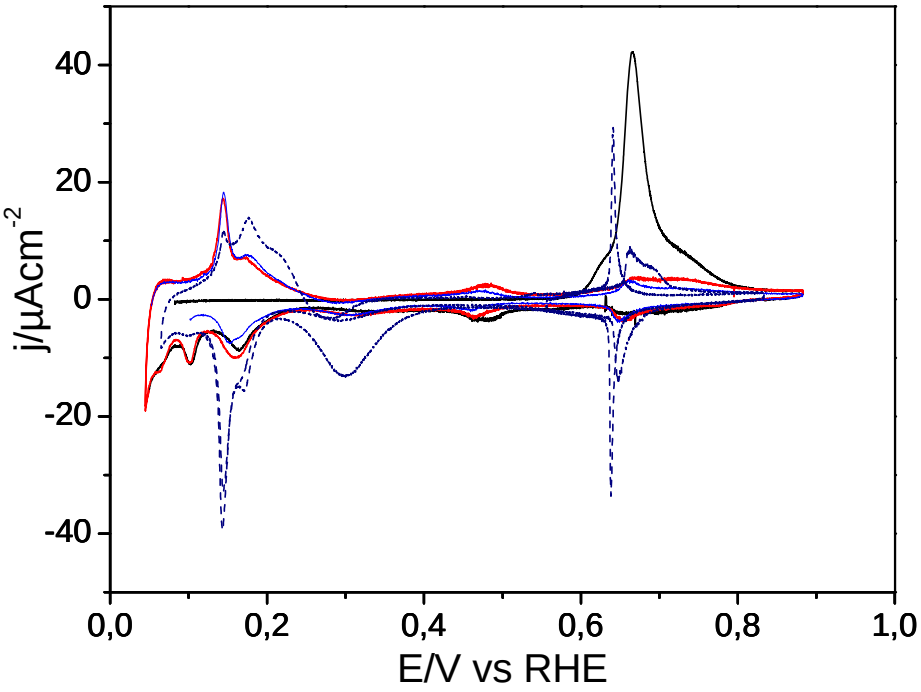

Figure 5.3: The cyclic voltammogram of Rh(111) (-------) together with CO stripping in 0.5 M $HClO_4$ (first scan: ——; second scan: ——; third scan: ——) sweep rate of 5 mV/s.

5.3.2 ORR on Rh(111)

ORR on Rh(111) and Se modified single crystalline Rh(111) surfaces were performed in the DTLFC. The optimization and general setup of DTLFC is explained briefly in Appendix C.

The CV for Rh(111) in O_2 saturated atmosphere (solid line at 10 mV/s) is shown in fig. 5.4 together with that in a deaerated solution (dashed line at 50 mV/s). These CVs

confirm that the electrode remained clean during transfer and also during the ORR. A sharp increase in the negative current during the cathodic scan at around 0.63 V is only in part due to the superposition of the pseudo capacitive currents for reduction of adsorbed hydroxyl (OH_{ads})[23]. In addition, it is caused by the increasing activity of the surface for O_2 reduction when the amount of the inhibiting OH_{ads} is decreasing. A similar feature was already observed on Pt(111) during ORR in weakly adsorbing electrolyte.[31]

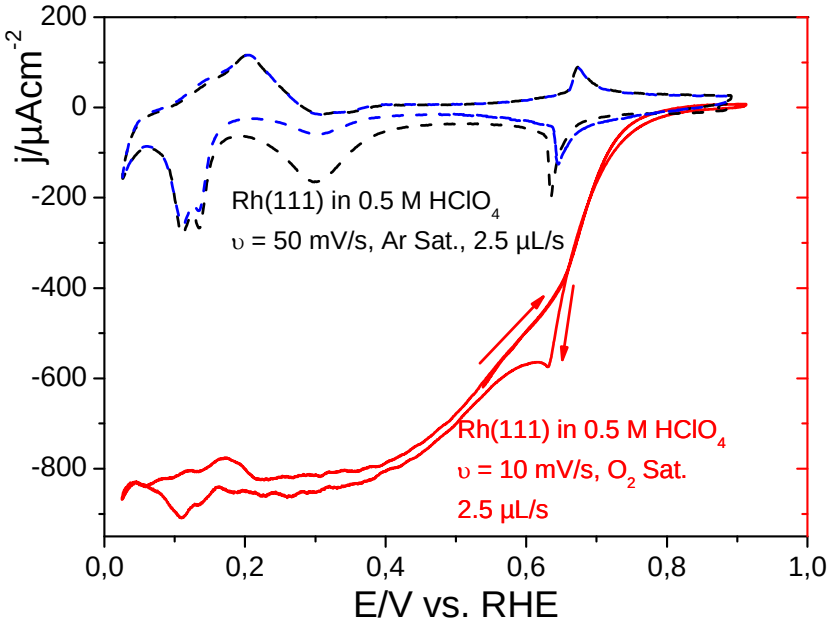

Figure 5.4: CVs of Rh(111) in DTLC containing Ar saturated 0.5 M $HClO_4$ first sweep (------) and second sweep (------), sweep rate of 50 mV/s, Rh(111) in oxygen saturated electrolyte (——), sweep rate of 10 mV/s, in both cases the flow rate was 2.5 µL/s.

Figure 5.5 shows the current potential profile describing the ORR activity of the Rh(111) disc electrode. The low current at the polycrystalline Pt disc electrode held at 1.2 V corresponds to an amount of H_2O_2 in the range of 0~3 %. The percentage yield of H_2O_2 was calculated using following equation [32]

$$X(H_2O_2) = \frac{(2 \cdot I_R / N)}{((I_D + I_R)/N)} \qquad 5.3$$

N was determined to be 0.38 at a flow rate of 2.5 µL/s (appendix C)

This implies that the oxygen reduction proceeds mainly via a direct four-electron pathway. (The currents around 0 V at the Pt electrode was due to the oxidation of the H_2 generated at Rh(111) electrode.

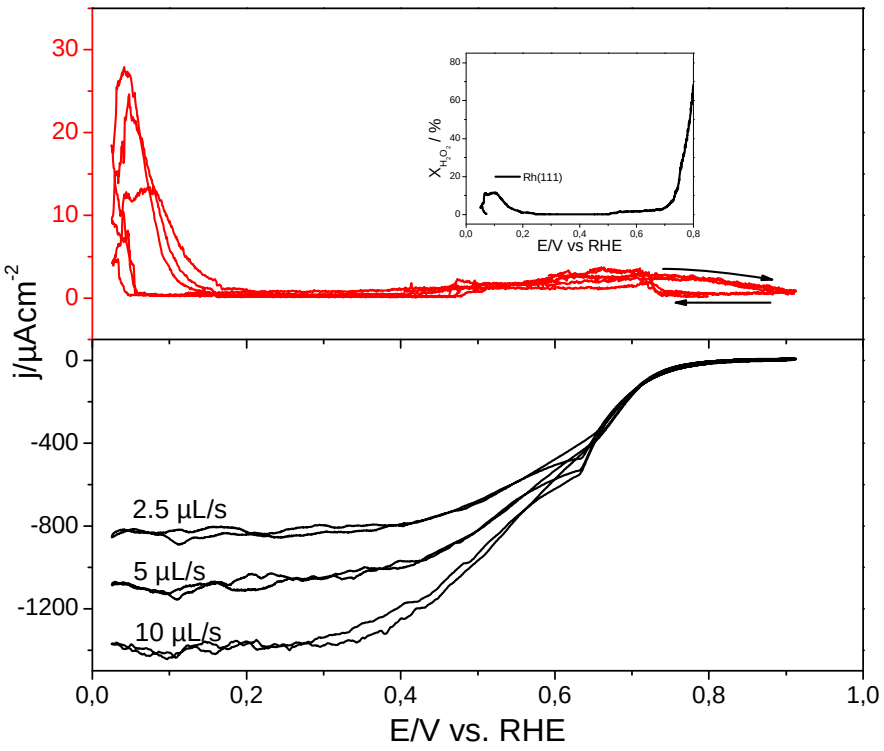

Figure 5.5: Simultaneously recorded CVs of Rh(111) (——) and related current signals on a polycrystalline Pt (——) held at 1.2 V in DTLC containing oxygen saturated 0.5 M $HClO_4$ for various flow rates of 2.5, 5 & 10 µL/s respectively at sweep rate of 10 mV/s. H_2O_2 generated as a function of potential is shown as inset.

A Tafel slope of around 84 mV/dec obtained from a plot of kinetic currents ($I_{kin} = (I_{lim} \cdot I) \cdot (I_{lim} - I)$) as a function of potential (fig. 5.6) [33]. This value of Tafel slope in the kinetic region resembles that of the Tafel slope obtained on the Pt electrode within this potential region. However the Tafel slope of 196 mV/dec in the mixed kinetic-diffusion limited region was much higher than that observed for the Pt electrode, which might be due to the involvement of the adsorbed oxygenated species on Rh(111) during ORR. Note that the slope changes exactly at the potential of the OH adsorption, i.e. at 0.63 V

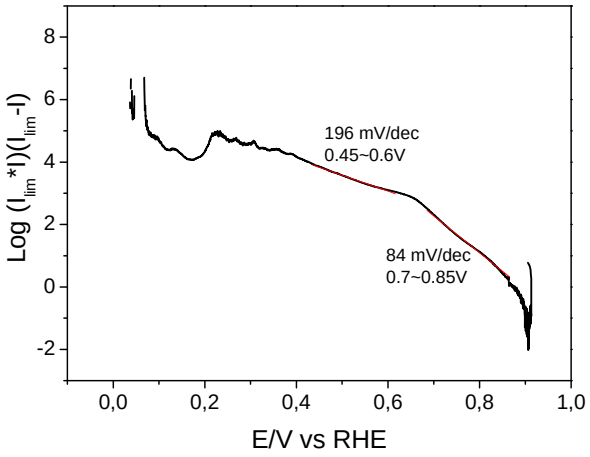

Figure 5.6: Tafel plot for current potential curve of Rh(111) in O_2 saturated 0.5 M $HClO_4$, sweep rate = 10 mV/s, u = 2.5 µL/s, corrected for the capacitive current.

5.3.3. ORR on Se modified Rh(111)

5.3.3.1 Surface modification of Rh(111) ($4x10^{-5}$ M H_2SeO_3)

These experiments were performed to examine the effect of the potential scanning on the submonolayer Se coverages on Rh(111). These were related to the earlier experiments conducted using EC-STM to observe surface morphologies (see chapter 3). In this investigation the Rh(111) electrode was modified by electrochemical Se deposition. The changed surface was then scanned continuously in Se free solution in a potential limit (0.03 to 0.9 V vs RHE) to avoid Se and substrate oxidation. After an hour of continuous cycling the adsorbed Se was stripped off anodically by extending the potential window to 1.4 V. The CVs of Rh(111), Se deposition and dissolution are shown in Fig. 5.7. The Se adsorption and stripping charges were calculated by integration of current time profile within potential range of 0.9 to 0.6 V and 0.9 to 1.2 V respectively after background correction (double layer charge subtraction). Both the adsorption and stripping charges were compared and were used to measure the surface coverages of each surface modification using the equation 5.2 with z = 4.

The Se modified Rh(111) electrode with different coverages resulted in suppression of the corresponding hydrogen charge, which was calculated by integration a potential region from 0.055 till 0.4 V. The calculated charges are summarized in table 5.1

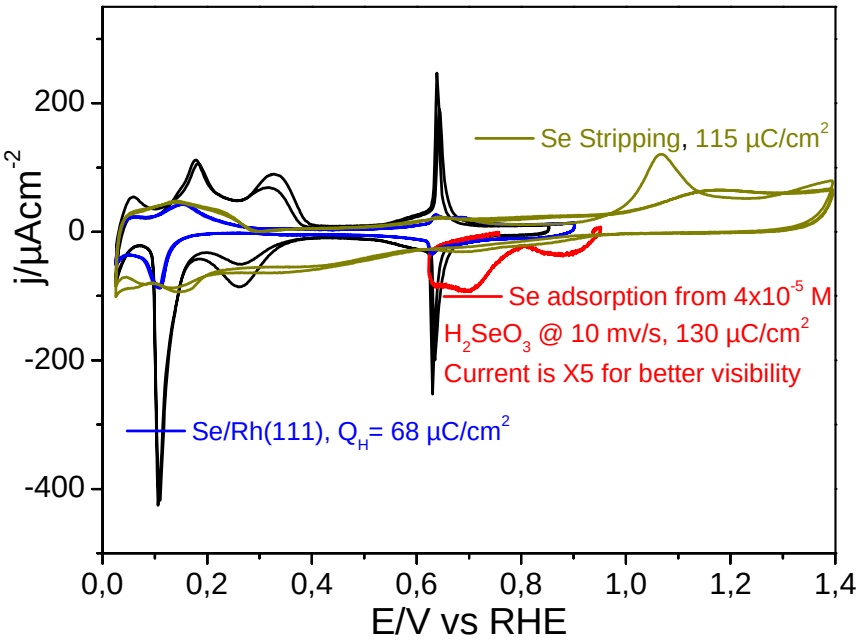

Figure 5.7: CV of Rh(111) surface (——), sweep rate 50 mV/s Se deposition (——) on Rh(111) from $4x10^{-5}$ M H_2SeO_5, sweep rate 10 mV/s, Se/Rh(111) in 0.1 M $HClO_4$ (——) and Se stripping (——), sweep rate 50 mV/s.

5.3.3.2 Surface modification of Rh(111) with diffusion controlled concentrated solution of Se (10^{-6} M H_2SeO_3) and its ORR activity

The diffusion controlled progressive deposition of Se on Rh(111) was performed in order to obtain submonolayer coverages of Se on Rh(111) electrode. The progressive diffusion controlled Se deposition was performed by scanning the potential in the hydrogen region only (0.03~0.35 V) in order to avoid perchlorate reduction. A gradual suppression of the hydrogen adsorption/desorption peaks with each cycle was observed. Different amounts of Se adlayer deposits on Rh(111) surfaces were thus achieved. Figure 5.8 shows a typical example of diffusion limited controlled Se deposition on a Rh(111) electrode. The Se coverage was determined indirectly by oxidative stripping of the adsorbed Se by extending the potential window till 1.3 V. The charge is calculated by integration of the potential region from 0.9 V till 1.3 V for the first after background correction (charge is calculated for the second sweep for the same potential region like in first sweep and than subtracted obtained charge from first sweep charge) and using eq. 5.2 resulted in surface coverage by Se. Also, the suppression of hydrogen coverage before Se stripping was determined and are summarized in table 5.1.

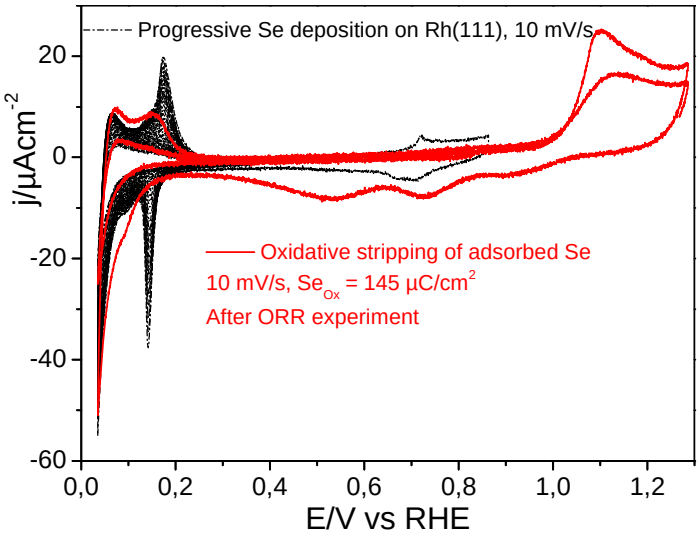

Figure 5.8: CV for Se modification of Rh(111) (——) together with oxidative Se stripping (——) at sweep rate of 10 mV/s in 10^{-6} M H_2SeO_3 + 0.1 M $HClO_4$

A comparison of the current potential profiles for the ORR on Se free and Se modified Rh(111) surfaces with different coverages is presented in fig. 5.9. A slight increase in ORR activity was observed with a surface coverage of ϑ_{Se} = 0.12 generate moderate H_2O_2 (10~15 %). Further increase in Se coverage surface caused a decrease in ORR activity. The respective Tafel plots and H_2O_2 production for each modified surface were also presented in fig. 5.10.

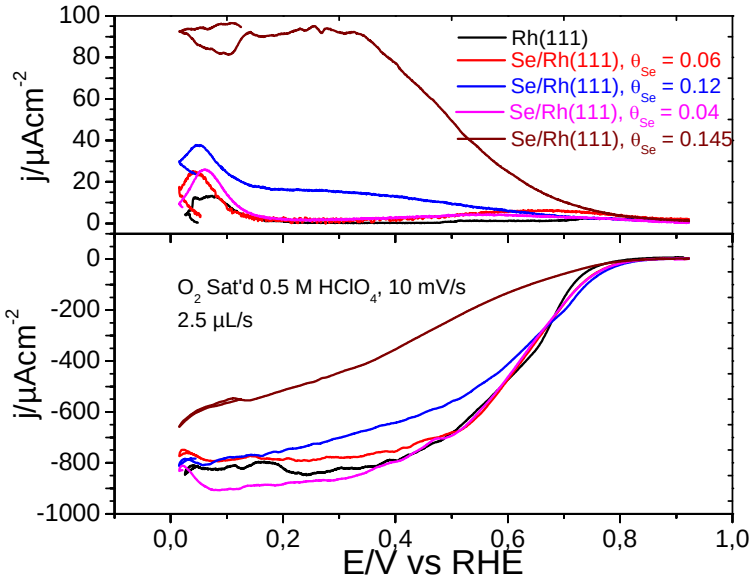

Figure 5.9: Simultaneously recorded CVs of difference coverages of Se modified Rh(111) (ϑ_{Se} = 0.04 (——), 0.06 (——), 0.12 (——), 0.145 (——) in the first compartment and related current signals on a polycrystalline Pt held at 1.2 V in the second compartment of the DTLFC containing oxygen saturated 0.5 M $HClO_4$ at a flow rates of 2.5 µL/s and at sweep rate of 10 mV/s at sweep rate of 10 mV/s. ORR on pure Rh(111) (——) is also shown for comparison.

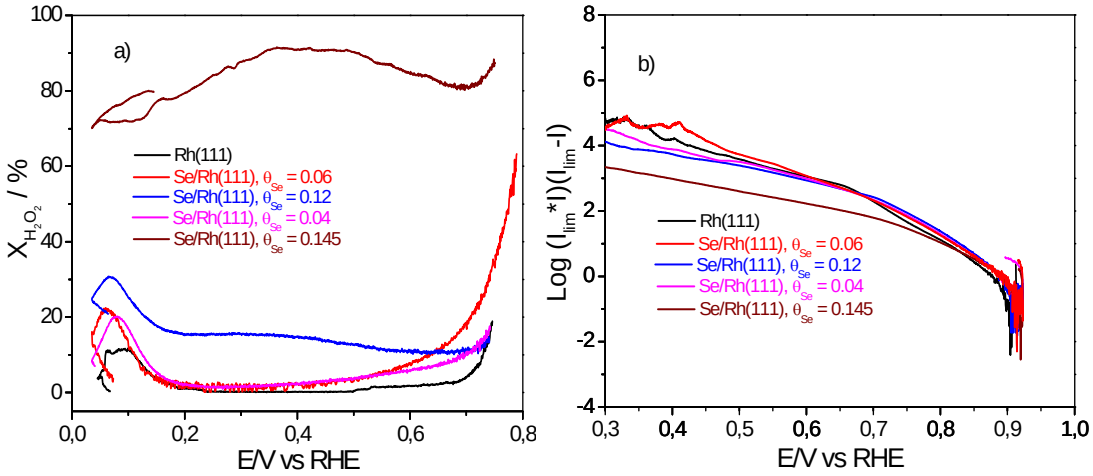

Figure 5.10: a): H_2O_2 production as a function of the electrode potential b): Capacitive current corrected Tafel plots for various coverages for Se modified Rh(111) surfaces.

5.3.3.3 Surface modification of Rh(111) with Se ($4x10^{-5}$ M H_2SeO_3)

The electrochemical deposition of Se on Rh(111) was performed to obtain submonolayer Se coverages similar to section 5.3.3.1. For this purpose $4x10^{-5}$ M H_2SeO_5 electrolyte was used, the reductive deposition of the Se was achieved by scanning the potential from open circuit (~0.95 V vs. RHE) to around 0.6 V. Different Se covered Rh(111) surfaces were prepared and their corresponding hydrogen suppression and Se adsorption charges were calculated in a similar manner as explained in section 5.3.3.1. As an example, CV for the electrochemical deposition of Se on Rh(111) with that of modified Rh(111) with different Se coverages (ϑ_{Se} = 0.09 and 0.13 respectively) is shown in fig. 5.11. The decrease in OH_{ads} peaks (which is a characteristic feature of Rh(111) at 0.63 V) with increasing Se coverage indicates blocking of the H-sites available on Rh(111) surface.

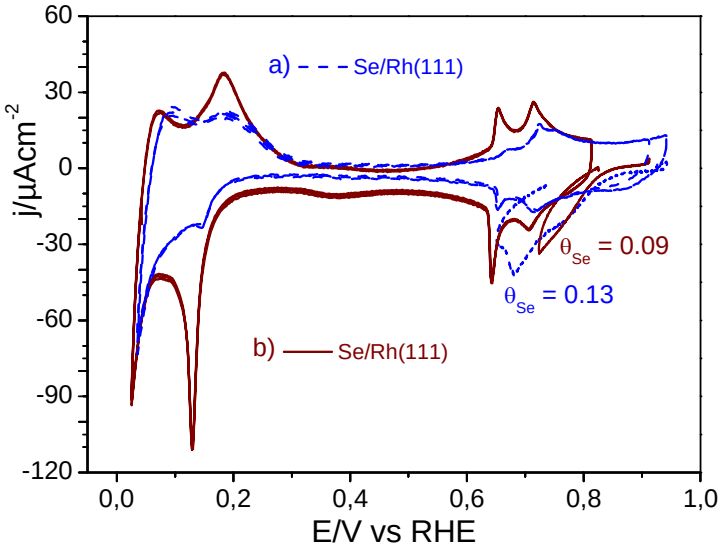

Figure 5.11: a) CV of Se/Rh(111) at 50mV/s together with Se deposition at 10 mV/s (- - -), b) CV of Se/Rh(111) at 50mV/s together with Se deposition at 10 mV/s (——) on Rh(111) from $4x10^{-5}$ M H_2SeO_3

A comparison for the ORR activity of Se modified surfaces with that of pure Rh(111) is presented in fig. 5.12. The optimal ORR activity was observed for a modified surface with a Se surface coverage of approximately 0.09 ML. Although a large part of the surface Rh atoms therefore should be recovered, only a small amount of CO could be adsorbed onto this surface (fig. 5.14). Moreover, the hydrogen inhibition charge on this modified surface agrees well with that of CO oxidation charge (whereas from hydrogen inhibitaion charge ~ 70 % of the surface blocks) This might be due to the mobile nature of Se adatoms at more negative potentials leads to merging of the islands of Se as already observed by STM for similar Se Surface converge (see chapter 3). In chapter 3, it was found that from small Se coverages domains are formed positive of 0.6V, probably because of the coadsorption of OH. The electrochemical data obviously show that this is not the case for coadsorbed CO and hydrogen. The reason most probably is that at the low potentials where hydrogen and CO coadsorbed, the roughening of the surface due to the place exchange of Rh and Se takes place.

Also, the generated H_2O_2 is comparable to that of Rh(111). The generated H_2O_2 at various surfaces was plotted vs. function of potential along with their Tafel plot in fig. 5.13.

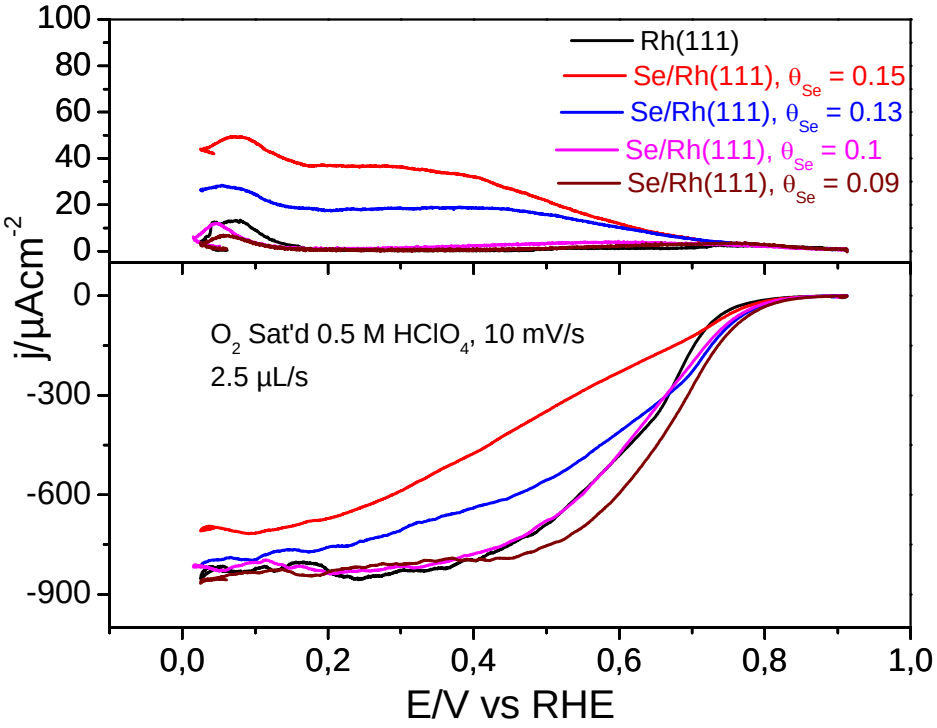

Figure 5.12: Simultaneously recorded CVs of difference coverages of Se modified Rh(111) (ϑ_{Se} = 0.09 (——), 0.1 (——), 0.13 (——), 0.15 (——) in the first compartment and related current signals on a polycrystalline Pt held at 1.2 V in the second compartment of the DTLFC containing oxygen saturated 0.5 M $HClO_4$ at a flow rates of 2.5 µL/s and at sweep rate of 10 mV/s at sweep rate of 10 mV/s. ORR on pure Rh(111) (——) is also shown for comparison.

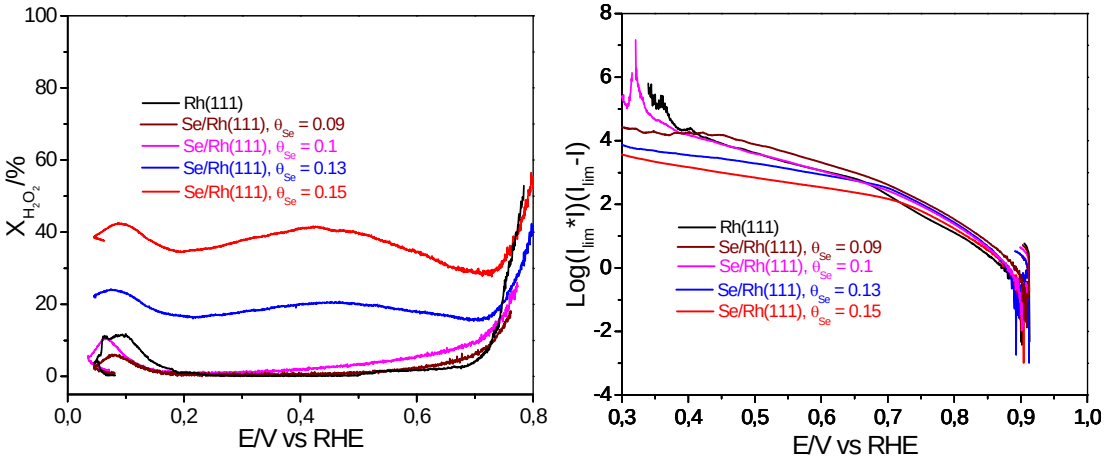

Figure 5.13: a): H_2O_2 production as a function of the electrode potential b): Capacitive current corrected Tafel plots for various coverages for Se modified Rh(111) surfaces.

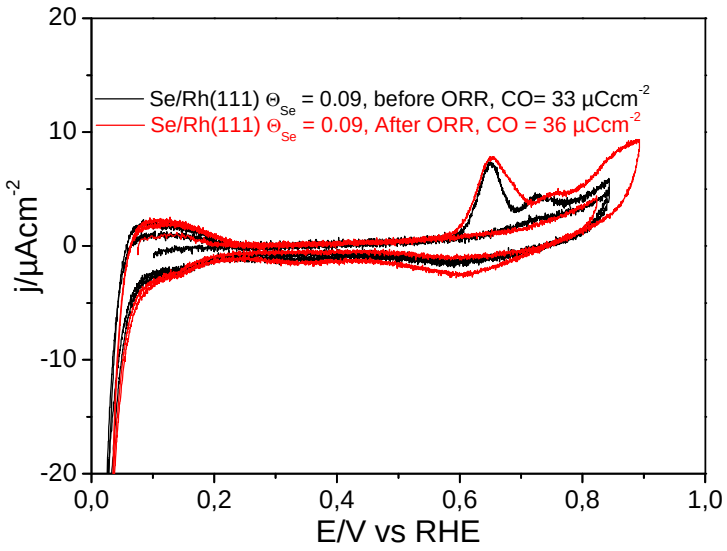

Figure 5.14: Oxidative CO stripping on Se/Rh(111) surface in 0.1 M $HClO_4$, sweep rate = 10 mV/s before (——) and after (——) ORR

A comparison of the surface coverages with Se with corresponding residual hydrogen obtained by various methods are presented in Table 5.1. It was observed that the number of rhodium sites decreases linearly with increasing adsorption of Se. ORR activity (E/V, ORR) of each modified surface was checked at fixed current of -0.1 mA. It was observed that the activity of modified surfaces with ϑ_{Se} = 0.1 were more active than pure Rh(111) surface.

Table 5.1: Se coverages with inhibited H-sites with ORR potential at fixed current,

Gradual EC Se deposition			Fast EC Se deposition		Fast EC Se deposition				Fast EC Se deposition			
ϑ_{Se}	ϑ_H	E/V (ORR)	ϑ_{Se}	ϑ_H	ϑ_{Se}	ϑ_H	E/V (ORR)	ϑ_{CO}	ϑ_{Se}	ϑ_H	E/V (ORR)	ϑ_{CO}
0.04	0.54	0.73	0.115	0.27	0.09	0.47	0.755	0.07	0.134	0.27	0.76	0.06
0.12	0.08	0.74	0.15	0.07	0.1	0.32	0.74		0.164	0.06	0.75	0.04
0.145	0.04	0.64	0.158	0.055	0.129	0.22	0.746					
					0.149	0.12	0.72					

A plot of the various Se surface coverages on Rh(111) vs. that of available H sites on the Se modified surface obtained by various methods as described in Section 5.3.3.1 and 5.3.3.2 (assuming ϑ_{Se} = 0 on Se free surface with ϑ_H = 1) resulted in a linear relation as shown in fig. 5.15. The extrapolation of this line shows that the complete blockage of the surface was achieved with a Se coverage of 0.18. This means that one adsorbed Se atom effectively blocks five Rh atoms. This also means that the adsorbed Se atoms are evenly distributed over the whole surface and that no domains of Se are formed. Feliu et

al. observed the irreversible adsorption of Se on Pt(hkl) surfaces by spontaneous deposition method [13]. They observed a linear dependence of adsorbed Se to the Pt-H inhibition site and complete blockage observed around 0.3 ML.

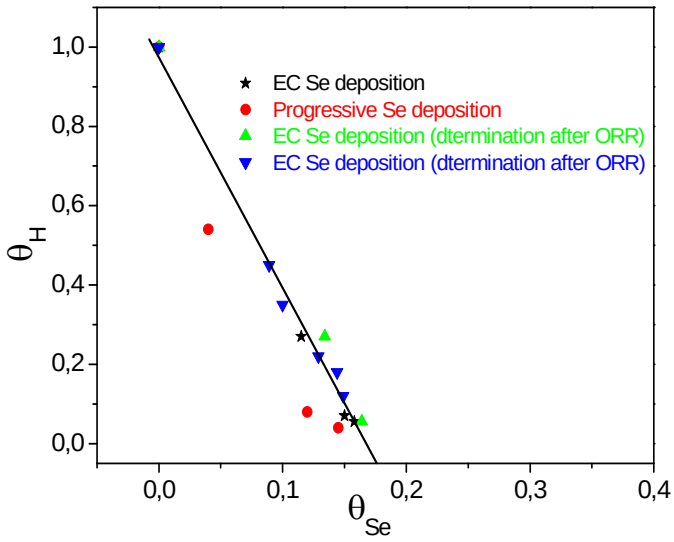

Figure 5.15: A Plot of the inhibited H coverage (ϑ_H) versus Se coverage (ϑ_{Se},) on Rh(111) in 0.1 M $HClO_4$.

5.4 Conclusions

The potential of zero charge was found to be ~0.2 V vs RHE from CO charge displacement experiment at various fixed potentials The oxygen reduction proceeds mainly via four electron with small amount of H_2O_2 generation on Rh(111) and Se modified Rh(111). Electrochemical modification of Rh(111) by Se submonolayers results in a better ORR activity. A Se coverage of ϑ_{Se} = 0.1 resulted improved ORR catalytic activity higher than that of pure Rh(111), however, a surface coverage of about 0.17 would completely block the Rh(111) sites and would hamper its ORR activity. Also, it was observed that a selenium coverage of 10 % resulted in ~50 % coverage of the Rh(111) surface (fig. 3.6 chapter 3), which coincided well with our results summarized in table 4.1. Additionally, this surface gives the best ORR activity. Astonishingly, one Se atoms block five Rh sites from both adsorbing hydrogen and CO. A large tolerance of such an ORR catalyst surface with respect to all kinds of organic fuel can thus be expected.

References

[1] A. S. Bondarenko, I. E. L. Stephens, H. A. Hansen, F. J. Perez-Alonso, V. Tripkovic, T. P. Johansson, J. Rossmeisl, J. K. Norskov, and I. Chorkendorff, Langmuir 27:2058 (2011).

[2] N. M. Markovic, H. A. Gasteiger, and P. N. Ross, Journal of Physical Chemistry 99:3411 (1995).

[3] N. M. Markovic, H. A. Gasteiger, and P. N. Ross, The Journal of Physical Chemistry 99:3411 (1995).

[4] C. G. Vayenas and N. s. Alonso-Vante, in Interfacial Phenomena in Electrocatalysis, Vol. 51, Springer New York, 2011, p. 255.

[5] R. Heindl, R. Parsons, A. M. Redon, H. Tributsch, and J. Vigneron, Surface Science 115:91 (1982).

[6] J. M. Ziegelbauer, A. F. Gulla, C. O'Laoire, C. Urgeghe, R. J. Allen, and S. Mukerjee, Electrochimica Acta 52:6282 (2007).

[7] F. Dassenoy, W. Vogel, and N. Alonso-Vante, Journal of Physical Chemistry B 106:12152 (2002).

[8] J. Ma, A. Habrioux, C. Morais, and N. Alonso-Vante, Physical Chemistry Chemical Physics 16:13820 (2014).

[9] I.-S. Park and Y. Y. J. Tong, Electrocatalysis 4:117 (2013).

[10] N. Bogolowski, S. Huxter, A. A. Abd-El-Latif, G. A. Attard, and H. Baltruschat, Journal of Electroanalytical Chemistry 646:68 (2010).

[11] N. M. Markovic and P. N. Ross, Surface Science Reports 45:117 (2002).

[12] H. Inoue, S. R. Brankovic, J. X. Wang, and R. R. Adzic, Electrochimica Acta 47:3777 (2002).

[13] J. M. Feliu, R. Gomez, M. J. Llorca, and A. Aldaz, Surface Science 289:152 (1993).

[14] Y. E. Sung, T. Chrzanowski, A. Wieckowski, A. Zolfaghari, S. Blais, and G. Jerkiewicz, Electrochimica Acta 44:1019 (1998).

[15] M. Alanyalioglu, U. Demir, and C. Shannon, Journal of Electroanalytical Chemistry 561:21 (2004).

[16] T. E. Lister and J. L. Stickney, Abstracts of Papers of the American Chemical Society 212:151 (1996).

[17] M. Neergat, V. G. and, and R. K. Singh, Journal of Electrochemical Society 158:7 (2011).

[18] D. Cao, A. Wieckowski, J. Inukai, and N. Alonso-Vante, Journal of The Electrochemical Society 153:A869 (2006).

[19] G. A. Tritsaris, J. K. Nørskov, and J. Rossmeisl, Electrochimica Acta 56:9783 (2011).

[20] H. Baltruschat, Journal of the American Society for Mass Spectrometry 15:1693 (2004).

[21] Z. Jusys, J. Kaiser, and R. J. Behm, Electrochimica Acta 49:1297 (2004).

[22] L. Colmenares, Z. Jusys, and R. J. Behm, Langmuir 22:10437 (2006).

[23] J. Clavilier, M. Wasberg, M. Petit, and L. H. Klein, Journal of Electroanalytical Chemistry 374:123 (1994).

[24] J. Clavilier, R. Albalat, R. Gómez, J. M. Orts, J. M. Feliu, and A. Aldaz, Journal of Electroanalytical Chemistry 330:489 (1992).

[25] P. Zelenay, G. Horanyi, C. K. Rhee, and A. Wieckowski, Journal of Electroanalytical Chemistry and Interfacial Electrochemistry 300:499 (1991).

[26] C. K. Rhee, M. Wasberg, P. Zelenay, and A. Wieckowski, Catalysis Letters 10:149 (1991).

[27] Q. Xu, U. Linke, R. Bujak, and T. Wandlowski, Electrochimica Acta 54:5509 (2009).
[28] R. Gomez, J. M. Orts, J. M. Feliu, J. Clavilier, and L. H. Klein, Journal of Electroanalytical Chemistry 432:1 (1997).
[29] T. H. M. Housmans and M. T. M. Koper, Journal of Electroanalytical Chemistry 575:39 (2005).
[30] S.-C. Chang, L.-W. H. Leung, and M. J. Weaver, Journal of Physical Chemistry 93:5341 (1989).
[31] A. M. Gomez-Marín and J. M. Feliu, ChemSusChem 6:1091 (2013).
[32] V. S. Murthi, R. C. Urian, and S. Mukerjee, Journal of Physical Chemistry B 108:11011 (2004).
[33] K. L. Hsueh, D. T. Chin, and S. Srinivasan, Journal of Electroanalytical Chemistry 153:79 (1983).

Chapter 6: Oxygen reduction at heat treated Se modified Rh(111) surfaces and its morphology

6.1 Introduction:

Widespread utilization of the low temperature fuel cells is mainly hampered due to sluggish kinetics of the oxygen reduction reaction (ORR). The rational design of new catalysts is quite challenging. The need to improve the kinetics of the ORR has resulted in the production of materials such as near surface alloys (NSAs) with novel catalytic properties[1] These NSAs modify the electronic structure of the host metal. The main objective of using NSAs is to obtain stable and active catalysts for ORR which show tolerance to small organic molecule as well. Extensive efforts have been devoted to the development of the surface and the near surface alloys of a Pt single crystal surface with other metals, especially Ni and Cu, for designing improved electrocatalysts [2-4]. Others have attempted to generate NSAs of Pt on different late transition metals (Au, Pd, Ir, Rh, Ru, Re, or Os) and a combination of Pt and one of the late transition metal to investigate obtained alloys for ORR activity [5]. High temperature treatment may lead to alloy formation instead of epitaxial ordering of the adlayer.

Metal chalcogenides are binary compounds, which promote electrocatalysis in a selective manner such as the ORR process in the presence of small organic molecules. In literature, less is known about electrocatalytic activity of the Rhodium selenide for ORR and their methanol tolerance ability [6-9]. It was observed that chalcogenides are usually stripped off under fuel cell operating conditions [9]. Reductive dissolution of adsorbed selenium on metal electrode surface is a well-known phenomenon and demonstrated already for single crystalline Au [10, 11], polycrystalline Au [12] and polycrystalline Pt [13] in selenium containing solution. Also, the oxidative stripping of selenides from their respective metal selenides during fuel cell operation conditions pose a major issue for their wide spread use in fuel cell application.

Therefore, in our current work, we achieved up to 50 % surface coverage of Rh(111) by electrochemical deposition of Se. These modified surfaces were then heat treated at different temperatures using induction heating method to generate NSAs. These generated NSAs were characterized by oxidative stripping of adsorbed CO. Their ORR

activities were measured using a dual thin layer flow through cell (DTLFC) which is an alternative to a rotating ring disk electrode (RRDE) setup. The main advantage of using DTLFC for ORR studies is the ease of using single crystal surfaces. The surface morphologies of these NSAs were also compared with simple Se modified surfaces using STM.

6.2 Experimental:

The Rh(111) was prepared by annealing followed by cooling down in a mixture of Ar:H_2 (2:1) [14]. Rh(111) single crystal with a diameter of 10 mm was used (Kristallhandel Kelpin, Germany). All solutions were prepared from 18.2 MΩ Milli-Q water and de-aerated with high purity argon gas (99.999%). Electrochemical experiments in 0.1 M $HClO_4$ and 0.1 M H_2SO_4 (spectro pure grade) were carried out in a conventional three electrode H-cell in a hanging-meniscus configuration with a large Pt sheet as counter electrode. A reversible hydrogen electrode was employed as a reference electrode. Selenium submonolayer and multilayer deposits were produced in a similar H-cell containing 1 mM H_2SeO_3 (Analytical grade). A bi-potentiostat from Pine Instruments Inc. model AFBPC1 in combination with a user interface developed in Labview software was used for recording cyclic voltammograms (CV).

The selenium modified Rh(111) electrode was heated using an induction heating unit of Himmelwerk (model HU 2000) and the temperature was monitored using infrared thermometer. The ORR was performed using DLTFC, in which Rh(111) disc electrode was fixed in the upper compartment and Pt polycrystalline disc electrode placed in the lower compartment. Continuous supply of oxygen saturated 0.5 M $HClO_4$ was maintained using hydrostatic pressure of the electrolyte present in a glass supply bottle, which was connected to the inlet of the DTLFC. Different flow rates mainly 2.5, 5 and 10 μL/s were adjusted using rate of suction of plunger in the syringe pump and by adjusting revolution per minute movement of the peristaltic pump at the outlet. The STM measurements were performed with a Nanoscope III E controller (Digital Instruments, Santa Barbara, CA) and a commercially available STM scanner (Molecular Imaging) fitted with an electrochemical cell.

6.2.2 Heat treatment of Se modified Rh(111) electrode

The Rh(111) electrode surface was modified in H_2SeO_3 containing solution by sweeping the potential in negative direction. The modified surface was then thermally treated using an induction heating unit coupled with an infrared thermometer. A gas tight quartz glass tube holding the modified electrode was used for contamination free heating. The rate of heating is controlled by adjusting the high frequency power switch to a desired value using potentiometer (30 % of full scale). For precise control a foot switch is used to apply high frequency power and the temperature was monitored using digital infrared pyrometer with laser light to guide for exact positioning on target electrode (model KTRD 1075, make Himmelwerk Germany). A flow of inert gas argon or argon/hydrogen mixture was maintained during the process of heating (usually ~1 minute) and slow cooling down for about 5 minutes. An actual picture of the whole setup is shown in fig. 6.1.

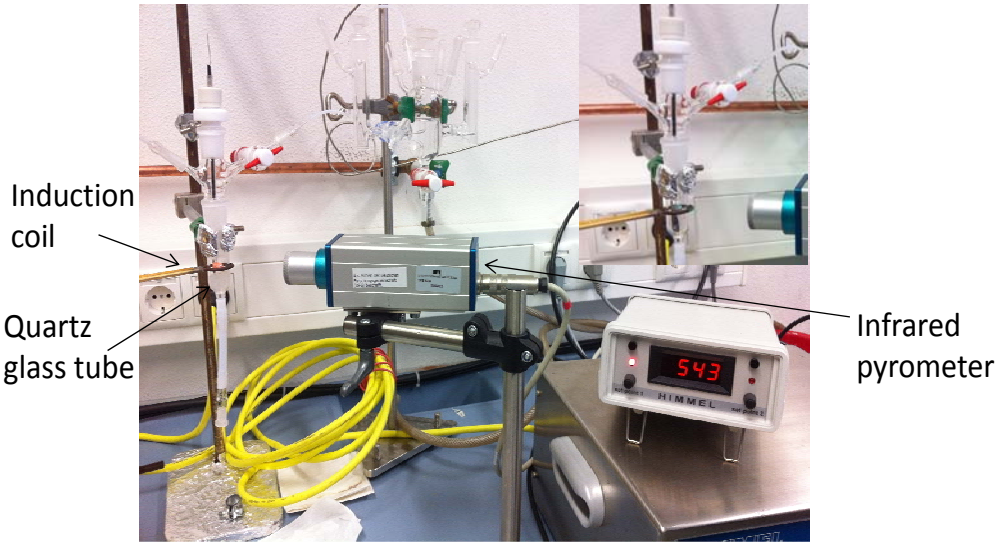

Figure 6.1: Actual setup of induction heating. Inset shows the close view of Quartz tube.

6.2.3 CO stripping

The surface area of the Se modified and NSAs of Se/Rh(111) surfaces was determined by CO stripping experiment. The CO was adsorbed on these surfaces at a potential of 0.1 V vs RHE by injecting 3 ml of CO saturated solution into the Ar saturated 0.1 M $HClO_4$. The CO was allowed to adsorb on these surfaces by closing off the Ar gas supply. While maintaining a hanging meniscus contact the Ar was purged gently through the solution to remove excess CO from the bulk. Finally, the oxidative stripping of the CO was performed by cycling the potential between 0.1 to 0.9 V vs. RHE.

6.3 Results and discussions

6.3.1 CO characterization of Se modified Rh(111) and its NSAs

The cyclic voltammogram for pure Rh(111) together with its Se modification using 1 mM selenous acid is shown in fig. 6.2. The surface characterization of heat treated (inductive heating to 310°C) selenium modified surface was performed by CO stripping and selenium oxidation experiments. The coverage of selenium before heat treatment was calculated by integrating the Se deposition curve from 0.9 V till 0.54 V in the cathodic direction. After performing background correction (subtraction of the double layer charge), deposited charge corresponds to a surface coverage of $\vartheta = 0.42$ assuming a four electron reduction.

Figure 6.2: CVs of Rh(111) (-----) and its Se modification (——) from 1mM H_2SeO_3 sweep rate 50 mVs^{-1}.

The oxidative stripping of CO on heat treated Se/Rh(111) is shown in fig. 6.3a. The CV clearly shows that the onset of CO oxidation started around 0.57 V with a maximum at 0.62 V followed by a broad shoulder peak at 0.72 V. The complete oxidation of CO on this modified surface was achieved in the first cycle. This is different from the case of the CO oxidation on a pure Rh(111) surface where a small but clear oxidation peak is also observed in the second sweep [15]. The calculated charge of CO oxidation (after background correction, substraction of the double layer) accounts for about 11 % free Rh(111) surface, the rest was blocked/covered by selenium adatoms or Se incorporated into the surface.

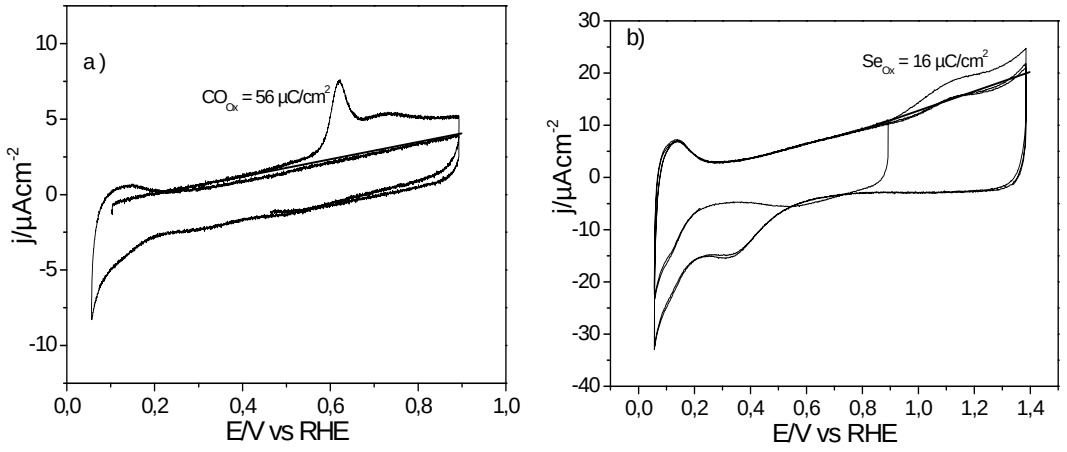

Figure 6.3: a) CVs for the CO oxidation at sweep rate of 10 mV/s and b) selenium oxidation on heat treated Se/Rh(111) surface with initial Se coverage of $\vartheta = 0.42$ in 0.1

M $HClO_4$, sweep rate of 50 mV/s.

In order to get some indication about the status of the adsorbed Se after heat treatment oxidative stripping of the selenium was performed. The oxidative stripping of selenium resulted in a broad peak starting around 1.0 V and ended at 1.23 V vs RHE as shown in fig. 6.3b. The calculated charge after background correction accounts for only 2 % in the first cycle. This suggests that most of the selenium enters into rhodium via place exchange mechanism or form alloy with Rh(111). However, we can't exclude the sublimation of adsorbed selenium due to the heat treatment. For detailed investigation XPS measurement would be helpful.

Interestingly, the total oxidation charge on this modified surface between 0.2 to 1.37 V only amounts to 74 μC cm^{-2}, as opposed to 430 μC cm^{-2} on the clean Rh(111) surface or 4.07 mC cm^{-2} on polycrystalline Rh. This demonstrate the inhibition of oxygen adsorption by Se modification. The justification of our assumption about place exchange or alloy formation was further strengthened by performing another similar set of experiment of Se adsorption on Rh(111), without heat treatment.

The oxidative stripping of adsorbed CO resulted in three times lower coverage coverage; differently from the heat treated surface the selenium stripping charge was in close agreement with the deposited charge as shown in fig. 6.4b. This clearly indicates that heat treatment results in either alloy formation or place exchange of selenium adatoms with rhodium surface atoms.

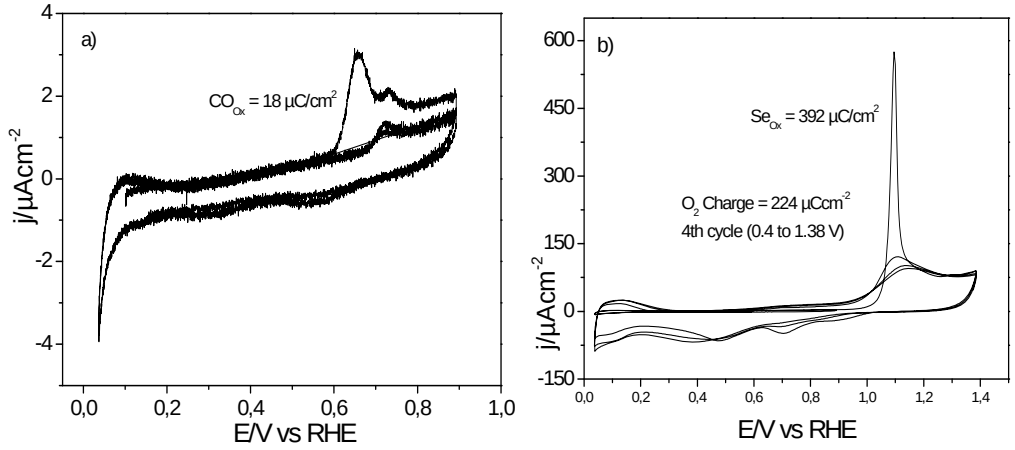

Figure 6.4: a) CVs for the CO oxidation at sweep rate of 10 mV/s and b) selenium

oxidation on Se/Rh(111) surface without heat treatment with initial Se coverage of $\vartheta = 0.44$ in 0.1 M $HClO_4$, sweep rate of 50 mV/s.

As observed in chapter 3, Rh(111) surface modified with Se having surface coverage of around $\vartheta = 0.1$ was found to be active for ORR than pure Rh(111) surface and also shows better tolerance to CO molecules. Therefore, another set of experiments was performed with the intention to deposit submonolayer selenium coverages. In the first set of experiments, a selenium coverage of approximately $\vartheta = 0.23$ was achieved on Rh(111) as shown in fig. 6.5. The modified surface was heat treated till 310 °C under continuous argon flow and then the surface was characterized again by oxidative CO and selenium stripping. The calculated CO stripping charge was comparable to that of a pure Rh(111) surface indicates that due to heat treatment most of the selenium either sublimes or makes place exchange with rhodium. This was also confirmed from selenium oxidation, which does not lead to visible features of a stripping peak (fig. 6.6b) (oxidation charge not more than 10 µC cm^{-2}). On the other hand, adsorbed CO is completely oxidized in the first sweep (differently from clean Rh(111)) and the hydroxide peaks at 0.63 V indicating of the clean Rh(111) are visible (fig. 6.6a), but much less sharp than would be expected after CO stripping from clean Rh(111).

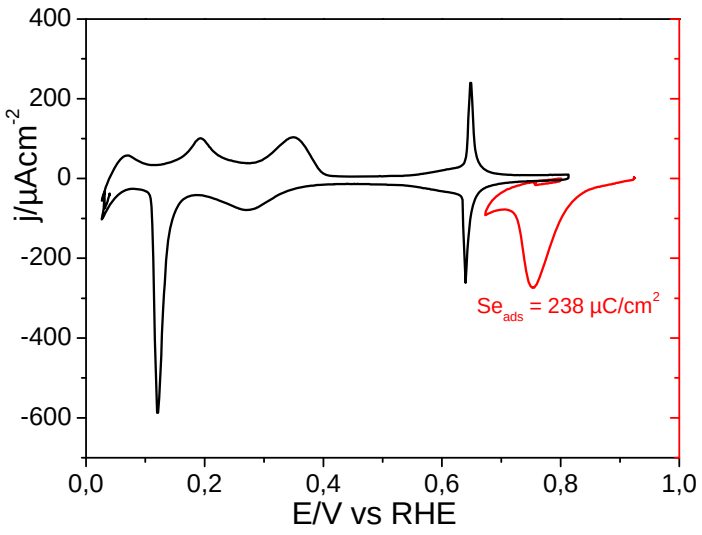

Figure 6.5: CVs of Rh(111) (-----) and its Se modification (——) from 1mM H_2SeO_3 sweep rate 50 mVs^{-1}.

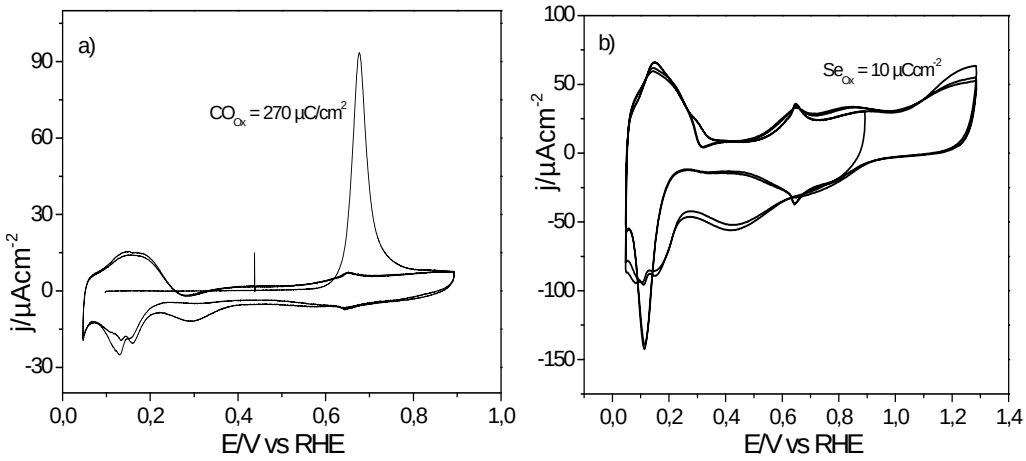

Figure 6.6: a) CVs for the CO oxidation at sweep rate of 10 mV/s and b) selenium oxidation on heat treated Se/Rh(111) surface with initial Se coverage of $\vartheta = 0.23$ in 0.1 M $HClO_4$, sweep rate of 50 mV/s.

In another experiment, the same coverage of selenium on Rh(111) surface was achieved as before, however, heat treatment was avoided. The modified surface was then characterized by the oxidative CO and Se stripping experiments as shown in fig. 6.7. The calculated CO stripping charge indicates that most of the surface was covered with selenium, which was also confirmed from the oxidative stripping of selenium. The calculated selenium stripping charge was comparable to that of deposited selenium. These set of experiment clearly indicates that heat treatment leads to change in surface morphology.

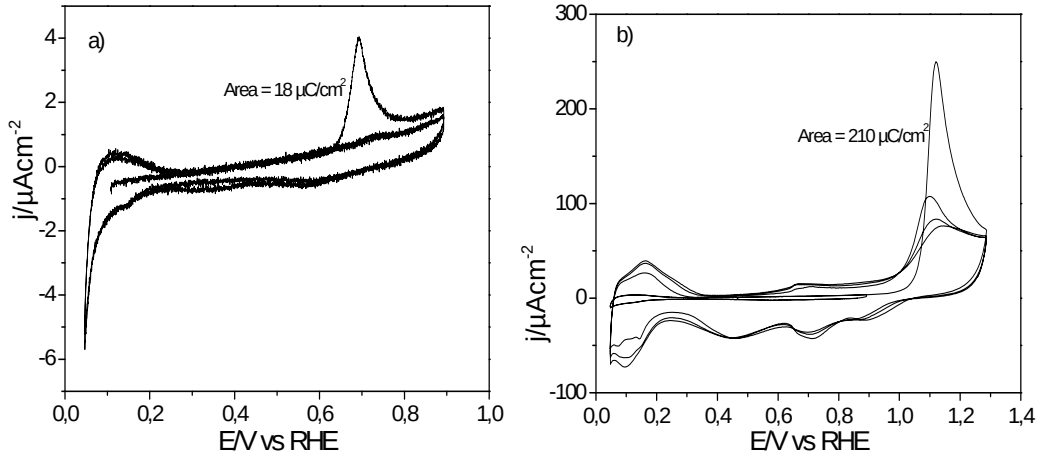

Figure 6.7: a) CVs for the CO oxidation at sweep rate of 10 mV/s and b) selenium oxidation on Se/Rh(111) surface without heat treatment with initial Se coverage of $\vartheta = 0.24$ in 0.1 M $HClO_4$, sweep rate of 50 mV/s.

6.3.2 ORR activity of heat treated Se/Rh(111)

The ORR catalytic activity of the Se modified heat treated surfaces as discussed above were performed using dual thin layer flow through cell (DTLFC) (details about this setup was already explained in chapter 5). In the first case the current-potential profiles of the Se modified heat treated surface with initial surface coverage of about $\vartheta = 0.42$ at various flow rates (2.5, 5 & 10 µL/s), which is controlled by a syringe pump and corresponding second electrode held at 1.2 V are shown in fig. 6.8. The reduction of oxygen started at around 0.85 V and increased continuously on scanning the potential negatively till 0.45 V vs RHE (The diffusion limited current achieved around 0.45V).

The Tafel plot and hydrogen peroxide generation for diffusion limited currents at flow rate of 2.5 µL/s are also shown in fig. 6.9.

A Tafel slope of around 120 mV/dec obtained from a plot of kinetic currents ($I_{kin} = (I_{lim} \cdot I) \cdot (I_{lim} - I)$) as a function of potential between (0.7-0.8 V) and a much higher value of 160 mV/dec was determined for (0.5 till 0.7V) region [16].
The low current at the polycrystalline Pt disc electrode held at 1.2 V corresponds to an amount of H_2O_2 in the range of 0~10 % between 0 to 0.7 V. The percentage yield of H_2O_2 was calculated using following equation [17]

$$X(H_2O_2) = \frac{(2 \cdot I_R / N)}{((I_D + I_R)/N)} \qquad 6.1$$

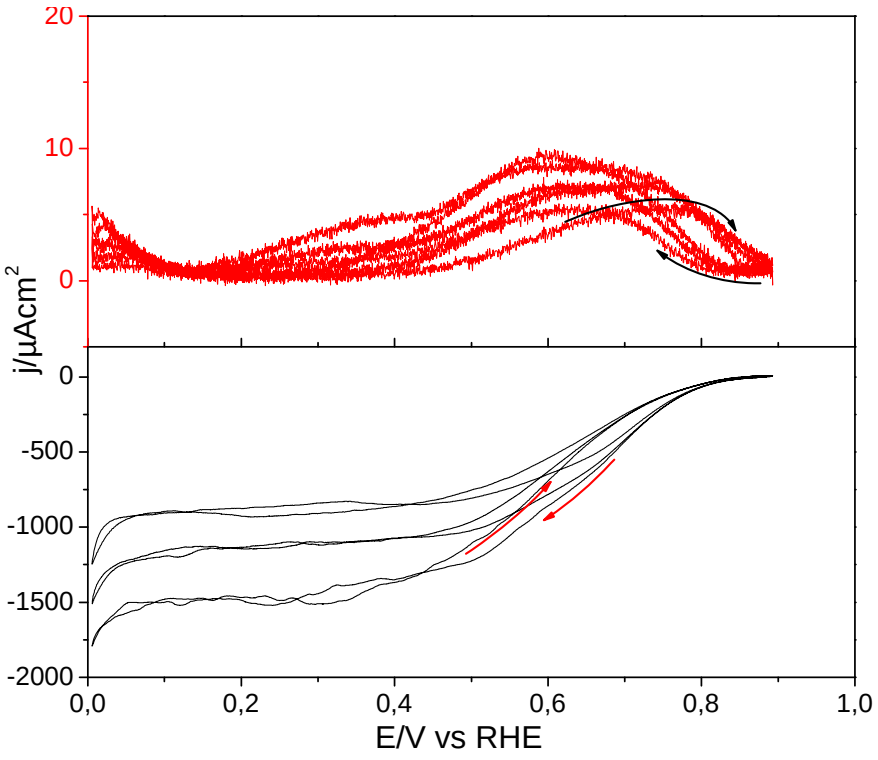

Figure 6.8: Simultaneously recorded CVs of heat treated Se modified Rh(111) (——) and related current signals on a polycrystalline Pt (——) held at 1.2 V in DTLC containing oxygen saturated 0.5 M $HClO_4$ for various flow rates of 2.5, 5 & 10 µL/s respectively at sweep rate of 10 mV/s.

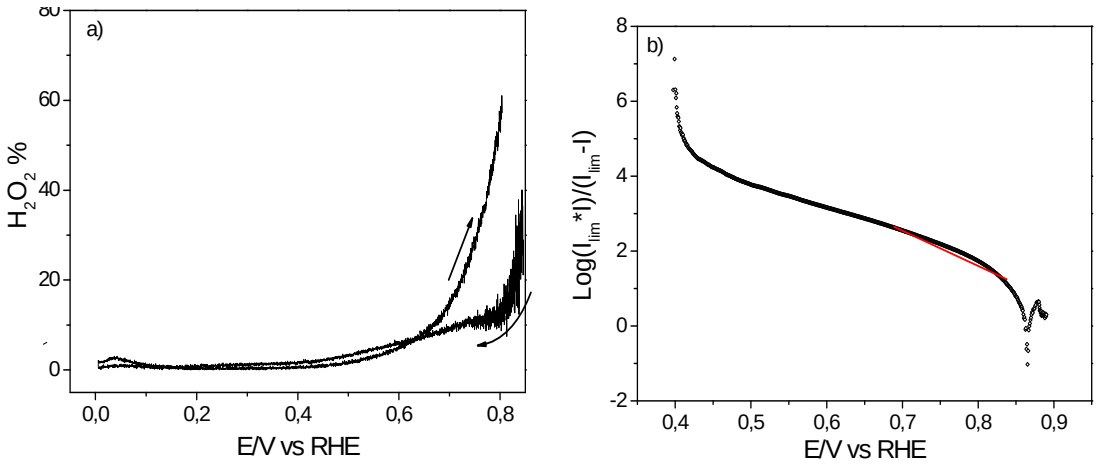

Figure 6.9: a): H_2O_2 production as a function of the electrode potential, b): Capacitive current corrected Tafel plots for heat treated Se modified Rh(111) surface.

Similarly the heat treated Se modified electrode with initial surface coverage of around $\vartheta = 0.23$ was also subjected to ORR studies and current potential profiles were obtained as shown in fig. 6.10. The Tafel plot and H_2O_2 detected are shown in fig. 6.11.

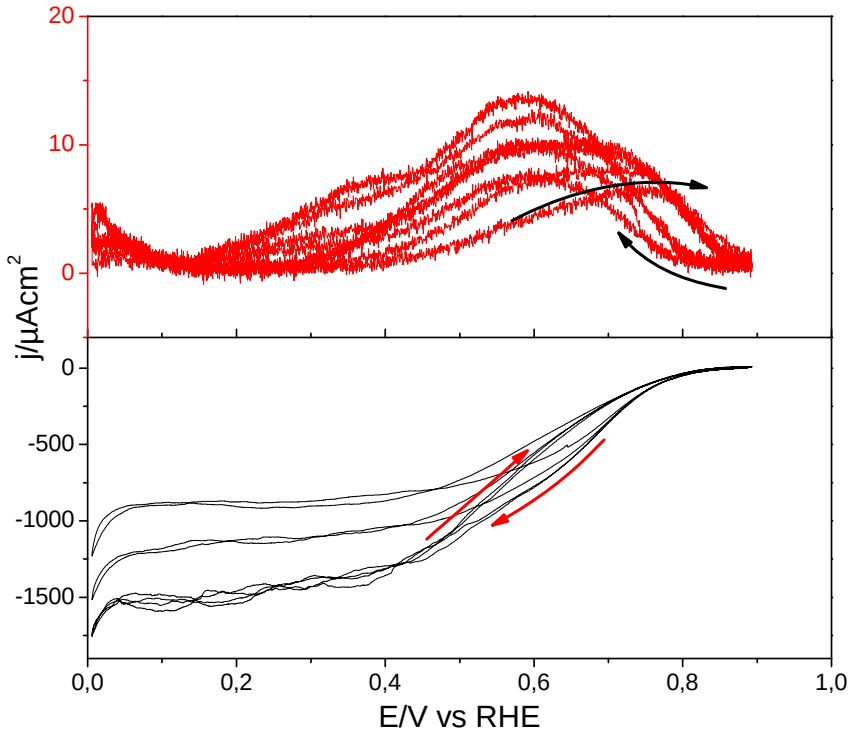

Figure 6.10: Simultaneously recorded CVs of heat treated Se modified Rh(111) (——) and related current signals on a polycrystalline Pt (——) held at 1.2 V in DTLC containing oxygen saturated 0.5 M $HClO_4$ for various flow rates of 2.5, 5 & 10 µL/s respectively at sweep rate of 10 mV/s.

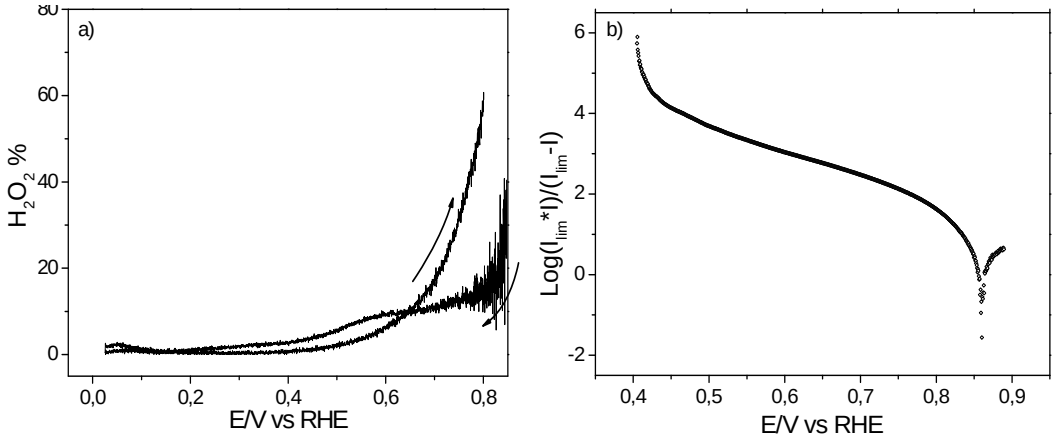

Figure 6.11: a): H_2O_2 production as a function of the electrode potential, b): Capacitive current corrected Tafel plots for heat treated Se modified Rh(111) surface.

A comparison of ORR activity for the heat treated Se/Rh(111) surfaces with that of pure Rh(111) and polycrystalline platinum is presented in fig. 6.12. This clearly shows that the ORR activities of heat treated Se/Rh(111) surfaces were better than that of pure Rh(111). In addition, heat treated surfaces with selenium coverages approximately $\vartheta = 0.42$ and approx. $\vartheta = 0.23$ shows equal activity for ORR despite of the different

amounts of the adsorbable CO (cf. fig. 6.3a & 6.6a).

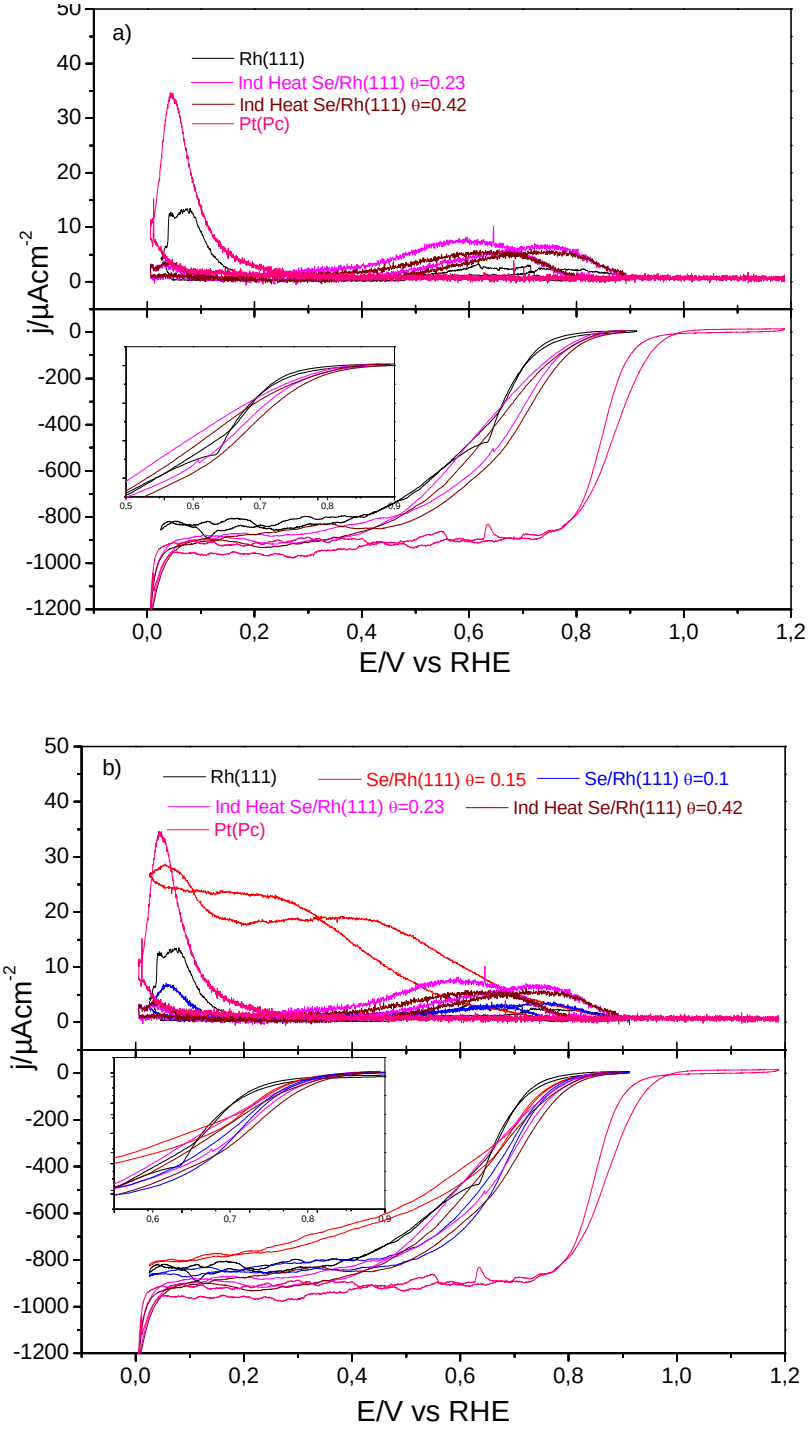

Figure 6.12: Simultaneously recorded CVs of heat treated Se/Rh(111) and pure Rh(111) a) and heat treated Se/Rh(111), simple Se modified Rh(111), pure Rh(111) and Pt(Pc) b) in the first compartment and related current signals on a polycrystalline Pt held at 1.2 V in the second compartment of the in DTLC containing oxygen saturated 0.5 M $HClO_4$ at 2.5 µL/s. υ = 10 mV/s. Inset shows the reduction currents.

It is quite interesting to notice that the heat treated Se modified surfaces behave similarly to that of polycrystalline Pt surface at more negative potentials with large

negative currents showing generation of hydrogen. Quite surprisingly, the oxidation of the generated hydrogen is very small as compared to that observed on Pt(Pc) and Rh(111) surfaces. The main advantage of heat treated Se/Rh(111) surfaces seems to be that the surface is a bit more stable and active for ORR catalysis.

6.3.3 Surface morphology of heat treated Se/Rh(111)

The heat treated Se/Rh(111) surface not only exhibit better ORR activity but also possesses improved stability than that of the pure Rh(111) and also for the Se modified surfaces without heat treatment (already discussed in chapter 5). In order to get further insight into the surface morphologies of these modified surfaces, in situ STM measurements were performed. Scanning tunnelling microscopy provides insight into the surface structure of metal surfaces and adlayers which is crucial for understanding electrochemical behaviour. STM images were obtained for approximately $\vartheta = 0.5$ coverage of Se on Rh(111) under electrochemical conditions with and without induction heat treatment at various temperatures. Figure 6.13 shows a STM image of Se modified Rh(111) surface with the corresponding CV indicating the substrate preparation and Se modification. The steps are totally covered with adsorbed selenium and some selenium islands are also present on terraces. The purpose of presenting this figure is to establish a comparison of a simple electrochemically prepared surface with that of the heat treated selenium modified surface.

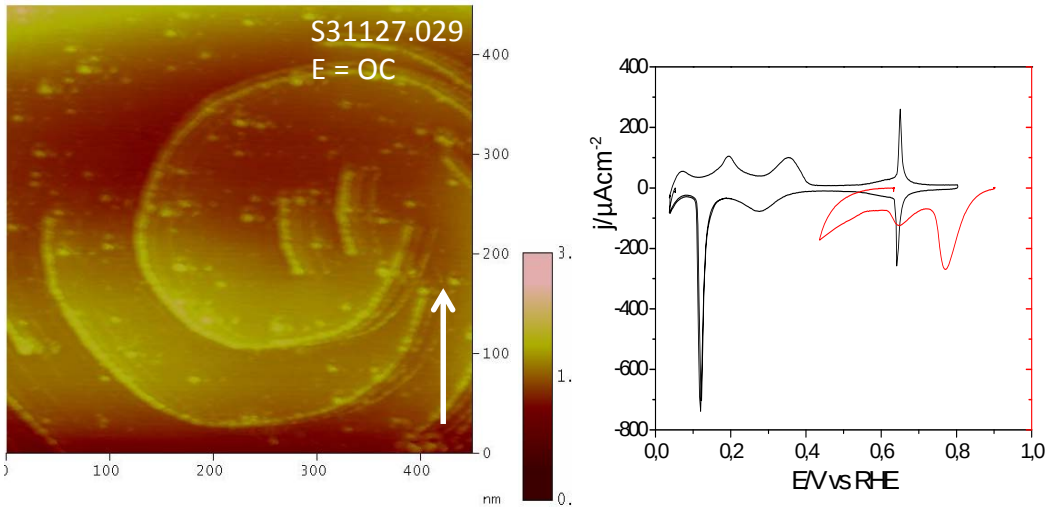

Figure 6.13: Topographic STM image of Se modified Rh(111) in 0.1 M $HClO_4$ at E = open circuit, with corresponding CV for surface preparation and Se modification. Set point =0.6 nA, sample bias= 15 mV

The STM image of the heat treated selenium modified surface with initial surface coverage of approximately $\vartheta = 0.5$ is shown in fig. 6.14. An atomically smooth and well ordered surface albeit with many monoatomic steps is thus generated.

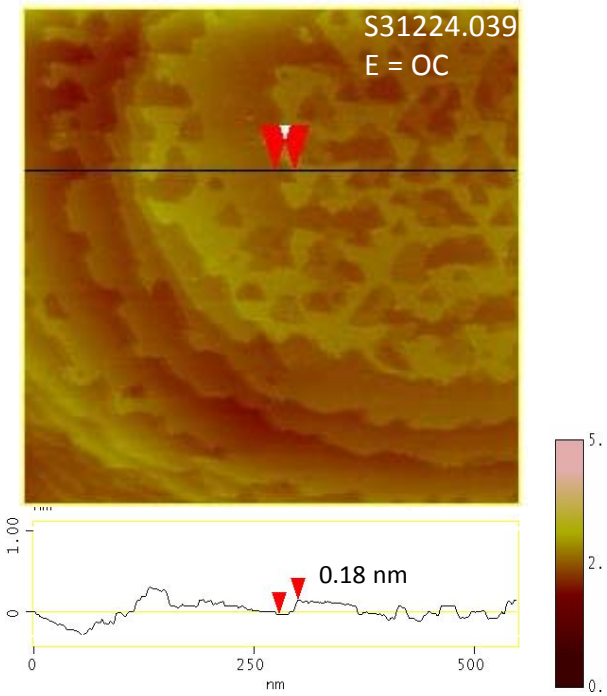

Figure 6.14: Topographic STM image of Se modified Rh(111) after inductively heated till 310 °C in 0.1 M $HClO_4$ at E = open circuit. Set point =0.7 nA, sample bias= 20 mV

6.3.4 Potential dependent stability

The ORR activity of these surfaces were measured in a potential range of 0 to 0.9 V vs RHE, therefore, the stability of these surfaces were monitored in situ for the same range of potential as shown in fig. 6.15. The potential was scanned in this region to avoid oxidation of selenium. Two consecutive STM images (fig. 6.15A) and B)) were taken while the potential was scanned in the region of ORR activity and no observable changes in the surface morphology were found (this is different for Se modified surfaces without heat treatment see chapter 3). However, once the potential window was extended till oxidation of selenium at 1.05 V vs RHE. STM image fig. 6.15C) only a blurred structure is seen, which was restored again at negative potential as shown in image fig. 6.15D) along with corresponding in situ CV. Even at higher oxidation potentials, some Se stripped off the surface which redeposit at negative potentials. The surface appears then smooth and better ordered.

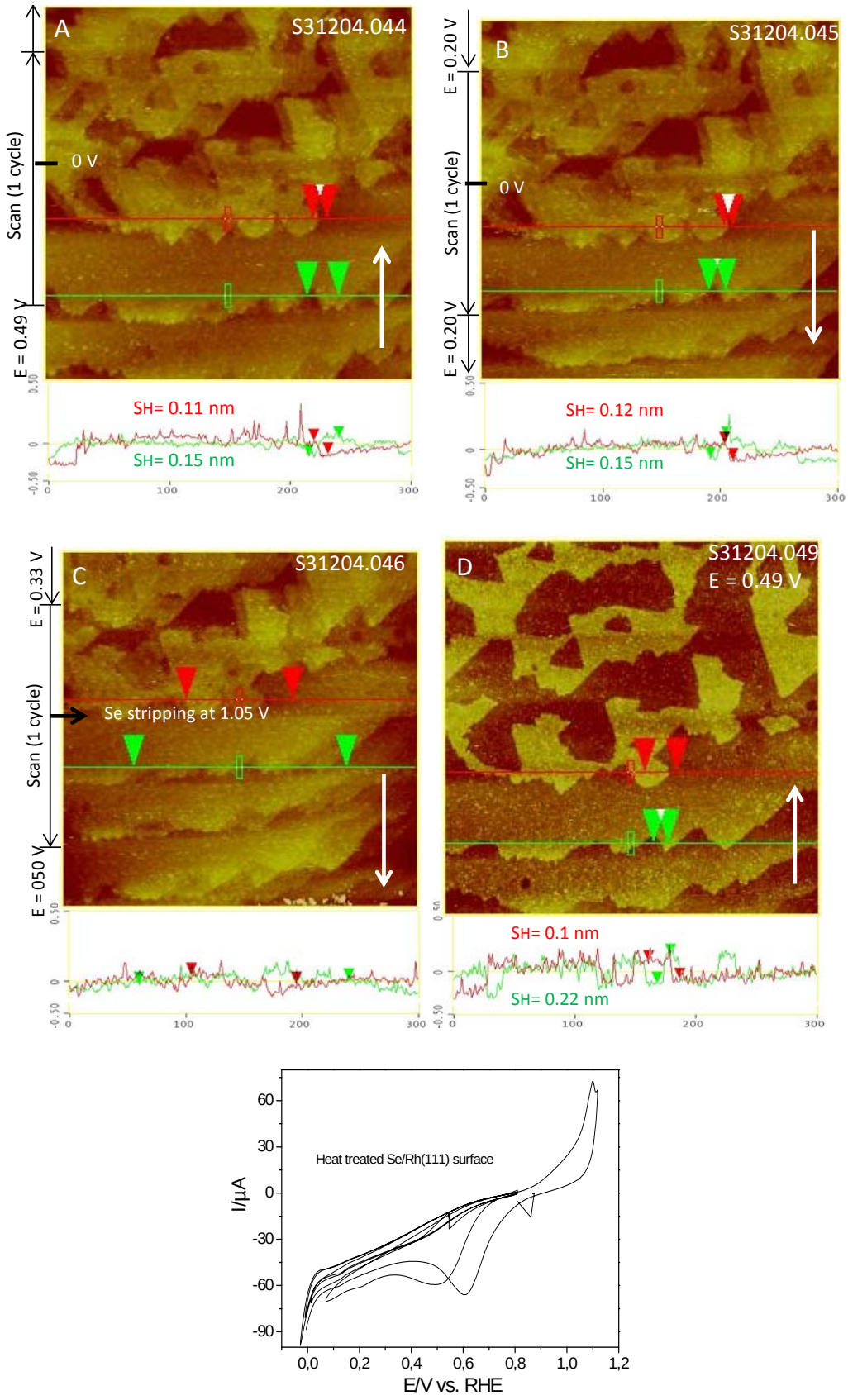

Figure 6.15: Topographic STM image of Se modified Rh(111) after inductively heated till 310 °C in 0.1 M $HClO_4$ with corresponding CV for potential dependence studies, sweep rate 50 mV/s. Set point =0.7 nA, sample bias= 20 mV. Line by line correction is used for above images.

6.3.4 Stability in air

In another set of experiment, a freshly prepared surface was examined in air in order to check the stability of the NSAs. It is well known that selenium protects the underlying metal core from oxidation [18]. We also observed that the selenium adlayer stabilizes the surface, and the surface appears similar to one under potential control as shown in fig. 6.16 for two examples.

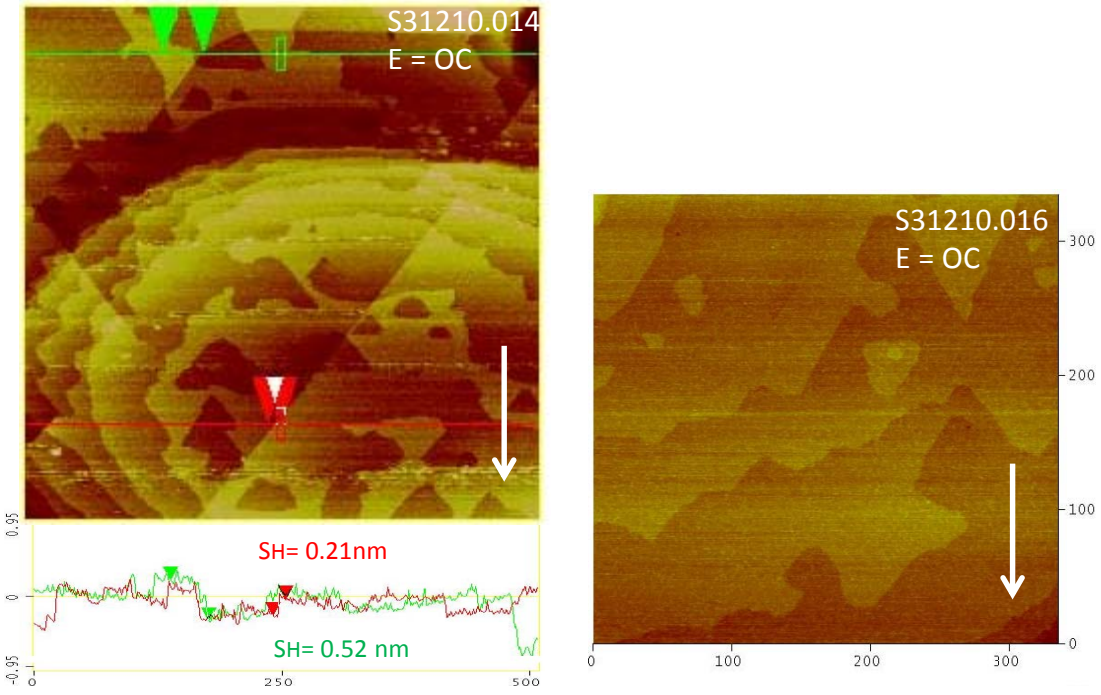

Figure 6.16: Topographic STM image of Se modified Rh(111) after inductively heated in air, Set point =0.6 nA, sample bias= 20 mV.

6.3.5 Effect of temperature on surface morphology

The temperature of the heat treatment was varied and its effects on surface morphologies were observed. The systematic and atomically smooth epitaxial restructuring was observed for surfaces heat treated at approx. 310 °C as discussed above. The other temperatures explored were approx. 400 and 150 °C. In the former case the temperature was enhanced to ~ 400 °C, which results in smooth and roughened multilayer structure. Multilayered structure STM topographic image along with 3D image was presented in fig. 6.17. At high temperature alloy formation may occur. The other possibility is the place exchange of Se with Rh atoms, which is also evident from the hydrogen adsorption/desorption features appeared on heat treated surface from in situ STM CV as shown in fig. 6.18.

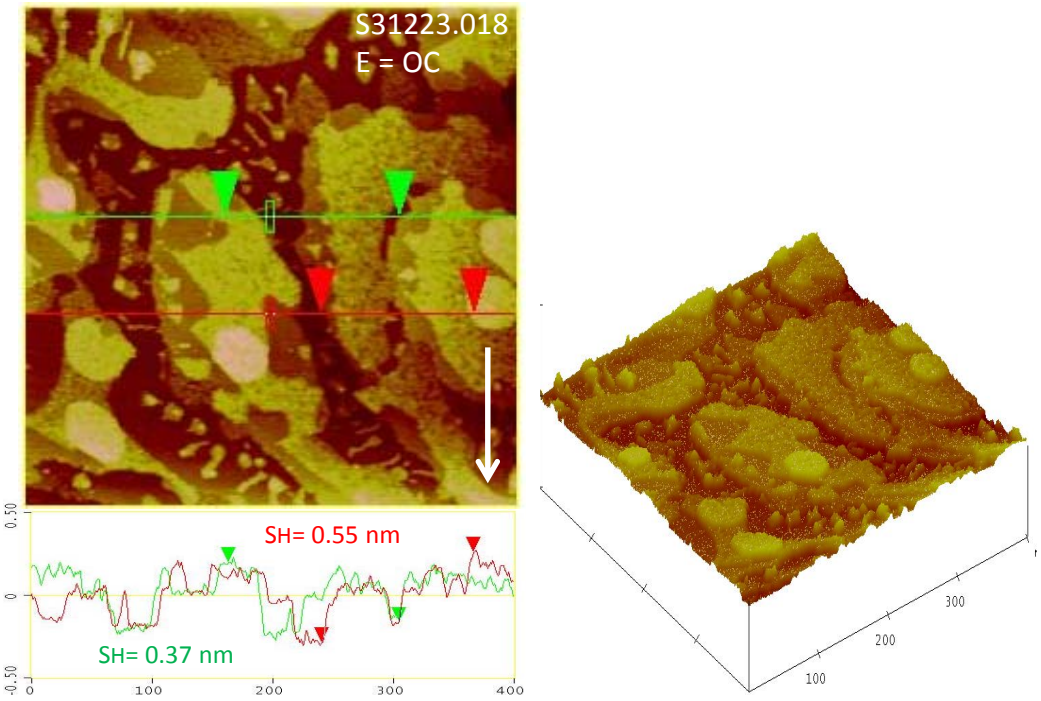

Figure 6.17: Topographic STM image of Se modified Rh(111) together with 3D image after inductively heated till ~410 °C in 0.1 M $HClO_4$ at E = open circuit, Set point =0.65 nA, sample bias= 20 mV.

During in situ potential scanning results in disappearance of roughed patches and resolution of the images becomes poorer. At more positive potentials selenium starts oxidizing, however, the structure prevailed and redeposited at more negative potentials. This results in smooth surface without roughed patches.

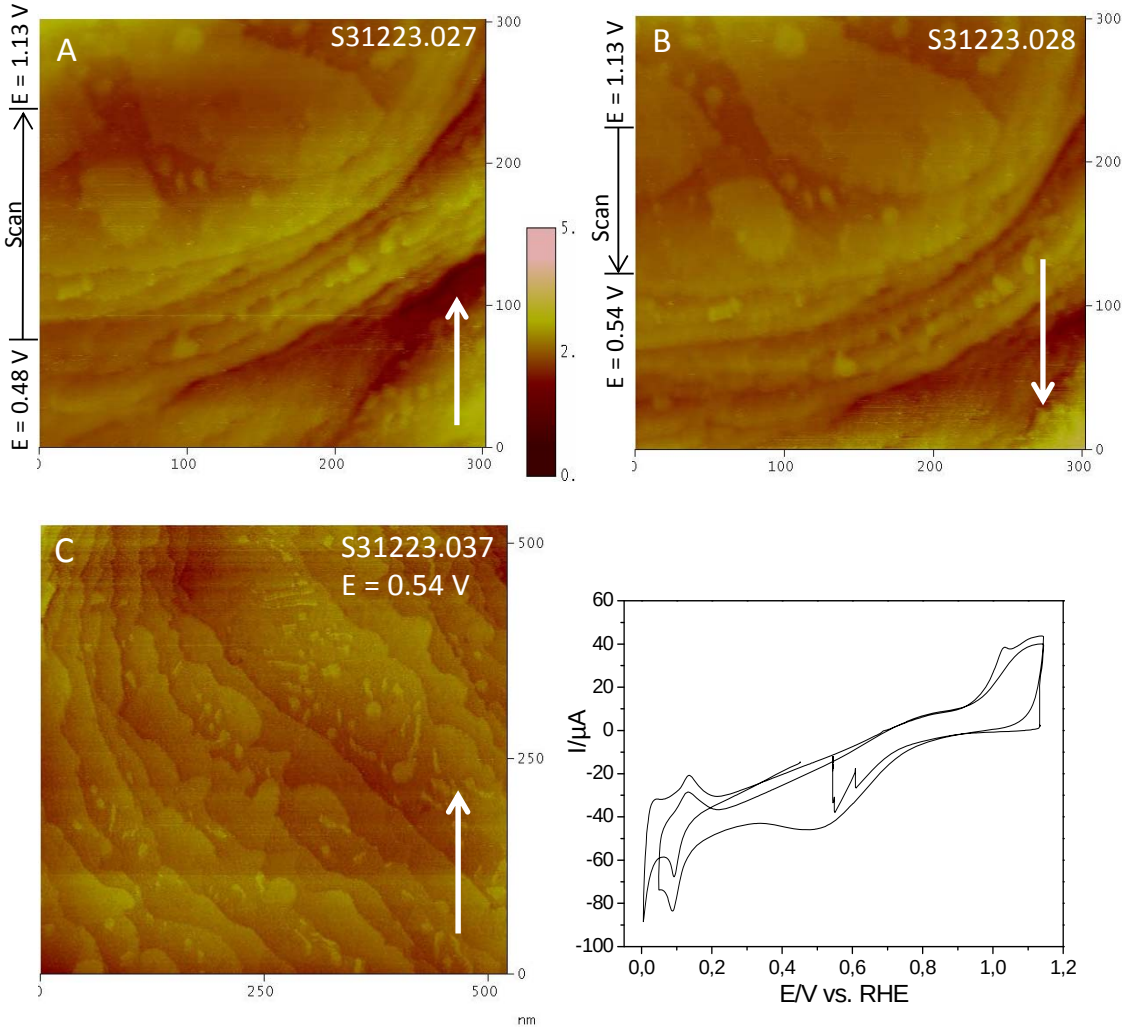

Figure 6.18: Topographic STM image of Se modified Rh(111) after inductively heated till 410 °C in 0.1 M $HClO_4$ with corresponding CV for potential dependence studies. Set point =0.65 nA, sample bias= 20 mV.

A lower temperature treatment produced poorly arranged adlayer deposits on the surface and was not explored further. A topographic STM image of heat treated Se modified surface ~ 150 °C was shown in fig. 6.19.

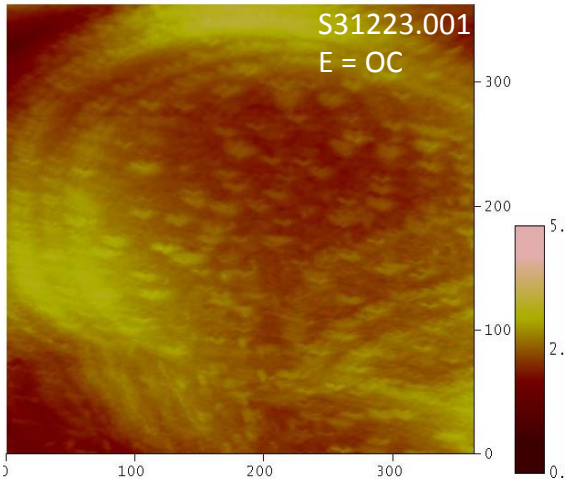

Figure 6.19: Topographic STM image of Se modified Rh(111) after inductively heated till ~150 °C.

6.4 Conclusions

This chapter focused on the effect of heat treatment of Se/Rh(111) surfaces on their ORR activity and morphological features. The generated NSAs showed better ORR activity as compared to simple electrochemical modified (chapter 5) and pure Rh(111) having better tolerance to CO. The heat treated Se/Rh(111) with initial Se coverage of $\vartheta = 0.42$ not only showed tolerance to CO but also showed improved activity for ORR as compared to electrochemically modified Se/Rh(111) surfaces with a surface coverage of $\vartheta = 0.1$. This enhanced ORR activity of heat treated surfaces might be due to the surface alloy formation. Additionally, the surface morphologies of heat treated surfaces resulted in atomically smooth deposits, which remained stable under potential window used for ORR studies. Even at higher oxidation potentials, some Se stripped off the surface which redeposit at negative potentials.

References

[1] J. A. Rodriguez and D. W. Goodman, Science 257:897 (1992).
[2] V. R. Stamenkovic, B. Fowler, B. S. Mun, G. Wang, P. N. Ross, C. A. Lucas, and N. M. Markovic, Science 315:493 (2007).
[3] J. Tymoczko, W. Schuhmann, and A. S. Bandarenka, ChemElectroChem 1:213 (2014).
[4] A. S. Bandarenka, A. S. Varela, M. Karamad, F. Calle-Vallejo, L. Bech, F. J. Perez-Alonso, J. Rossmeisl, I. E. L. Stephens, and I. Chorkendorff, Angewandte Chemie International Edition 51:11845 (2012).
[5] A. Nilekar, Y. Xu, J. Zhang, M. Vukmirovic, K. Sasaki, R. Adzic, and M. Mavrikakis, Topics in Catalysis 46:276 (2007).
[6] D. Cao, A. Wieckowski, J. Inukai, and N. Alonso-Vante, Journal of The Electrochemical Society 153:A869 (2006).
[7] J. M. Ziegelbauer, D. Gatewood, A. F. GullaÌ , M. J. F. Guinel, F. Ernst, D. E. Ramaker, and S. Mukerjee, The Journal of Physical Chemistry C 113:6955 (2009).
[8] M. Neergat, V. G. and, and R. K. Singh, Journal of Electrochemical Society 158:7 (2011).
[9] D. C. Papageorgopoulos, F. Liu, and O. Conrad, Electrochimica Acta 53:1037 (2007).
[10] M. Alanyalioglu, U. Demir, and C. Shannon, Journal of Electroanalytical Chemistry 561:21 (2004).
[11] T. E. Lister and J. L. Stickney, Journal of Physical Chemistry 100:19568 (1996).
[12] M. F. Cabral, V. A. Pedrosa, and S. A. S. Machado, Electrochimica Acta 55:1184 (2010).
[13] M. C. Santos and S. A. S. Machado, Journal of Electroanalytical Chemistry 567:203 (2004).
[14] J. Clavilier, M. Wasberg, M. Petit, and L. H. Klein, Journal of Electroanalytical Chemistry 374:123 (1994).
[15] T. H. M. Housmans and M. T. M. Koper, Electrochemistry Communications 7:581 (2005).
[16] K. L. Hsueh, D. T. Chin, and S. Srinivasan, Journal of Electroanalytical Chemistry 153:79 (1983).
[17] V. S. Murthi, R. C. Urian, and S. Mukerjee, Journal of Physical Chemistry B 108:11011 (2004).
[18] F. Dassenoy, W. Vogel, and N. S. Alonso-Vante, The Journal of Physical Chemistry B 106:12152 (2002).

Chapter 7: Friction studies

7.1 Importance of friction on selenium modified fcc(111) surface

In this chapter, friction studies on metal chalcogenides model surfaces were discussed. The main objective is to get fundamental level of information about these modified surfaces. Furthermore, the influnce of friction due to the presence of foreign metal adlayers and anions at working electrodes, and the influnce of potential control on normal force and interaction of the cantilever with the adsorbed adlayer are explored.

7.1.1 Introduction:

Friction is an important process in our daily lives which exist between two bodies interacting with each other. It is advantageous in some cases and disadvantageous in others. In general friction opposes movement, makes a moving thing to stop and during this process energy is dissipated. Despite the discovery of this phenomenon by Leonardo da Vinci in the sixteenth century, it is still least understood in the processes at the atomic scale [1]. Friction in rough interfaces such as plastic dislocation and scratching results in the reordering of the inter-atomic bonds which causes heat dissipation. However, in case of smooth or weakly interacting surfaces, energy dissipation from macroscopic (bodies in contact) to microscopic (phonons or electronic excitation) occurs. A considerable development was made in determining the frictional force at the atomic level, which helps in familiarization of the related microscopic mechanism [2]. This is feasible with enhanced refinement in available and developing techniques and the use of model surfaces which are flat at atomic scale. Moreover, parallel developments of experimental and theoretical approaches pave the way for better understanding of these micro scale processes.

Investigations at surfaces performed under electrochemical conditions offer some advantages in comparison to those performed under ultra high vacuum (UHV) conditions; simply by varying the potential of the working electrode, the electrode surface can quickly and reversibly be modified by adsorption of a foreign metal or other substances, while the degree of unwanted contamination can be kept as low as under UHV conditions.

7.1.2 Experimental:

Preparation and modification of massive single crystal electrodes with Se

The usual annealing process followed by cooling down in argon atmosphere was successfully used for the preparation of Pt(111) and Au(111) was also used for Rh(111) electrode using a mixture of Ar:H_2 (2:1) gas as described elsewhere [3-5]. Rh(111), Pt(111) and Au(111) single crystal electrodes with a diameter of 10 mm were used (Kristallhandel Kelpin, Germany, Goodfellow UK and Mateck Germany). All solutions were prepared from 18.2 MΩ Milli-Q water and de-aerated with high purity argon gas (99.999%).

Electrochemical experiments in 0.1 M $HClO_4$ and 0.1 M H_2SO_4 (spectro pure grade) were carried out in a conventional three electrode H-cell in a hanging-meniscus configuration with a large Pt sheet as counter electrode. A Reversible hydrogen electrode was employed as a reference electrode. Selenium submonolayer and multilayer deposits were produced in a similar H-cell containing 1 mM H_2SeO_3 (Analytical grade). A bi-potentiostat from Pine Instruments Inc. model AFBPC1 in combination with a user interface developed in Labview software was used for recording cyclic voltammograms (CV).

All AFM measurements were performed with a Nanoscope III E controller (Digital Instruments, Santa Barbara, CA) and a commercially available STM and AFM scanner (Molecular Imaging) fitted with an electrochemical cell. A Pt wire was used as the counter electrode and as quasi-reversible reference electrode. All potentials were converted to the reversible hydrogen electrode. It was immersed in the same solution separated from the STM cell by a capillary. All AFM experiments were performed with soft cantilevers: n+-doped Si cantilever by Nanosensors (PPP-CONT-10), k = 0.09 N/m and Si cantilevers (Vecco MP31100) with k = 0.65 N/m. For quantitative estimation of frictional forces in atomic force microscopy, the output voltage signal of the photodiode has to be converted to force using the torsional spring constant of the cantilever. The torsional force constant was determined via Sader's method [6] and found to be 50 N/m and 190 N/m respectively [7]. This method is based on the measurement of the resonant frequency and quality factor of the cantilever. For atomic stick slip analysis ASCII data was extracted from both trace and retrace AFM image using GWYDDION

(http://gwyddion.net/) free ware software and obtained data process using ORIGIN software.

7.1.3 Results and Discussion:

7.1.3.1 Friction on a pure Rh(111)

The friction studies were performed on a pure rhodium single crystal in weakly absorbing electrolyte ($HClO_4$) and strongly absorbing electrolyte (H_2SO_4). The CVs for Rh(111) in the AFM cell in 0.1 M $HClO_4$ and also in 0.1 M H_2SO_4 are shown in fig. 7.1.1. These CVs clearly shows the cleaniliness of the setup used.

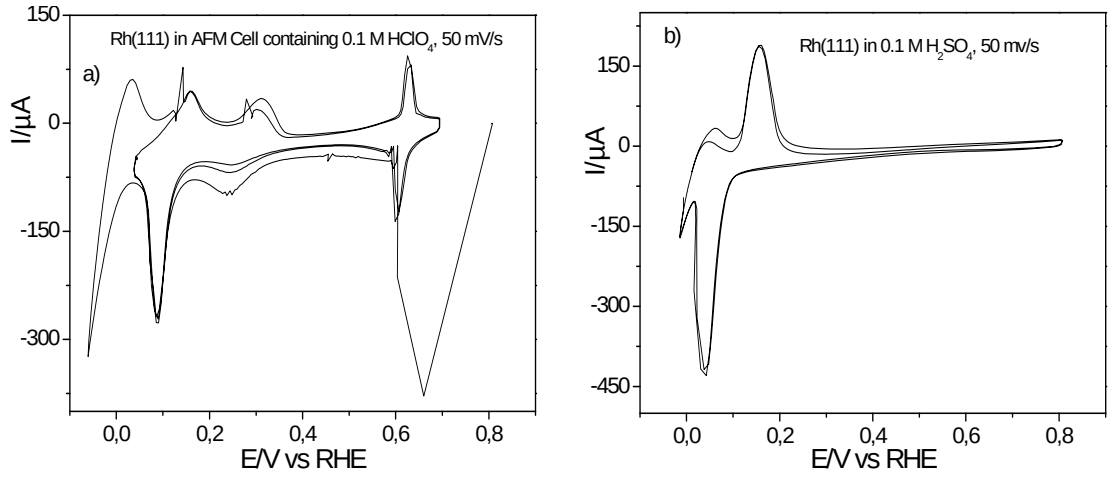

Figure 7.1.1: a) CVs for Rh(111) in 0.1 M $HClO_4$, and b) in 0.1 M H_2SO_4 at sweep rate of 50 mV/s, in the AFM cell.

A typical topograghic AFM image of Rh(111) in 0.1 M $HClO_4$ under potential control (0.05 V vs RHE) with monoatomic steps of height around 0.3 nm is shown in fig. 7.1.2A. The corresponding friction trace image (B), friction retrace image (C) and difference fircion image (D) of the above topographic images are also shown. Moreover, AFM topographic along with friction trace, retrace and friction difference images in 0.1 M H_2SO_4 is also shown in fig. 7.1.3. Due to adsroption of contaminants, it is difficult to get images with good resoltion.

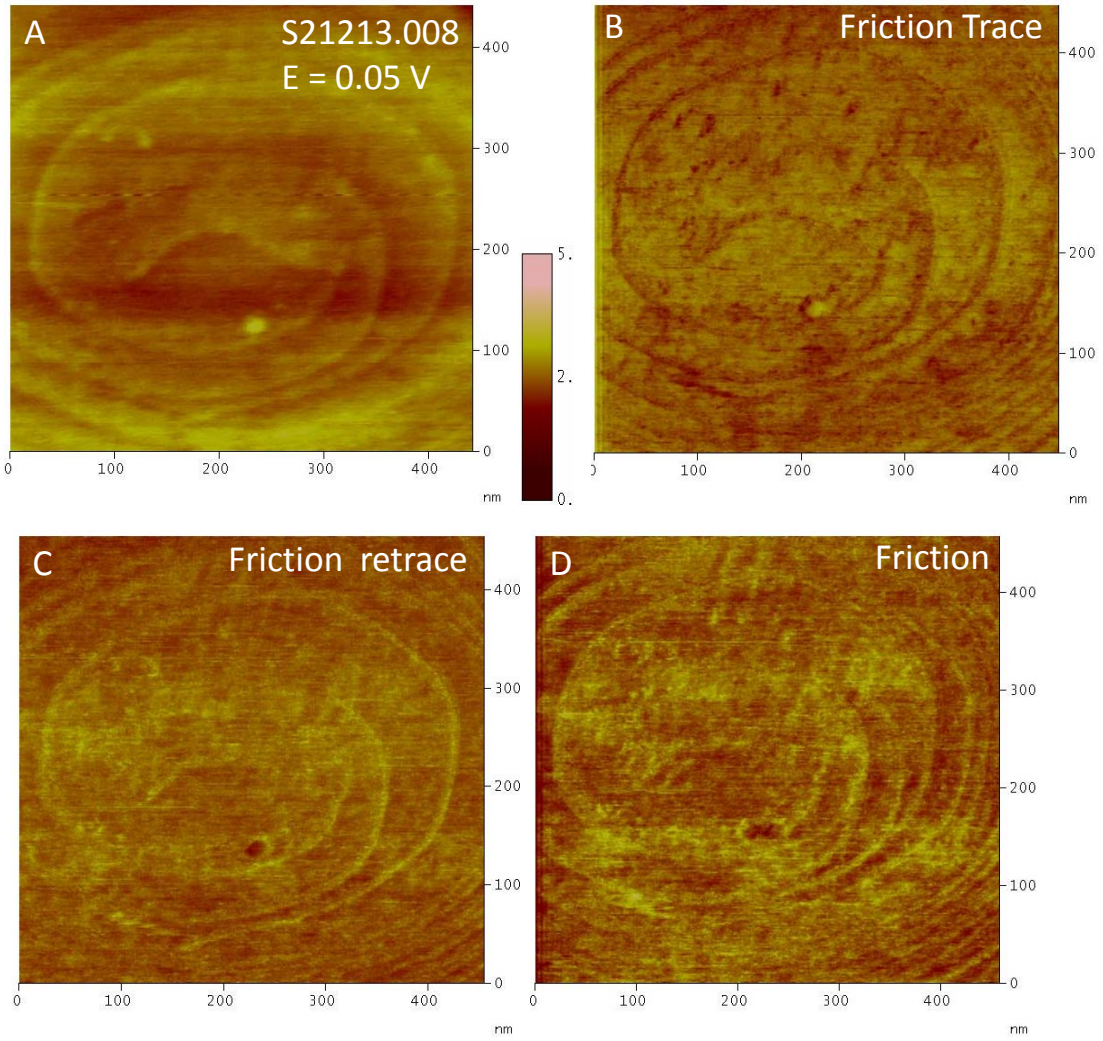

Figure 7.1.2: A) AFM topographic and friction images B) trace, C) retrace and D) difference of a Rh (111) single crystal in $HClO_4$, Normal force: ~ 3 nN, scan rate: 1.97 Hz, electrolyte: 0.1 M $HClO_4$, electrode potential: 0.05 V vs. RHE, cantilever: PPP-CONTSC-20; kN = 0.09 N/m

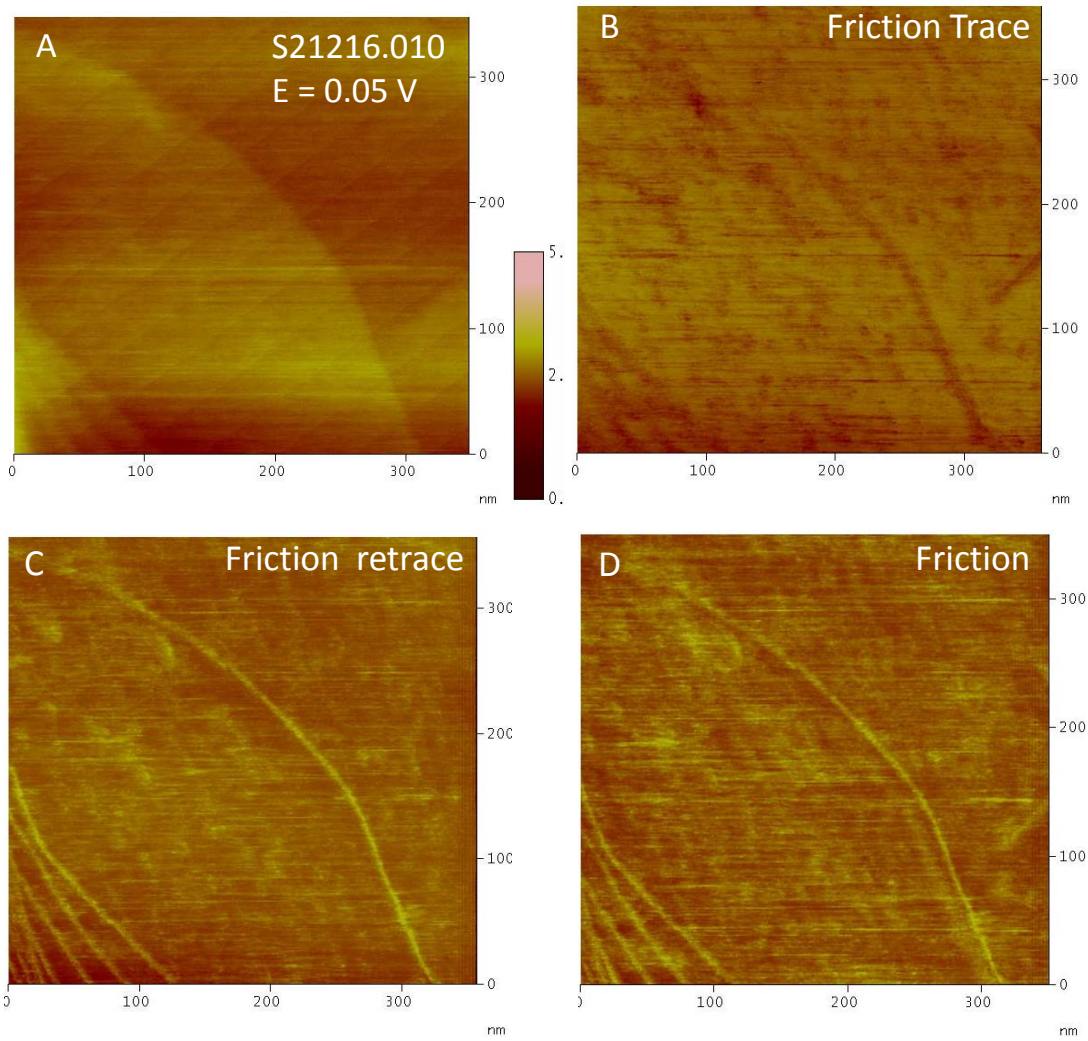

Figure 7.1.3: A) AFM topographic and friction images B) trace, C) retrace and D) difference of a Rh (111) single crystal. Normal force: ~ 3 nN, scan rate: 1.97 Hz, electrolyte: 0.1 M H_2SO_4, electrode potential: 0.05 V vs. RHE, cantilever: PPP-CONTSC-20; kN = 0.09 N/m

In fig. 7.1.4, the influence of changing normal force on rhodium electrode in 0.1 M $HClO_4$ acid and associated friction are presented. The normal load increases from 3 nN up to 13 nN, gradual increase in friction was observed. The section analysis of the difference friction image provides information, that by increasing the normal force frictional force also increased linearly, and therefore, follow the classical laws of friction. Friction is increased at the steps in both directions due to the Schwoebel-barrier effect, as already noted by Hausen et al. [8].

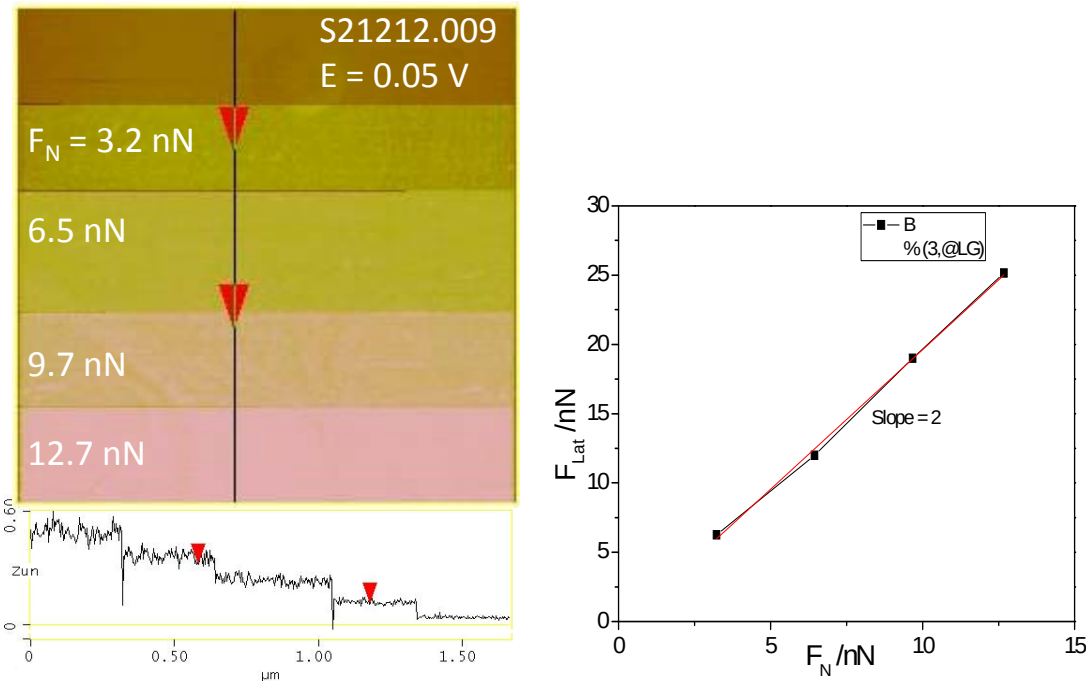

Figure 7.1.4: Friction on Rh(111) surface in 0.1 M $HClO_4$. A plot of lateral vs normal friction is also shown. scan rate: 1.97 Hz, electrolyte: 0.1 M $HClO_4$, electrode potential: 0.05 V vs. RHE, cantilever: PPP- CONTSC-20; k_N = 0.09 N/m

7.1.3.2 Friction on selenium modified Rh(111) surface

The Se modified Rh(111) system is complex and was not explored previousely for friction studies. STM studeis of selenium modified surface showed that less than monlayer deposits resulted in much smoother deposits. It also confirmed from STM and AFM measurements (chapter 3 fig. 3.6). However potential dependence roughening transitions of these deposits in the presence of selenite ions made it more complex and difficult for friction purposes.

Friction studies were examined on Se modified rhodium single crystal surface. This system (especially nanoparticles of rhodium selenide) was widely studied as an attractive alternate for ORR catalyst for mixed reactant fuel cell applications [9]. The prepared Rh(111) was modified with Se in the AFM cell containing $4X10^{-4}$ M H_2SeO_3 + 0.1 M $HClO_4$ solution and a surface coverage of ϑ = 0.2 was obtained as evident in the CV (fig. 7.1.5a). In order to avoid further modification of the surface as observed already in case of STM studies (chapter 3) the potential was kept slightly positive of the surface modification.

The surface topographic image and corresponding friction image (fig. 7.1.5) of selenium modified Rh(111) surface clearly shows that initial modification occurred at the steps. In addition, submonolayer coverage of selenium on the rhodium surface, not only protect from contamination but also from oxidation [10].

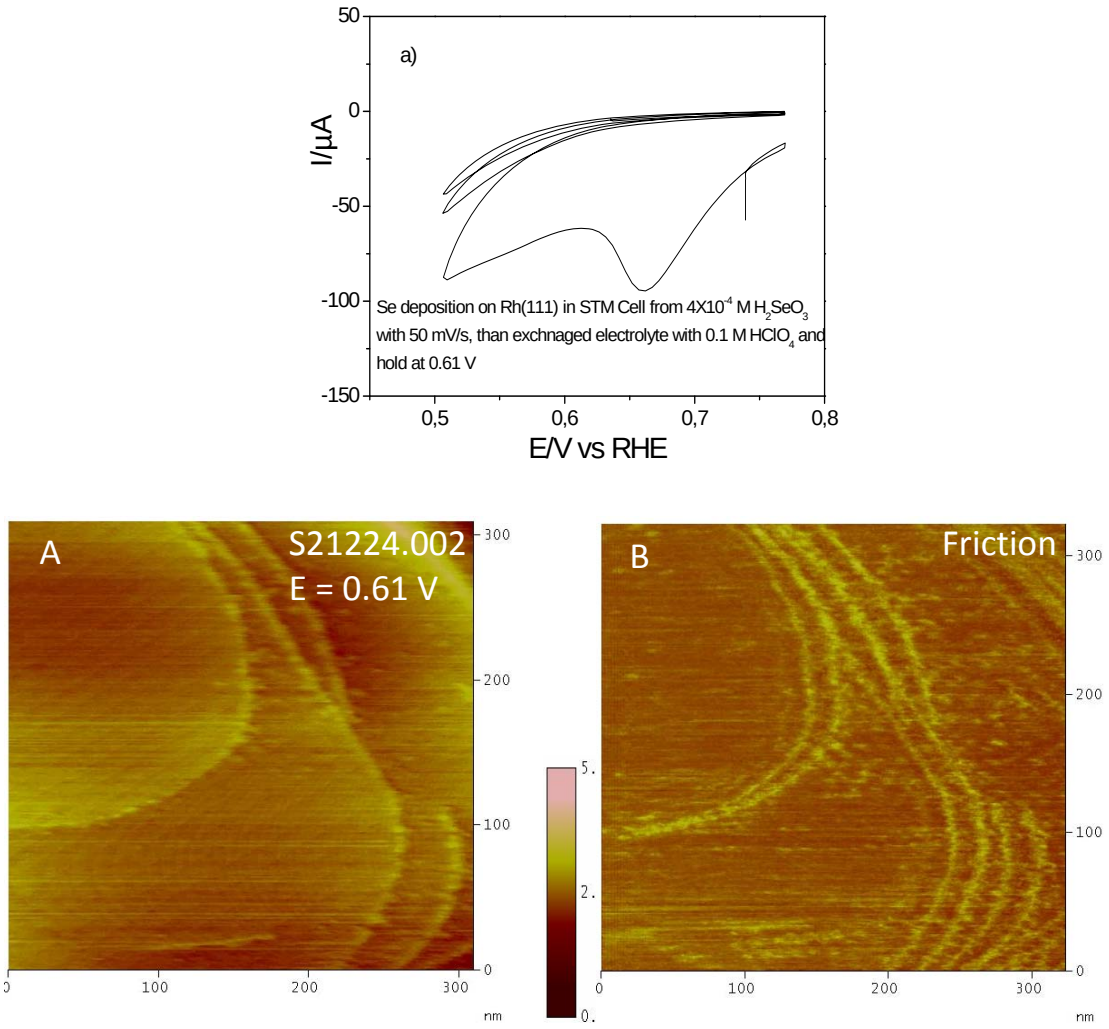

Figure 7.1.5: A) Topographic and B) friction image of Se modified Rh(111) in 0.1 M $HClO_4$ normal force: 2.7 nN; Scan speed: 3.05 Hz, cantilever: PPP CONTSC-20, k = 0.09 N / m. A corresponding in situ CV for Se modification of Rh(111) is also shown.

The influence of normal load on friction was carried out on Se modified Rh(111) surface with surface ecoverage of $\vartheta = 0.2$ in 0.1 M $HClO_4$. is shown in fig. 7.1.6.

A linear relationship between normal force and lateral force with a slope of 1 is observed.

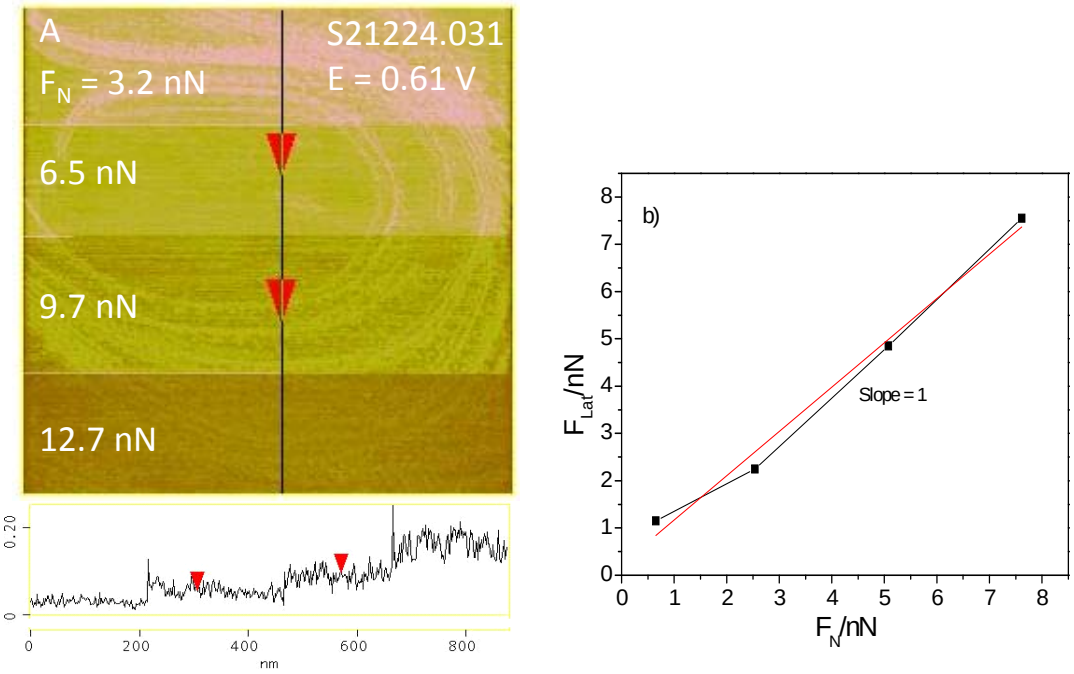

Figure 7.1.6: a) Friction image of Se modified Rh(111) in 0.1 M $HClO_4$ normal force was increased in steps of 1.2 nN to 7.5 nN; Scan speed: 3.05 Hz, cantilever: PPP CONTSC-20, k = 0.09 N/m. b) plot of normal load vs lateral force presented at E = 0.61 V.

Additionally, friction studies were also performed on multilayer Se surface coverages on Rh(111) in selenious acid solution are shown in fig. 7.1.7. At multilayer Se coverages, surface roughenining is not much visible like observed in STM due to large cantilever tip as compared to atomically sharp tips in STM.

The topogarphic image shows a smooth surface at potential 0.8 V, once the potential was scanned from 0.8 V to 0.35 V vs RHE and than held at this potential. This leads to multilayer deposits of selenium. At this surface coverage friction was monitored by varying the normal force.

A comparison of frictional forces pure Rh(111) with that of Se covered surfaces with surface coverage of ϑ = 0.2 (smooth surface) and of ϑ = 1.5 are plotted in fig. 7.1.8. The friction on Se covered surface with surface coverage of ϑ = 0.2 leads to a decreased friction in comparison to that of pure Rh(111). However, an increased surface coverage results in increase in friction. This increase in friction is probably due to roughened structure of Se deposits.

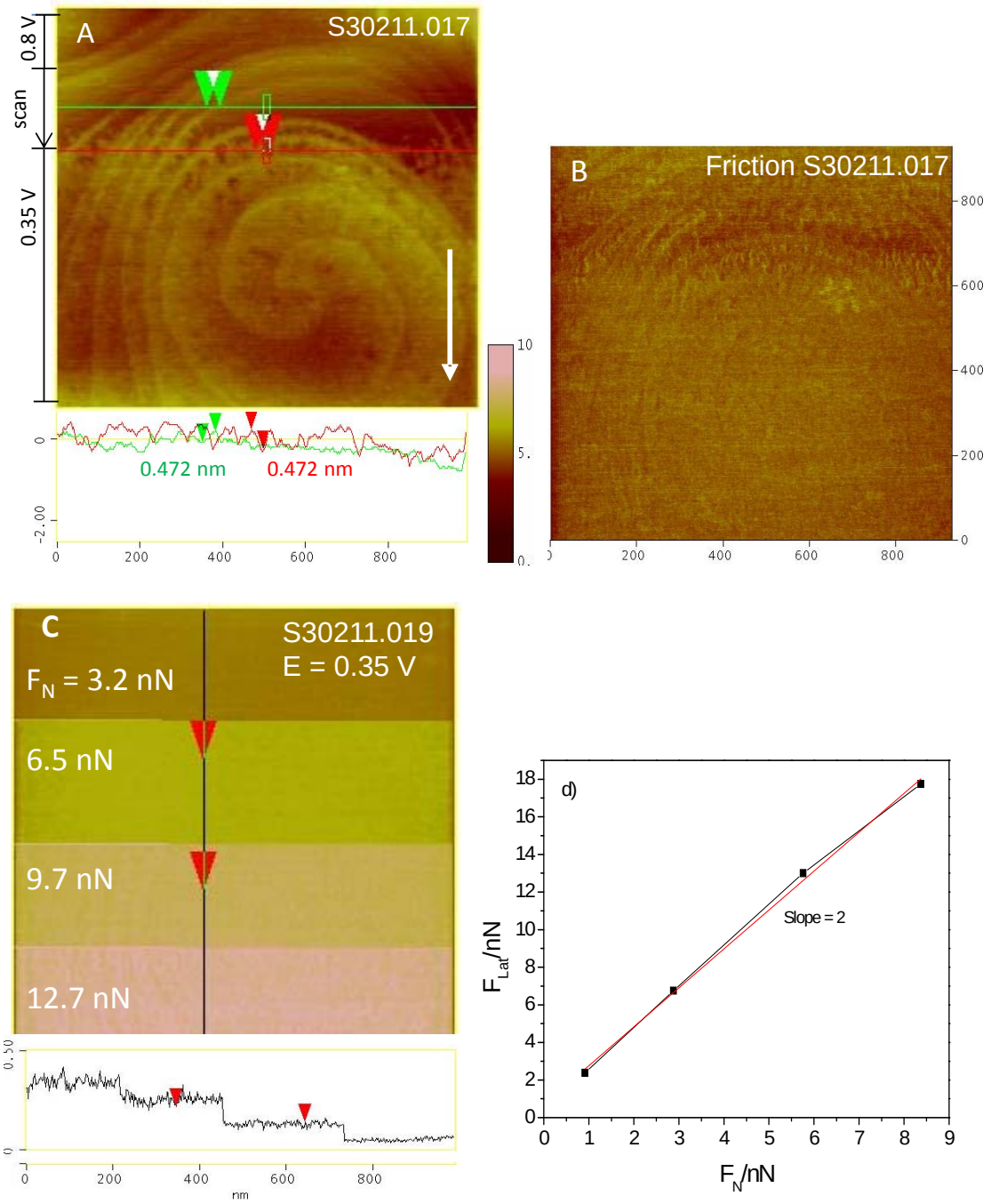

Figure 7.1.7: A) Topographic and B) friction image of Se modified Rh(111) multilayer in 1 mM H_2SeO_3 normal force: 2.8 nN; Scan speed: 3.05 Hz, cantilever: PPP CONTSC-20, k = 0.09 N/m, corresponding friction difference image C) with variation of normal load and a plot of d) friction force as a fuction of normal load is also shown, E= 0.35 V.

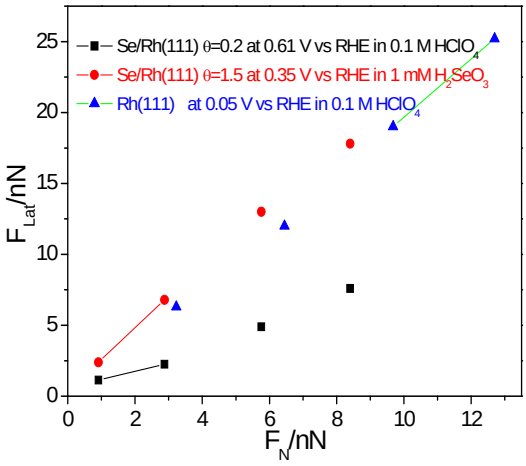

Figure 7.1.8: A plot of dependence of lateral friction on normal friction on Se modified Rh(111) a) ϑ = 0.2 in 0.1 M $HClO_4$ at 0.61 V vs. RHE and ϑ = 1.5 in 1 mM H_2SeO_3 at 0.3 V vs RHE.

The comparison of lateral friction forces on Se covered Rh(111) surface with coverage ϑ = 1.5 to that of pure Rh(111) resulted in more or less same frictional forces. However, on submonolayer ϑ = 0.2 deposit of Se reduced the frictional force. This might be due to the Se mobile nature of isolated deposited islands of Se which are mobile as already shown by STM (Chapter 3)

7.1.3.3 Atomic stick slip on Se modified Rh(111)

The atomically resolved stick slip images shown in the present work were obtained on a rhodium crystal modified with selenium. This system (Se/Rh(111)) was used mostly for ORR measurements being a prominant catalyst in fuel cell, also in current thesis more or less similar modified surfaces were already explored using STM, and their ORR actitivties using DTLFC.

The lateral force at the nanoscale was determined differently than that at the microscale. At nanoscale due to thermal dirft issues friction maxima of trace image might coincide with that of friction minima of retrace image. Thus, resulted in a very complicated friction image. Therefore, trace and retrace images were not subtracted and crossection of each image was plotted together.

This method is illustrated graphically for the Se modified Rh(111) surface. The slope

during stick gives the stiffness of the cantilever tip. The area under one stick slip is the dissipated energy. The whole process is depicted in fig. 7.1.9.

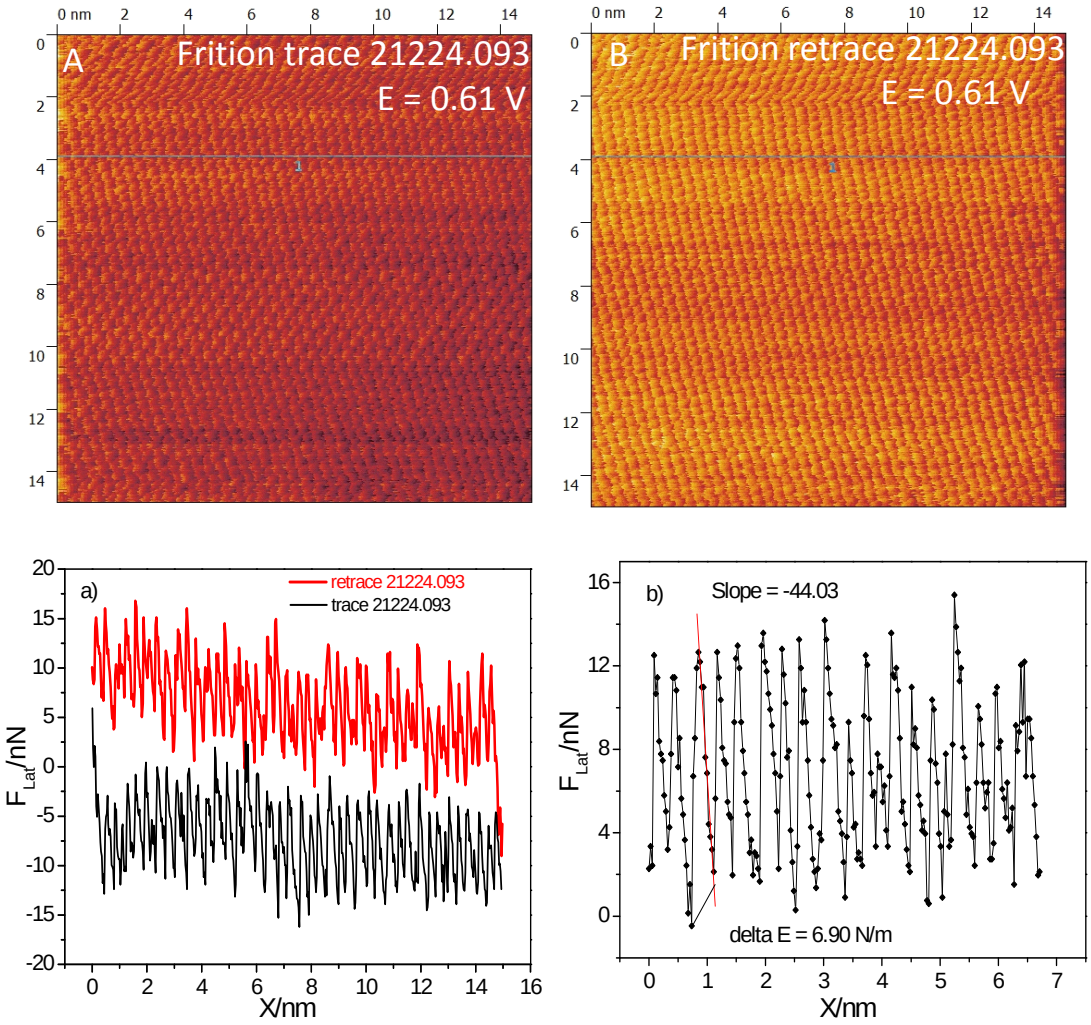

Figure 7.1.9: Stick-slip atomic resolution on Se modified Rh(111) A) trace, B) retrace E = 0.61 V; F_N = 2.5 nN; Scan speed 98 nm /s, corresponding trace retrace cross-section a) and b) small trace cross section for cantilever stiffness and energy dissipation calculations.

The slope of the sawtooth stick-slip curve (image 4 bottom) characterizes the effective lateral stiffness of the contact surface-tip. For a Se/Rh(111) surface with Se coverage of ϑ = 0.2 it is found to be 44 N/m and is very close to that of the lateral stiffness of the cantilever (50 N/m). In addition, the average energy dissipated during stick slip transitions ($\Delta E = F_{Lat} \cdot \Delta X$) is 6.9 N/m.

7.1.3.4 Friction on selenium modified Au(111) and Pt(111) surfaces

The friction studies were also performed on Au(111) and Pt(111) surfaces modified with

submonolayer Se coverages (ϑ = 0.2) at a fixed potential, similar to Se modified Rh(111) surface. At this surface coverage of Se on Au(111), friction was monitored as a function of normal load. The friction image with corresponding frictional forces plot is presented in fig. 7.1.10. It is observed that the initially friction increases linearly with increasing normal load up to 5 nN and afterwards not increases linearly. In addition, similar experiments were performed on Se modified Pt(111) surface. The friction image with corresponding frictional forces plot is presented in fig. 7.1.11.

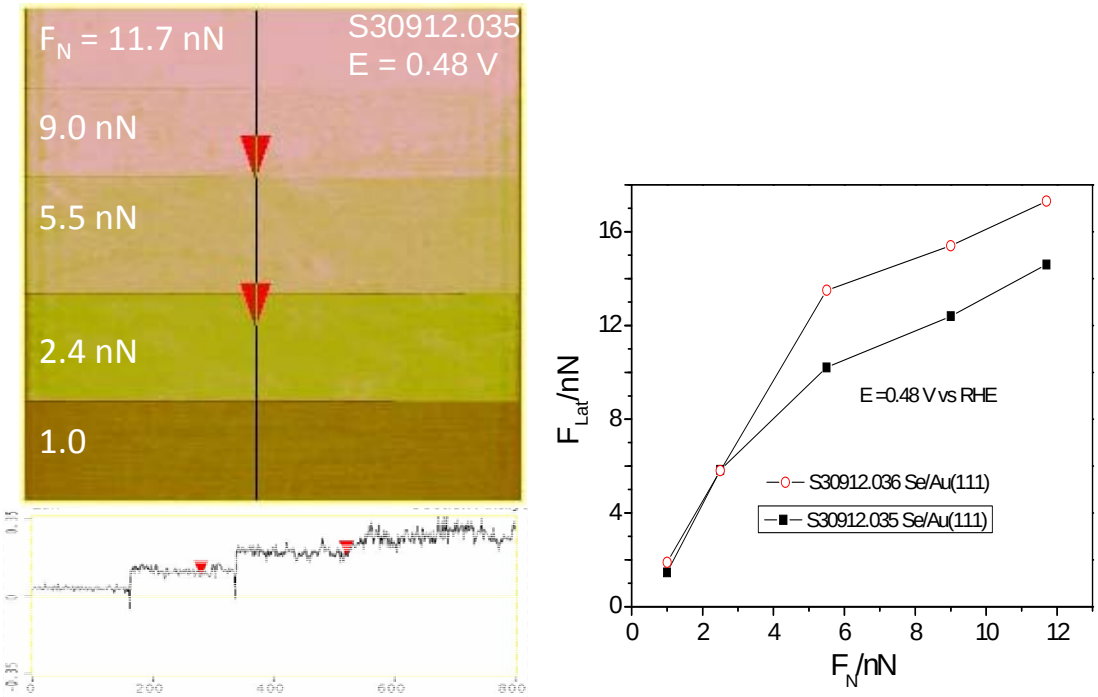

Figure 7.1.10: Friction image of Se modified Au(111) in 1 mM H_2SeO_3 normal force: 2.8 nN; Scan speed: 3.05 Hz, cantilever: PPP CONTSC-20, k = 0.09 N/m, corresponding frictional force plot is also shown

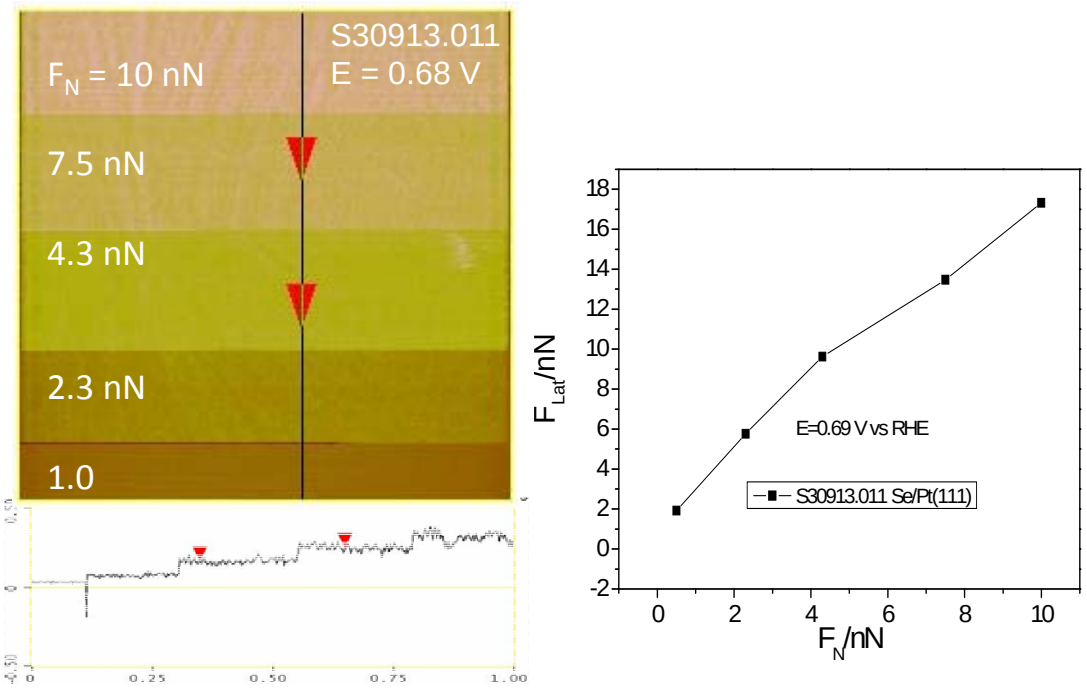

Figure 7.1.11: Friction image of Se modified Pt(111) in 1 mM H_2SeO_3 normal force: 2.8 nN; Scan speed: 3.05 Hz, cantilever: PPP CONTSC-20, k = 0.09 N/m, corresponding frictional force plot is also shown

A detailed comparison of friction forces on Se modified *fcc*(111) with Se surface coverage of ϑ = 0.2 as a function of normal load at fixed potential using cantilever with spring constant of 0.09 N/m is shown in fig. 7.1.12.

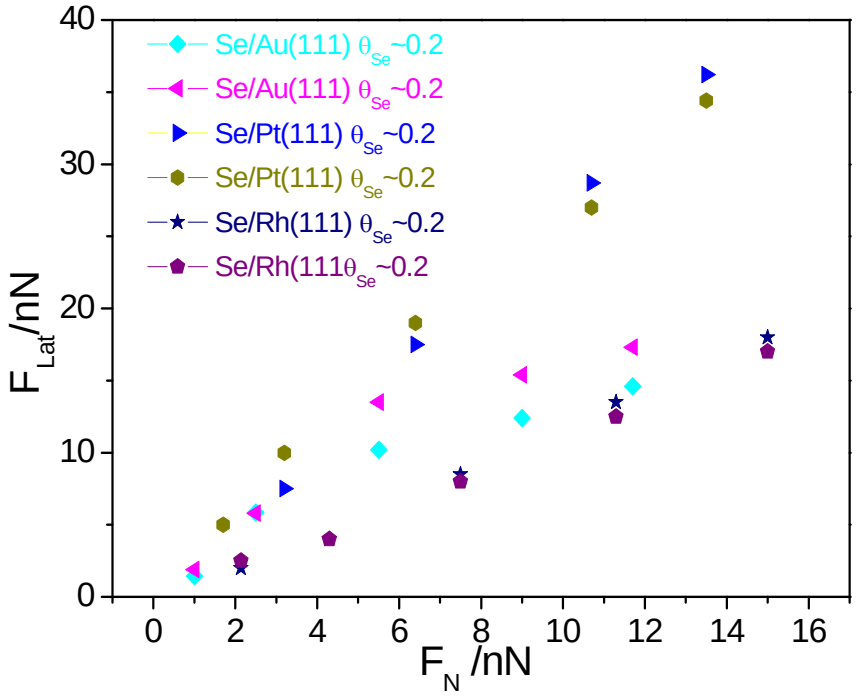

Figure 7.1.12: Plot of the lateral force as a function of normal load for Se modified Rh(111), Pt(111) and Au(111) in 0.1 M $HClO_4$ using soft (Nanosensors PPP-CONT-10) cantilevers with spring constants k = 0.09 N/m. Friction on two consecutive images is shown.

Moreover, friction forces on submonolayer Se coverages (ϑ = 0.2) on Rh(111) and Pt(111) were also determined using cantilever with large spring constant of k = 0.65 N/m. Although, the friction force increases linearly with normal load, however, the slope is about four times lower than measured with a cantilever having spring constant of k= 0.09 N/m as shown in fig. 7.1.13. It is known that cantilever with large spring constant mechanically erode while interacting with the substrate surface [7]. This mechanical erosion leads to increase surface area of the cantilever and hence decrease in friction force.

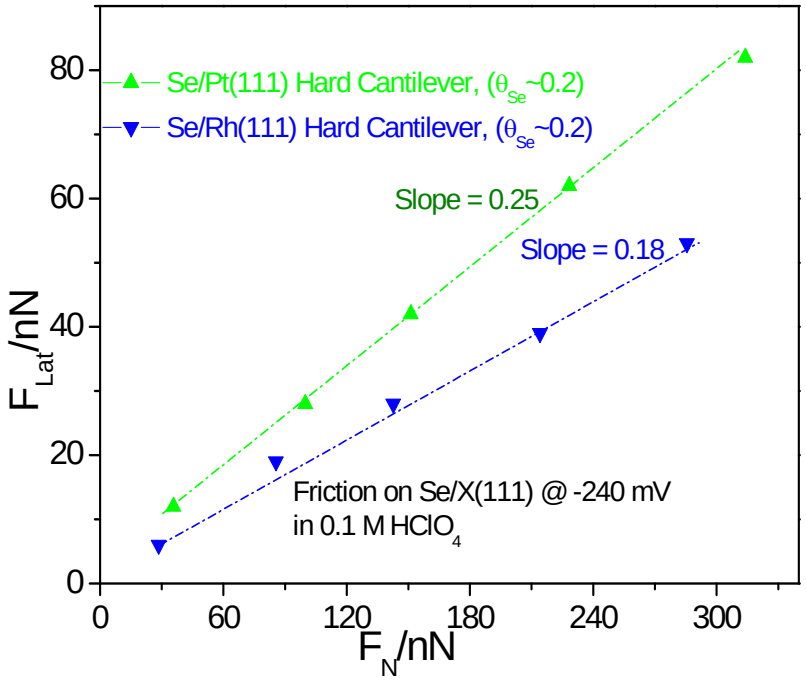

Figure 7.1.13: Plot of the lateral force as a function of normal load for different coverages of Se on Rh(111), Pt(111) and Au(111) in 0.1 M $HClO_4$ using hard (Vecco MP31100) and soft (Nanosensors PPP-CONT-10) cantilevers with spring constants k = 0.65 N/m and k = 0.09 N/m respectively.

7.2 Friction at organic adsorbates

7.2.1: Friction on pyridine

The microscopic friction studies of molecular adsorbates are normally performed in ultra high vacuum (UHV). In real life, even in dry condition surfaces have an adsorbed layer of moisture, which is not the case in UHV. The friction force microscopy (FFM) coupled with electrochmistry, can generate conditions close to that of UHV from cleaniless point of view. Additionally not only the well defined surface structure are maintained but also adsorbate coverage can be varied by either change of electrolyte or electrode potential. The extent to which an organic adsorbate at metal surfaces can influence friction is of fundamental importance. We make use of pyridine adsorbed on Au (111) as a model system. This system was previousely characterized through surface-enhanced Raman spectroscopy and IR spectroscopic studies [11, 12] and scanning tunneling microscopy [13] Lipkowski and co-workers demonstrated that pyridine at low potentials on Au (111) adsorbs flat (π-bound formation between pyridine and metal surface) and at higher potential adsorb vertically (linked via N) [14].

.

Frictional studies of pyridine at the Au(111) surface was previously performed in our group [7]. In the above studies, influence of background electrolyte and other organic adsorbents (contaminants) were not discussed in detail. Current studies focus on the contribution of friction in supporting electrolyte and organic adsorbents (contaiminants) other than pyridine.

7.2.2 Preparation and modification of massive single crystal electrodes

The Au(111) electrode surface was prepared as per procedure described elsewhere [15]. Au(111) single crystal electrodes with a diameter of 10 mm was used (Mateck Germany). All solutions were prepared from 18.2 MΩ Milli-Q water and de-aerated with high purity argon gas (99.999%). For experiments with pyridine, 0.1 M $NaClO_4$ supporting electrolytes were used. All AFM experiments were also performed in an Argon atmosphere at room temperature.

All AFM measurements were performed with a Nanoscope III E controller (Digital Instruments, Santa Barbara, CA) and a commercially available AFM scanner (Molecular Imaging) fitted with an electrochemical cell. A Au wire was used as the counter

electrode and a Pt wire as quasi-reversible reference electrode. All potentials were converted to the reversible hydrogen electrode (RHE) using E (Pt) = 0.9 V vs. RHE. All AFM experiments were performed with soft cantilevers: n^+-doped Si cantilever by Nanosensors (PPP-CONT-10), k_n = 0.09 N/m. The torsional force constant was determined via Sader's method [6] and found to be 50 Nm^{-1} [7]. This method is based on the measurement of the resonant frequency and quality factor of the cantilever.

7.2.3 Results and Discussion:

Pyridine on Au(111)

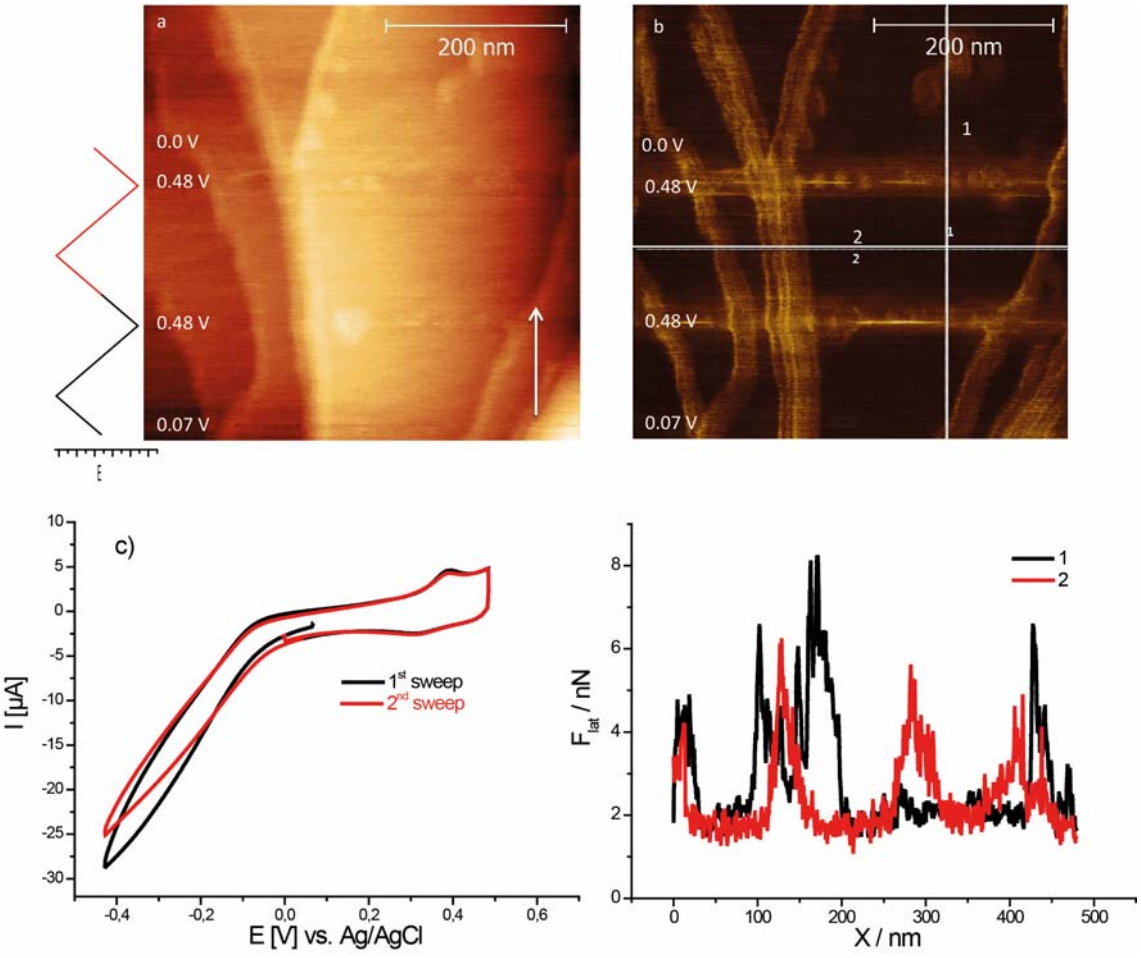

Figure 7.2.1: Simultaneous recorded topographic (a) and friction images (a) of Au(111) in 0.1 M $NaClO_4$, with continuous cycling at 20 mV/s: recorded CV and cross section of friction image is also shown. Normal load of 3 nN, cantilever: PPP-CONTSC-20; kN = 0.09 N/m.

To rule out any background contamination possibility, we performed friction stidies on Au(111) in argon saturated 0.1 M $NaClO_4$ (supporting electrolyte). Simultaneously recorded topographic friction images were taken while the potential was scanned from

1.1 to 0 V vs RHE as shown in fig. 7.2.1. Friction starts to increase at a potential of 0.8 V vs RHE during the anodic scan and persisted till 0.75 V in the cathodic scan, which is evident from friction images. The highest friction observed at 1.0 V (anodic potential limit). Form these set of experiments, it is clear that the supporting electrolytes did not play any role in surface contamination.

High resolution atomic slick slip image (fig. 7.2.2) of Au(111) adllatice in the supporting electrolyte at potential of 0.4 V further confirms the absence of contaminants.

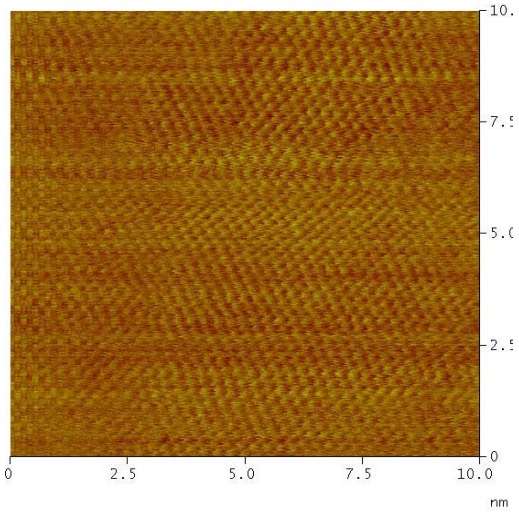

Figure 7.2.2: Atomic stick slip resolved AFM image of Au (111) in 0.1 M $NaClO_4$ solution. Potentials E = 0.4 V vs RHE with normal load of 3 nN, cantilever: PPP-CONTSC-20; kN = 0.09 N/m

The influence of pyridine on friction on Au(111) was determined as follows: The pyridine was adsorbed in situ on Au(111) from 10^{-2} M pyridine +0.1 M $NaClO_4$. A sharp peak at around 0.49 V indicates the flat lying adsorption of pyridine and the second sharp peak around 0.88 V was a result of tilting or standing position of pyridine (fig. 7.2.3) [14], slightly broad peak at more negative potential (0.4 V) is due to reduction of oxygen

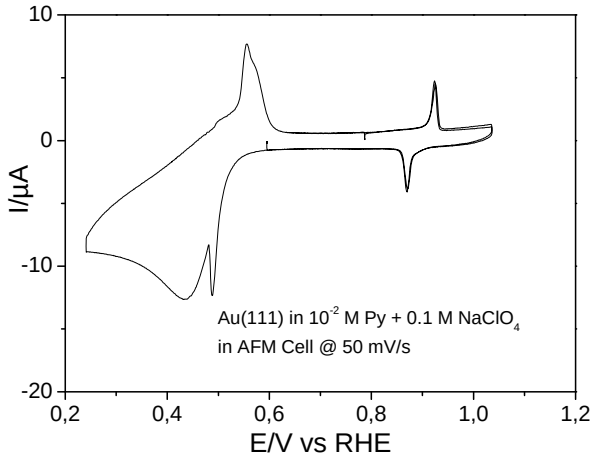

Figure 7.2.3: CV of 10^{-2} M Py + 0.1 M $NaClO_4$ in AFM cell on Au(111): sweep rate 50 mV/s

The topographic and friction force images of pyridine on an Au (111) surface are shown in fig. 7.2.4. The bright isolated features on Au(111) surface in the topographic image starts to appear at a potential of 0.8 V in the anodic sweep and persisted till 0.8 V in the cathodic sweep. As mentioned earlier, the pyridine might have a vertical position with the change in potential. These "islands" indicate the positions where pyridine adsorbed perpendicular to the Au surface.

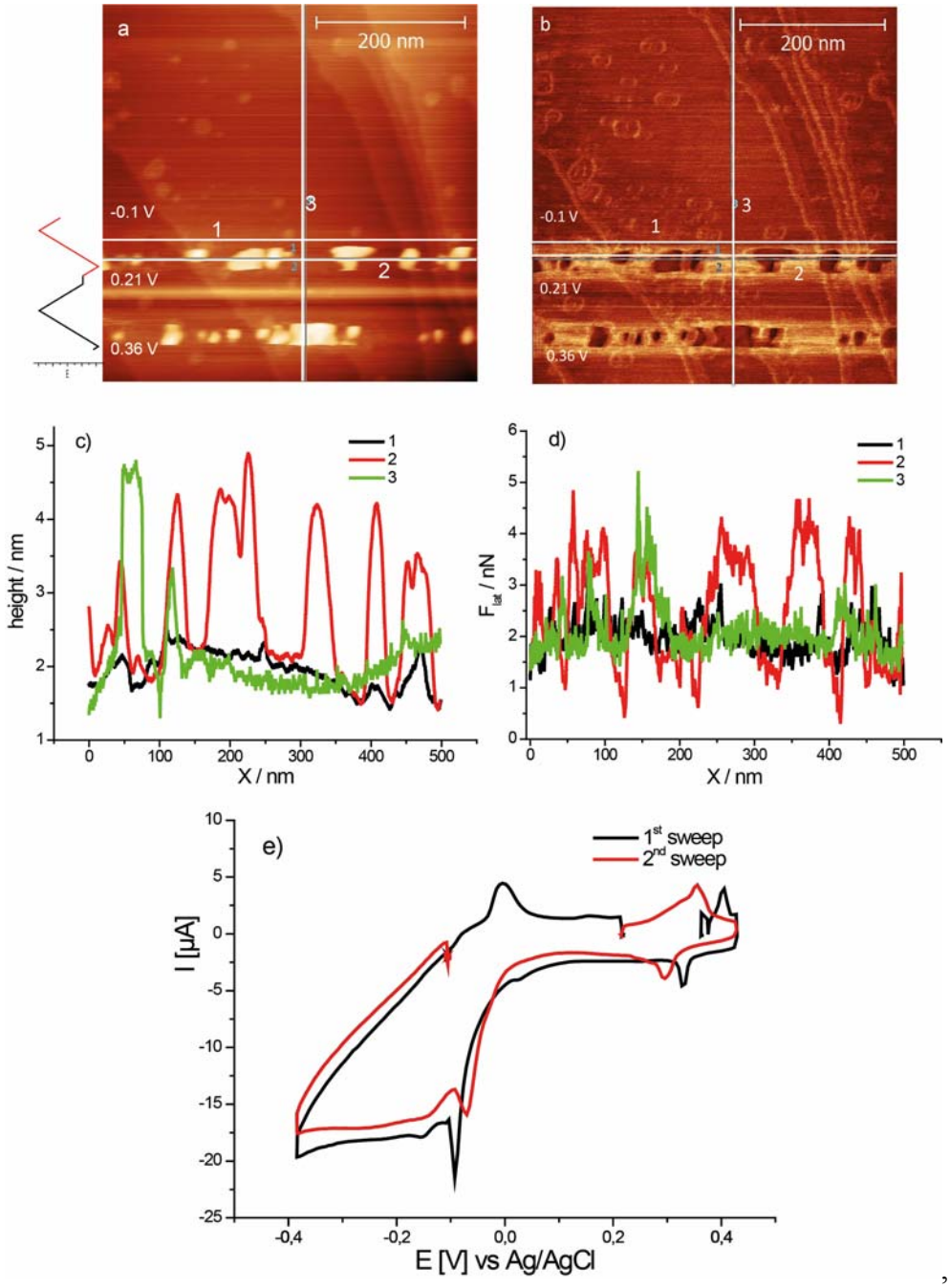
a
200 nm
-0.1 V
0.21 V
0.36 V
1
2
3
b
200 nm
-0.1 V
0.21 V
0.36 V
1
2
3
c)
height / nm
X / nm
1
2
3
d)
F_lat / nN
X / nm
1
2
3
e)
1st sweep
2nd sweep
I [µA]
E [V] vs Ag/AgCl

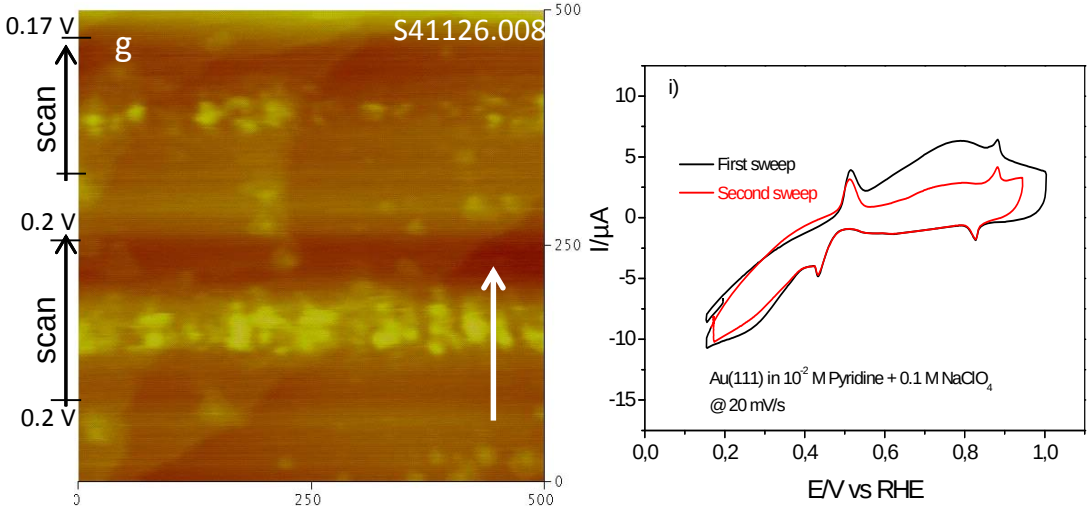
0.17 V
scan
0.2 V
scan
0.2 V
g
S41126.008
500
250
0
0
250
500
i)
First sweep
Second sweep
I/µA
Au(111) in 10-2 M Pyridine + 0.1 M NaClO4
@ 20 mV/s
E/V vs RHE

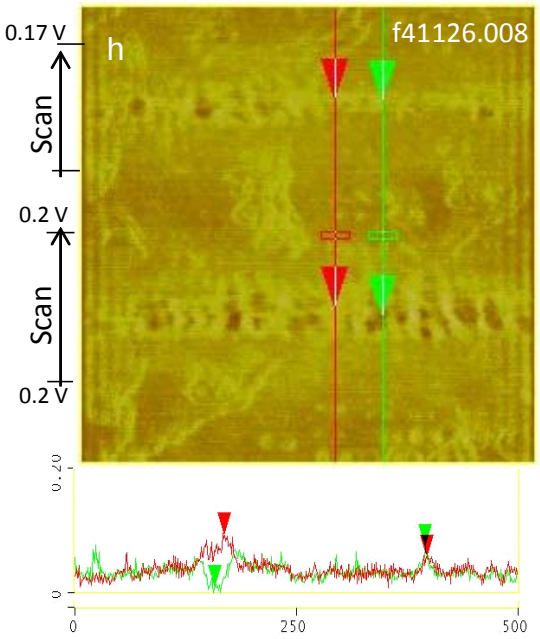

Figure 7.2.4: a), b) and g),h) are simultaneously recorded topographic and friction images of Au(111) in 10^{-2} M pyridine + 0.1 M $NaClO_4$, with continuous cycling at sweep rate of 50 and 20 mV/s respectively: recorded CV e) and i) and cross section of the friction image is also shown, normal load of 3 nN, cantilever: PPP-CONTSC-20; kN = 0.09 N/m. The black mark at highest friction indicates the anodic potential limit.

A well defined atomic stick slip prevails in the pyridine free and in the pyridine flat lying region (fig. 7.2.5A), while the stick slip in not very clear in fig. 7.2.5B. Once the pyridine is in vertical position the atomic stick slip disappears. Friction remains more or less constant in pyridine flat lying region and pyridine free region. however, once the pyridine starts being adsorbed vertically as observed in both topographic and friction images at around 0.8 V vs RHE, substantial decrease in friction is observed only at patches where pyridine adsorbed vertically and persist till 0.8 V in the cathodic direction. In general, friction increases within this potential region while using supporting electrolytes (0.1 M $NaClO_4$, fig. 7.2.1). The most probable explanation is that the pyridine molecules in vertical adsorbing state are very elastic decreasing the interaction of the tip with the surface.

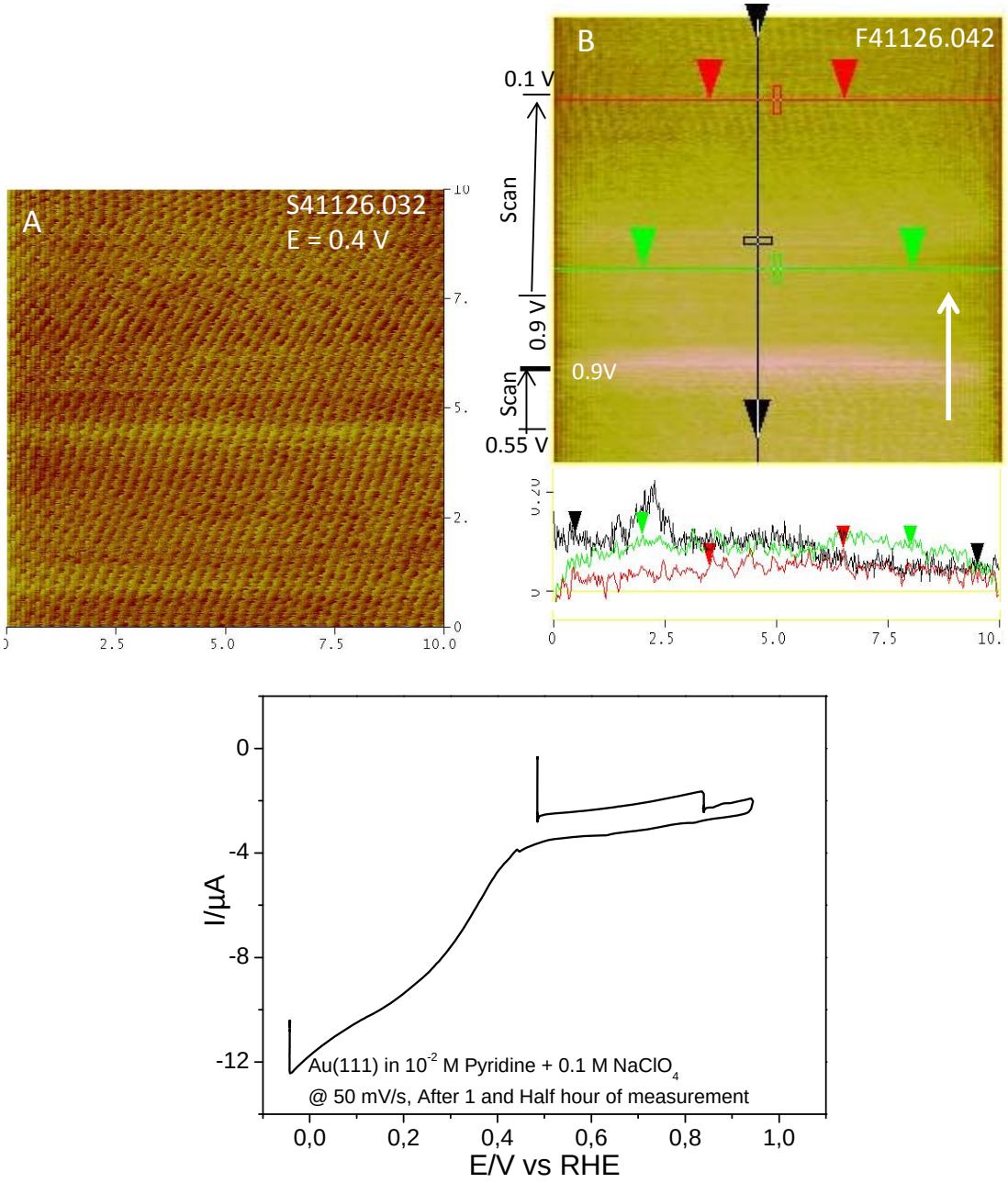

Figure 7.2.5: Atomic stick slip resolved AFM image of Au (111) in 10^{-2} M Pyridine + 0.1 M $NaClO_4$ solution. Potentials E = 0.4 V and continuous scanning, recorded CV with crossection of friction is also shown, F_N = 3 nN. The black mark at highest friction indicates the anodic potential limit.

7.3 Surface morphological studies of Nafion®/Pt(100) interface

7.3.1 Introduction

Scanning probe microscopic techniques have been shown to be excellent for characterising the nanoscale surface morphology of the electrolyte/electrode interface. Despite a significant research effort into the properties of bulk Nafion® membranes however, there is still a paucity of information regarding the ionomer Nafion® (and polymers in general) at the nanometre scale associated with the polymer membrane-electrode interface. Hiesgen and coworkers quite recently presented a detailed review concerning the nanoscale behaviour of ionomers and the components of polymer electrolyte fuel cells (PEFC) in general [16]. More recently, efforts have been made to study the electrochemical processes taking place at Nafion® coated single crystal electrodes.

Markovic and coworkers were the pioneers of this approach. They studied the nature of the Pt/ Nafion®/electrolyte three phase interface for Pt(hkl) surfaces using voltammetric techniques. In addition, they examined the kinetics of the oxygen reduction reaction (ORR) at the metal/ Nafion® interface. Utilizing CO charge displacement measurements, they identified sulfonate anions as the adsorbing species on the electrode [17, 18]. Feliu et al also used cyclic voltammetry together with in situ infra-red reflection adsorption spectroscopy (IRRAS) to investigate the Nafion®-electrode-electrolyte interface at a Pt(111) electrode [19]. Thus, they could follow the structural changes with potential of the membrane in contact with the electrode surface and found notable difference between the character of CO adsorption and oxidation at Pt(111) with and without polymer electrolyte membrane being present. For example, they observed that CO electrooxidation proceeded at more positive potentials when the electrode was Nafion® modified compared to when the Pt(111) electrode was free of ionomer. Similarly, Attard and coworkers examined the voltammetric behaviour of Pt(hkl) electrodes as a function of both Nafion surface coverage and platinum surface step density [20]. They found that Nafion®-induced voltammetric peaks on Pt stepped surfaces showed a marked structural sensitivity as a function of average terrace width. Moreover, the thickness and composition of the thin Nafion® adlayer on Pt(111) was determined using XPS. Excellent agreement with the predicted nominal stoichiometry of the 1100 EW Nafion® ionomer used and surface atomic composition utilizing XPS sensitivity factors was observed. A thickness of 3.3 nm for the Nafion® film giving the

most intense Nafion® "spike" peak on Pt(111)[20] was also obtained by comparing the attenuation of the Pt 4f XPS peak intensity of the clean Pt(111) surface with the Nafion® modified surface at a fixed experimental geometry.

Scanning probe microscopy (SPM) has proven to be a valuable addition to the armoury of techniques capable of probing the electrode-electrolyte interface at the nanometre and sub-nanometre scale and under ambient conditions with proper potential and temperature control. Hiesgen and coworkers thus provide a detailed study of a Nafion® layer deposited upon both a flame annealed gold film on glass (with gold (111) orientation) and a highly orientated pyrolytic graphite (HOPG) electrode using STM [21]. They obtained STM images of Nafion® as a structured film with relatively ordered domains under fully humidified conditions. These ordered domains consisted of globular substructures of about 8 nm diameter and of height approximately 2 nm. Bright spots in the STM images were ascribed to collections of sulphonate moieties whereas hydrophobic parts of the Nafion® film appeared not to be visible. Koestner et al. also studied thin Nafion® layers on HOPG and mica. These were prepared by spin coating and characterised using AFM. These workers found the slow formation of single "globules" exhibiting a typical height of 5 nm [22]. Mauritz et al provide a detailed review concerning Nafion®, with a strong emphasis on its structure and properties [23].

Quite recently, Uosaki and coworkers investigated in situ electrochemical potential dependant properties of Nafion® on gold and platinum single crystal surfaces using a quartz microbalance and atomic force microscopy [24, 25]. They found that Nafion® adsorption/desorption depended upon the condition of the metal electrode surface. On a reduced surface, Nafion® was found to adsorb whereas desorption was observed from an oxidized surface. This result is somewhat astonishing in that previous studies of Nafion® adsorbed on platinum have found that it is stable when the electrode surface forms an electrosorbed oxide layer [20]. It should be noted however that in references 9 and 10, no heat treatment was applied to the Nafion® adlayer in order to stabilise it at the surface. Rather, adsorption was carried out reversibly from an aqueous solution.

It is the aim of the present investigation to obtain further information concerning the structure of such thermally prepared, thin films of Nafion® on Pt(100) using scanning probe techniques, thereby continuing previous work by Attard et al [20]. The Pt(100)

surface has the advantage of being smooth on the atomic scale, but also is of significant interest for catalytic studies because of its much higher activity for many reactions than Pt(111) [26]. The main task is to investigate the nature of the coordination of Nafion® to an electrode surface, specifically thickness and mechanical stability of the Nafion® film. Not only is the degradation and mechanical stability of a fuel cell electrode dependant on the interaction of Nafion® with the electrode or nanoparticle surface, this interaction may also be of practical relevance in the optimization of the manufacturing process.

We hope these studies will help to better understand processes at electrode/membrane interfaces relevant to fuel cell applications. On the other hand, the analysis of frictional forces is part of our continuing effort in determining the influence of adsorbates and surface modifications on friction at electrode surfaces [8, 27]. Friction is the origin of all - in most cases unwanted - conversion of energy into heat. Its reduction would have significant impact on energy consumption.

7.3.2 Experimental

The Pt(100) single crystal electrode used in this work was flame-annealed and cooled in an argon or H_2/argon atmosphere respectively, then immersed into ultra-pure water and finally transferred to the electrochemical cell to form a meniscus contact with the electrolyte. The concentration of the aqueous perchloric acid used for the experiments was 0.1 M. All electrolytes were prepared using 18.2 MΩ cm Milli-Q water and Aristar grade $HClO_4$. The Nafion used for the experiments was obtained from Sigma Aldrich (5% solution of 1100 equivalent weight). All gases (Ar and H_2) were provided by Praxair (99.999%). 1 mM KBr solution was used as a source of bromine adatoms, irreversibly adsorbed, in order to protect the pristine electrode surface from contamination during Nafion® film preparation. After an initial voltammograms was collected confirming cleanliness and surface order, the single crystals were washed with ultra-pure water and dipped into a 10^{-3} M solution of KBr to form a monolayer of irreversibly adsorbed bromide adatoms [20]. The electrode was then rinsed with ultra-pure water and a droplet of the diluted 5% EW1100 Nafion® solution (typically by a factor of 1000) was added to the disc electrode to form a hanging hemispherical droplet such that only the polished, crystal face was covered with Nafion®. The electrode was then heated to approximately 145 °C (which is slightly above the first glass transition of 130 °C, [28, 29] using a hair dryer for 4~5 minutes to evaporate away the excess of the

liquid droplet attached and allow the polymeric film to flow to yield a smooth layer. The temperature reached was previously calibrated using a chromel-alumel thermocouple attached to the electrode. This method, developed for Pt bead single crystal surfaces by Attard and coworkers [20], had to be slightly modified for the larger disc electrodes. For the much larger Pt disc electrodes (diameter 1 cm, thickness 3-4 mm), a micropipette was used to deposit a sufficient amount of diluted Nafion® solution to cover the polished side of the electrode and then the electrode was slowly heated to evaporate the solvent. The crystal was then re-introduced to the electrochemical cell with a meniscus contact and the cyclic voltammogram was recorded. Rapid potential cycling between hydrogen evolution potential and the onset of surface oxide formation (0.0 V to 0.985 V versus RHE, sweep rate = 0.2 V/s) ensured that the attached bromide adlayer was desorbed whilst allowing the Nafion® film to be both re-deposit and hydrate on the platinum surface without contamination. Previous studies demonstrated that the bromide ions desorbing from the electrode gradually diffused away from the double layer region as signified by the diminution of the bromine-induced H upd peak at 0.15V. After twenty potential cycles at 0.2 V/s, all vestiges of the bromine induced feature were lost and no re-adsorption was ever observed suggesting that sufficient dilution of the bromide ions had occurred such that their impact on subsequent measurements was negligible. Once the solvent was completely evaporated, heating was continued until the desired temperature was reached. Electrochemical experiments were performed in a usual three-electrode, three-compartment, home-made glass H-Cell. Cyclic voltammetry was performed using a AFCBP1E model Pine Instrument potentiostat.

The STM and AFM measurements were performed with a Nanoscope III E controller (Digital Instruments, Santa Barbara, CA) and the STM and AFM scanner (1μm and 6 μm maximum scan size) was purchased from Molecular Imaging and was incorporated into the Teflon based electrochemical cell. The nominal spring constants of the commercial Si cantilevers used (Nano Sensors PPP-CONTSC-20) were 0.09 N/m and radius of the cantilever tip < 10 nm. The torsional force constant of these cantilevers was determined using the so-called Sader's method to be typically 50 N/m. This method is based on the measurement of the resonant frequency and quality factor of the cantilever [6]. All measurements with AFM were performed at room temperature. All STM and AFM measurement were performed using the Pt(100) disc electrode obtained from Kristallhandel Kelpin (im Schilling 18, 6906 Leimen b. Heidelberg Germany) (Ø

= 10 mm).

7.3.3 Results and Discussion

CVs of Nafion®-free and Nafion®-covered Pt(100) single crystal bead electrodes in 0.1 M $HClO_4$ are shown in fig. 7.3.1. Figure 7.3.1a is typical of previously reported CV profiles for contaminant free Nafion® modified Pt(100) electrode surfaces. The detailed interpretation of both the large Nafion® "spike" (at 0.4 V vs RHE) together with modifications to OH_{ad} and hydrogen underpotential deposition (H_{upd}) features has already been given in reference 5. However, in summary and in agreement with Markovic et al. [18], the large Nafion® spike is ascribed to electrosorption/desorption of sulphonate groups close to or at the potential of zero total charge of the Pt(hkl) electrode.

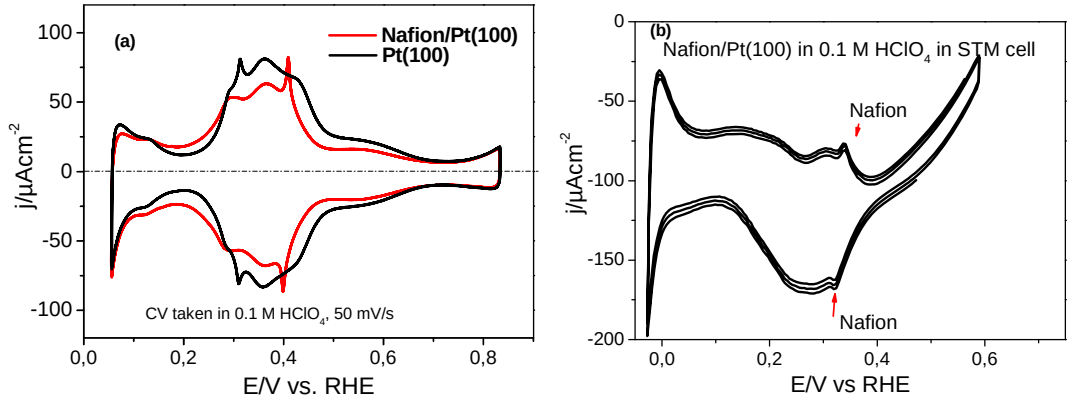

Figure 7.3.1: Cyclic voltammograms of a Nafion-free and a Nafion-covered Pt(100) disc electrodes in 0.1 M $HClO_4$ in (a) the H-Cell and (b) the STM cell. The Nafion®-covered electrodes were prepared by depositing one drop of 5 % solution of Nafion® EW 1100 (diluted 1000 times with Milli-Q water). Sweep rate = 50mV/s.

Figure 1(b) shows the CV obtained in the STM electrochemical cell. Although some residual oxygen in the cell causes distortion of the CV, the Nafion® "spike" at -0.56 V vs. Pt/PtO (+0.34 V vs. NHE) is still clearly seen. It should be emphasised that the presence of the Nafion® spike is extremely sensitive to contamination thus signifying a lack of surface contamination by adventitious impurities in the EC-STM cell.

An STM image of Nafion® on Pt(100) in 0.1 M $HClO_4$ acid at -0.3 V vs. Pt/PtO (+0.6 V vs. NHE) is shown in fig. 7.3.2. This image demonstrates that the adsorbed Nafion® layer is atomically smooth. Astonishingly, mono atomic steps of the substrate are still clearly seen. The film is structured with ordered circular spots of ~ 2.7 nm diameter. These bright spots are regularly arranged; although we cannot completely exclude that

they are caused by residual bromine (or the interaction of bromine with Nafion®) from stripping of the protective Br adlayer into solution, we ascribe these features to ion channels within the Nafion® membrane since bright spots correspond to areas of high conductivity and bromine structures on Pt(100) are not reported to give rise to such surface arrangements [30, 31]. Furthermore, bromine adsorption is found to quench the Nafion® spike intensity so overlayer structure cannot be due to bromine since spike is always present. These spots probably mark the sites where the SO_3 groups are situated and the proton assisted current is largest. In addition, height variations of ~ 0.2 nm with an average periodicity of ~ 40 nm are also visible (darker areas in fig. 7.3.2). These results and interpretation are quite consistent with data obtained by Hiesgen and co-workers [32].

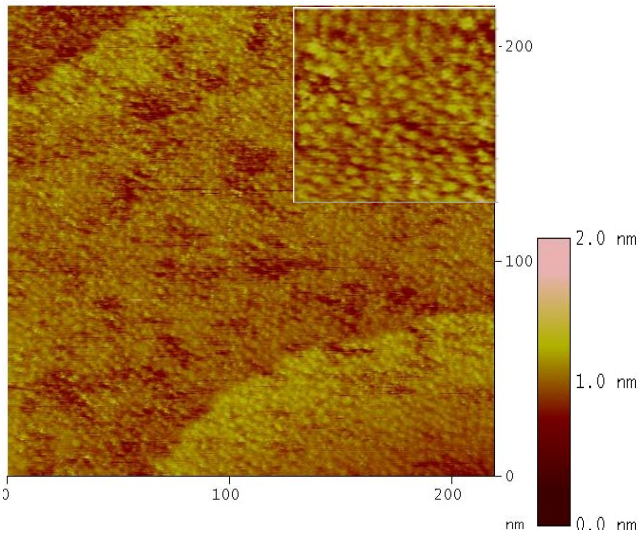

Figure 7.3.2: STM images of Nafion® on Pt(100). Set point = 1 nA, E = -300 mV vs Pt/PtO, bias voltage = 8mV; 220 nm x 220 nm. Inset: higher resolution of Nafion® (45 x 45 nm with z-range = 1 nm).

A topographic AFM image of the Nafion® covered Pt(100) surface is presented in fig. 7.3.3. Here, the load (normal load) was varied in different sections of the image as indicated. Not surprisingly, the resolution is not as good as in the STM image. Nonetheless, the roughness in these images appears much lower than in the STM image. Also, roughness appears to increase somewhat above 6 nN. The section analysis of this image shows a maximum height variation of ~4.3 nm. This height difference corresponds to the expected thickness of the Nafion® layer on the substrate [20] and therefore may be due to some holes in the layer. The distance between these depressions is ~ 40 nm and thus corresponds to those observed in the STM data. The average height variation, however, is larger (~1 nm) which could be due to the compressibility of the

Nafion® layer as discussed below. While acquiring the topographic image, normal load (F_N) is gradually increased up to 24 nN as shown in figs. 7.3.3a and 7.3.3b. Surface modification is not observed until the highest value of normal load is reached.

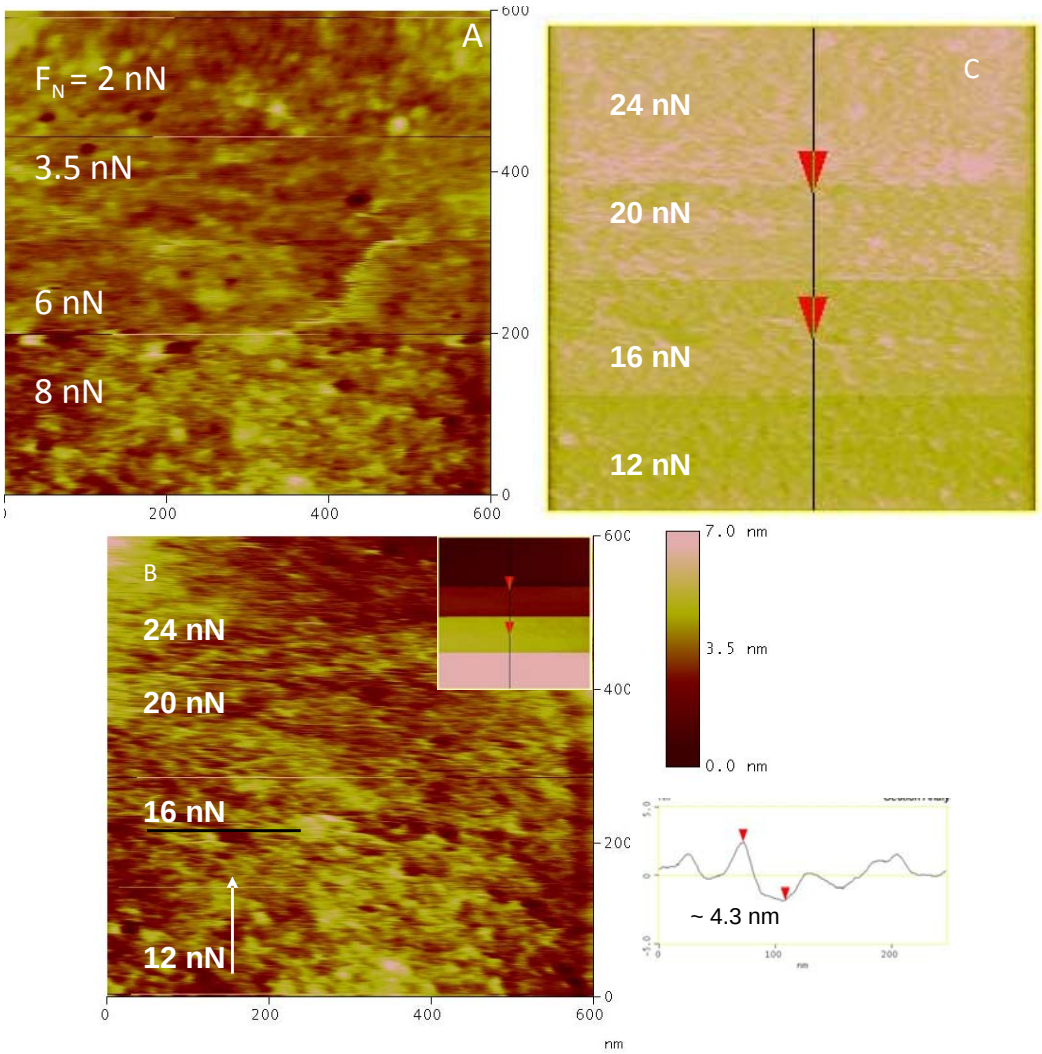

Figure 7.3.3a: Background corrected AFM Image of Nafion® covered Pt(100) surface. The application of normal load on the Nafion® layer from bottom to top is indicated by the arrow head. Scan rate 3.6 µm s^{-1}, E = -0.3 V vs. Pt/PtO, cantilever spring constant of 0.09 N/m.
Figure 7.3.3b: same as fig. 3a but with increased normal load. A plane corrected image of fig. 7.3.3b is shown as inset. Black line shows the position of cross section.
Figure 7.3.3c: Friction force image of fig. 7.3.3b on Nafion®/Pt(100) in the $HClO_4$ electrolyte.

In the image presented in figs. 7.3.3a and 7.3.3b, background subtraction was achieved line-by-line. Therefore, height changes upon increasing the normal force (caused by the increased deflection of the cantilever) are not visible. When the background was only corrected by a plane (as shown in inset in fig. 7.3.3b), the height change becomes visible. Figure 7.3.3c shows an image of the lateral friction force.

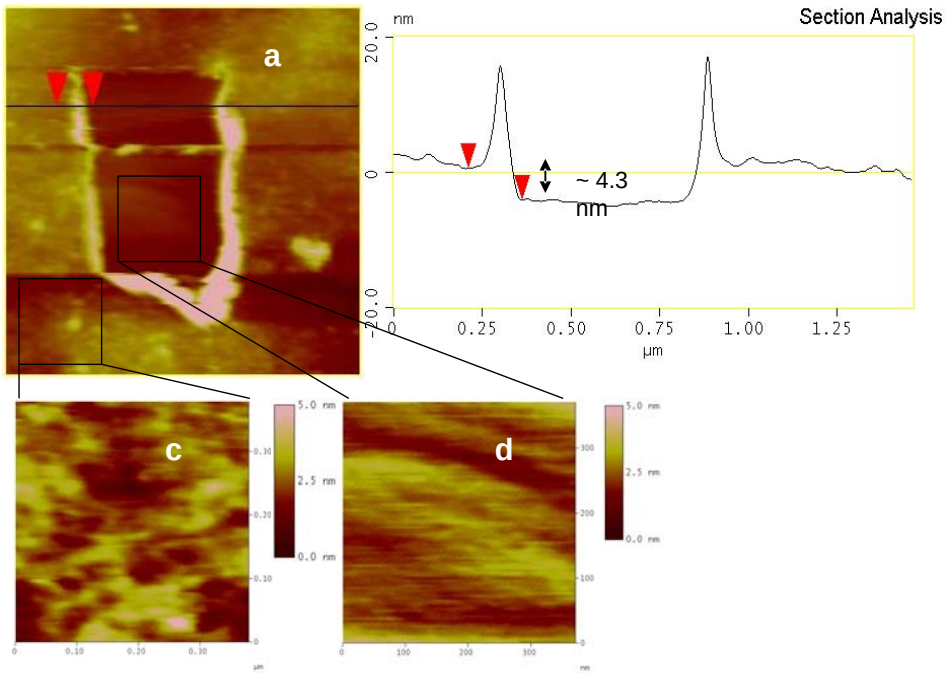

Figure 7.3.4: AFM Image of Nafion® covered Pt(100) surface. Black line shows the position of were the cross section was taken. F_N = 1.5 nN, scan rate 3.6 µms^{-1}. A line by line background subtraction was taken for these images.

Upon continuous increase of the normal load up to 30 nN, scratching of the Nafion® layer from the electrode surface is observed. Figure 4a shows a subsequent (after continuously scanning for 5 minutes with F_N = 30 nN) topographic image of the Nafion® covered Pt(100) surface with a larger scan area of 1.6 µm at low normal load. In the middle of the image a square, irreversible modification caused by application of a normal load of 30 nN can be seen. On the cross section (fig. 4b) it becomes clear that the region of modification is 4.5 to 6 nm deeper than that of a non-modified (Nafion®-covered) surface. The higher value at the edge corresponds to Nafion® which was removed from the surface and piled up at the edge by the tip. This modification is quite consistent with the work performed by Fang and coworkers on polycarbonate materials where nanomechanical properties were evaluated using AFM [33]. Two modified and non-modified areas of fig. 4a are shown as expanded regions in figures 4c and 4d respectively. Obviously, the modified part of the surface is much smoother than the non-modified part, although not smooth on the atomic level. Some Nafion® residues still also seem to adhere to this part of the surface.

The dependence of friction (lateral) force on normal force is shown in fig. 7.3.5. The relationship is quite linear as expected from classical friction laws with a coefficient of friction on Nafion® of 1 to 2. For comparison, the coefficient of friction on metal

electrode surfaces in H_2SO_4 is in the range of 0.1 [8, 27, 34]; on alkanethiol modified gold it is smaller than 0.3 for chain lengths larger than 10 C atoms [35] but increasing up to 1.7 for decreasing chain lengths. For comparison, the coefficient of friction on n-alkane self-assembled monolayers is 0.1 [36]. Obviously, a lubricating effect of organic layers is only observed in the case of well ordered, densely packed films.

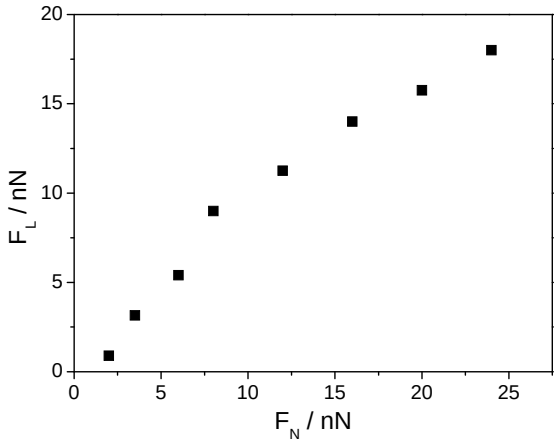

Figure 7.3.5: Lateral vs. normal force on Nafion®/Pt(100) in the $HClO_4$ electrolyte.

Force-deflection curves demonstrate the penetration of the tip into the Nafion® layer. Data are presented as force vs tip-sample distance curves. On a Pt(100) surface which is not modified by Nafion®, the force rises sharply when the tip comes in contact with the surface (fig. 7.3.6a). On a Nafion® covered surface, the tip gradually penetrates or deforms the Nafion® layer (fig. 7.3.6b). After first contact at point a, the tip begins to deform the Nafion® until point b, possibly because some water is expelled from the layer; another possibility is a simple mechanical deformation. The slope between points a and b corresponds to a force constant of the Nafion® layer of 1.2 N/m. After complete penetration, a tip-jump from point b to c is observed; the cantilever relaxes because no more Nafion® is held between the tip and the Pt-surface. The distance of tip-jump corresponds to ~ 4 nm. Typically, the normal force just before complete penetration through the Nafion® is $2 < F_N < 15$ nN. (In some cases, however, force-deflection curves on the Nafion® coated sample were identical to those obtained at the Nafion® free surface. This is certainly due to the incomplete coverage by the film of the electrode surface.) The Cantilever penetration distance (b - c on fig. 7.3.4) has a similar value as the thickness of the Nafion® layer as determined from XPS (3.3 nm) [20]. In reference [20], XPS data for the Nafion® film attached to a Pt(111) electrode followed by subsequent measurements on the freshly argon sputtered surface were compared. This allowed for a thickness of the film to be evaluated based on the known escape

depth of Pt photoelectrons and the geometry of X-ray gun, analyser and crystal surface. Quantification of the various elements present in the layer confirmed a stoichiometry consistent with a dry Nafion® layer, i.e. all water had been driven from the layer upon transfer to vacuum. From the results in fig. 7.3.6b, we also conclude that the thickness of the uncompressed Nafion® layer is about 10 nm (distance between points a and c), whereas the distance of the tip-jump of 4 nm corresponds to a thickness of the Nafion® in a compressed state, probably water-poor state and that determined by XPS (3.3 nm) to the water free state. For figure 7.3.4, where a normal load of 1.5 nN was used, we would expect a depth of about 8 nm, which is close to the maximum depth of 6 nm observed. (Here it has to be taken into account that some residues are left at the 'bottom of the hole'.)

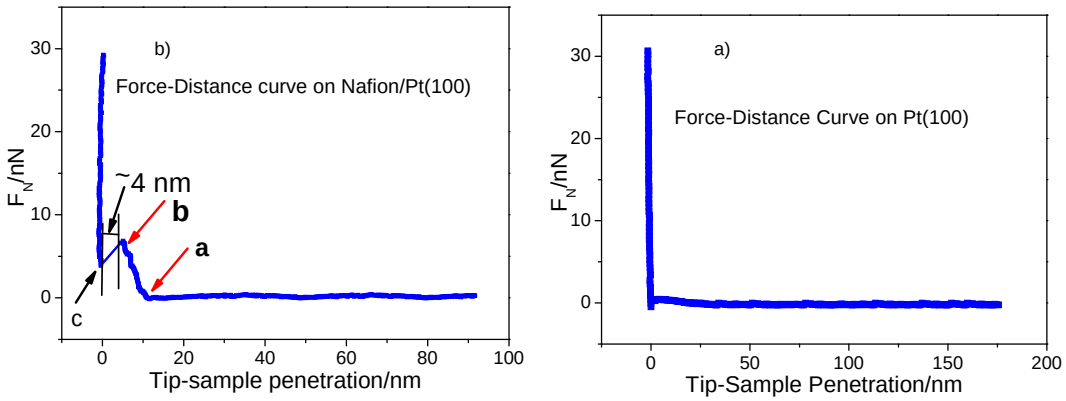

Figure 7.3.6: Deflection (normal load) as a function of tip-sample separation distance curves on Nafion®covered Pt(100) electrode (right, fig. 7.3.6a) and comparison with the behaviour of clean Pt(100) (left, fig. 7.3.6b).

Knowing the normal force at which the tip penetrates the Nafion® layer, we have to discuss the results of figures 7.3.3 and 7.3.4 again. It is clear that at load forces below the critical value for "scratching", i.e., 30 nN, the tip can penetrate into the Nafion® layer under static conditions, i.e. when the tip velocity is zero. Therefore, the height variation in fig. 7.3.3 might correspond to cases where sometimes the tip is penetrating and then when it is not penetrating into the surface. On the other hand, it may well be that under these dynamic conditions, the tip is penetrating only at the higher load, and then the deeper points on the surface would correspond to some holes.

Even at the lowest normal load of 1 nN the tip is compressing the Nafion® layer by 1 nm (cf. fig. 7.3.6b). This is obviously a large perturbation of the Nafion® layer and may well be the origin of the increased roughness as compared to the STM image shown in fig. 7.3.2. Since ordering within the Nafion® layer is much less prevalent than e.g., in

self assembled monlayers (SAM), such a disordering occurs at a much lower normal load. For comparison, in reference [36], tip penetration into an alkaline SAM only occurred around at 30 nN, leading to disordering.

7.3.4 Conclusions

From the STM measurements, we conclude that our preparation method leads to a very smooth, homogeneous Nafion® layer. Unsurprisingly, this layer is soft in that it can be compressed by about 5 nm by the tip and itself has a force constant of about 1.2 N/m. At a normal load of typically 5 nN, the tip completely penetrates the Nafion® layer, and the tip jumps to the Pt surface by another 4 nm, which corresponds to the Nafion® layer thickness previously estimated to be ~ 3.3 nm [20] for a dry Nafion® layer. The friction coefficient is larger than on clean metal electrodes. The Nafion® layer can be removed using a normal force of more than 24 nN. The height difference between the (partially compressed) layer and a part of the surface where the layer had been largely removed corroborates the thickness.

References

[1] R. Wiesendanger, H.-J. Güntherodt, and D. Tomanek, in Scanning Tunneling Microscopy III, Vol. 29, Springer Berlin Heidelberg, 1993, p. 269.
[2] C. M. Mate, G. M. McClelland, R. Erlandsson, and S. Chiang, Physical Review Letters 59:1942 (1987).
[3] L. A. Kibler, Preparation and Characterization of Noble Metals Single Crystal Electrodes, University of Ulm, 2003.
[4] J. A. Rodriguez, S. Chaturvedi, and M. Kuhn, Journal of Chemical Physics 108:3064 (1998).
[5] J. Clavilier, M. Wasberg, M. Petit, and L. H. Klein, Journal of Electroanalytical Chemistry 374:123 (1994).
[6] J. E. Sader, J. W. M. Chon, and P. Mulvaney, Review of Scientific Instruments 70:3967 (1999).
[7] N. Podgaynyy, in department of chemistry, Vol. PhD, University of Bonn, Bonn, 2013.
[8] F. Hausen, M. Nielinger, S. Ernst, and H. Baltruschat, Electrochimica Acta 53:6058 (2008).
[9] D. C. Papageorgopoulos, F. Liu, and O. Conrad, Electrochimica Acta 53:1037 (2007).
[10] F. Dassenoy, W. Vogel, and N. s. Alonso-Vante, The Journal of Physical Chemistry B 106:12152 (2002).
[11] M. Hoon-Khosla, W. R. Fawcett, A. C. Chen, J. Lipkowski, and B. Pettinger, Electrochimica Acta 45:611 (1999).
[12] A. G. Brolo, D. E. Irish, and J. Lipkowski, Journal of Physical Chemistry B 101:3906 (1997).
[13] W. B. Cai, L. J. Wan, H. Noda, Y. Hibino, K. Ataka, and M. Osawa, Langmuir 14:6992 (1998).
[14] L. Stolberg, S. Morin, J. Lipkowski, and D. E. Irish, Journal of Electroanalytical Chemistry 307:241 (1991).
[15] A. Hamelin, in Modern Aspects of Electrochemistry, Vol. 16 (B. E. Conway, R. E. White, and J. O. M. Bockris, eds.), Plenum Press, 1985, p. 4.
[16] R. Hiesgen, I. Wehl, E. Aleksandrova, E. Roduner, A. Bauder, and K. A. Friedrich, International Journal of Energy Research 34:1223 (2010).
[17] R. Subbaraman, D. Strmcnik, A. P. Paulikas, V. R. Stamenkovic, and N. M. Markovic, ChemPhysChem 11:2825 (2010).
[18] R. Subbaraman, D. Strmcnik, V. Stamenkovic, and N. M. Markovic, The Journal of Physical Chemistry C 114:8414 (2010).
[19] A. M. Gomez-Marin, A. Berna, and J. M. Feliu, Journal of Physical Chemistry C 114:20130 (2010).
[20] M. Ahmed, D. Morgan, G. A. Attard, E. Wright, D. Thompsett, and J. Sharman, The Journal of Physical Chemistry C 115:17020 (2011).
[21] R. Hiesgen, D. Eberhardt, E. Aleksandrova, and K. A. Friedrich, Fuel Cells 06:425 (2006).
[22] R. Koestner, Y. Roiter, I. Kozhinova, and S. Minko, Langmuir 27:10157 (2011).
[23] K. A. Mauritz and R. B. Moore, Chemical Reviews 104:4535 (2004).
[24] T. Masuda, K. Ikeda, and K. Uosaki, Langmuir 29:2420 (2013).
[25] T. Masuda, F. Sonsudin, P. R. Singh, H. Naohara, and K. Uosaki, The Journal of Physical Chemistry C 117:15704 (2013).
[26] F. J. Vidal-Iglesias, J. Solla-Gullon, J. M. Feliu, H. Baltruschat, and A. Aldaz, Journal of Electroanalytical Chemistry 588:331 (2006).

[27] M. Nielinger and H. Baltruschat, Physical Chemistry Chemical Physics 9:3965 (2007).
[28] H.-Y. Jung and J. W. Kim, International Journal of Hydrogen Energy 37:12580 (2012).
[29] H. R. Corti, F. Nores-Pondal, and M. P. Buera, Journal of Power Sources 161:799 (2006).
[30] A. M. Bittner, J. Wintterlin, B. Beran, and G. Ertl, Surface Science 335:291 (1995).
[31] N. Garcia-Araez, V. Climent, E. Herrero, and J. M. Feliu, Surface Science 560:269 (2004).
[32] R. Hiesgen, E. Aleksandrova, G. Meichsner, I. Wehl, E. Roduner, and K. A. Friedrich, Electrochimica Acta 55:423 (2009).
[33] T.-H. Fang, W.-J. Chang, and S.-L. Tsai, Microelectronics Journal 36:55 (2005).
[34] F. Hausen, N. N. Gosvami, and R. Bennewitz, Electrochimica Acta 56:10694 (2011).
[35] M. T. McDermott, J.-B. D. Green, and M. D. Porter, Langmuir 13:2504 (1997).
[36] L. Lu and Y. Cai, Langmuir 27:5953 (2011).

Summary

Apart from expensive metals, metal chalcogenides are considered as catalyst because they facilitate the ORR and tolerate organics. Existing studies in this area concentrate on nanoparticles, consequently offering little knowledge of the role of the atomic surface structure and composition in the promotion of selective ORR catalysis. Additionally, research has not yet resolved the stability issues of the adsorbed chalcogenide layer. Therefore, it is vital to study cathode surfaces in low temperature fuel cells to improve the efficiency of energy conversion and to furnish environmental benefits.

The selenium modified model catalysts were examined with the scanning probe microscope in order to visualize the adlattices of adsorbed atoms, ions or molecules at atomic level. The adlayer structure of SO_4^{2-} on Rh(111) was also studied. Based on the images obtained, the orientation of the Rh(111) substrate was determined and a mathematical procedure was developed to determine the drift, to correct for it and to calibrate the STM scanner (appendix A). The Se adlayer structure was atomically resolved by both STM and AFM. A $2x\sqrt{3}$ structure was obtained by STM with a surface coverage of $\vartheta = 0.25$, coinciding well with the deposited charge. A similar structure was also observed in friction images (atomic stick slip). These images could only be obtained at coverages close to but just below those at which the roughening of the surface starts. This roughening is most probably due to the place exchange between Rh and Se atoms similar to the well known roughening of Pt surfaces in the oxygen adsorption region.

The in situ STM studies of the Se/Rh(111) system showed that with Se surface coverage of around $\vartheta = 0.25$, a roughening starts at the steps and then extends to terraces; within a short time the whole surface becomes modified. It was observed that the surface roughening occurs around 0.55 V in SeO_3^{2-} containing solution. Moreover, around $\vartheta = 0.1$ atomically smooth isolated domains of Se were observed which merged together at more negative potentials in Se free solution. A minimum surface coverage of $\vartheta = 0.2$ was required to observe this roughening in SeO_3^{2-} free solution, which, however occurred at more negative potentials than observed in SeO_3^{2-} containing solution.

Additionally, the stability of the adsorbed selenium on model metal *fcc* surfaces such as Rh(111), Pt(111) and Au(111) was explored. The focus was on the electrochemical desorption of the selenide from selenium modified model surfaces through differential electrochemical mass spectrometry under controlled flow through conditions.

Through the experiments with DEMS, not only was qualitative data obtained but also a quantitative study of the amounts of reductively dissolved selenium as selenide at low potentials could be made. At these potentials close to hydrogen evolution, and in the absence of selenium containing solution, the formation of the H_2Se species involved the transfer of two electrons only. However, in the presence of selenious acid H_2Se species could also proceed via six electrons. The SPM technique, especially AFM, also confirmed the formation of Se particles at a lower potential of around 0 V vs. RHE.

The ORR activity of Rhodium single crystalline surface (Rh(111)) and its electrochemical modification with Selenium (Se) submonolayer loadings was investigated in acidic media. ORR activity of these model Se/Rh(111) surfaces was carried out in the modified dual thin layer flow through cell (DTLFC) developed in our group for differential electrochemical mass spectrometric (DEMS) studies.

The potential of zero charge was found to be ~0.2 V vs RHE from CO charge displacement experiment at various fixed potentials. The oxygen reduction proceeds mainly via four electrons with small amount of H_2O_2 generation on Rh(111) and Se modified Rh(111). Electrochemical modification of Rh(111) by Se submonolayers resulted in a better ORR activity. A Se coverage of ϑ_{Se} = 0.1 leads to the best ORR catalytic activity with an anodic shift of the onset potential by ~ 40 mV that of pure Rh(111). However, a surface coverage of about 0.18 would completely block the Rh(111) sites and would hamper its ORR activity. Astonishingly, one Se atoms block five Rh sites from both adsorbing hydrogen and CO. A large tolerance of such an ORR catalyst surface with respect to all kinds of organic fuel can thus be expected.

I compared the surface morphologies of inductively heated selenium modified Rh(111) surfaces under controlled environment with that of simple selenium modified surfaces using scanning tunnelling microscopy (STM). Additionally, the surface morphologies of heat treated surfaces resulted in atomically smooth deposits, which remained stable with

in the potential window used for ORR studies. A higher oxidation potentials, some Se stripped off the surface which redeposited at negative potentials. Surface areas of (Se/Rh(111) surfaces modified and heat treated at different temperatures were also determined using CO stripping experiments. Oxygen reduction activity of these heat treated modified surfaces was monitored using dual thin layer flow cell under controlled conditions. The heat treated Se/Rh(111) showed better ORR activity than that of pure Rh(111).

Also friction was studied on a selenium modified *fcc*(111) surfaces (namely Rh, Pt and Au) for various coverages. Investigations at three surfaces were performed under electrochemical conditions which offered some advantages in comparison to those performed under ultra high vacuum (UHV) conditions. Furthermore, friction was studied in the presence of pyridine. Pyridine adsorbed on Au (111) was used as a model system to understand the effect of organic adsorbates.

In the third part of these AFM experiments the surface morphology of the Nafion®/Pt(100) interface was studied. The structure and molecular processes occurring at the Nafion® membrane/electrode interface are least understood. To have a better understanding the nano-scale properties of the Pt(100)/ Nafion® interface were investigated by using STM and AFM. In STM, the surface morphology of the thin Nafion® film appeared smooth on the atomic scale; monoatomic steps of the substrate were clearly visible. The thickness of the Nafion® membrane was determined using AFM tip penetration experiments and also by scratching the Nafion® layer from the electrode surface. Force deflection ("approach") curves demonstrated that the tip penetrated in the Nafion® layer at a normal force greater than 5 nN.

Appendix A: Drift calculation for atomically resolved images

Thermal drift is a normal problem in scanning probe microscopic techniques, especially when acquiring atomically resolved images in liquid and under potential control. Calculations are performed to determine drift, based on below mentioned assumptions.

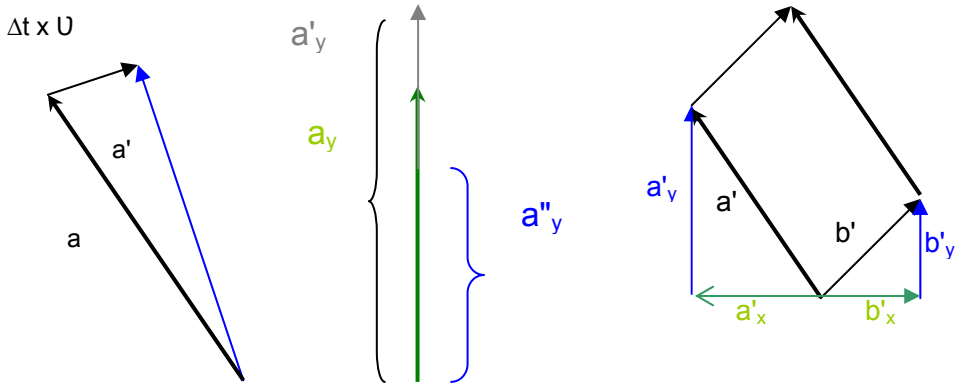

a is actual vector, however, due to drift a‘ is visualised	Due to drift, atomic distances vary in consecutive scans.	Simple trigonometric principles were used to calculate drift.

a'_y and a''_y are apparent lattice vectors along scan 'up' and scan 'down'; respectively.

Drift velocity $\vec{\upsilon} = (\upsilon_x, \upsilon_y)$

Scan velocity = C'_y = (Scan size X Scan rate) / No. of lines of scan Images along Y-direction

For Vector a':

$$\vec{a} + \vec{\upsilon} \cdot a'_y / C'_y = \vec{a'}$$

For Vector b':

$$\vec{b} + \vec{\upsilon} \cdot b'_y / C'_y = \vec{b'} \qquad \text{A.1}$$

After rearrangement

$$\vec{a} = \vec{a'} - \vec{\upsilon} \cdot a'_y / C'_y$$

$$\vec{b} = \vec{b'} - \vec{\upsilon} \cdot b'_y / C'_y \qquad \text{A.2}$$

For Vector a'':

$$\vec{a} - \vec{\upsilon} \cdot a''_y / C'_y = \vec{a''}$$

For Vector b'':

$$\vec{b} - \vec{\upsilon} \cdot b''_y / C'_y = \vec{b''} \qquad \text{A.3}$$

After rearrangement

$$\vec{a} = \vec{a''} + \vec{\upsilon} \cdot a''_y / C'_y$$

$$\vec{b} = \vec{b''} + \vec{\upsilon} \cdot b''_y / C'_y \qquad \text{A.4}$$

By comparing eqn. A.2 with A.4, the drift velocity is calculated

$$\vec{a}' - \vec{\upsilon} \cdot a'_y / C'_y = \vec{a}'' + \vec{\upsilon} \cdot a'_y / C'_y \qquad \vec{b}' - \vec{\upsilon} \cdot b''_y / C'_y = \vec{b}'' + \vec{\upsilon} \cdot b''_y / C'_y \qquad \text{A.5}$$

$$\vec{\upsilon} \cdot (a'_y - a''_y) / C'_y = (\vec{a}' - \vec{a}'') \qquad \vec{\upsilon} \cdot (b'_y - b''_y) / C'_y = (\vec{b}' - \vec{b}'') \qquad \text{A.6}$$

$$\vec{\upsilon} = (\vec{a}' - \vec{a}'') \cdot C'_y / (a'_y - a''_y) \qquad \vec{\upsilon} = (\vec{b}' - \vec{b}'') \cdot C'_y / (b'_y - b''_y) \qquad \text{A.7}$$

Atomic Vector calculations for SO_4^{2-} on Rh(111)

Atomic distance Vector a' = 0.7605 nm, & Atomic distance Vector b' = 0,505 nm

(Image S120607.032) (fig. 3.9)

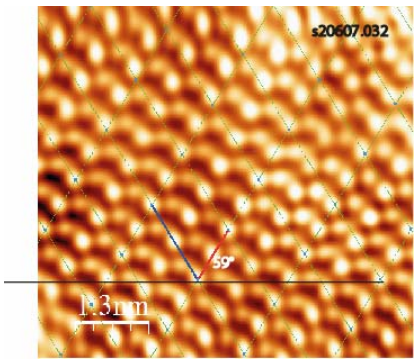

Two atoms taken along Vector a' 1.521 Vector a'

Two atoms taken along Vector b' 1.01 Vector b'

Calculation for a'_x & a'_y using Phythagorus theorem

Angle for Vector a along Perpendicular = 59 °

a'_y = Sin59° x magnitude of Vector a' = 1.304 nm,

a'_x = Cos59° x magnitude Vector a' = -0.783 nm

Vector a' = (a'_x, a'_y) = (-0.783, 1.304)

Calculation for b'_x & b'_y using Phythagorus theorem

Angle for Vector a along Perpendicular = 59°

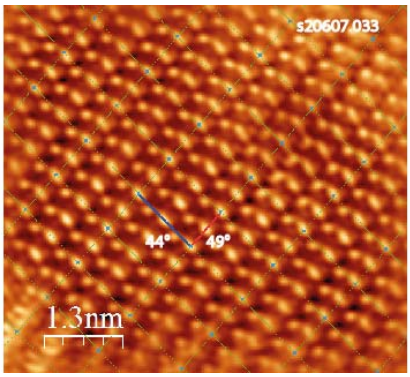

b'_y = Sin59° · magnitud Vector b' = 0.866 nm,

b'_x = Cos59° · magnitud Vector b' = 0.52 nm

Vector b' = (b'_x, b'_y) = (0.52, 0.866)

Calculations for Image S120607.033 for SO_4^{2-}

Atom distance Vector a'' = 0.6025 nm,

Atom distance Vector b'' = 0.372 nm

Two atoms taken along Vector a'' = 1.205 Vector a''

Two atoms taken along Vector b'' = 0.744 Vector b''

Calculation for a''x & a''y using Phythagorus theorem

Angle determined for Vector a along Perpendicular = 44°

a''_y = Sin44° · magnitud Vector a'' = 0.837 nm,

a''_x = Cos44° · magnitud Vector a'' = -0.867 nm

Vector a'' = (a''_x, a''_y) = (-0.867, 0.837)

Calculation for b''x & b''y using Phythagorus theorem

Angle determined for Vector a along Perpendicular = 49°

b''_y = Sin49° · magnitud Vector b'' = 0.562 nm,

b''_x = Cos49° · magnitud Vector b'' = 0.49 nm

Vector b'' = (b''_x, b''_y) = (0.49, 0.562)

Drift velocity $\vec{\upsilon} = (\upsilon_x, \upsilon_y)$

Scan velocity = C'_y = (Scan Size · Scan Rate)/No. of lines of Scan Images along Y-dir.

Scan Velocity (C'_y) 0.745 (nm/s)

The drift velocities were calculated by substituting the scan velocity with vector components in eq. A.7

$$\vec{\upsilon} = (\vec{a'} - \vec{a''}) \cdot C'_y / (a'_y - a''_y) \qquad \vec{\upsilon} = (\vec{b'} - \vec{b''}) \cdot C'_y / (b'_y - b''_y) \qquad \text{A.7}$$

For Vector a': **For Vector b':**

$\vec{\upsilon} = (0.017,\ 0.097)$ $\vec{\upsilon} = (0.01,\ 0.095)$

Calculating the components of vector a & b using eqn. A.2 and A.4

$$\vec{a} = \vec{a'} - \vec{\upsilon} \cdot a'_y / C'_y \qquad \vec{b} = \vec{b'} - \vec{\upsilon} \cdot b'_y / C'_y \qquad \text{A.2}$$

$$\vec{a} = \vec{a''} + \vec{\upsilon} \cdot a''_y / C'_y \qquad \vec{b} = \vec{b''} + \vec{\upsilon} \cdot b''_y / C'_y \qquad \text{A.4}$$

Based on above equation components of vector **a & b** are calculated as under

Vector a = (a_x, a_y) = (-0.834, 1.02) & Vector b = (b_x, b_y) = (0.50, 0.682)

Calculations of Vector a and vector b from its components vectors

$|a| = \mathrm{Sqrt}(a_x^2 + ay^2)$ $\quad$ $|\mathbf{b}| = \mathrm{Sqrt}\,(b_x^2 + b_y^2)$

$|a|$ **= 1.32** $\quad$ $|\mathbf{b}|$ **= 0.85**

As both vectors compose of 2 lattice vectors, one lattice would be

$\left|\vec{a}\right| = 0.66$ $\quad$ $\left|\vec{b}\right| = 0.423$

$\theta_a = \tan^{-1}(a_y / a_x) = 50.7^\circ$ $\quad$ $\theta_b = \tan^{-1}(b_y / b_x) = 53.7^\circ$

Therefore angle between vector a & b is = 180-50,7-53,7 = **75.6°**

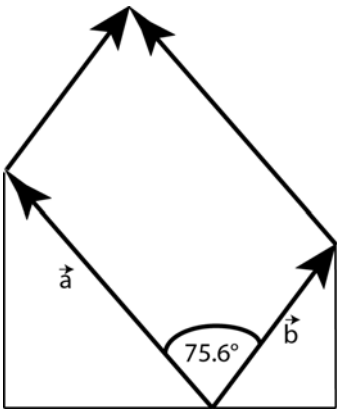

Calibration of the scanner using the SO_4^{2-} adlayer

Drift Corrected Vectors a & b

$$\left|\vec{a}\right| = 0.66 \qquad \left|\vec{b}\right| = 0.423$$

Actual (theoretical) sulfate adlayer vectors are

$$\left|\vec{A}\right| = 0.71 \qquad \left|\vec{B}\right| = 0.46$$

Vector components of a,A and b, B can be written as

$$\mathbf{A} = \begin{pmatrix} A_{1x} & A_{2x} \\ A_{1y} & A_{2y} \end{pmatrix} \qquad \mathbf{a} = \begin{pmatrix} a_x & b_x \\ a_y & b_y \end{pmatrix}$$

Also, Vector **a** is compared to theoretical vector using matrix vector as below

$$A = M \cdot a \qquad \text{A.8}$$

$$\begin{pmatrix} M_{11} & M_{12} \\ M_{21} & M_{22} \end{pmatrix} = \begin{pmatrix} A_{1x} & A_{2x} \\ A_{1y} & A_{2y} \end{pmatrix} \begin{pmatrix} b_y & -b_x \\ -a_y & a_x \end{pmatrix} 1/(a_x \cdot b_y - b_x \cdot a_y)$$

Matrix is determined using component vectors

Component Vector for the theoretical sulfate adlayer

Vector A_1

$A_{1y} = A_1.\text{Sin}56.5° = 0.59206$

$A_{1x} = A_1.\text{Cos}56.5° = 0.39186$

$A_1 (A_{1x}, A_{1y})$ **= (-0.392, 0.592)**

Vector A_2

$A_{2y} = A_2.\text{Sin}51.5° = 0.2864$

$A_{2x} = A_2.\text{Cos}51.5° = 0.36$

A_2 (A_{2x}, A_{2y}) = (0.2864, 0.36)

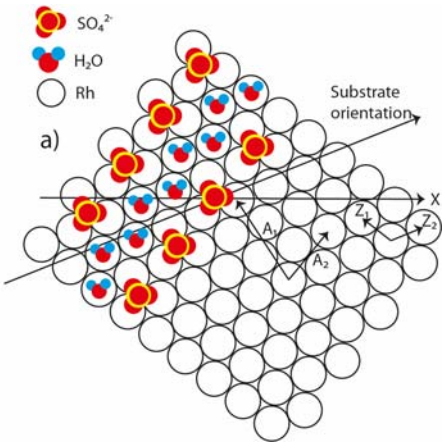

Similarly, drift corrected vectors A_1 & A_2 for sulfate adlayer

Vector **a** = ($\mathbf{a_x}$, $\mathbf{a_y}$) = (-0.834, 1.02) & Vector **b** = ($\mathbf{b_x}$, $\mathbf{b_y}$) = (0.50, 0.68)

a_x = -0.4171, a_y = 0,5098 b_x = 0.2504, b_y = 0.3406

By substituting the values of vector a, & b' to determine transpose of vector **a**

$$\mathbf{a}^{-1} = 1/(-0{,}27) \begin{pmatrix} 0.34 & -0.25 \\ -0.51 & -0.42 \end{pmatrix} = \begin{pmatrix} -1.26 & 0.93 \\ 1.9 & 1.55 \end{pmatrix}$$

Evaluation of calibration matrix using the eqn. 3.8 by substituting the value of matrix a

$$\begin{pmatrix} M_{11} & M_{12} \\ M_{21} & M_{22} \end{pmatrix} = \begin{pmatrix} -0.392 & 0.27 \\ 0.592 & 0.372 \end{pmatrix} \begin{pmatrix} -1.26 & 0.93 \\ 1.9 & 1.55 \end{pmatrix}$$

Hence, the matrix would be

$$\begin{pmatrix} M_{11} & M_{12} \\ M_{21} & M_{22} \end{pmatrix} = \begin{pmatrix} 1.037 & 0.079 \\ -0.066 & 1.11 \end{pmatrix}$$

Control of the calculation of the martix M

$$\begin{pmatrix} A_{1x} & A_{2x} \\ A_{1y} & A_{2y} \end{pmatrix} = \begin{pmatrix} 1.037 & 0.0796 \\ -0.066 & 1.11 \end{pmatrix} \begin{pmatrix} -0.4171 & 0.2504 \\ 0.5097 & 0.3406 \end{pmatrix}$$

$$\begin{pmatrix} A_{1x} & A_{2x} \\ A_{1y} & A_{2y} \end{pmatrix} = \begin{pmatrix} (1.037*-0.4171)+(0.079*0.5097) & (1.037*0.2504)+(0.079*0.3406) \\ (-0.066*-0.4171)+(1.13*0.5097) & (-0.066*0.2504)+(1.11*0.3406) \end{pmatrix}$$

$$\begin{pmatrix} A_{1x} & A_{2x} \\ A_{1y} & A_{2y} \end{pmatrix} = \begin{pmatrix} -0.392 & 0.27 \\ 0.59206 & 0.36 \end{pmatrix}$$

Hence, after substituting the experimental values and multiplying matrix a with calibration matrix the matrix A is obtained again.

Drift Corrected vectors for Selenium using images s20607.082 & s20607.083 (fig. 3.10)

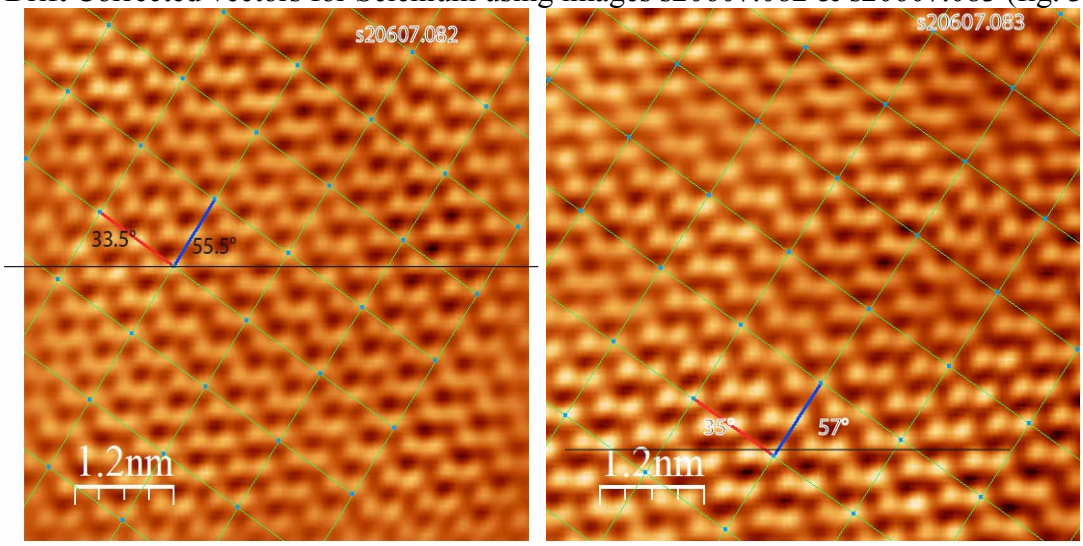

Vector $l_1 = (l_{1x}, l_{1y}) = (-0.82, 0.583)$ and vector $l_2 = (l_{2x}, l_{2y})) = (0.50, 0.748)$

Calculations of Vector a and vector b from its components vectors

$|\mathbf{l_1}| = \text{Sqrt}(L_{1x}^2 + L_{1y}^2)$ $\qquad$ $|\mathbf{l_2}| = \text{Sqrt}\,(l_{2x}^2 + l_{2y}^2)$

$|\mathbf{l_1}| = \mathbf{1.005}$ $\qquad$ $|\mathbf{l_2}| = \mathbf{0.9}$

As both vectors compose of 2 lattice vectors, one lattice would be

$|\mathbf{l_1}| = \mathbf{0.503}$ $\qquad$ $|\mathbf{l_2}| = \mathbf{0.45}$

$\theta_{l1} = \tan^{-1}(l_{1y}/l_{1x}) = 33.45^\circ$ $\qquad$ $\theta_{l_2} = \tan^{-1}(l_{2y}/l_{2x}) = 56.24^\circ$

Therefore angle between vector $\mathbf{l_1}$ and $\mathbf{l_2}$ is = 180-50.7-53.7 = **88.31°**

Similarly, drift corrected vectors L_1 & L_2

$l_{1x} = -0.409$, $l_{1y} = 0.292$ $\qquad$ $l_{2x} = 0.2498$, $l_{2y} = 0.3728$

with , $L = M \cdot l$ A.9

$$\begin{pmatrix} L_{1x} & L_{2x} \\ L_{1y} & L_{2y} \end{pmatrix} = \begin{pmatrix} 1.037 & 0.079 \\ -0.066 & 1.11 \end{pmatrix} \begin{pmatrix} -0.409 & 0.245 \\ 0.292 & 0.373 \end{pmatrix}$$

$$\begin{pmatrix} L_{1x} & L_{2x} \\ L_{1y} & L_{2y} \end{pmatrix} = \begin{pmatrix} -0.401 & 0.289 \\ 0.3497 & 0.3975 \end{pmatrix}$$

$|\mathbf{L_1}| = \mathbf{0.532}$ $\qquad$ $|\mathbf{L_2}| = \mathbf{0.4914}$

$\theta_{L1} = \tan^{-1}(L_{1y}/L_{1x}) = 41^\circ$ $\qquad$ $\theta_{L_2} = \tan^{-1}(L_{2y}/L_{2x}) = 54^\circ$

Therefore angle between vector L_1 and L_2 is = 180-54-41 = **85°**

Drift Corrected vectors for Selenium using images s20503.016 & s20503.017 (fig. 3.12)

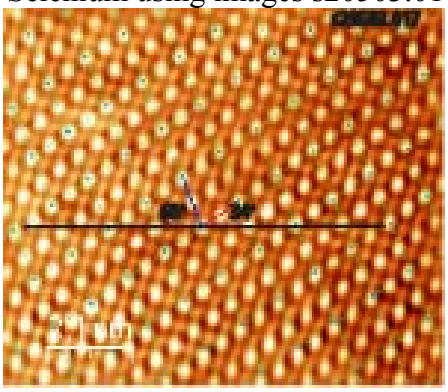

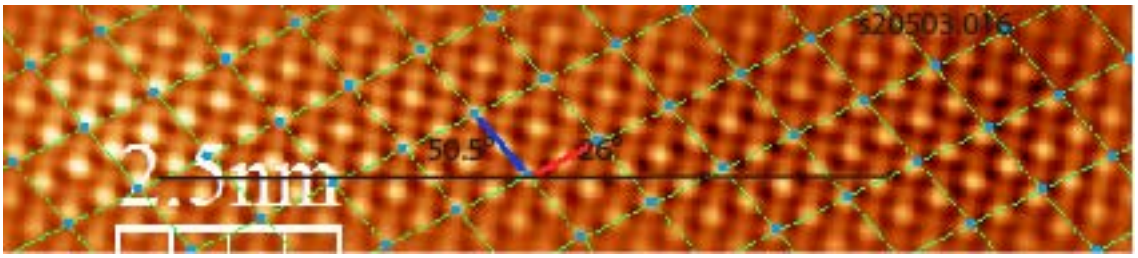

Vector $l'_1 = (l'_{1x}, l'_{1y}) = (0.511, 0.953)$ and vector $l_2' = (l'_{2x}, l'_{2y}) = (0.81, 0.457)$

Calculations of Vector a and vector b from its components vectors

$|\mathbf{l'_1}| = \text{Sqrt}(\mathbf{l'_{1x}}^2 + \mathbf{l'_{1y}}^2)$ $\qquad$ $|\mathbf{l'_2}| = \text{Sqrt}(\mathbf{l'_{2x}}^2 + \mathbf{l'_{2x}}^2)$

$|\mathbf{l'_1}| = \mathbf{1.08}$ $\qquad$ $|\mathbf{l'_2}| = \mathbf{0.93}$

As both vectors compose of 2 lattice vectors, one lattice would be

$|\mathbf{l'_1}| = \mathbf{0.54}$ $\qquad$ $|\mathbf{l'_2}| = \mathbf{0.465}$

$\theta_{l'1} = \tan^{-1}(l'_{1y}/l'_{1x}) = 61.8^\circ$ $\qquad$ $\theta_{l'_2} = \tan^{-1}(l'_{2y}/l'_{2x}) = 29.5^\circ$

Therefore angle between vector $\mathbf{l'_1}$ and $\mathbf{l'_2}$ is = 180-61.8-29.5 = **88.7°**

Similarly, drift corrected vectors L'_1 and L'_2 for calibration scanner

$\mathbf{l'_{1x}} = -0.2555$, $\mathbf{l'_{1y}} = 0.476311$ $\quad$ $\mathbf{l'_{2x}} = 0.40403$, $\mathbf{l'_{2y}} = 0.228726$

with, $L' = M \cdot l'$ A.10

$$\begin{pmatrix} L'_{1x} & L'_{2x} \\ L'_{1y} & L'_{2x} \end{pmatrix}_y = \begin{pmatrix} 1.037 & 0.079 \\ -0.066 & 1.11 \end{pmatrix} \begin{pmatrix} -0.256 & 0.404 \\ 0.476 & 0.229 \end{pmatrix}$$

$$\begin{pmatrix} L'_{1x} & L'_{2x} \\ L'_{1x} & L'_{2x} \end{pmatrix} = \begin{pmatrix} -0.2271 & 0.4372 \\ 0.5441 & 0.2266 \end{pmatrix}$$

$L'_1 = 0.5896$ $\qquad$ **$L'_2 = 0.4925$**

$\theta_{L'1} = \tan^{-1}(L'_{1y}/L'_{1x}) = 67.35^\circ$ $\qquad$ $\theta_{L'_2} = \tan^{-1}(L'_{2y}/L'_{2x}) = 27.5^\circ$

Therefore angle between vector $\mathbf{L'_1}$ and $\mathbf{L'_2}$ is = 180-67.35-27.5 = **85.15°**

Evaluation of the adlayer structure in matrix notation

The two lattice vectors Z_1 and Z_2 considers for the substrate (Rh(111)) as per model.

The substrate vectors (matrix Z) and the sulfate vectors (matrix A) are related by

$$A = S \cdot Z \qquad \text{A.11}$$

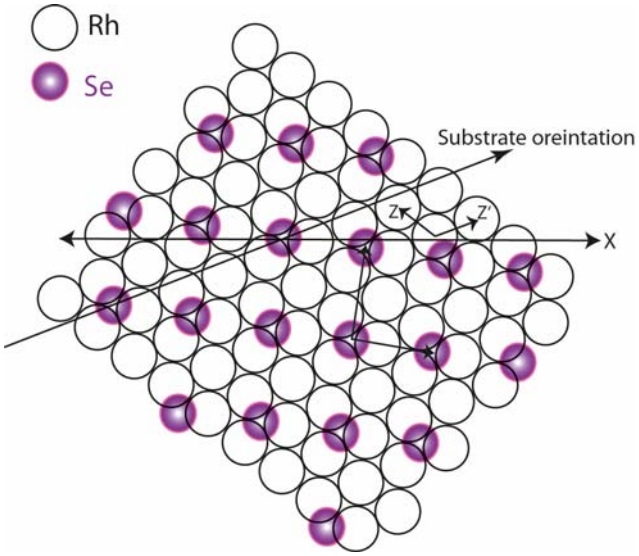

Vector $Z_1 = (Z_{1x}, Z_{1y}) = (-0.208275, 0.168658)$ and Z_2 ($Z_{2x}, Z_{2y}) = (0.2502, 0.096043)$

Hence the substrate Matrix would be

$$\begin{pmatrix} Z_{1x} & Z_{2x} \\ Z_{2x} & Z_{2y} \end{pmatrix} = \begin{pmatrix} -0.21 & 0.25 \\ 0.17 & 0.096 \end{pmatrix}$$

We also determined the Sulfate adlayer matrix, which is

$$\begin{pmatrix} A_{1x} & A_{2x} \\ A_{1y} & A_{2y} \end{pmatrix} = \begin{pmatrix} -0.392 & 0.286 \\ 0.592 & 0.36 \end{pmatrix}$$

These matrices relate each other with eq. A.11 which is used to get Matrix for sulfate adlayer

$$A = S \cdot Z \quad \Leftrightarrow \quad S = Z^{-1} \cdot A \qquad \text{A.12}$$

$$S = \begin{pmatrix} 2.99 & 1.0 \\ 0.92 & 1.98 \end{pmatrix}$$

Similarly, matrix is determined for Se adlayer

$$L = T \cdot 1 \quad \Leftrightarrow \quad T = 1^{-1} \cdot L \qquad \text{A.13}$$

$$T = \begin{pmatrix} 1.81 & 1.1 \\ -0.13 & 1.93 \end{pmatrix} \sim \begin{pmatrix} 2 & 1 \\ 0 & 1 \end{pmatrix}$$

Evaluation of the adlayer structure in matrix notation

The two lattice vectors Z_1 and Z_2 considers for the substrate (Rh(111)) as per model.

The substrate vectors (matrix Z) and the sulfate vectors (matrix A) are related by

$$A = S \cdot Z \qquad \text{A.11}$$

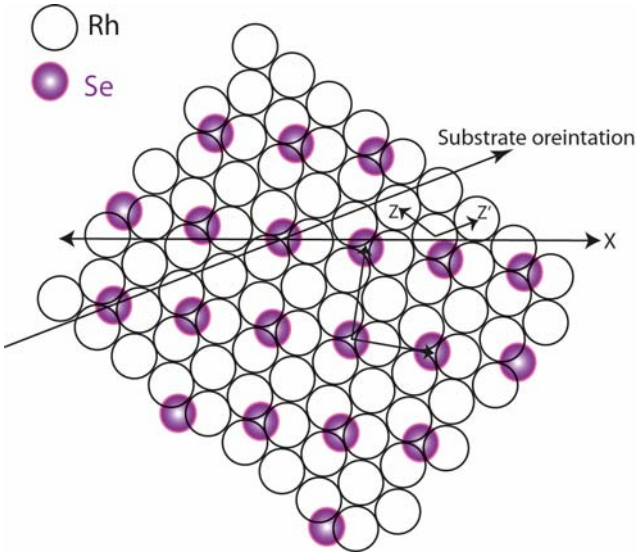

Vector $Z_1 = (Z_{1x}, Z_{1y}) = (-0.208275, 0.168658)$ and Z_2 ($Z_{2x}, Z_{2y}) = (0.2502, 0.096043)$

Hence the substrate Matrix would be

$$\begin{pmatrix} Z_{1x} & Z_{2x} \\ Z_{2x} & Z_{2y} \end{pmatrix} = \begin{pmatrix} -0.21 & 0.25 \\ 0.17 & 0.096 \end{pmatrix}$$

We also determined the Sulfate adlayer matrix, which is

$$\begin{pmatrix} A_{1x} & A_{2x} \\ A_{1y} & A_{2y} \end{pmatrix} = \begin{pmatrix} -0.392 & 0.286 \\ 0.592 & 0.36 \end{pmatrix}$$

These matrices relate each other with eq. A.11 which is used to get Matrix for sulfate adlayer

$$A = S \cdot Z \quad \Leftrightarrow \quad Z = S^{-1} \cdot A \qquad \text{A.12}$$

Where S from the model is ,

$$S = \begin{pmatrix} 3 & 1 \\ 1 & 2 \end{pmatrix}$$

Therefore,

From this, the matrix of the Se adlayer is calculated

$$L = T \cdot S \quad \Leftrightarrow \quad T = S^{-1} \cdot L \qquad \text{A.13}$$

$$T = \begin{pmatrix} 1.81 & 1.1 \\ -0.13 & 1.93 \end{pmatrix} \sim \begin{pmatrix} 2 & 1 \\ 0 & 1 \end{pmatrix}$$

Appendix B: Selenium electrochemistry on single crystal electrode surfaces

B.1 Introduction:

The Selenium electrochemistry on metal electrode surfaces plays a vital role in a diverse field of applications such as in solar cell, direct alcohol fuel cells electrocatalysts, batteries and in optoelectronic application [1, 2]. Our interest in the selenium electrochemical deposition on metal electrodes, being the simplest method to generate metal selenides. A detailed introduction about the Se electrochemistry already discussed in chapter 4.

Till now, in the literature, fundamental studies on chalcogenides of model surfaces are not performed experimentally except Au single crystalline surfaces [3, 4]. Rossimal and co-workers were the first to explain the effect of the chalcogen coverages on model catalysts in relation to their activity, selectivity and stability by employing theoretical approach [5]. Among all metal chalcogenides, chalcogenides of ruthenium are considered more active. Stolbov tried to explain activity of Se/Ru(0001) surface by using DFT. His explanation was based on the argument that Se adatoms enhanced electrostatic repulsion of adsorbed intermediates. Therefore, intermediate bind to modified surface, less strongly resulted in better ORR activity [6].

In our current work, electrochemistry of Se of noble model metals such Au, Pt and transition metal model surfaces namely Rh and Ru surfaces were explored in detail. We have done preliminary work on the electrochemical deposition of Se on above mentioned electrodes to generate their respective metal selenides.

B.2 Experimental

Preparation and electrochemistry of massive single crystal electrodes

The usual annealing process followed by cooling down in argon atmosphere was successfully used for the preparation of Pt(111), Pt(100) and Au(111) was also used for Rh(111) and Rh(100) electrode using a mixture of Ar:H_2 (2:1) gas as described elsewhere [7-9]. Also, the Ru(0001) electrode was prepared using induction heating method [10]. Rh(111), Pt(111), Pt(100), Ru(0001), Rh(100) and Au(111) single crystal electrodes with a diameter of 10 mm were used,(Kristallhandel Kelpin, Germany,

Goodfellow UK and Mateck Germany respectively). All solutions were prepared from 18.2 MΩ Milli-Q water and de-aerated with high purity argon gas (99.999%).

Electrochemical experiments in 0.1 M $HClO_4$ and 0.1 M H_2SO_4 (spectro pure grade) were carried out in a conventional three electrode H-cell in a hanging-meniscus configuration with a large Pt sheet as counter electrode. A reversible hydrogen electrode was employed as a reference electrode. Selenium submonolayer and multilayer deposits were produced in a similar H-cell containing 1 mM H_2SeO_3 (Analytical grade). A bi-potentiostat from Pine Instruments Inc. model AFBPC1 in combination with a user interface developed in Labview software was used for recording cyclic voltammograms (CV).

B.3 Results and discussion

B.3.1 Electrochemistry of Se on massive Rh, Pt and Au single crystalline electrodes

The electrochemistry of Se on massive single crystalline electrode surfaces (Rh, Pt, Au and Ru would be described in detail.

B.3.1.1 Spontaneous Se deposition

Spontaneous deposition of selenium on electrode surface may occur at rest potential. This can be achieved by simply immersing the freshly prepared single crystalline surfaces into 1 mM H_2SeO_3 solution. The adsorbed adlayer quantity may differ based on the immersion time, solution concentration and the type of electrode. In our case each single crystal electrode was immersed in Se containing solution for 1 minute at rest potential. The modified surface was than transferred back to the H-cell and the surface was checked by cyclic voltammetry. An overlay of Rh(111) voltammogram with spontaneous selenium deposited Rh(111) surface is shown in Fig. B.1. This clearly indicates that Se deposition is slightly hindered due to presence of oxygenated species on Rh(111) surface. This is also evident in case of polycrystalline rhodium electrode as well, even at more negative potential in order to reduce these oxygenated species (not shown here).

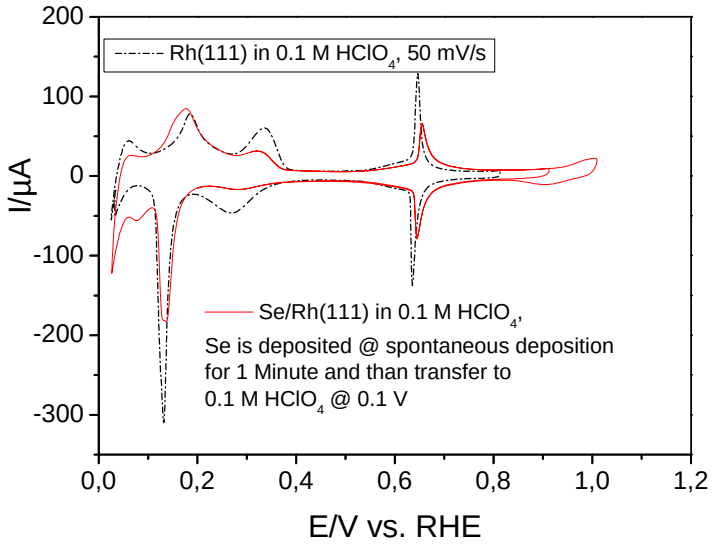

Figure B.1: The cyclic voltammograms of Rh(111) (dotted line) together with spontaneous deposited Se on Rh(111) in 0.1 M $HClO_4$, sweeprate 50 mV/s,

The spontaneous deposition of Se on Pt(111) and Au(111) was also observed and found that Se readily covered most of the surface within 1 minute of immersion time, which confirm the results of Feliu and co-workers is presented in fig. B.2 [11].

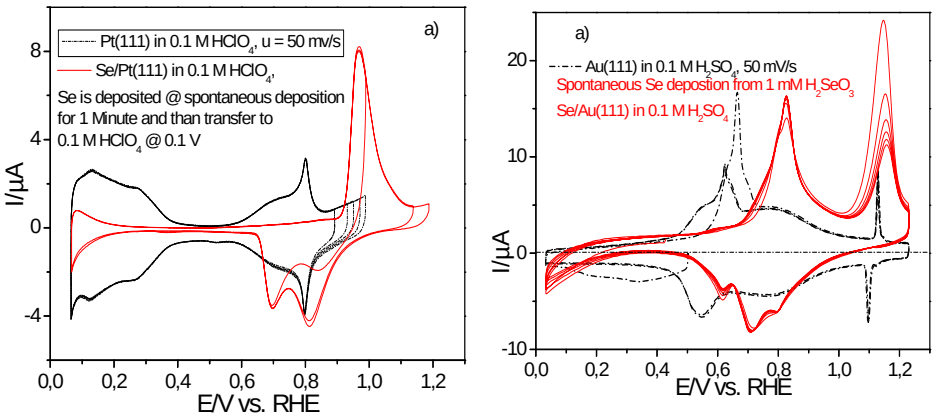

Figure B.2: The Cyclic voltammograms of a) Pt(111) (dotted line) with spontaneous deposited Se/Pt(111) and b) Au(111) (dotted line) with spontaneous deposited Se/Au(111) in 0.1 M $HClO_4$, sweeprate 50 mV/s.

B.3.2 Electrodeposition of Se on Rh(111)

The simplest method to obtain monolayer and multilayer Se deposits on an electrode surface is the reductive deposition of Se(IV). The voltammetric profiles for submonolayer and multilayer deposits of selenium on Rh(111) were shown in fig. B.3. For Se monolayer deposits the potential was scanned from 1.0 V vs RHE which was close to the rest potential. The Se submonolayer on Rh(111) manifests itself in figure

B.3a by three peaks C_1, C_2 & C_3 in a surface limited way before the multilayer deposition start as per following reaction.

$$H_2SeO_{3\ ads} + 4H^+ + 4e^- \rightarrow Se + 3H_2O \qquad \text{B.1}$$

The total selenium deposition charge density calculated after background correction was found to be 246 μCcm^{-2}. The irreversible nature of the Se adlayer is evident from the oxidative stripping of the adsorbed selenium around 1.1 V (Peak A_4) with a calculated charge density of around 242 μCcm^{-2} after background correction. On scanning the potential to a more negative potential of around 0.35 V as shown in fig. B.3b, another surface limited deposit (peak C_4) appeared. This peak C_4 represents a multilayer and not bulk deposition, this might be due to high resistivity of Se (10^{10} Ω-cm) also observed by Stickney and co-workers on Au single crystalline surfaces [12].

Peak C_5 is caused by generation of Se(II) from multilayer adsorbed Se (Peak C_4) and can react chemically with H_2SeO_3 present in the solution and hence form metallic Se:

$$Se + 2H^+ + 2e^- \rightarrow H_2Se \qquad \text{B.2}$$

$$2H_2Se + H_2SeO_3 \rightarrow 3Se + 3H_2O \qquad \text{B.3}$$

During oxidative stripping of Se, bulk Se stripped off around 1.0 V (Peak A_4) followed by stripping of the monolayer (peak A_3). Peak A_2 is probably due to stripping of a intermetallic compound similar to the one observed in case of Se on Au(111).

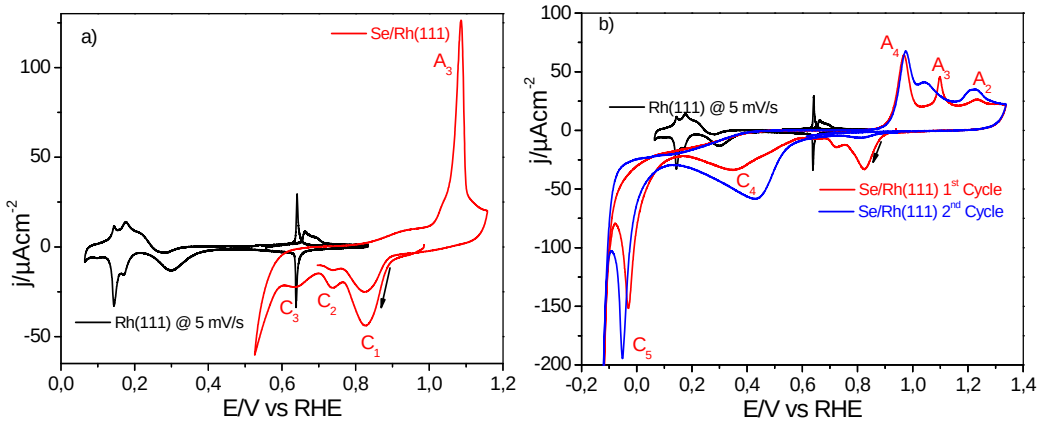

Figure B.3: An overlay of cyclic voltammograms of Rh(111) with a) monolayer and b) multilayer of Se deposition on Rh(111) from 1mM H_2SeO_3 + 0.1 M $HClO_4$, sweep rate 10 mV/s, (figure a, Se submonolayer Se deposition and stripping, figure b, Multilayer Se deposition and stripping).

B.3.3 Electrodeposition of Se on Pt(111)

Electrochemical behaviour of selenium on Pt(111) single crystal surfaces is not widely studied. Electrochemistry of selenium was performed only on polycrystalline platinum electrode using voltammetry and quartz electrochemical microbalance [13]. Quite recently, Alonso Vante and co-workers used selenium modified Pt surface(nanoparticles) for ORR catalysis [14] and for selective H_2O_2 generation [15]. Here, we present electrochemistry of selenium on Pt(111). We explore selenium UPD and monolayer deposits systematically. The first two cathodic peaks C_1 and C_2 correspond to UPD as shown in fig. B.4a. It was observed that selenium somehow showed reversibility in the UPD region. On further expanding the potential window, two additional cathodic peaks C_3 and C_4 appeared represents the bulk Se deposition with corresponding Se stripping peak at more positive potential as shown in fig, B,4b. The cathodic peak C_5 at more negative potential represents the H_2Se formation as shown in fig. B.4c. Our results shows deviations to already published results on Pt(Pc), this deviation might be because we used single crystal electrode surface [13].

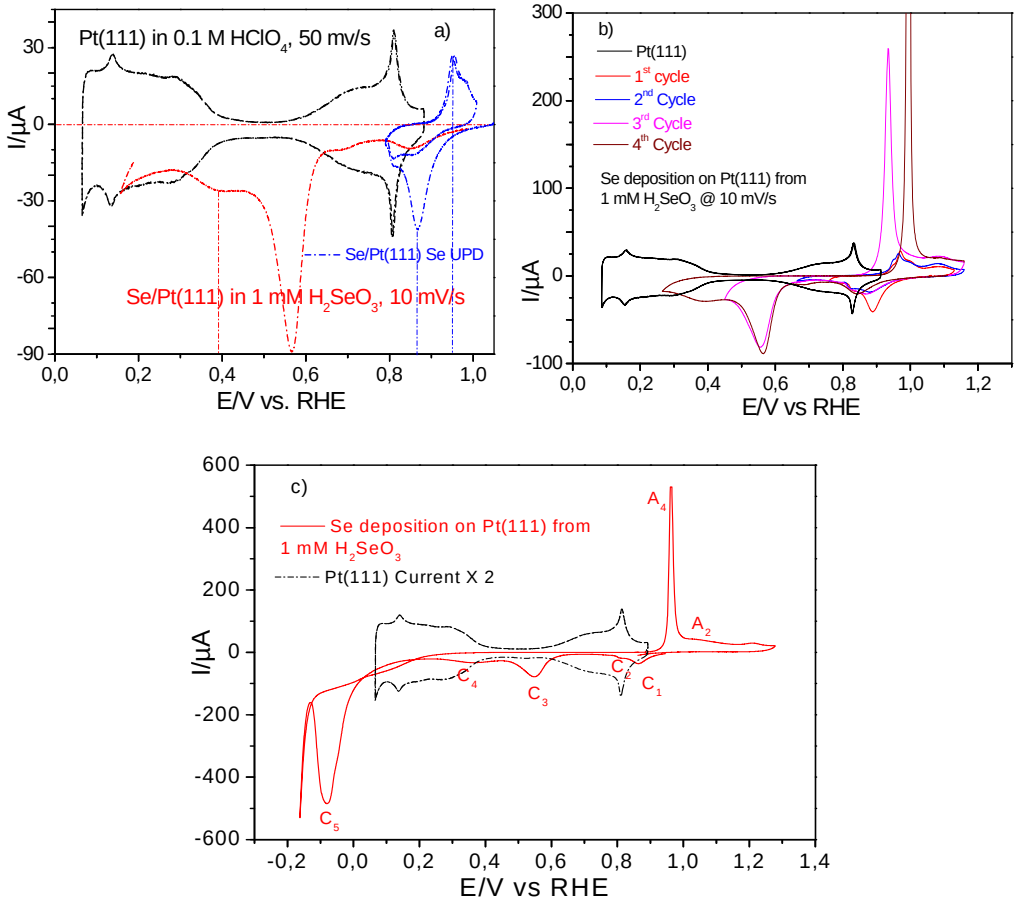

Figure B.4: a) Cyclic voltammograms of Se UPD and bulk on Pt(111) b) Se bulk deposition and stripping, c) selenide formation from 1mM H_2SeO_3 + 0.1 M $HClO_4$, sweep rate 10 mV/s.

B.3.4 Electrodeposition of Se On Au(111)

Electrochemical behaviour of selenium on Au(111) electrode was extensively studied [3, 4]. Sharon et al described the first three reduction peaks corresponds to Se UPD. In our experiments we observed that first reduction peak lead to the monolayer deposit, on extending the potential to second peak results in a shoulder peak and third peak leads to initiation of bulk selenium and intermetallic selenium as evident from cyclic voltammogram presented in fig. B.5. Peak C_4 leads to bulk deposition which stripped off anodically as peak A_4 at 0.95 V. On further expanding the potential window resulted in the generation of H_2Se denoted by peak C_5 followed by a broad peak C_6 centered at -0.2V. The reductive dissolution of the Se as H_2Se at peak C_5 either a six electron process (direct conversion of Se(IV) to Se(-II)) or indirect two electron process (reductive dissolution of already deposited Se(0) to Se(-II) [16-18]. In our current studies for selenide determination using DEMS and SPM, we found that both two electrons and six electron processes takes place simultaneously.

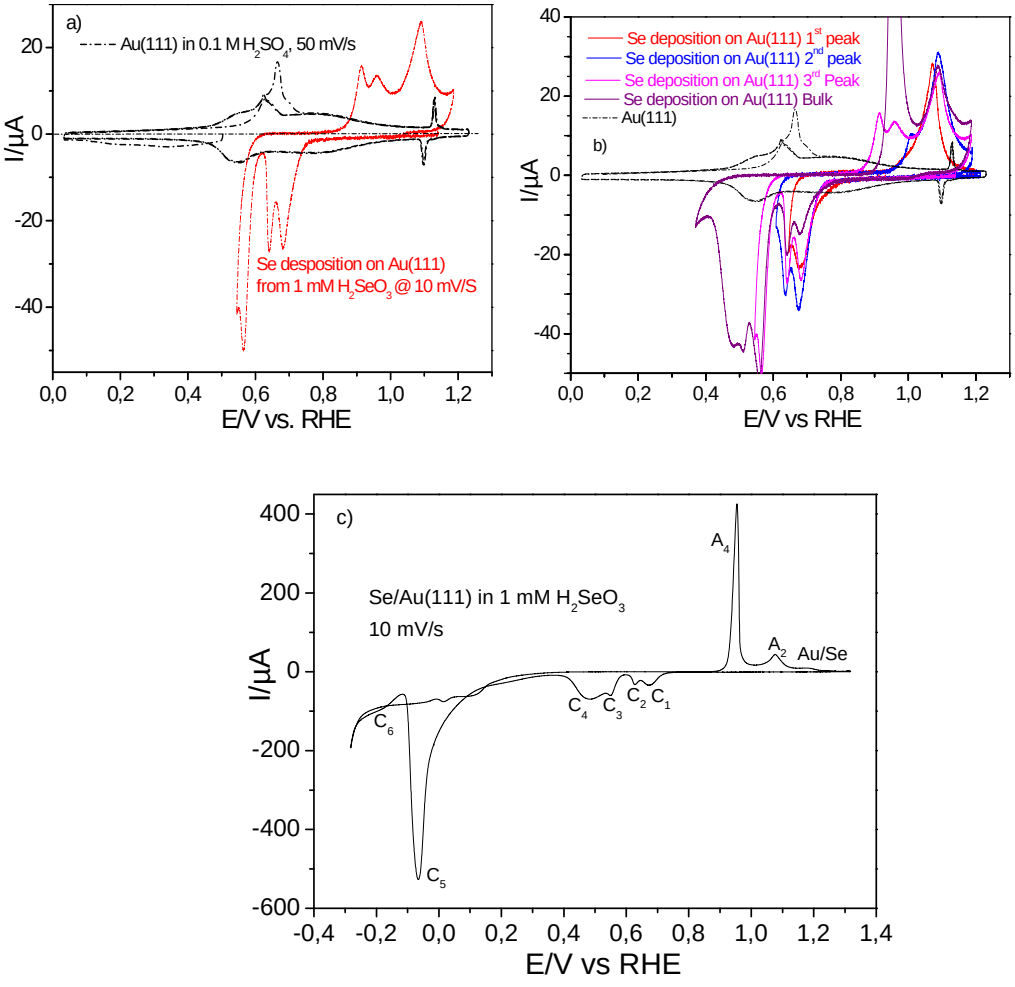

Figure B.5: a) CVs of Se UPD on Au(111) b) Se bulk deposition and stripping, c) selenide formation from 1mM H_2SeO_3 + 0.1 M $HClO_4$, sweep rate 10 mV/s.

B.3.5 Electrodeposition of Se on Ru(0001)

Electrochemistry of Se on Ru(0001) surfaces proceed differently than that of fcc(111) surfaces. The irreversible Se deposition started around 0.6 V vs. RHE followed by initiation of the multilayer with another broader peak with a shoulder as shown in fig. B.6. Further expanding the potential to more negative leads to H_2Se formation. The anodic dissolution of the adsorbed Se resulted in two major peaks that first one corresponds to bulk and the second one with a shoulder peak corresponds to monolayer dissolution. We are interested to check ORR activities of these modified surfaces and also surface composition using XPS. In addition adlayer structure using STM and LEED.

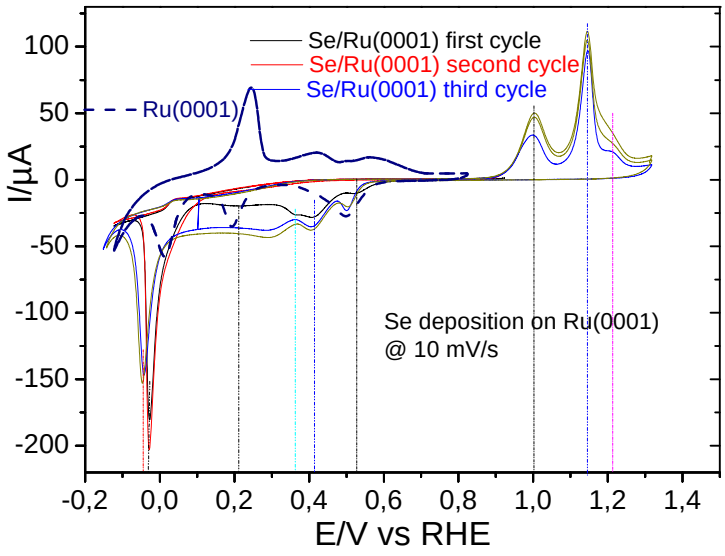

Figure B.6: The cyclic voltammogram of Ru(0001) (-------) together with Se deposition from 1mM H_2SeO_3 + 0.1 M $HClO_4$, sweeprate 10 mV/s.

B.3.6 Selenium Electrochemistry on Pt(100) and Rh(100) surfaces

The electrochemistry of Se on *fcc*(100) surface proceed differently than fcc(111) surfaces. In case of Pt(100) Se UPD begins with single peak centered around 0.9 V followed by the initiation of the multilayer deposits at second reductive peak and completed with a diffusion limited broad third peak. On further expanding the potential to more negative resulted in generation of H_2Se. Once the potential was scanned continuously in the anodic direction and returned back to cathodic direction without Se oxidative stripping as shown in fig. B.7. No more Se deposition takes place in the second cycle and the generation of H_2Se was most probably due to the direct conversion of Se(IV) to Se(-II) via 6 electron process as per below equation.

$$H_2SeO_3 + 6H^+ + 6e^- \rightarrow \quad H_2Se + 3H_2O \qquad \text{B.4}$$

The oxidative stripping of multilayer Se resulted in a large peak with a shoulder (probably Se monolayer) peak. It seems that the multilayer and monolayer Se stripped together. At higher potential oxidation of the substrate surface takes place which is evident in the next cycle with reduction of the Pt(100)

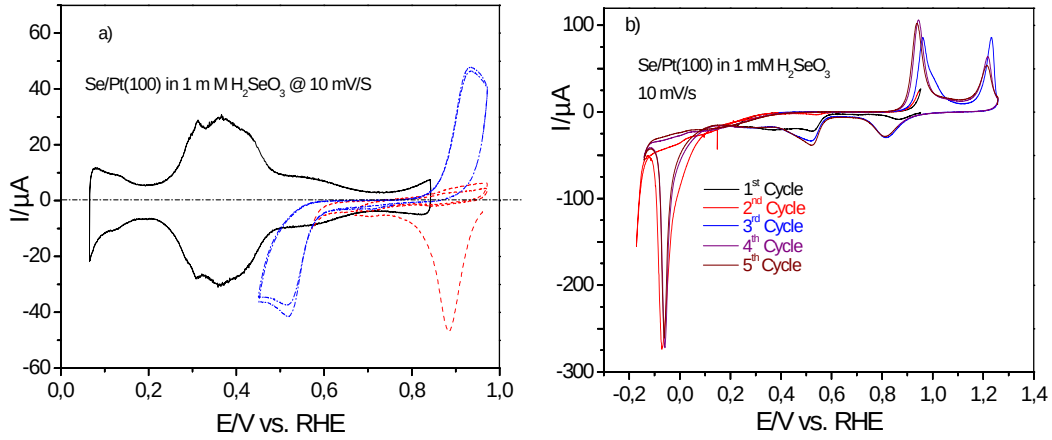

Figure B.7: Cyclic voltammograms of a) Se UPD on Pt(100) b) Se bulk deposition and stripping and selenide formation from 1mM H_2SeO_3 + 0.1 M $HClO_4$, sweep rate 10 mV/s.

Se deposition on Rh(100) proceeds at more negative potentials than Pt(100). i Se UPD results due to single peak centred at 0.6 V vs RHE. It was followed by multilayer deposits, a boarder peak cantered around 0.3 V as shown in fig. 3.8. And H_2Se formation around 0 V. The oxidative stripping of multilayer Se resulted in a large peak (more or less similar to Pt(100)) peak. Probably the multilayer and monolayer Se stripped together. At higher potential oxidation of the substrate surface takes place which is evident in the next cycle with reduction of the oxide layer along with Se deposition on roughened Rh(100).

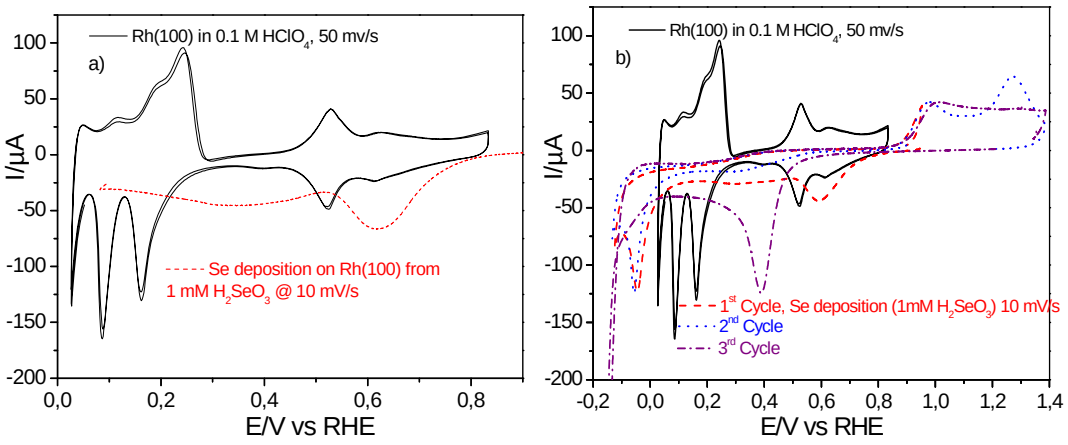

Figure B.8: Cyclic voltammograms of a) Se UPD on Rh(100) b) Se bulk deposition and stripping and selenide formation from 1mM H_2SeO_3 + 0.1 M $HClO_4$, sweep rate 10 mV/s.

B.3.7 Current time transient for Se adsorption at various fixed potentials

B.3.7.1 Se on Pt(111)

The current-time transient for selenium adsorption on Pt(111) and Rh(111) surface were recorded at various potentials to check the influence of adsorbed OH^{-1}. For this purpose at different fixed potential such as 0.7 and 0.4 current time transient were recorded by dosing 1.5 ml of 1 mM H_2SeO_3 into 0.1 M $HClO_4$ containing the single crystal P(111) electrode in hanging meniscus configuration. Subsequent oxidative stripping of selenium was performed to monitor the adsorbed selenium as shown in fig. B.9. The transient experiments reveals that the initial Se deposition is fast and proceed similar to normal potentiodynamic way, however, large time is allowed to the remaining Se present in the solution. This causes more Se deposition from dilute solutions.

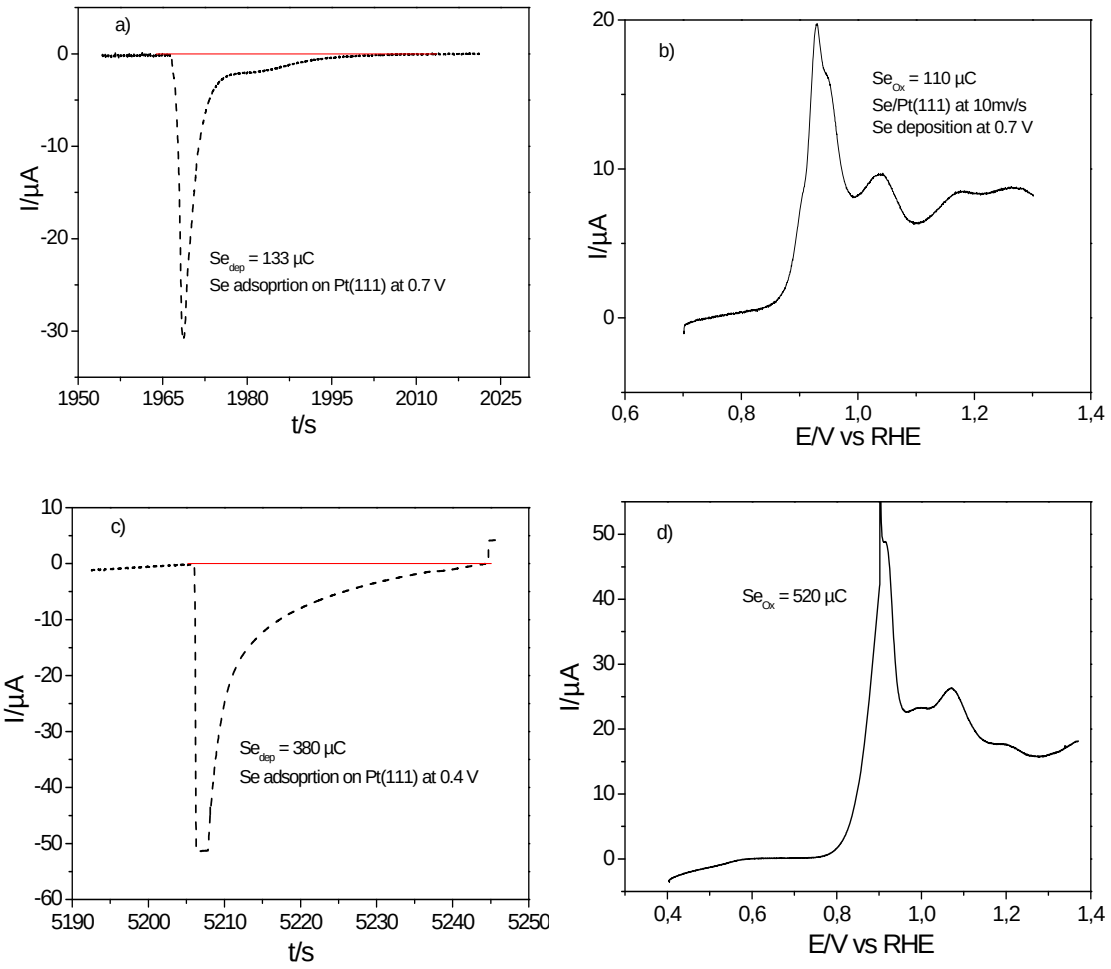

Figure B.9: Current-time transient (a, c) (-------) at 0.72 and 0.4 V and corresponding oxidative stripping (b, d) (——) of Se on Pt(111) by dosing 1.5 ml of from 1mM H_2SeO_3 into 0.1 M $HClO_4$ sweeprate 10 mV/s.

B.3.7.2 Se on Rh(111)

The current-time transient for selenium adsorption on Rh(111) at 0.72 & 0.4 V fixed potentials were recorded by dosing 1.5 ml of 1 mM H_2SeO_3 into 0.1 M $HClO_4$ containing the electrode in hanging meniscus. Subsequent oxidative stripping of selenium was performed to monitor the adsorbed selenium as shown in fig. B.10.

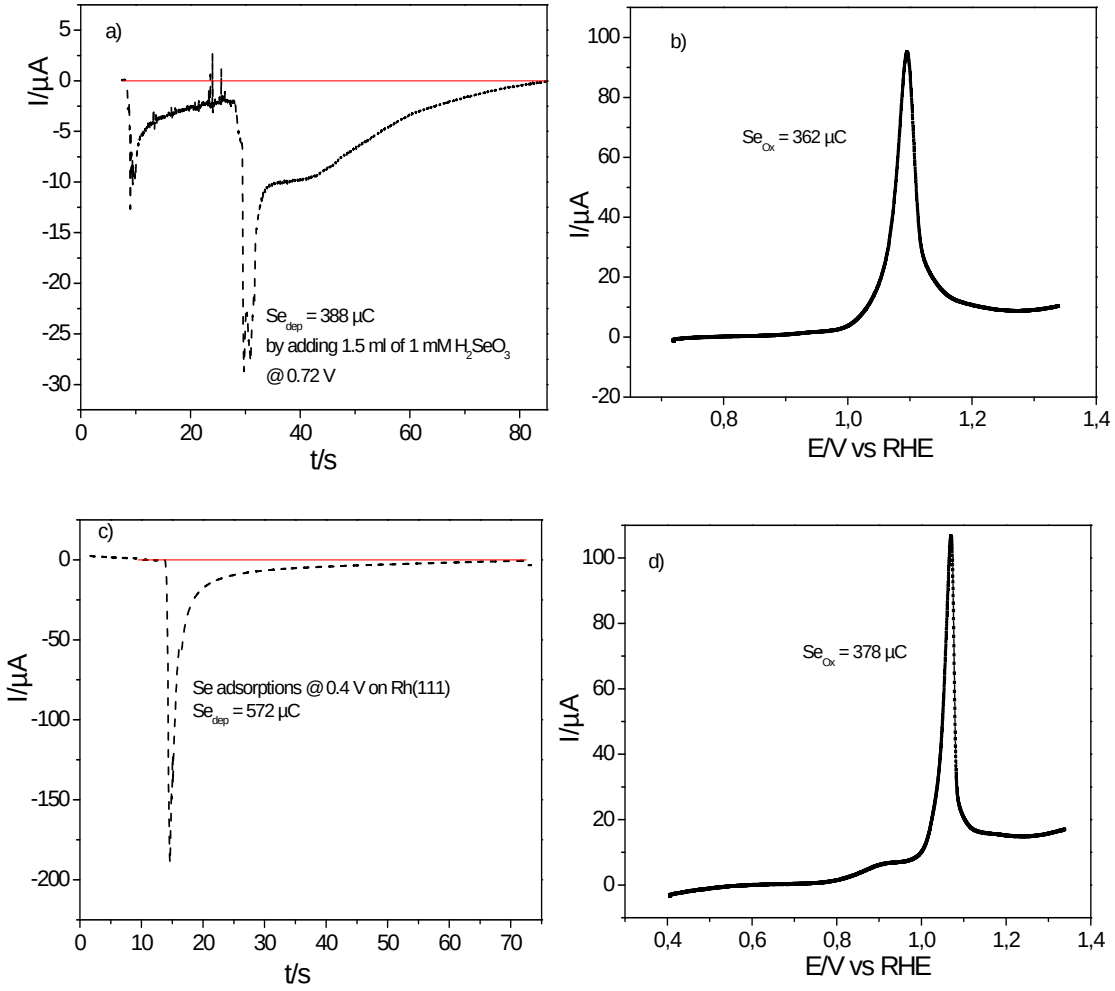

Figure B.10: Current-time transient (a, c) (-------) at 0.72 and 0.4 V and corresponding oxidative stripping (b, d) (——) of Se on Rh(111) by dosing 1.5 ml of from 1mM H_2SeO_3 into 0.1 M $HClO_4$ sweep rate 10 mV/s.

References

[1] D. C. Papageorgopoulos, F. Liu, and O. Conrad, Electrochimica Acta 53:1037 (2007).
[2] R. Heindl, R. Parsons, A. M. Redon, H. Tributsch, and J. Vigneron, Surface Science 115:91 (1982).
[3] T. E. Lister and J. L. Stickney, Journal of Physical Chemistry 100:19568 (1996).
[4] M. Alanyalioglu, U. Demir, and C. Shannon, Journal of Electroanalytical Chemistry 561:21 (2004).
[5] G. A. Tritsaris, J. K. Norskov, and J. Rossmeisl, Electrochimica Acta 56:9783 (2011).
[6] S. Stolbov, The Journal of Physical Chemistry C 116:7173 (2012).
[7] L. A. Kibler, Preparation and Characterization of Noble Metals Single Crystal Electrodes, University of Ulm, 2003.
[8] J. A. Rodriguez, S. Chaturvedi, and M. Kuhn, Journal of Chemical Physics 108:3064 (1998).
[9] J. Clavilier, M. Wasberg, M. Petit, and L. H. Klein, Journal of Electroanalytical Chemistry 374:123 (1994).
[10] A. M. El-Aziz and L. A. Kibler, Electrochemistry Communications 4:866 (2002).
[11] J. M. Feliu, R. Gomez, M. J. Llorca, and A. Aldaz, Surface Science 289:152 (1993).
[12] J. L. Stickney, T. E. Lister, B. M. Huang, and L. B. Goetting, Electrochimica Acta 40:143 (1995).
[13] M. C. Santos and S. A. S. Machado, Journal of Electroanalytical Chemistry 567:203 (2004).
[14] J. Ma, A. Habrioux, C. Morais, and N. Alonso-Vante, Physical Chemistry Chemical Physics 16:13820 (2014).
[15] Y. B. Mo and D. A. Scherson, Journal of the Electrochemical Society 150:E39 (2003).
[16] M. S. Kazacos and B. Miller, Journal of The Electrochemical Society 127:869 (1980).
[17] M. O. Solaliendres, A. Manzoli, G. R. Salazar-Banda, K. I. B. Eguiluz, S. T. Tanimoto, and S. A. S. Machado, Journal of Solid State Electrochemistry 12:679 (2008).
[18] R. W. Andrews and D. C. Johnson, Analytical Chemistry 47:294 (1975).

Appendix C: Characterization of DTLFC for ORR

This is part of the chapter 5 and explains the systematic characterization of the hydrodynamic technique, the dual thin layer flow through cell (DTLFC) for evaluating ORR in general.

The basic chemistry of the multi-electron charge transfer reactions is mentioned in the beginning of this thesis (chapter 1), it is followed by the ORR which is considered to be an essential reaction in energy conversion applications. Even though oxygen is a strong oxidizing molecule, its reduction is complex process and generally proceeds through acceptance of two or four electrons with the involvement of protons. For the last few decades this multi-electron charge transfer process has been explored extensively on various oxygen cathodes in aqueous solution (acidic or basic) [1].

C.1 The oxygen reduction reaction mechanism

Despite the decades of research involving experimental and theoretical approaches [2] the mechanism of the oxygen reduction reaction is still not very well understood. For a general review of various models for oxygen reduction reaction see [3]. However, the most accepted model for the reaction on a Pt surface is presented in fig. C.1

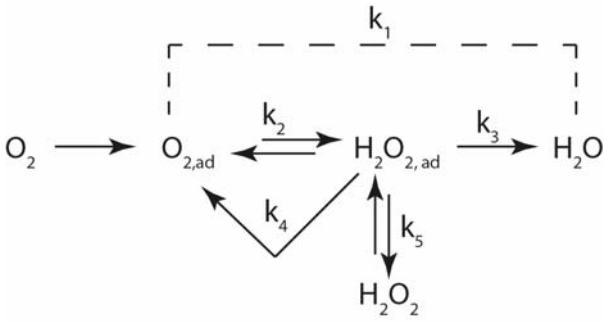

Fig. C.1: The oxygen reduction reaction mechanism on Pt [4].

According to this model, oxygen is first adsorbed onto the electrode surface from an aqueous solution. The adsorbed oxygen molecules can be reduced to water in three ways.

a) directly by accepting four electrons and four protons.

b) indirectly via hydrogen peroxide followed by the generation of water

c) indirectly via hydrogen peroxide followed by direct release from the electrode surface.

The key factor for this ambiguous behaviour is thought to be irreversible nature of the

ORR process on a large number of catalytic surfaces. The reaction becomes irreversible because the energy to break the O-O bond at these surfaces is greater. The most probable reasons for this increase in energy are the generation of the intermediates and coupled chemicals (Proton transfer) and electrochemical processes (Charge transfer), which proceed in different ways and at different rates on different surfaces.

C.2 Characterization of dual thin layer low through cell for oxygen reduction reaction (ORR) activity measurements

C.2.1 Dual thin layer flow through cell design:

To ascertain defined convection during the oxygen reduction reaction (ORR) and to detect generated H_2O_2, we used the modified dual thin layer flow through cell (DTLFC), identical to that developed in our group for differential electrochemical mass spectrometers (DEMS) [5]. A constant flow of electrolyte is achieved in these cells using syringe/peristaltic pumps.

The DTLFC was manufactured from Kel-F. This cell consisted of two separate compartments; the upper compartment contained the first Pt disc electrode and also the electrolyte, which was introduced through the electrolyte inlet using hydrodynamic pressure. The electrochemical process took place at the electrode surface; reaction products and intermediates were transported with the electrolyte through six capillaries to the lower compartment. There, the second Pt disk electrode was used to detect products before the electrolyte left the cell via a capillary at the centre. (First Pt electrode is an old Pt(111) electrode with 10 mm diameter and 3 mm thickness, whereas the second Pt electrode is Polycrystalline Pt with diameter of 10 mm with 3 mm thickness) A peristaltic/syringe pump at the outlet of the cell controlled the flow rate of the electrolyte. To assure a continuous operation of a flow through reactor, a supporting electrolyte served as a medium for both reactants and products. A reversible hydrogen electrode (RHE) was used as the reference electrode. Two Pt wires were used as counter electrodes in the inlet and the outlet, which connected to the potentiostat via two different resistances (100 kΩ and 1100 Ω respectively). These resistances are used to optimize the current distribution and also to decrease the ohmic losses. The experiments were carried out at room temperature. A schematic view and actual setup is shown in

fig. C.2.

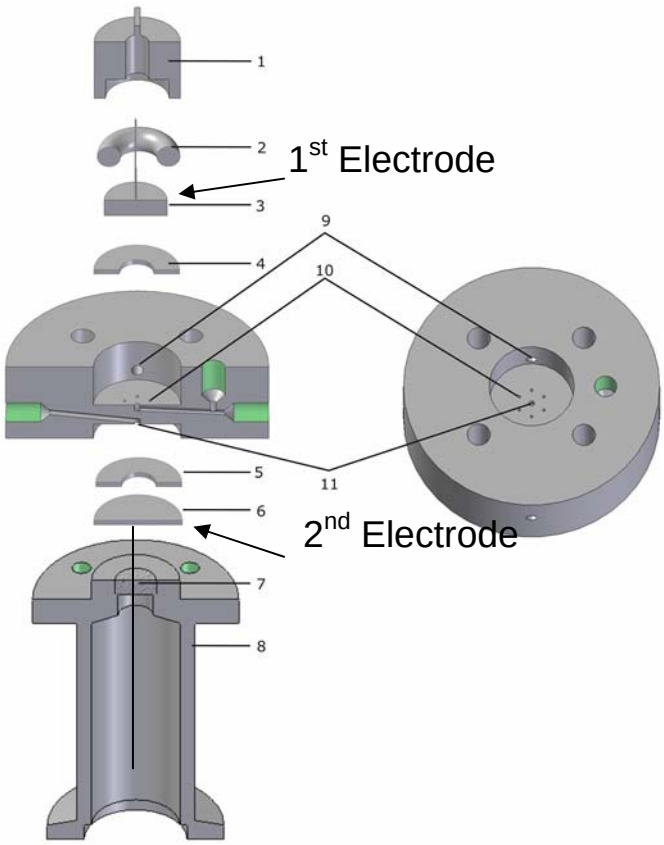

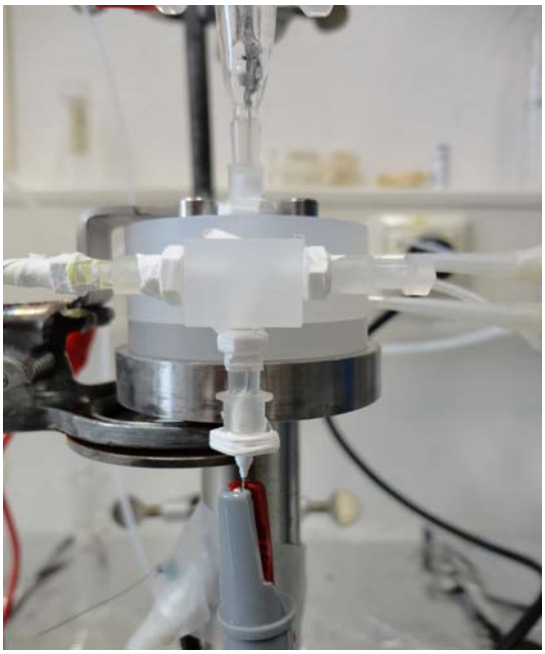

Figure C.2: Schematic drawing of the dual thin layer flow through cell carton, disk electrodes (3&6), Gortex Teflon spacers (4&5), six capillaries links upper and lower compartment for electrolyte movement (10), holes for argon purging (9), holes for incoming and outgoing of electrolyte (11) along with actual photo of the setup.

C.2.2 Dual thin layer flow through cell characterization

As mentioned above the DTLFC was designed to couple with a mass spectrometer. Characterization of the DTLFC setup has to be ensured for checking the ORR activity of the Se modified Rh(111) surfaces. In order to characterize the dual thin layer cell for ORR experiments; a series of experiments was performed.

C.2.2.1 Electrochemical Impedance Spectroscopy

Electrochemical impedance spectroscopy (EIS) is one of numerous methods that depend on the perturbation of the d.c signal with an a.c signal of relatively small amplitude to gather information about the processes taking place on the interface. The main focus of this technique is to isolate the faradaic response of an electrochemical cell from the non-faradaic components (solution resistance and capacitance) [6]. Ohmic drop issues are very serious in DTLFC setup. Hence, impedance analyses were performed to check the solution resistance. For this purpose different thickness solution gaps were created by placing Gortex^{TM} spacers between the electrode and the cell compartment. Two configurations were tried, one using two spacers (each 75 µm thick) and the other using four spaces. In the first configuration, a solution resistance of approximately 500 Ohm was observed, however the system behaviour was complex and no meaningful impedance spectra could be measured.

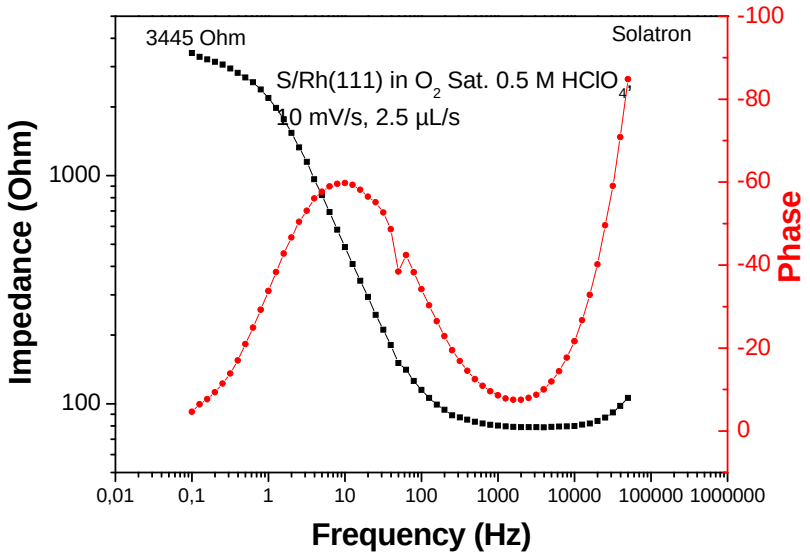

Figure C.3: The Bode plot for Pt electrode in DTLFC under constant flow condition of 2.5 µL/s at potential of 0.1 V vs RHE and 10 mV(amplitude) of a.c signal.

However, in the case of the second configuration, a solution resistance of 86 Ohm was obtained and the system behaved in a reasonable manner as shown in fig. C.3. For further experiments, this second configuration was used.

C.2.2.2 Voltammetric studies in DTLFC

The DTLFC is characterized by the usual cyclic voltammetric technique using Ar saturated 0.5 M $HClO_4$ under continuous flow-through condition. An overlay of representative CVs for the Pt(Pc) in upper (solid line) and in lower (dotted line) compartment of DTLFC are shown in fig. C.4. Both compartments contained Pt(Pc) disk electrodes. Four (75 µ thickness) Teflon spacers were placed on each side in order to make the volume of the electrolyte the same for each compartment. Both electrodes were mirror polished and further smoothness was achieved by flame annealing. This resulted in a real surface area of 1 and 1.25 cm^2 for the upper and lower compartment whereas the geometric area of each is 0.785 cm^2. The CVs represent clean polycrystalline electrode and were in good agreement with literature cited CVs of clean Pt electrode surface [7]. Also, these CVs are important (as in case of DTLFC) due to the complex geometry of the cell design causing a large ohmic drop, which influences the potential at the electrode surfaces. Hence, in the absence of any noteworthy disturbance, these result showed that further electrochemical experiments can be performed using this setup without further optimization.

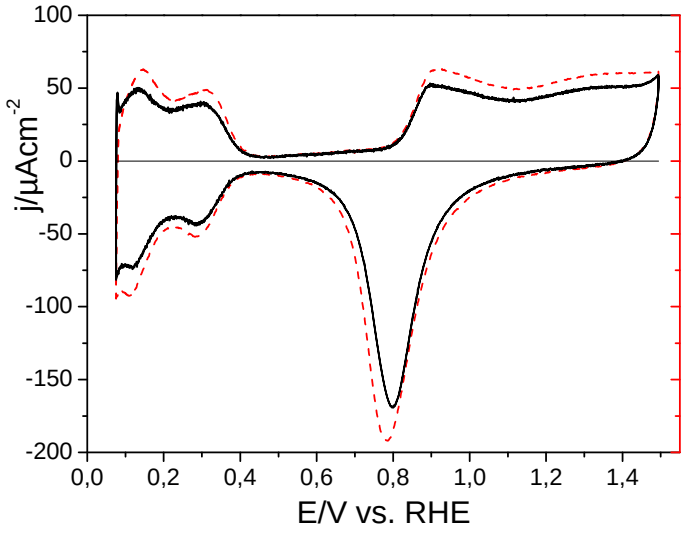

Figure C.4: Simultaneously recorded cyclicvoltamogram for first (——) & second (------) electrode in 0.5 M $HClO_4$, sweep rate 50 mV/s, flow rate 2.5 µl/s.

C.2.2.3 Calculation of collection efficiency using Fe(III) & Fe(II)

The calibration of the setup (DTLFC) was performed to get a quantitative estimate of the electro-active species that were generated at the first electrode. The collection efficiency of the second electrode (where the species were detected) needed to be calibrated in a similar way to the rotating ring disc electrode (RRDE) setup. The collection efficiency of a thin layer cell is the ratio of the number of reacting species to the number of species entering the cell. This was measured for the Fe(III)/Fe(II) redox couple. The amount of Fe(II) formed by reduction of Fe(III) at the first electrode was compared with the oxidation of Fe(II) at the second electrode and vice versa.

For all iron measurements $3.3x10^{-4}$ M $Fe_2(SO_4)_3$ or $2.2x10^{-4}$ M $FeSO_4$ solution in 0.5 M $HClO_4$ were used. The electrochemical measurements were performed at different flow rates of 2.5, 5 and 10 µL/s with a sweep rate of 10 mV/s. The cyclic voltammograms of Fe(III) reduction in the upper compartment showed broadening due to pseudo-capacitive double layer charging due to oxygen adsorption, which can be corrected by utilizing baseline currents for the generated Fe(II) oxidation at second electrode held at a fixed 1.0 V at positive potentials). The resulting mass transport limited current in our case is approx. 57 μAcm^{-2} for Fe(III) reduction to Fe(II). In addition, electro-oxidation of Fe(II) in the lower compartment was achieved by holding the potential at 1 V vs. RHE and monitored the current simultaneously as a function of the potential of the electrode in the upper compartment as represented in fig. C.5. The currents due to the electro-oxidation of the Fe(III) and electro-reduction of the Fe(II) closely followed the trend. The hysteresis in the anodic and cathodic scans was due to the time requirements for transfer of species from upper to lower compartment (~ 1 s at a flow rate of 5 µL/s). In another experiment, the Fe(III) species which were not reduced in the upper compartment were reduced again in the lower compartment by holding the potential of the electrode in the second compartment at 0.5 V vs. RHE. The currents were monitored as a function of potential of upper electrode.

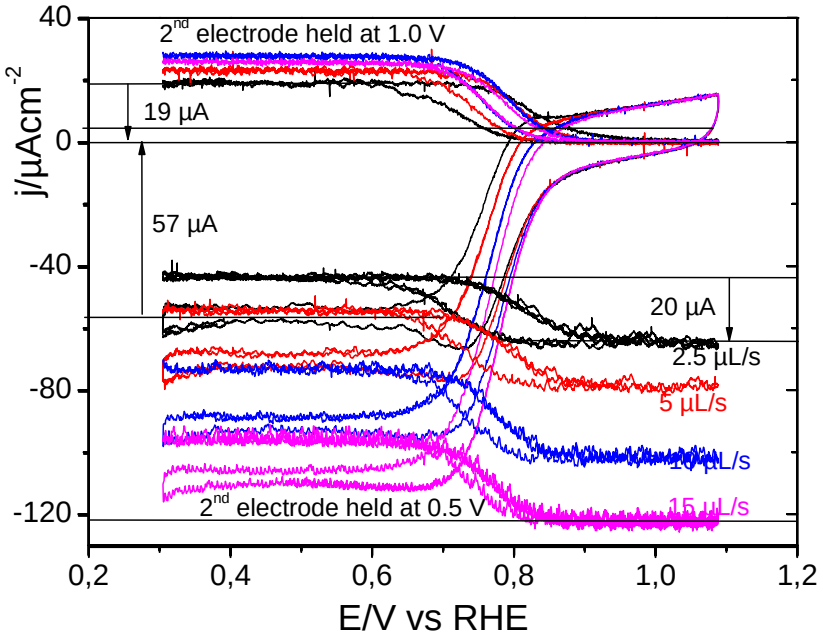

Figure C.5: The simultaneous recorded CVs for Pt(Pc) electrode in the upper compartment and another Pt(Pc) in the lower compartment of the DTLFC held at 1 V and 0.5 V at flow rates of 2.5 (——), 5 (——) 10 (——) and 15µL/s (——) in argon saturated $3.3x10^{-4}$ M $Fe_2(SO_4)_3$ + 0.5M $HClO_4$ solution, sweep rate of 10 mV/s.

The same set of experiments were conducted for Fe(II)/Fe(III) redox couple are presented in fig. C.6.

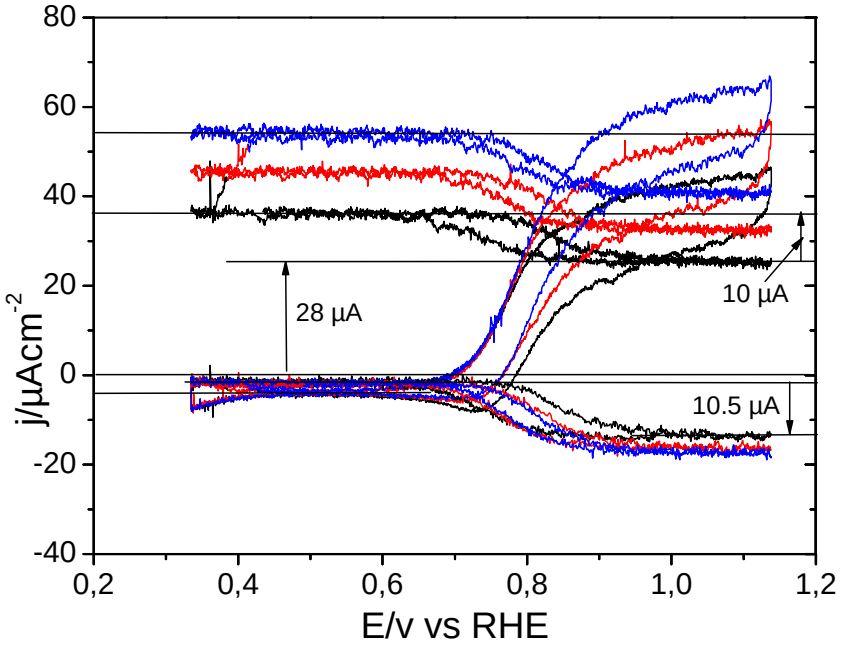

Figure C.6: The simultaneous recorded CVs for Pt(Pc) electrode in the upper compartment and another Pt(Pc) in the lower compartment of the DTLFC held at 1 V and 0.5 V at flow rates of 2.5 (——), 5 (——) and 10µL/s (——) in argon saturated $2.2\ x10^{-4}$ M $FeSO_4$ + 0.5M $HClO_4$ solution, sweep rate of 10 mV/s.

In another set of experiment, mass transport limited currents were also obtained for O_2 saturated solution as shown in fig. C.7.

The hydrodynamic behaviour of the laminar flow channel in our DTLFC was determined by obtaining linear dependences of diffusion limited currents for various analytes (Fe_2SO_3, Hydroquinone and Hydrogen) to that of $u^{1/3}$ of flow rate (Mehdi's experiments)

Yamada and Matsuda developed and tested experimentally a relationship between mass transport limited current and the flow rate for channel electrodes, based on the fundamental considerations of the Levich [8]. Assuming that the same equation also holds for the DTLFC after replacing the numeric factor by a general factor g, eqn. C.1 is obtained.

$$I_F = g \cdot z \cdot F \cdot c \cdot D^{2/3} \cdot u^{1/3} \qquad \text{C.1}$$

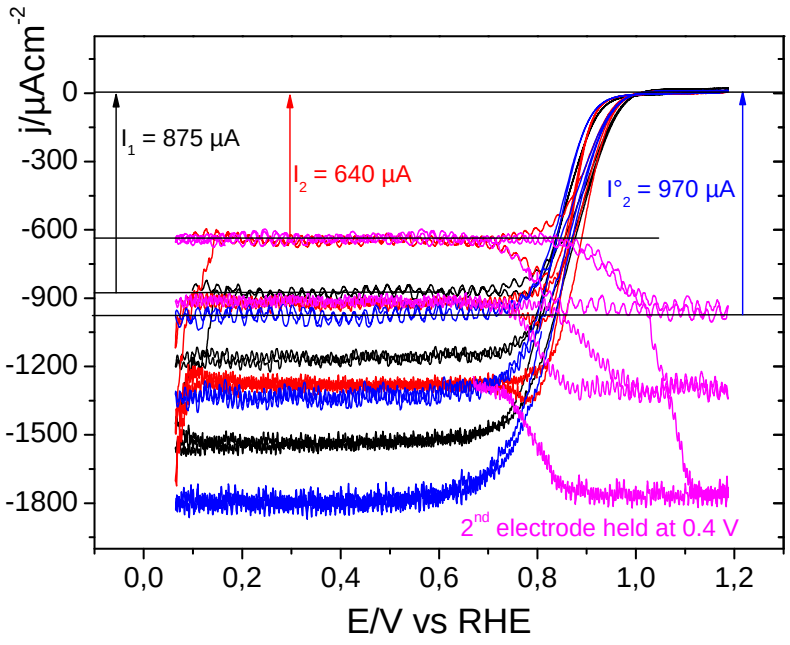

Figure C.7: Simultaneously recorded CVs for second electrode (——), when the first electrode is scanning (——), when the first electrode is disconnected (——). Also, when first electrode scanning and second electrode held at 0.4 V (——) in oxygen saturated 0.5 M $HClO_4$, sweep rate 10 mV/s, flow rate 2.5, 5 & 10 µl/s.

In this equation, g is consider as constant and its value in our case found to be vary $g = 5.0 \sim 10\ cm^{2/3}$, where z is the number of the electrons, F is the Faraday constant, c is the concentration of the analyte, µ is flow rate of electrolyte, D is the diffusion

coefficient of the analyte and I_F is the experimentally determined mass transport limited current.

The theoretical mass transport limited current for the Fe(III)/Fe(II) redox couple was calculated by inserting values such as z =1, F = 96,480 A s/mol, c = 3.3×10^{-7} for Fe(III) and 2.2×10^{-7} mol/cm^3 for Fe(II), μ = 2.5×10^{-3} cm^3/s, D = 7.7×10^{-6} cm^2/s [9], and for the ORR assuming z = 4, O_2 diffusion coefficient of D = 1.93×10^{-5} cm^2/s and O_2 concentration in O_2 saturated 0.5 M $HClO_4$ is c = 1.26×10^{-6} mol/cm^3, A is the surface area of the electrode and b is thickness of the thin layer gap [10] in eqn. 5.1 assuming $g = 1.467(A/b)^{2/3}$

The calculated mass transport limited current is 0.016 mA, which corresponds to approx. 1.4 times that determined experimentally. In addition, the calculated mass transport limited currents for ORR were also found higher than that of the experimental value. The larger theoretical value might be due to the non-uniform distribution of electrolyte on the electrode surface and also a decrease in the thickness of the thin layer gap due to the pressure exerted by the electrode. One further possible reason for the difference between the theoretical and experimental values is that the theoretical approach assumed a uniform flux over the overall surface of the electrode inside the cell with uniform thickness.

The theoretical mass transport limited current for the Fe(III)/Fe(II) redox couple and that for ORR was calculated by inserting values in eqn. C.1 and are summarized in table C.1.

Table C.1: Mass transport limited currents for Fe(II)/Fe(III) redox couple and for the ORR

u μL/s	I_F for Fe(III) μAcm^{-2}		g for Fe(III)	I_F for Fe(II) μAcm^{-2}		g for Fe(II)	I_F for ORR mAcm^{-2}		g for ORR	I_F for H_2O_2 mAcm^{-2}		g for H_2O_2
	Theo	Exp	cm$^{2/3}$	Theo	Exp	cm$^{2/3}$	Theo	Exp	cm$^{2/3}$	Theo	Exp	cm$^{2/3}$
2.5	78	56	5.1	26	28	10.1	1.04	0.88	5.5	0.174	0.16	6.3
5	98	71	5	33	37	10	1.32	1.2	6	0.22	0.2	6.2
10	124	91	5	41.2	45.5	9	45.5	1.55	6.11			

The collection efficiency for the electrochemical redox system of Fe(II)/Fe(III) and for the ORR was calculated using eqn. C.2

$$f = \frac{I_f/zF}{c \cdot u} \qquad C.2$$

The shielding factors and transfer efficiency at various flow rates were also calculated for all above mentioned redox systems. The following equations were used to calculate these parameters.

Shielding Factor $S = I_2 / I_2^{\circ}$ C.3

where,

I_2 = Diffusion limited current for second electrode when first electrode is also scanning (i.e., same reaction is also occurring at the first electrode)

I_2° = Diffusion limited current for second electrode when first electrode is disconnected (i.e., when no reaction is taking place at the first electrode)

Hence, shielding factors at various flow rates are

Similarly,

Transfer Efficiency (N) $N = (I_2^{\circ} - I_2)/I_1$ C.4

Where,

I_1 = Diffusion limited current for first electrode when second electrode is also scanning

The calculated collection and transfer efficiencies and shielding factor for Fe(II)/Fe(III) redox couple and for the reduction currents of oxygen at various flow rates (2.5, 5 & 10 μL/s) are summarized in table C.2.

Table C.2: The collection and transfer efficiency and shielding factor of the DTLFC for Fe(II)/Fe(III) redox couple and for the reduction currents of oxygen.

u μL/s	Collection efficiency (f)			Transfer efficiency (N)			Shielding factor (S)		
	Fe(III)	Fe(II)	ORR	Fe(III)	Fe(II)	ORR	Fe(III)	Fe(II)	ORR
2.5	0.36	0.53	0.73	0.36	0.36	0.38	0.67	0.71	0.66
5	0.22	0.35	0.49	0.32	0.35	0.355	0.68	0.71	0.69
10	0.14	0.21	0.32	0.3	0.3	0.34	0.71	0.75	0.70

We found a similarity between the data obtained from Fe(II)/Fe(III) redox couple and that from experiments performed in oxygen saturated solution. The calculated collection efficiency for DTLFC system was around 73~36 % at flow rate of 2.5 μL/s for various system (such as O_2 and Fe(III)/Fe(II) redox couple respectively). However, the transfer efficiency was found slightly higher than that of a typical RRDE setup (depending upon system design and dimensions of the ring-disk electrode. However, the RRDE setup performed better for short lived intermediates as a slightly moderate residence time was required for DTLFC.

C.2.2.4 Standardization with $4x10^{-4}$ M H_2O_2

All the apparatus used for the evaluation for the reduction of oxygen has to be optimized for the detection of the generated H_2O_2 during the ORR.

Further performance and system suitability of the DTLFC was ensured by calibrating the system with hydrogen peroxide. It is well known that the hydrogen peroxide redox reaction on noble metal surfaces is a diffusion-limited reaction in aqueous acids. The diffusion limited current-potential profile for the redox reaction of $4x10^{-4}$ M H_2O_2, which was monitored in the DTLFC using the polycrystalline Pt electrodes is shown in fig. C.8. Diffusion limited current-potential profiles (red & green) were obtained for the second electrode, while the first electrode is either scanning or disconnected respectively. Differences in the cathodic diffusion limited currents for the second electrode indicated the shielding factor of the first electrode. The difference in the diffusion limited currents for the cathodic and anodic scans (green solid line) of the first electrode was due to continuous oxidation of the H_2O_2 even at open circuit potential [11]. The Pt electrode surface states were dependent on the applied potential. At lower potentials the Pt has a reduced surface state which decomposed H_2O_2 to OH species. At higher potentials the oxidized surface states of Pt caused the formation of O_2. This resulted in an increase in the diffusion limited currents at higher potentials when the detecting second electrode was held at 0.4 V, (magenta solid line). The overall reaction can be shown by the following equations.

$$H_2O_2 + 2H^+ + 2e^- \rightarrow 2H_2O \quad \text{(at 0.4 V)} \quad \text{Cathodic} \qquad \text{C.5}$$

$$H_2O_2 \rightarrow O_2 + 2H^+ + 2e^- \quad \text{(at 1.2 V)} \quad \text{Anodic} \qquad \text{C.6}$$

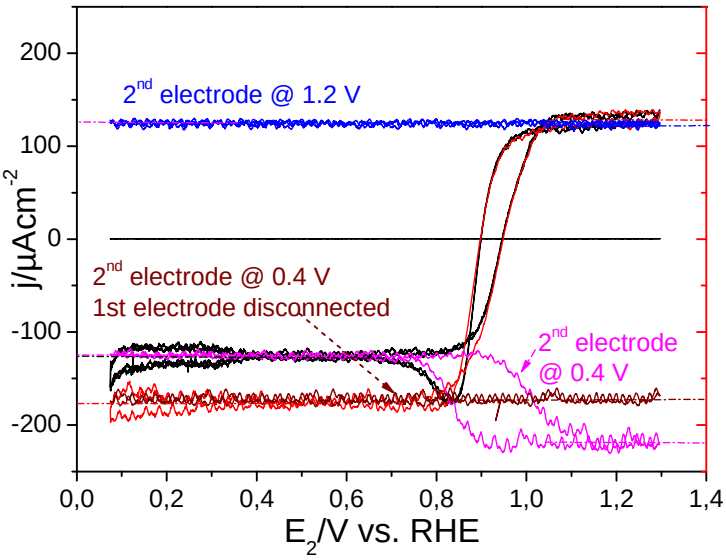

Figure C.8: Simultaneously recorded CVs for second electrode, when the first electrode is scanning (——) when first electrode is disconnected (——). (—— and ——) when second electrode held at 1.2 and 0.4 V respectively. (——) when first electrode held at 0.4 V and second electrode is scanning in a solution containing $4x10^{-4}$ M H_2O_2 + 0.5 M $HClO_4$ solution. Sweep rate: 10mV/s. The flow rate of electrolyte: 2.5 & 5 µL/s.

Redox processes of H_2O_2 at the Pt electrode surfaces at open circuit (rest potential) were avoided by using Kel-F dummy electrode instead of Pt in the upper compartment as the first electrode. Diffusion limited current-potential profile for redox processes for H_2O_2 were obtained by scanning the potential at the second electrode in the lower compartment and also by holding the potential at 1.2 & 0.4 V respectively at various flow rates as shown in fig. C.9.

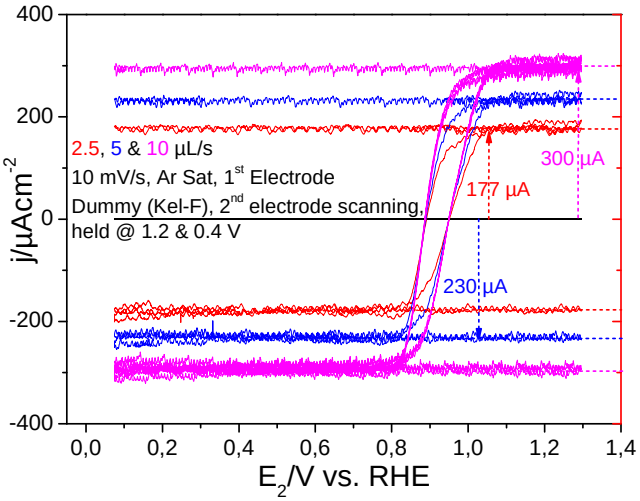

Figure C.9: Simultaneously recorded CVs for second electrode scanning, held at 0.4 V and 1.2 (——). (—— and ——) , when the first electrode is Kel F respectively in a solution containing $4x10^{-4}$ M H_2O_2 + 0.5 M $HClO_4$ solution. Scan rate: 10mV/s. The flow rate of electrolyte: 2.5, 5 & 10 µL/s.

The calculated collection and transfer efficiencies and shielding factor for electrochemical behaviour of H_2O_2 using equations C.2, C.3 and C.4 for various flow rates (2.5, 5 & 10 µL/s) are summarized in table C.3.

Table C.3: The collection and transfer efficiency and shielding factor of the DTLFC for H_2O_2.

u µL/s	Collection efficiency (f)		Transfer efficiency (N)		Shielding factor (S)	
	Pt	Kel-F	Pt	Kel-F	Pt	Kel-F
2.5	0.71	0.74	0.3		0.71	
5		0.48				
10		0.31				

C.3 Oxygen reduction reaction studied in DTLFC.

Figure C.10 shows the ORR on the Pt(Pc) in the DTLFC. For the detection of H_2O_2 generated at the first electrode in the O_2 saturated electrolyte at various flow rates, the second electrode was held at 1.2 V vs. RHE. It was quite apparent that almost no H_2O_2 was generated between 0.7 V to 1.0 V. ORR generally precedes via $4e^-$ to H_2O. The increase of the current close to 0.05 V is due to the oxidation of the hydrogen which was produced at the first electrode. The position of the peak for the hydrogen oxidation indicates the time required for the solution to move from the first compartment to the second compartment (which is typically ~1 s at a flow rate of 5 µL/s in our case). Also negligible amount of H_2O_2 is detected.

The hysteresis observed between the anodic and cathodic scan in the kinetic region (0.8 to 1 V) is caused by the quasi-reversible oxidation/reduction of the Pt surface [12].

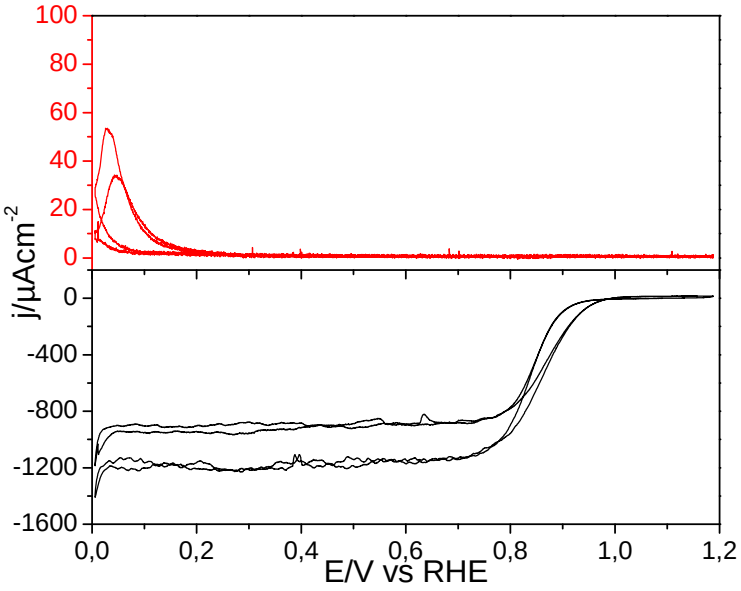

Figure C.10: Simultaneously recorded cyclic voltammograms of polycrystalline Pt in the first compartment and related current signals on a polycrystalline Pt held at 1.2 V in the second compartment of the in DTLFC containing oxygen saturated 0.5 M $HClO_4$ for various flow rates of 2.5, 5 µL/s respectively at sweep rate of 10 mV/s.

As mentioned earlier, the Pt surface state depends on the applied potential. At higher potentials (>0.8 V), the Pt surface is partially covered by adsorbed oxygen, and the kinetics of the ORR is different at different potentials. Therefore, a Tafel plot of the O_2 reduction kinetic current (defined as $I_{kin} = I_{lim} \times I/(I_{lim} - I)$) vs potential in fig. C.11 showed two different slopes. In the high potential region (E > 0.85 V) a Tafel slope of 75 mV/dec was obtained and in the low potential region (E < 0.8 V) a Tafel slope of 125 mV/dec was obtained (assuming the limitation of much smaller diffusion limited current was achieved under DTLFC Setup). This is in good agreement with that reported earlier for the Pt surface in the usual RRDE setup [13].

On a mixed oxide (Pt/PtO) surface, a Tafel slope of 60 mV/dec is indicative of a pseudo 2-electron transfer to the adsorbed O_2 as the rate determining step. Whereas, a Tafel slope of 120 mV/dec at clean Pt surface in lower potential region, the first-single electron is the rate determining step [13, 14].

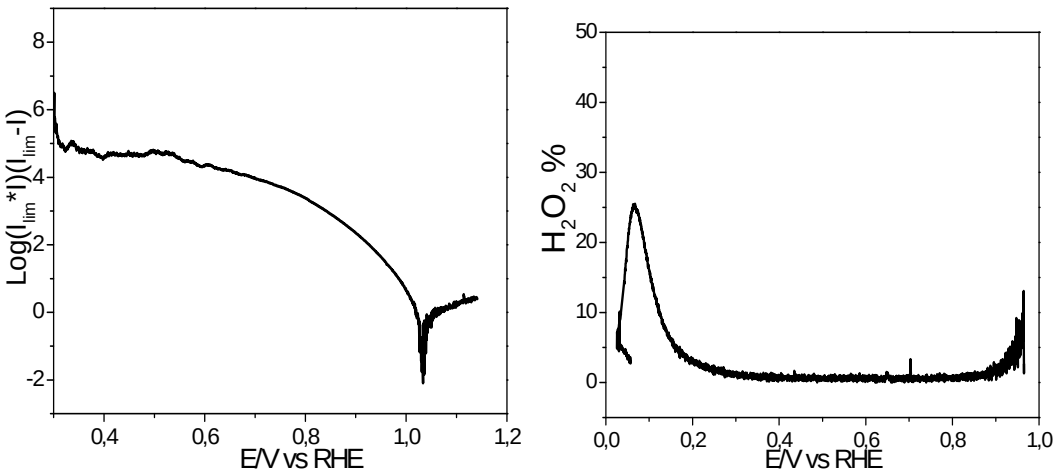

Figure C.11: Tafel plot (with and without capacitive current correction) and % yield of H_2O_2 are plotted for ORR at Pt surface in 0.5 M O_2 saturated $HClO_4$ under continuous flow rate of 2.5 µl/s respectively in a DTLFC setup.

The percentage yield of H_2O_2 vs. potential was plotted in fig. C.11 was calculated using following equation [15].

$$X(H_2O_2) = \frac{(2 \cdot I_R / N)}{((I_D + I_R)/N)} \qquad C.7$$

Where I_D and I_R are the currents of disk and ring and N is the collection efficiency. The higher value of H_2O_2 at lower potential around 0.05 V was due to the oxidation of H_2 generated at the Pt surface, whereas in the potential region from 0.2 V till 0.8 V no H_2O_2 was detected. 3~10 % of H_2O_2 was detected between 0.9 to 0.96 V in our setup.

References

[1] A. J. Appleby, Journal of Electroanalytical Chemistry 357:117 (1993).
[2] A. B. Anderson, J. Roques, S. Mukerjee, V. S. Murthi, N. M. Markovic, and V. Stamenkovic, Journal of Physical Chemistry B 109:1198 (2005).
[3] K. L. Hsueh, D. T. Chin, and S. Srinivasan, Journal of Electroanalytical Chemistry 153:79 (1983).
[4] N. M. Markovic and P. N. Ross, Surface Science Reports 45:117 (2002).
[5] H. Baltruschat, Journal of the American Society for Mass Spectrometry 15:1693 (2004).
[6] A. J. Bard and L. R. Faulkner, Electrochemical Methods: Fundamentals and Applications, John Wiley & Sons Inc., New York, Weinheim, 2001.
[7] H. Angerstein-Kozlowska, B. E. Conway, and W. B. A. Sharp, Journal of Electroanalytical Chemistry and Interfacial Electrochemistry 43:9 (1973).
[8] J. Yamada and H. Matsuda, Journal of Electroanalytical Chemistry 44:189 (1973).
[9] S. Vandeputte, B. Tribollet, A. Hubin, and J. Vereecken, Electrochimica Acta 39:2729 (1994).
[10] N. M. Markovic, H. A. Gasteiger, and P. N. Ross, The Journal of Physical Chemistry 99:3411 (1995).
[11] I. Katsounaros, W. B. Schneider, J. C. Meier, U. Benedikt, P. U. Biedermann, A. A. Auer, and K. J. J. Mayrhofer, Physical Chemistry Chemical Physics 14:7384 (2012).
[12] S. Gottesfeld, I. D. Raistrick, and S. Srinivasan, Journal of The Electrochemical Society 134:1455 (1987).
[13] U. A. Paulus, T. J. Schmidt, H. A. Gasteiger, and R. J. Behm, Journal of Electroanalytical Chemistry 495:134 (2001).
[14] J. Zhang, C. Song, and J. Zhang, in PEM Fuel Cell Electrocatalysts and Catalyst Layers, Springer London, 2008, p. 89.
[15] V. S. Murthi, R. C. Urian, and S. Mukerjee, Journal of Physical Chemistry B 108:11011 (2004).

Acknowledgement

I would like to express my deepest gratitude to my research advisor Professor Dr. Helmut Baltruschat. I am appreciative of his constant guidance, and support during the entire period of my research. This would not have been possible without his encouragement.

I appreciate the member of my thesis committee Prof. Dr. Thomas Bredow, Prof. Dr. Werner Mader and Prof. Dr. Karl Maier. I thank them for their availability and eagerness to evaluate my thesis.

I would like to thank Prof. Gary Attard and his research group in Cardiff, UK. I value his helpful suggestions and feedback on membrane electrode interface that is part of chapter 7.

I am thankful to DAAD for their helpful contribution to support my PhD.

My deepest gratitude to my research group in the University of Bonn, I have learned a lot working with them, Ali, Ana, Bondü, Ehab, Hatem, Jan, Podgaynyy, Martina, Mehdi, Molls, Nemes, Philipp, Sevda, Zan, and Frau Rossignol and Frau Thome for their support.
Special thanks to Dr. Ernst for his valuable suggestion on my work related to oxygen reduction and optimizing of DTLFC.
I am grateful to my Professors in Pakistan, Prof. Dr. Inam ul Haque, Prof. Dr. Muhammad Amjad, Prof. Dr. Jamil Anwar and Prof. Dr. Fazeelat Tahira for their guidance.
I would also like to thank my research group in University of Engineering and Technology, Lahore, Dr. Kaleem A. Asghar, Dr. Samina Akbar, Wajiha, Ashi, Shumaila, Hina, Sobia, Aakifa and Muqaddas.

I am appreciative of Dave Barrington for his useful suggestions on my writing.

My gratitude to my family; My late father Muhammad Murad, My mother, Hameeda Begum, my brothers and sisters for their support, love, and prayers.

Special thanks to my dear wife whose constant support; love and encouragement helped and sustained me all the way through.
Above all I thank almighty Allah.

Contributions

Publications

1. Iqbal, S.; Podgaynyy, N.; Ahmed, M.; Attard, G. A.; Baltruschat, H. Surface morphological studies of Nafion/Pt(100) interface Electrochim. Acta 2014, 144, 141-146.
2. Podgaynyy, N.; Iqbal, S.; Baltruschat, H. Friction force microscopy at a regularly stepped Au(665) electrode: Anisotropy effects. Surf. Sci. 2015, 631, 67-72.
3. Podgaynyy, N. Wezisla, S.; Molls, C.; Iqbal, S.; Baltruschat, H. Stick–slip behaviour on Au(111) with adsorption of copper and sulfate. Beilstein J. Nanotechnol. 2015, 6, 820-830.

Lectures

1. Quantitative determination of H_2Se formation at Chalcogenide surface: DEMS and SPM studies, GDCh, (Electrochemistry 2014 in Mainz) Sept. 22-24, 2014
2. Oxygen reduction at inductively heated modified chalcogenide surfaces, The 65^{th} annual meeting of the international society of electrochemistry, 31 Aug.-5 Sep. 2014, Lausanne, Switzerland
3. Electro-deposition of Se on Rh(111) and its *in situ* STM studies, The 63^{th} annual meeting of the international society of electrochemistry, 23rd Aug.- 2012, Prague, Czech Republic

Posters

1. Probing surface structure and coverage of Se adsorbed on Rh(111) using scanning probe microscopy, Zing conference, Spain, 2013.
2. Surface morphological studies of Nafion/Pt(100) interface, GDCh, (Electrochemistry 2012 in Munich) 2012
3. Electrochemical characterization of Ruthenium modified platinum surface, Electrochemistry Conference, University of Bath, UK, 2011